JETS AT LOW Q^2 AT HERA AND RADIATION DAMAGE STUDIES FOR SILICON SENSORS FOR THE XFEL

Dissertation
zur Erlangung des Doktorgrades
des Department Physik
der Universität Hamburg

vorgelegt von
Hanno Perrey
aus Bad Oldesloe

Hamburg
2011

Gutachter der Dissertation: Prof. Dr. Robert Klanner
Dr. Andreas Meyer

Gutachter der Disputation: Prof. Dr. Peter Schleper
Dr. Thomas Schörner-Sadenius

Datum der Disputation: 23.06.2011

Vorsitzender des Prüfungsausschusses: Dr. Georg Steinbrück

Vorsitzender des Promotionsausschusses: Prof. Dr. Peter Hauschildt

Dekan der MIN Fakultät: Prof. Dr. Heinrich Graener

Leiter des Department Physik: Prof. Dr. Daniela Pfannkuche

Abstract

In the first part this thesis, jet cross-sections were measured for inclusive jet, inclusive dijet, and inclusive trijet production at photon virtualities in the range of $10 < Q^2 < 100\,\mathrm{GeV}^2$.

The data analyzed were recorded with the ZEUS detector in the years 2004 – 2007 corresponding to an integrated luminosity of $296\,\mathrm{pb}^{-1}$. Events in neutral current deep inelastic scattering were selected in the above stated Q^2 region for an inelasticity of $0.2 < y < 0.6$. The jets were reconstructed in the Breit frame, where the virtual boson and the proton collide head on. The jets were required to carry a transverse momentum in the Breit frame of $p_{T,\mathrm{B}} > 8\,\mathrm{GeV}$ and to have a pseudorapidity in the laboratory frame in the range of $-1 < \eta_{\mathrm{lab}} < 2.5$. For the dijet and trijet samples, an additional requirement was imposed on the invariant dijet mass of $M_{jj} > 20\,\mathrm{GeV}$ to avoid phase space regions where the fixed order calculations are sensitive to infrared divergences. The presented analysis is the first jet analysis at such low values of Q^2 to exploit the full HERA-II ZEUS data set, and as such is performed at significant higher luminosities than previous publications.

Overall, the next-to-leading order (NLO) calculations correctly predict the measured cross-sections within the uncertainties in all studied quantities and over most of the investigated regions of phase space, except in the pseudorapidity region close to the proton beam direction ("forward" region) in inclusive jet production where the prediction is considerably below the data. The uncertainty of the NLO prediction, dominated by the uncertainty associated with the choice of the renormalization scale, is typically larger than the experimental uncertainty, which is for the most part dominated by the uncertainty of the jet energy scale.

The large theoretical uncertainties indicate the need for calculations including higher-orders. Such NNLO calculations will allow to fully exploit the sensitivity of the low Q^2 jet data in QCD PDF fits and in fits to extract values of α_s.

In the second part of this thesis, a study of radiation damage of silicon sensors by 12 keV X-rays for doses up to 1 GGy is presented. For this study, an irradiation facility has been set up at HASYLAB at DESY. Test structures (*gate-controlled diodes*) have been irradiated and the properties of the Si-SiO_2 interface under high irradiation have been studied using current versus voltage (I/V), capacitance versus voltage (C/V), and thermally depolarization relaxation current (TDRC) measurements. In addition to a strong increase and subsequent decrease of the interface current and the flat-band voltage as function of dose, strong hysteresis effects have been found.

The data can be qualitatively described by a model which includes interface traps and fixed oxide charges. The model predictions were used in combination with in C/V and TDRC measurements to separately determine the different types of traps present at the Si-SiO_2 interface and the charges in the SiO_2.

The parameters extracted in this studies are to be implemented into simulations with the goal of reproducing the measurements and later use them for the design of radiation hard sensors for the AGIPD project.

Kurzfassung

Im ersten Teil dieser Arbeit wird eine Messung von Jet-, Zweijet- und Dreijet-Wirkungsquerschnitten in tiefunelastischer Elektron-Proton-Streuung mit einer Virtualität des einlaufenden Photons im Bereich von $10 < Q^2 < 100\,\text{GeV}^2$ und einer Inelastizität im Bereich von $0.2 < y < 0.6$ präsentiert. Die verwendeten Daten wurden 2004 – 2007 mit dem Zeus-Detektor bei Hera aufgenommen und entsprechen einer Luminosität von $296\,\text{pb}^{-1}$. Für die Messung wurden Jets mit Hilfe des inklusiven k_T-Algorithmus im Breit-System rekonstruiert. Verlangt wurde für die Jets eine transversale Energie im Breit-System von mindestens 8 GeV und eine Pseudorapidität im Laborsystem im Bereich von $-1 < \eta_{\text{lab}} < 2.5$. Zu den Dijet- und Trijet-Wirkungsquerschnitten wurden weiter nur solche Ereignisse gezählt, deren zwei härtesten Jets eine invariante Masse von mehr als 20 GeV aufwiesen.

Insgesamt stimmen die Vorhersagen aus QCD-Rechnungen nächstführender Ordnung (NLO) innerhalb der Unsicherheiten mit den gemessenen Wirkungsquerschnitten über weite Bereiche des Phasenraums überein. Nur bei Pseudorapiditäten im Bereich nahe der Protonstrahlrichtung fallen die Vorhersagen für inklusive Jets deutlich zu niedrig aus. Generell sind die Unsicherheiten auf die NLO-Vorhersage dominiert von der Unsicherheit auf die Renormalisierungsskala und signifikant größer als die experimentellen Unsicherheiten, die durch die Unsicherheit der Jet-Energieskala bestimmt werden. Die große Unsicherheit der Theorievorhersage ist ein Indiz für die Notwendigkeit, höhere Ordnungen in den QCD-Berechnungen zu berücksichtigen.

Insbesondere mit diesen in Zukunft zu erwartenden QCD-Rechnungen höherer Ordnung sollen diese Daten benutzt werden, um die Parton-Dichteverteilungen des Protons und α_s genauer zu bestimmen.

Im zweiten Teil der Arbeit wird eine Untersuchung von Strahlenschäden durch Röntgenstrahlung an der Si-SiO_2 Oberfläche von Silizium-Sensoren präsentiert.

Wenn der Röntgenlaser Xfel am Deutschen Elektronen-Synchrotron (Desy) ab 2015 in Betrieb geht, werden die geplanten Silizium-Pixeldetektoren einem Fluss von 10^{16} Photonen/cm^2 von 12 keV ausgesetzt, was einer Oberflächendosis von etwa 1 GGy entspricht. Zur Untersuchung der auftretenden Effekte wurde eine Anzahl von Teststrukturen (*gate-controlled diodes*) am F3/F4-Strahl des Doris-Speicherrings mit 10 keV Photonen im Dosisbereich von 1 kGy bis 1 GGy bestrahlt. Mit Hilfe von Messungen der Kapazität (C/V) und des Stroms (I/V) als Funktion der angelegten Spannung, sowie TDRC-Messungen[1] wurden unter anderem die Änderungen der Flachbandspannung und des Oberflächenstroms als Funktion der Photondosis bestimmt. Beide Größen zeigen einen starken Anstieg und anschließenden Abfall als Funktion der Dosis. Weiter wurde ein ausgeprägter Hysterese-Effekt in den C/V-Kurven bestrahlter Strukturen beobachtet. Dieser wird als Hinweis auf das Vorhandensein von *border traps* gedeutet.

Mit Hilfe von Modelrechnungen können die C/V-Messungen qualitativ beschrieben werden. Dies erlaubt in Kombination mit TDRC-Messungen die getrennte Extrahierung der verschiedenen Oberflächenladungstypen. Die in dieser Studie bestimmten Parameter sollen in Simulationen einfließen, mit dem Ziel, die Messungen zu beschreiben und später strahlenharte Sensoren für das Agipd-Projekt zu entwickeln.

---

[1] **T**hermally **D**epolarization **R**elaxation **C**urrent

Contents

List of Figures

List of Tables

1. Introduction

This year, 2011, marks the 100th anniversary of E. Rutherford's famous interpretation [1] of the results from scattering experiments by H. Geiger and E. Marsden [2], which established the nuclear structure of the atom.

Since then, our knowledge of the constituents of matter and their interactions, as studied in particle physics, has increased spectacularly. Many more results from high-energy scattering experiments, such as performed at SLAC[1], DESY[2], FNAL[3], or CERN[4], helped to demonstrate the sub-structure of the proton and to confirm Quantum Chromodynamics (QCD), the theory of the strong nuclear force. Together with two additional gauge theories, Quantum Electrodynamics (QED) and the theory of the weak interactions, QCD forms the foundation of the so-called Standard Model of particle physics, a framework to describe all known fundamental forces with the exception of gravity.

All elementary particles of the Standard Model are grouped into two categories, namely fermions and bosons. The latter are the mediators of the forces, with the photon γ as the field quantum of the electromagnetic force, the W and Z as the quanta of the weak interaction, and the gluons g as the field quanta of the strong force. The Higgs boson H is believed to be responsible for the masses of all particles and is required for the unitarity of the Standard Model, but remains the only particle of the Standard Model that has not been observed yet.

The group of fermions comprises leptons and quarks. While leptons only interact through the electroweak force, the quarks additionally carry the charge of the strong force, called color, and therefore couple to the also colored gluons. One feature of the strong force is that quarks can not be observed directly, but are confined to colorless hadrons. Even though perturbative QCD calculations offer precise predictions of the strong interactions for many processes in high energy physics, the structure of these hadrons is not easily assessable through theoretical predictions. As perturbative approaches fail at low energies, theorists have turned toward numerical solutions using a formulation of QCD on a discrete space-time lattice, with exciting prospects [3]; nevertheless, the parton density functions (PDF), which describe the structure of the hadrons and are assumed to be universally valid, can currently only be determined from experimental data.

Therefore, high-energy scattering experiments at colliders continue to play an important role in the development of particle physics by testing theoretical predictions and by providing precision measurements as input for theoretical models.

Currently, the most prominent high-energy hadron storage rings operating are the

---

[1] **S**tanford **L**inear **A**ccelerator **C**enter

[2] **D**eutsches **E**lektronen-**Sy**nchrotron

[3] **F**ermi **N**ational **A**ccelerator **L**aboratory

[4] **C**onseil **E**uropéen pour la **R**echerche **N**ucléaire

TEVATRON, a proton-antiproton collider with a center-of-mass energy of almost 2 TeV and the LHC[5], a proton-proton collider running at a center-of-mass of 7 TeV with the aim to reach the unprecedented center-of-mass energy of 14 TeV by 2013. Such high energies open up possibilities to find new physics beyond the Standard Model and to verify one of its predictions through the discovery of the Higgs boson.

The HERA[6] storage ring, on the other hand, offered unique possibilities for instance for probing the structure of the proton or for precision tests of electroweak and QCD physics. Operated until June 2007 at DESY in Hamburg, HERA accelerated both electrons and protons up to the still unprecedented *ep* center-of-mass energy of 318 GeV. The phase space accessible by HERA consequently reached down to smallest values of the Bjorken scaling variable of $x_{Bj} \approx 10^{-5}$ and up to largest four-momentum transfers of $Q^2 \approx 10^5\,\mathrm{GeV}^2$.

For the study of the strong interaction, investigations of the details of the hadronic final state and specifically of jets are of particular interest, since the jets are the signature of the partonic interaction. At HERA, jet cross-sections have been measured for many years, and have been used e.g. to extract values of the strong coupling, α_s, [4–9] or as input to next-to-leading order (NLO) QCD fits to determine the proton parton density functions [10], where they had a significant impact on the uncertainty on the gluon contribution. The knowledge of the proton structure thus gained is of immense importance for hadron collider experiments such as the TEVATRON and the LHC. Furthermore, the sensitivity of the jet data to the hard QCD process has been used for stringent tests of predictions of perturbative QCD and the factorization ansatz in many regions of phase space.

In this work, jet cross-sections were measured for inclusive jet, inclusive dijet, and inclusive trijet production at low photon virtualities in the range of $10 < Q^2 < 100\,\mathrm{GeV}^2$. This region of Q^2 is expected to have a considerable impact on the QCD PDF fits due to its sensitivity to the gluon density [11].

Perturbative NLO QCD predictions were tested and compared to the measured cross-sections. The precision of the theoretical prediction was investigated in more detail by studying its dependence on the choice of the renormalization scale and by contrasting the calculations at different scales with the data.

The presented analysis is the first jet analysis at such low values of Q^2 to exploit the 2004 – 2007 ZEUS data set, and as such is performed at significantly higher luminosities than previous publications [7, 12].

The precision of the data and their impact on above mentioned QCD PDF and α_S fits is expected to be further improved by a combination of the measured cross-sections of the H1 and ZEUS experiments. In the case of the presented analysis, the strategy for the future combination has been significantly simplified by an agreement on the phase space, the observables, and the binning of the cross-sections.

With increasing center-of-mass energies and luminosities desired by the particle physicists for the experiments, the requirements on the detectors in terms of *radiation*

---

[5] **L**arge **H**adron **C**ollider

[6] **H**adron-**E**lektron-**R**ing-**A**nlage

hardness become more demanding and must be taken into consideration in the detector design.

However, the radiation tolerance of sensors depends significantly on the specific experimental conditions. The European X-ray Free Electron Laser (XFEL), currently under construction at DESY, will deliver ultra-short coherent X-ray flashes of the order of 10 fs duration at a peak brilliance of $5 \cdot 10^{33}$photons/s mm^2 mrad^2 (0.1% bandwidth), resulting in expected integrated photon fluxes of up to 10^{16}[12 keV photons/cm^2]. This poses unprecedented requirements to the detectors in terms of radiation tolerance.

Within the context of this thesis, silicon test structures were irradiated to study the effects on their electrical properties and with the aim to determine the relevant parameters for device simulations, thus allowing to reliably predict the sensor performance as function of dose.

This thesis is presented in two parts and is organized as follows:

- **Part one, Jets at Low Q^2 at HERA:**

  An overview of the key features QCD and the kinematics of $e^{\pm}p$ scattering at HERA are given in chapter 2. The ZEUS detector and its most relevant components for this analysis are outlined in chapter 3. Chapter 4 describes the leading order (LO) Monte Carlo generators used for correcting the data for detector effects and the NLO calculation used for the QCD predictions. Chapter 5 describes the electron finding algorithms and the reconstruction of the kinematic event variables. The online and offline selection criteria are presented in chapter 6. The correction procedures for the jet energy, and the Monte Carlo reweighting are discussed in chapter 7. Chapter 8 presents control distributions of the final data sample and introduces the method used in the unfolding of the cross-sections. Both the experimental and theoretical systematic uncertainties are estimated in chapter 9 before the measured cross-sections are presented and compared to perturbative QCD predictions in chapter 10. Finally, chapter 11 contains a summary and discussion of the results, as well as an outlook onto future prospects.

- **Part two, Radiation Damage Studies for Silicon Sensors for the XFEL:**

  A brief introduction to study at hand is given in chapter 12. The irradiation facility at HASYLAB and the irradiation procedure are presented in chapter 13. Chapter 14 gives an overview of the investigated test-structures, the experimental techniques used, and the implemented model calculations. The results of the measurements are then presented in chapter 15 and discussed as well as summarized in chapter 16.

Part I.

Jets at Low $\mathbf{Q^2}$ at HERA

2. Theoretical Framework

This chapter[1] gives an overview of the key features of quantum chromodynamics, the theory of strong interactions, and of the kinematics involved in $e^{\pm}p$ deep inelastic scattering at HERA. The definitions of jets through a jet reconstruction algorithm and of the Breit reference frame can be found at the end of this chapter.

2.1. Deep Inelastic $e^{\pm}p$ Scattering at HERA

HERA provided collisions between two distinct species of particles, namely electrons[2] and protons. The basic process of this interaction is shown in figure 2.1. At high proton momenta, the proton appears as stream of collinear free quarks and gluons.[3] In the *quark-parton model* as described below, the electron interacts with a quark inside the proton via the exchange of a $W^{\pm}$ boson in case of a charged current (CC) reaction, or a γ or a Z boson in case of a neutral current (NC) reaction.

Before detailing the kinematics involved in *ep* interactions, this section starts with a brief introduction to the history of *ep* experiments and early models aiming at a description of the underlying physics, as these offer an intuitive picture of the *ep* scattering process.

2.1.1. Quark-Parton Model

Following electron-hydrogen scattering experiments at HEPL[4] [14] in Stanford by R. Hofstadter, which mark the beginning of the search for the substructure of the proton, the construction of a new linear accelerator was proposed in 1957: SLAC[5]. One of the major objectives of SLAC was to investigate the structure of the proton and neutron [15] using a beam of 20 GeV electrons in elastic and inelastic scattering off liquid hydrogen.

In the late 1960s, measurements at SLAC [16–18] indicated a feature of the proton structure in inelastic *ep* scattering previously suggested by J. Bjorken [19] and termed *scaling*: in the limit of large energies, the proton structure was found to only depend on a dimensionless quantity, x_{Bj} [20].

---

[1] Parts of this chapter are based on a previous diploma thesis of the author [13].

[2] By reversing the magnet polarity and performing minor changes to the optics, the accelerator was able to switch between electron and positron operation. In the following, the term "electron" will be used to denote both the electron and the positron, unless explicitly stated otherwise.

[3] This is true for any reference frame with a high proton momentum, referred to as *infinite momentum frame*, where transverse momenta and masses are negligible. At HERA such a reference system is given by the laboratory system due to the high proton energy of 920 GeV.

[4] **H**igh **E**nergy **P**hysics **L**aboratory

[5] **S**tanford **L**inar **A**ccelerator **C**enter

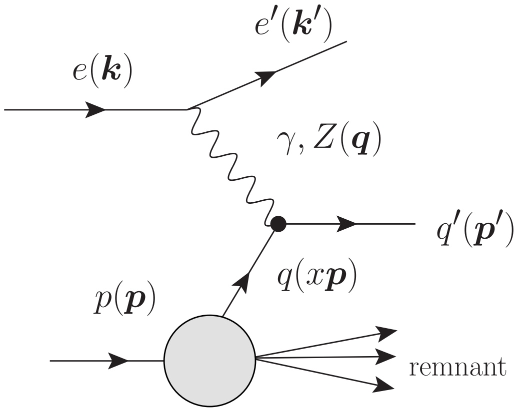

Figure 2.1: The kinematic variables of $e^{\pm}p$ scattering at HERA.

R. Feynman gave a physical explanation to scaling: in his *parton model*, an electromagnetic or electroweak probe scatters elastically off a point-like constituent of the proton, the parton [21,22]. This interpretation naturally leads to the Bjorken scaling behavior, as the scattering center is a point with no additional structure. Feynman introduced the term *deep inelastic scattering* (DIS) to describe the kinematic realm of these scattering processes.

M. Gell-Mann [23] and G. Zweig [24] independently used the concept of proton constituents to explain the diversity of hadronic resonances in hadron spectroscopy as excitations of "quarks". These were later identified with the partons considered by Feynman. This gave rise to the *quark-parton model* (QPM) which could be used to explain an *ep* scattering process as depicted in figure 2.1.

In the QPM, the proton is assumed to consist of point-like constituents, each with a spin of $1/2$. At large energies, *inelastic* electron-proton scattering is then described by the *elastic* scattering of the electron off a "free" quark[6], a process with well-known cross-section [25].

The QPM was later superseded by Quantum Chromodynamics (QCD) as described in the next section. However, the QPM is still useful in the interpretation of the kinematic variables in *ep* scattering, as discussed below.

2.1.2. Kinematic Variables

The analysis presented in this thesis is only concerned with neutral current (NC) reactions in which generally either a γ or Z boson is exchanged.[7] Resulting from the exchange and the part of the proton which is not participating in the hard scattering, a number of hadrons in the final state are created. Therefore, the scattering process

---

[6] This is a valid assumption e.g. in the infinite momentum frame.

[7] In this analysis, the exchanged boson is practically always a photon, since in the region of virtuality investigated $Q^2 \ll M_Z$ always holds.

depicted in figure 2.1 can be written symbolically as

$$e + p \rightarrow e' + X \ ,$$

with the proton p and the hadrons in the final state X. This kind of reaction with an exchanged photon is typically described by the following kinematic variables:

- The *photon virtuality* Q^2: the negative squared momentum transfer from the electron to the parton in the proton,

  $$Q^2 = -\boldsymbol{q}^2 = (\boldsymbol{k} - \boldsymbol{k}')^2 \ , \tag{2.1}$$

  where $\boldsymbol{k}$ and $\boldsymbol{k}'$ are the four-momenta of the incoming and outgoing electron respectively, and $\boldsymbol{q}$ is the momentum transfer.

- The Bjorken scaling variable x: interpreted in the QPM as the fraction of the proton momentum carried by the struck quark,

  $$x = \frac{Q^2}{2\boldsymbol{p} \cdot \boldsymbol{q}} \ , \tag{2.2}$$

  with the four-momentum of the proton $\boldsymbol{p}$.

- The *inelasticity* y: the fraction of the electron energy transferred to the proton,

  $$y = \frac{\boldsymbol{p} \cdot \boldsymbol{q}}{\boldsymbol{p} \cdot \boldsymbol{k}'} \ . \tag{2.3}$$

When neglecting the masses, the above kinematic variables are related by

$$Q^2 = s \cdot x \cdot y \ , \tag{2.4}$$

with s as the square of the center-of-mass energy of the electron-proton system $E_{\mathrm{CMS}} = \sqrt{s} = \sqrt{(\boldsymbol{k} + \boldsymbol{p})^2}$, and only two of the above kinematic variables are needed to fully describe the $e^{\pm}p$ scattering kinematics for a given E_{CMS}. The center-of-mass energy for the photon-proton system W is given by

$$W = 2\sqrt{4yE_eE_p - Q^2} \ . \tag{2.5}$$

For large values, Q^2 provides a hard scale of the ep interaction needed for perturbative calculations. This holds true down to a limit of Q^2 in the order of a few GeV. Events with $Q^2 \gg 1\,\mathrm{GeV}^2$ are classified as deep inelastic scattering (DIS), while events with a lower value of Q^2 are referred to as photoproduction (PhP). Due to the low virtuality of the photon in PhP events, the exchanged photon is said to be quasi-real.

2.2. Quantum Chromodynamics

The quark-parton model introduced the idea of quarks as the hadronic substructure, but it couldn't offer explanations for various observations, such as the non-observation of free quarks and the missing momentum in the sum of the proton's constituents momenta. This required a new theory: Quantum Chromodynamics (QCD).

QCD is a field theory of the strong nuclear force presented in the early 1970s [26]. It is a non-Abelian gauge theory based on a SU(3) symmetry and introduces a new quantum property, called color charge, to which only the strong force couples. It exhibits three quantum states denoted by *red*, *green*, and *blue*. Strong interactions between color-charged particles are mediated by 8 colored massless gluons. Direct evidence for the gluon was first found in e^+e^- collisions at PETRA [27–32]. The self-interaction of the gluon contributes to some remarkable features of QCD which will be discussed in sections 2.2.1 and 2.2.2.

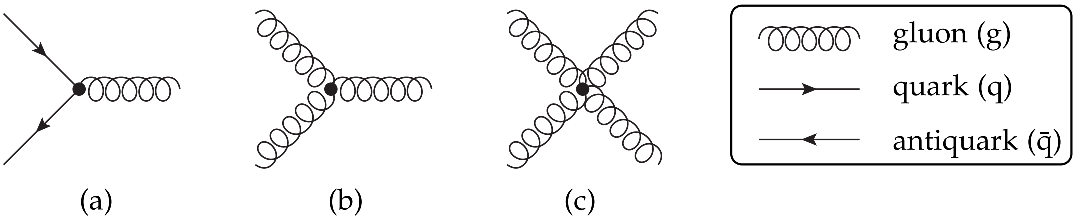

Figure 2.2: The fundamental vertexes of QCD.

Figure 2.2 shows the fundamental interaction vertexes of QCD: the coupling of two (anti)quarks and a gluon and the coupling of three (four) gluons. From these vertexes, Feynman diagrams are constructed, where each vertex is associated with one power of the strong coupling constant, α_s.

In *ep* scattering, gluon Bremsstrahlung ($q \to qg$) and gluon splitting ($g \to q\bar{q}$) result in gluonic "radiative corrections" to the QPM-type process depicted in figure 2.1 and give rise to additional processes. Examples for such processes are shown in first order of the strong coupling parameter, $\mathcal{O}(\alpha_s)$, in figure 2.3. In this order of α_s, the scattering process in which a quark from the proton emits a gluon is referred to as *QCD Compton* (QCDC), while the process involving quark-pair production by a gluon emitted from the proton is referred to as *boson-gluon fusion* (BGF).

The final state partons cannot be directly detected, as will be discussed in the following.

2.2.1. Renormalization, Asymptotic Freedom, and Confinement

In quantum field theories like QCD and QED, physical quantities such as cross-sections can analytically be calculated using a perturbation series in powers of the coupling parameter. This perturbative approach might provide realistic predictions even with only a limited number of perturbative orders if the coupling parameter is sufficiently small ($\ll 1$) and the series converges quickly enough.

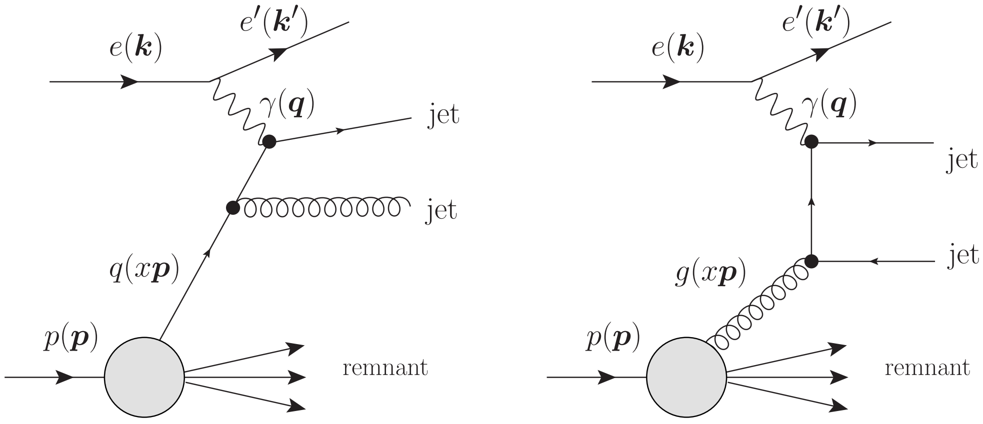

(a) QCD Compton (b) Boson-Gluon Fusion

Figure 2.3: Examples of leading-order ($\mathcal{O}(\alpha_s)$) processes in deep inelastic scattering.

In such a QCD calculation of a physical quantity in orders of the coupling parameter α_s, ultraviolet divergences occur, caused by the integration over all possible momenta in virtual loop corrections. These divergences are removed by a procedure known as *renormalization* [33] that introduces a new energy or momentum scale μ_R as arbitrary parameter, which is commonly identified with a physical hard scale of the process under study [34]. α_s may then be written as [25]

$$\alpha_s(\mu_R^2) = \frac{12\pi}{(33 - 2N_f)\ln(\mu_R^2/\Lambda^2)}, \tag{2.6}$$

where N_f is the number of active quark flavors at the energy scale μ_R and the parameter Λ is the "cut-off" scale of QCD, which marks the energy scale where $\alpha_s(\mu_R^2)$ diverges and perturbative expansions in α_s are no longer meaningful. This fundamental parameter needs to be determined experimentally and has a value[8] in the order of 300 MeV [35].

Because of its energy-scale dependence, $\alpha_s(\mu_R^2)$ is called a *running coupling constant*. Figure 2.4 shows an example of the dependence of the strong coupling on the energy scale from Hera jet data along with the QCD prediction. These data result in an average value for α_s with the mass of the Z boson chosen as reference scale of $\bar{\alpha}_s(M_Z) = 0.1186^{\pm 0.0011\,\text{(exp.)}}_{\pm 0.0050\,\text{(theo.)}}$ [36].

For large values of the renormalization scale ($\mu_R^2 \gg \Lambda^2$) corresponding to high momentum transfers and small distances ($\ll 1\,\text{fm}$), equation 2.6 demonstrates the property of *asymptotic freedom* [37,38] inherent to QCD: A vanishing strong coupling ($\alpha_s \to 0$ for $Q^2 \to \infty$) leading to quarks that behave like weakly bound or free particles. At such a high energy scale, which is referred to as *hard* scale, α_s is sufficiently small

---

[8] This value for Λ corresponds approximately to the inverse of the radius of a nucleus, $\Lambda^{-1} \approx 1\,\text{fm}$.

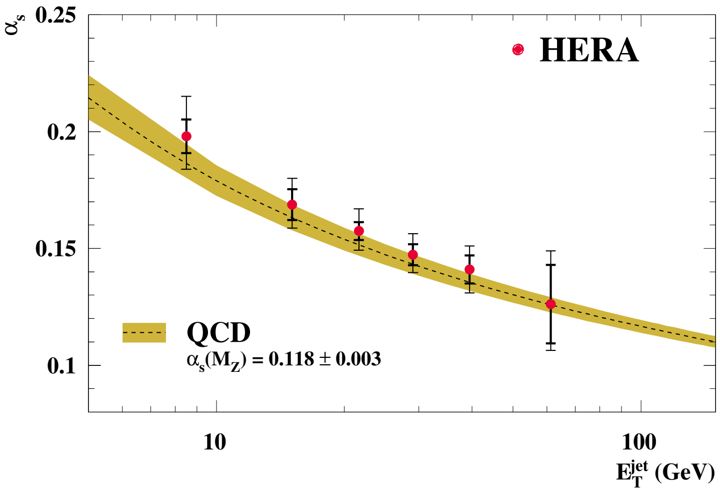

Figure 2.4: α_s as function of the transverse energy of the hardest jet E_T^{jet1} from HERA jet data and the QCD prediction of the running of α_s [36].

to allow the prediction of physical quantities through perturbative calculations.

At small energies and large distances (referred to as *soft* scales) the strong coupling rises steeply, leading to the *confinement* of quarks and gluons within hadrons. When trying to separate two quarks, the required energy for the process increases with the distance until it reaches the point where the potential energy built up in the color field between the quarks can be minimized through the creation of two new quarks out of the vacuum. This process results, after all created quarks and gluons have been combined into colorless hadrons, in the hadron showers observed in high-energy scattering experiments. Even though no isolated quark can be detected, many properties of the original outgoing particle can be reconstructed from the final hadronic state, as described later in this chapter.

This process of *fragmentation*, the transformation of colored partons into colorless hadrons, is not accessible by perturbative methods but can be described by approximate models as detailed in chapter 4.1.2.

2.2.2. The Factorization Theorem, Parton Density Functions, and Parton Evolution

The basic idea behind the factorization theorem is that physical processes at very different scales do not interfere with each other, i.e. they factorize. In consequence, the cross-section σ of an observable in ep scattering can be written as the convolution of two terms: the perturbatively calculable hard scattering cross-section, $\hat{\sigma}_{i\gamma}$, for the short-distance interaction and non-perturbative (incalculable) parton densities, f_i, describing the long-distance interaction with the proton structure,

$$\sigma = \sum_i f_{i/p}(x, \mu_F^2) \otimes \hat{\sigma}_{i\gamma}(x, \alpha_s(\mu_R^2), \mu_F^2) \quad . \tag{2.7}$$

Here, the sum runs over all partons i of the proton, x denotes the fraction of the proton momentum carried by the struck quark, α_s denotes the strong coupling, and μ_R the renormalization scale as introduced in the previous section. The scale at which the perturbatively calculable hard scattering cross-section is separated from the non-perturbative parton densities is called the *factorization scale* and denoted by μ_F. It defines the boundary at which the cross-section is factorized: A parton emitted from the incoming quark or gluon at a scale larger than μ_F is considered part of the hard interaction, while a parton emitted at a smaller scale than μ_F is considered part of the proton. The latter is absorbed into the *parton density functions* (PDFs), $f_{i/p}(x, \mu_F^2)$, corresponding to probability densities of finding a parton of type i with a momentum fraction x when probing the hadron at a scale μ_F. Such density functions are non-perturbative objects which contain information about the structure of the respective hadron. They need to be extracted from experimental data and are assumed to be universally valid, i.e. they do not depend on the hard process under study.

However, since the result of the extraction depends on the parametrization and the data set used, there is a large number of different PDF sets available [39,40]. Figure 2.5 shows examples of recently extracted proton PDFs from Hera data at a specific value of $Q^2 = 10\,\text{GeV}^2$ of the factorization scale. The figure clearly demonstrates the strong increase of the gluon contribution to the proton structure at low values of x and the contribution from valence quarks at x values of ~ 0.25.

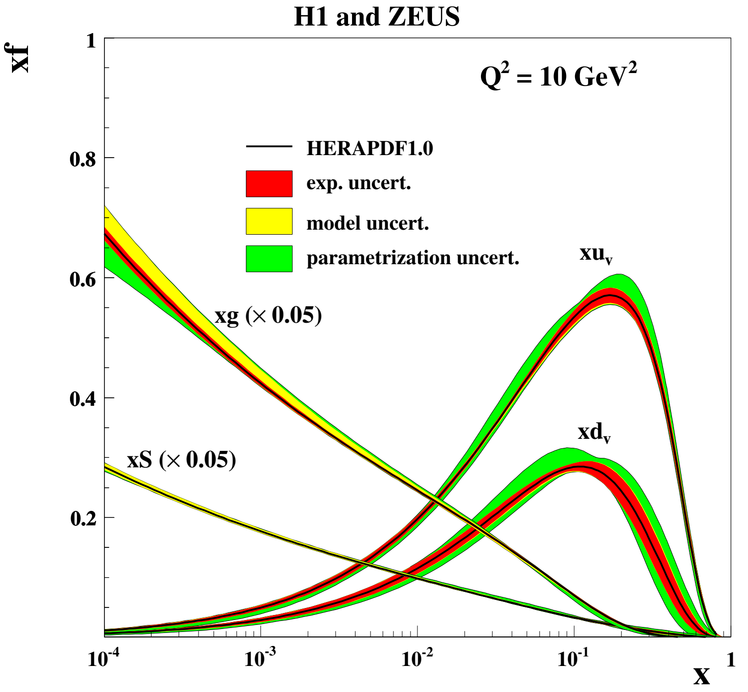

Figure 2.5: Parton density functions for valence-quarks, sea-quarks, and the gluon of the proton at $Q^2 = 10\,\text{GeV}^2$, from the Herapdf1.0 fit [41]. The experimental, model and parametrization uncertainties are shown separately.

Both the renormalization scale μ_R and the factorization scale μ_F are arbitrary parameters and are an artifact of the omission of higher orders in the perturbative calculations, while the actual physics is independent of μ_R and μ_F. The sensitivity of the fixed order predictions on the choice of scales is therefore considered an estimate of the effects of omitting higher orders from the calculations. This uncertainty associated with the choice of scales is usually the dominant theoretical uncertainty.

While the actual parton density functions cannot be assessed by perturbative QCD calculations, the dependence of the PDFs on the scale μ_F can be described. For this purpose, diagrams of processes such as depicted in figure 2.6 for gluon Bremsstrahlung are considered, in which n partons are emitted before the hard scattering process. Due to the large number of such processes and mathematical difficulties such as ultra-violet divergences, the contribution of each to the cross-section is approximated by selectively adding the respective terms up.

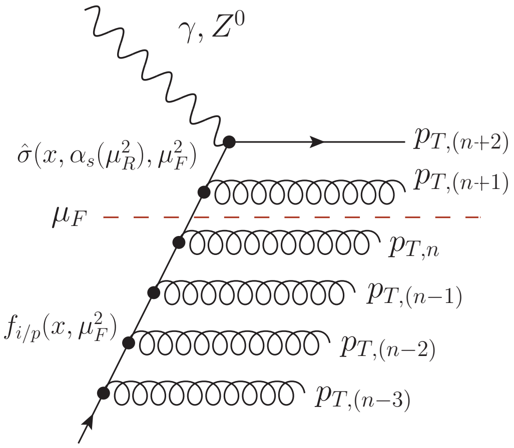

Figure 2.6: Process of higher order in α_s: Multiple gluon emissions from a quark line with transverse momenta p_T. The factorization of emissions in hard scattering process ($\hat{\sigma}$) and PDF ($f_{i/p}$) at scale μ_F is indicated by a dashed line.

In the DGLAP[9] approach [42–45], this is accomplished through *splitting functions*, e.g. $P_{qq}(z)$, $P_{qg}(z)$, and $P_{gg}(z)$, which can be interpreted as probability distributions for the respective transitions $\mathrm{q} \rightarrow \mathrm{q}(z)\mathrm{g}(1-z)$ (gluon Bremsstrahlung), $\mathrm{g} \rightarrow \mathrm{q}(z)\bar{\mathrm{q}}(1-z)$ (gluon splitting), and $\mathrm{g} \rightarrow \mathrm{g}(z)\bar{\mathrm{g}}(1-z)$, where z is the fraction of the initial parton's momentum.

The change of the gluon and quark densities with $\ln Q^2$ can then be calculated with the coupled DGLAP equations

---

[9] **D**okshitzer, **G**ribov, **L**ipatov, **A**ltarelli, and **P**arisi.

$$\begin{aligned}\frac{\partial q_i(x,Q^2)}{\partial \ln Q^2} &= \frac{\alpha_s(Q^2)}{2\pi}\sum_j \int_x^1 \frac{\mathrm{d}\xi}{\xi} q_j(\xi,Q^2) P_{q_i q_j}\left(\frac{x}{\xi},\alpha_s(Q^2)\right) \\ &\qquad + g(\xi,Q^2) P_{q_i g}\left(\frac{x}{\xi},\alpha_s(Q^2)\right) \quad \text{, and} \qquad (2.8a)\\ \frac{\partial g(x,Q^2)}{\partial \ln Q^2} &= \frac{\alpha_s(Q^2)}{2\pi}\sum_j \int_x^1 \frac{\mathrm{d}\xi}{\xi} q_j(\xi,Q^2) P_{g q_j}\left(\frac{x}{\xi},\alpha_s(Q^2)\right) \\ &\qquad + g(\xi,Q^2) P_{gg}\left(\frac{x}{\xi},\alpha_s(Q^2)\right) \quad . \qquad (2.8b)\end{aligned}$$

In the DGLAP approximation, only terms of the form $\alpha_s \ln(Q^2/\mu_F^2)$ are considered, corresponding to diagrams such as shown in figure 2.6 where the partons are strongly ordered by their transverse momenta, i.e. $\mu_F \ll p_{1,T}^2 \ll p_{2,T}^2 \ll \ldots \ll p_{n,T}^2 \ll Q^2$.

Alternative parton evolution schemes to the DGLAP formalism are the BFKL[10] [46, 47] approach and the CCFM[11] [48–50] model, of which the latter attempts a combination of DGLAP and BFKL.

The BFKL approach offers a formalism for the resumation of multiple gluon emissions in the small-x regime. The evolution is performed in terms of $\ln(1/x)$, corresponding to an ordering of the partons in the diagram of figure 2.6 with respect to their longitudinal momenta, x_i, instead of $p_{i,T}^2$: $x_0 \gg x_1 \gg \ldots \gg x_n \gg x$ [51].

Consequently, the BFKL evolution results in a larger fraction of small-x events with partons emitted at large fractions of the proton's momentum, i.e. at pseudorapidities close to the proton beam direction (referred to as "forward" region).

2.3. The inclusive $e^{\pm}$p Cross Section

The double-differential cross-section for neutral current deep inelastic $e^{\pm}p$ scattering is given by

$$\frac{\mathrm{d}^2\sigma(e^{\pm}p)}{\mathrm{d}x\,\mathrm{d}Q^2} = \frac{2\pi\alpha^2}{xQ^4}\left[Y_+ F_2(x,Q^2) \mp Y_- xF_3(x,Q^2) - y^2 F_L(x,Q^2)\right] \ , \qquad (2.9)$$

where

$$Y_{\pm} = 1 \pm (1-y)^2 \ . \qquad (2.10)$$

The dimensionless functions F_L, F_2, and F_3 are called *structure functions*; they define the structure of the proton: in first order approximation, F_L describes the contribution to the cross-section through the absorption of longitudinally polarized virtual photons, F_2 the electromagnetic structure due to the electrically charged quarks, and F_3 takes the exchange of parity violating Z particles into account. Additionally, F_2 and F_3 include γ-Z interference terms, which are suppressed in the Q^2 region investigated in this analysis, however. The contributions from F_L are typically small and F_3 is generally

---

[10] **B**alitsky, **F**adin, **K**uraev, and **L**ipatov.

[11] **C**iafaloni, **C**atani, **F**iorani, and **M**archesini.

negligible for $Q^2 \ll M_Z^2$, which is the case in this analysis. F_3 can therefore be omitted in equation 2.9.

The structure function F_2 quantifies the contribution to the cross-section from the absorption of transversely polarized virtual photons and dominates the cross-sections in the kinematic region considered in this analysis. In leading order, F_2 can be written in terms of the parton density functions (PDFs), $f_{i/p}$, of the quarks and anti-quarks of the proton,

$$F_2(x, Q^2) = \sum_i e_i^2 [x f_{i/p}(x, Q^2) + x \bar{f}_{i/p}(x, Q^2)] \ , \tag{2.11}$$

where the sum runs over all quark flavors i, e_i is the electric charge of quark flavor i in units of elementary charge, and $f_{i/p}$ represents the probability density of the quarks of a given flavor inside the proton. Even though F_2 of equation 2.11 shows no direct dependence on the gluon distributions within the proton, the gluon emissions from the constituent partons are accounted for through the evolution realized by equation 2.8. The subsequent dependence of F_2 on Q^2 is called *scaling violation* and makes F_2 indirectly dependent on the gluon density.

This dependence is demonstrated in figure 2.7, which shows the reduced cross-sections, $\sigma_{r,\mathrm{NC}}^{\pm} = (\mathrm{d}^2 \sigma_{\mathrm{NC}}^{e^{\pm}p} / \, \mathrm{d}x \, \mathrm{d}Q^2) \cdot (Q^4 x / 2\pi\alpha^2 Y_+)$, in neutral current DIS for HERA and fixed-target data as function of Q^2 at different values of x. At values of $x \approx 0.25$, where the contributions from valance quarks peak as shown in figure 2.5, the cross-section distributions do not exhibit any slope in Q^2, which is referred to as "scaling". On the other hand, at higher values of x the reduced cross-section drops while at lower values of x it rises with increased Q^2. This is the result of the ability to resolve more "soft" gluons in the proton at higher Q^2 which depletes the large-momentum quark-component ($x \approx 1$) and shifts it toward low momentum ($x \approx 0$) [25].

2.4. Hadronic Final States and the Definition of Jets

As discussed earlier in this chapter, individual quarks are not measurable in the detector. Instead, showers of hadrons originating from the quarks of the original hard scattering and the subsequent parton showering are observed. However, the four-vectors of these hadron showers are closely related to the initial outgoing partons [52, 53], as the hard partonic scattering and the hadronization happen on different time scales and distances and little to no transverse momentum is generated in the parton shower.

Therefore, the study of these bundles of almost collinear hadrons, or *jets*, offers a handle on the kinematic properties of the hard partonic scattering.

The transverse energy, the pseudorapidity[12], and the azimuthal angle of the jet are typically defined according to the Snowmass convention [54] as:

$$E_T^{\mathrm{jet}} = \sum_i E_{T,i}, \tag{2.12}$$

---

[12] The pseudorapidity of a parton is defined as $\eta = -\ln \tan(\theta/2)$, where θ denotes the polar angle of the parton.

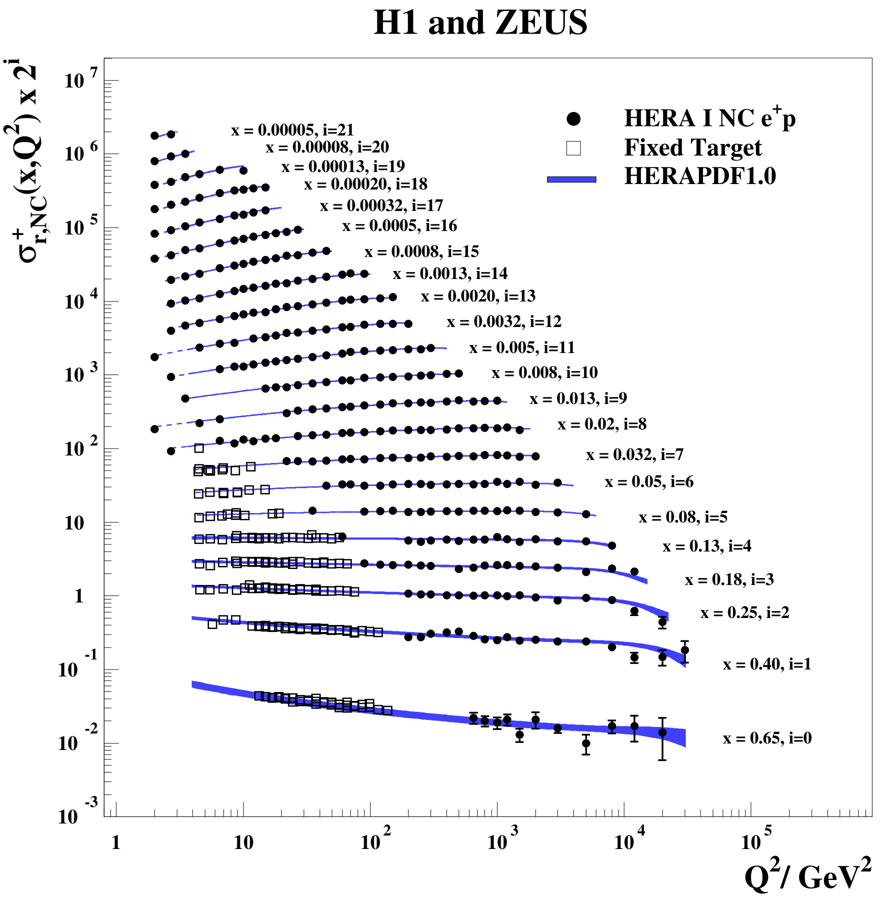

Figure 2.7: HERA combined NC ep reduced cross-sections, $\sigma^{\pm}_{r,\mathrm{NC}} = (\mathrm{d}^2\sigma^{e^{\pm}p}_{\mathrm{NC}} / \mathrm{d}x\,\mathrm{d}Q^2) \cdot (Q^4 x / 2\pi\alpha^2 Y_+)$, and fixed-target data as function of Q^2 compared to the HERAPDF1.0 fit [41].

$$\eta^{\text{jet}} = \frac{\sum_i E_{T,i} \cdot \eta_i}{E_T^{\text{jet}}}, \text{ and} \tag{2.13}$$

$$\phi^{\text{jet}} = \frac{\sum_i E_{T,i} \cdot \phi_i}{E_T^{\text{jet}}}, \tag{2.14}$$

where the sum runs over all particles grouped into the jet. As this analysis is primarily concerned with jets, the superscript "jet" will only be used where explicitly needed for clarity.

For massless jets, as considered throughout this analysis, the four-vector of the jet can be written as

$$\boldsymbol{p} = \begin{pmatrix} E \\ p_x \\ p_y \\ p_z \end{pmatrix} = E_T \begin{pmatrix} \cosh\eta \\ \cos\phi \\ \sin\phi \\ \sinh\eta \end{pmatrix} . \tag{2.15}$$

In this notation, the invariant mass of a dijet system M_{jj} is given by

$$M_{jj} = \sqrt{(\boldsymbol{p}_1 + \boldsymbol{p}_2)^2} = \sqrt{2E_{T,1} \cdot E_{T,2} \cdot [\cosh(\eta_1 - \eta_2) - \cos(\phi_1 - \phi_2)]} . \tag{2.16}$$

More generally, the invariant mass of an n-jet system is given by

$$M = \sqrt{\left(\sum_i^n \boldsymbol{p}_i\right)^2} . \tag{2.17}$$

The absolute value of the center-of-mass scattering angle is given by

$$|\cos\theta^*| = |\tanh\left(\frac{\eta_1 - \eta_2}{2}\right)| . \tag{2.18}$$

In leading order, the proton's momentum fraction entering into the hard scattering is given by

$$\xi = x_{\text{Bj}} \left(1 + \frac{M_{jj}^2}{Q^2}\right) . \tag{2.19}$$

Jet Reconstruction

The actual assignment of individual particles of the hadronic final state to a jet is performed by a jet finding algorithm. There are two major requirements for such an algorithm: The returned result should not be different if an infinitesimally small amount of energy is added, nor should it change when two collinear particles are combined into a single one with the same overall four-momentum. These two criteria are called infrared safety and collinear safety [55]. The algorithm is further required to be applicable to partons from next-to-leading order calculations, to partons and hadrons from Monte Carlo generators, as well as to real or simulated detector information.

One commonly used jet finding algorithm at HERA is the k_T-clustering algorithm [56, 57], which offers inherent infrared- and collinear-safe cross-sections at any order of pQCD calculations, and has been demonstrated to result in the smallest uncertainties in the reconstruction of jets in *ep* collisions [58].

Other choices for modern jet finding algorithms include recent developments specifically for the reconstruction of jets in hadron-hadron collisions at the LHC: the anti-k_T [59] and the "Seedless Infrared-Safe" cone (SIScone) [60] algorithms. A recent study comparing these two algorithms with the k_T algorithm in NC *ep* collisions at ZEUS showed comparable performance and precision for all jet finding procedures [58].

This analysis employs the k_T-clustering algorithm, which reconstructs jets by the iteration of merging two close clusters of particles. For each potential pair of particles i and j a "distance" d_{ij} is calculated, quantifying the separation in phase-space of the two particles:

$$d_{ij} = \min(E_{T,i}^2, E_{T,j}^2)[(\eta_i - \eta_j)^2 + (\phi_i - \phi_j)^2] \ . \tag{2.20}$$

Additionally, for each particle i the quantity

$$d_i = E_{T,i}^2 \cdot R^2 \tag{2.21}$$

is calculated, where R is a radius parameter that is chosen to be $R = 1$ for this analysis. Two particles k and l are merged using the rules 2.12 – 2.14 if d_{kl} was the smallest number obtained for the parameters d_{ij} and d_i. This process is repeated until d_k becomes the smallest number, at which point the object k is considered a jet and removed from further calculations.

In this analysis the k_T-clustering algorithm is used in the longitudinally invariant inclusive mode [57] according to the Snowmass convention [54] for both the offline jet selection in data and Monte Carlo, as well as the jet selection in the NLO QCD calculations.

2.5. The Breit Reference Frame

The Breit reference frame [51, 61] is defined as the frame where the exchanged virtual boson is fully space-like, with 3-momentum $\boldsymbol{q} = (0, 0, -Q)$, and collides head-on with the initial state quark from the proton, i.e.

$$\boldsymbol{q} + 2x \cdot \boldsymbol{p} = 0 \ . \tag{2.22}$$

In the quark-parton-model process, the quark, when absorbing the virtual boson, is back-scattered without generating any transverse momentum. Only in processes of $\mathcal{O}(\alpha_s)$ and above, with two partons in the final state, transverse momentum is observed in the Breit frame.

The reconstruction of jets in the Breit frame is therefore ideal for the study of QCD processes as QPM processes can be suppressed by simply requiring a minimum transverse energy of the jets in the Breit frame.

Using the Breit frame in jet analyses has further advantages: from the experimentalist point of view it offers a maximum separation between the hadronic final state and the proton remnant; for the theorist, it allows complete factorization between the beam fragmentation and the hard process [62] when reconstructing the jets with the k_T algorithm.

In the analysis presented in this work, quantities defined with respect to the Breit reference frame are denoted in the subscript either with "Breit" or just "B".

2.6. Summary

High-energy *ep* scattering is a valuable tool for the study of the proton structure and for tests of QCD, the established theory of the strong interaction.

QCD describes the interaction between the constituents of the proton, quarks and gluons, and explains why no free parton is observed. Instead, in deep-inelastic scattering experiments, collinear showers of colorless hadrons are observed in the detector, which are referred to as jets.

With the help of well-defined algorithms, the jets can be reconstructed and used to gain insights into underlying parton dynamics in the hard scattering process.

3. Experimental Setup

This chapter[1] introduces the Zeus experiment, which was operated during the years 1992 – 20007 at the Hera accelerator located at Desy, and which recorded the data analyzed in the study presented here.

3.1. DESY and HERA

The "Deutsches Elektronen Synchrotron" (Desy), Hamburg, Germany, is one of the leading particle accelerator centers in the world. It is a member of the German Helmholtz Association of large-scale research facilities. The "Hadron-Elektron-Ring-Anlage" (Hera) was the largest accelerator ring located at Desy. Operating during the years 1992 – 2007, it was the world's first and only collider to study the interactions between beams of electrons[2] and protons, two distinct species of particles, at center-of-mass energies of up to $\sim 318\,\mathrm{GeV}$. As such, Hera has been termed a "super electron microscope" and provides new insights into the structure of the proton and the nature of the fundamental forces.

Due to the large differences in mass of the electron and the proton, two distinct pre-accelerator setups were needed before the beams could be injected into Hera as shown in figure 3.1.

For the protons, the acceleration process occurred in four stages. First, H^- ions were accelerated to an energy of 50 MeV in a linear accelerator. These ions were then stripped of their electrons before being injected into the Desy III storage ring. After further acceleration, the protons were passed on to the Petra II storage ring, where they reached an energy of 40 GeV, with which they were injected into Hera. Here they were accelerated to their their final energy, which was upgraded from 820 GeV to 920 GeV in 1998, resulting in a center-of-mass energy of $\sqrt{s} \approx 318\,\mathrm{GeV}$. The limiting factor of the proton energy were the strengths of the superconducting magnets guiding the proton beam.

The acceleration process of the electrons also occurred in four stages. After an acceleration up to 450 MeV by the linear accelerators Linac's I and II, the beam of electrons was transferred to Desy II. There it reached an energy of 7 GeV, was passed on to Petra II and further accelerated before being injected into Hera at an energy of 12 GeV. The final electron energy was 27.5 GeV. It was limited by the radio frequency power required to compensate for energy losses due to synchrotron radiation.

Protons and electrons each traveled through an evacuated storage ring, which could hold as many as 210 bunches of more than 10^{10} particles each. Both were collided at

---

[1] Parts of this chapter are based on a previous diploma thesis of the author [13].

[2] In the context of this work, the term "electron" is used to denote both the electron and the positron, unless explicitly stated otherwise.

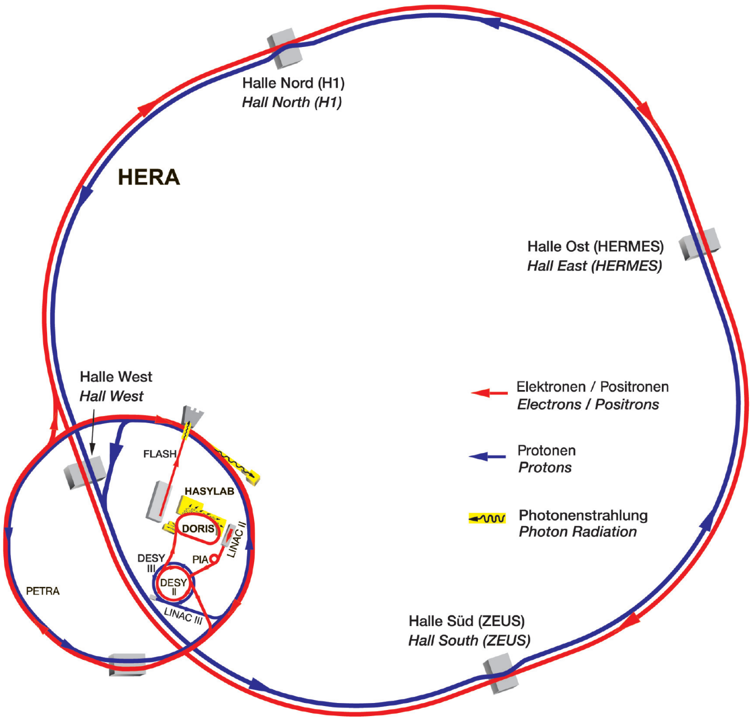

Figure 3.1: Schematic layout of Hera and its pre-accelerator system. © Desy

the two interaction points of Hera: inside the Zeus and the H1 detectors, located in the south and north halls, respectively. The west and east halls contained two fixed target experiments: Hera-B[3] and Hermes. The beam pipes were located in a tunnel of 6.3 km circumference, 10 – 25 m below the surface. The particles had a revolution frequency of $4.73 \cdot 10^4\,\mathrm{s}^{-1}$. The time difference between bunch crossings was ~ 96 ns.

3.2. The ZEUS Detector

The Zeus detector was a multi-purpose detector with almost full solid-angle coverage, designed for high-energy lepton-proton scattering. The arrangement of its main components and their dimensions are illustrated in figure 3.2. The nominal interaction point is used as origin for the right-handed Zeus coordinate system, with the z-axis pointing in the proton beam direction (also referred to as "forward" direction), the y-axis pointing up, and the x-axis pointing toward the center of Hera. The polar angle θ and the azimuth angle ϕ are measured relative to the z and x axes, respectively.

While a detailed description of the Zeus detector can be found elsewhere [63], the components which are most relevant for this analysis will be briefly introduced in the following, namely the central tracking detector (CTD), the uranium-scintillator calorimeter (CAL), the trigger, the data acquisition system, and the luminosity monitor.

---

[3] Hera-B completed its data taking in 2003.

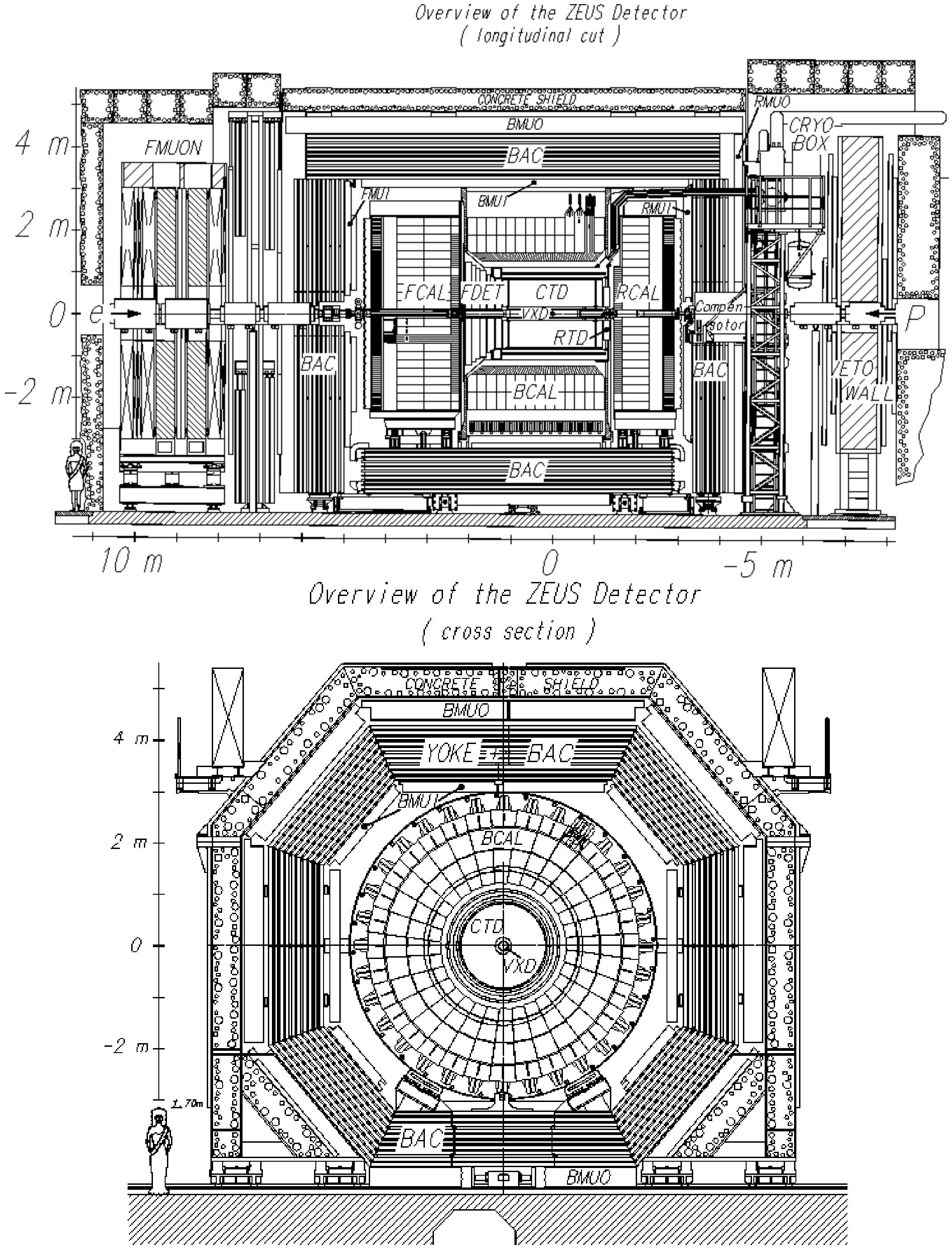

Figure 3.2: Cross section of the Zeus detector in the (y,z)-plane (top) and in the (x,y)-plane (bottom). From [63].

3.2.1. The Central Tracking Detector

The central tracking detector (CTD) [64, 65] was a large volume cylindrical multi-wire drift chamber, designed to measure the trajectories and momenta of charged particles with high precision. It had a length of 205 cm, an inner radius of 18.2 cm and an outer radius of 79.4 cm, covering polar angles $15^\circ < \theta < 164^\circ$. The CTD consisted of 4,608 sense wires, arranged in 72 radial layers, which were grouped into 9 superlayers. The odd superlayers contained wires which were parallel to the beam axis, while the remaining layers contained wires which were tilted at a stereo angle of $\pm 5^\circ$ to the beam axis. The respective layers were referred to as axial and stereo superlayers. The stereo layers allowed a z resolution of ~ 2 mm and aided the z position reconstruction of the tracks. Three of the axial layers were also equipped with a z-by-timing system, which provided information for the first level trigger.

In addition to the sense wires, the CTD consisted of 19,584 field wires, providing a uniform electric field. The CTD was situated inside a 1.43 T magnetic field of a superconducting solenoid. The ionization medium inside the CTD was a gas mixture composed of Argon, Ethane, and Carbon Dioxide.

The transverse momentum resolution for a track that has passed through all nine superlayers was $\sigma(p_T)/p_T \approx \sqrt{(0.0058\,p_T)^2 + (0.0065)^2 + (0.0014/p_T)^2}$, with p_T measured in GeV [66].

3.2.2. Uranium Calorimeter

The uranium calorimeter (CAL) [67–69] was a high-resolution sampling calorimeter which covered $\sim 99.7\%$ of the solid angle. It was subdivided into the forward (FCAL), barrel (BCAL), and rear (RCAL) calorimeters. The angular coverage of each section is shown in table 3.1.

CAL Section	Polar Angle	Pseudorapidity
FCAL	$1.6^\circ \leq \theta < 36.7^\circ$	$1.1 < \eta \leq 4.3$
BCAL	$36.7^\circ \leq \theta < 129.1^\circ$	$-0.75 < \eta \leq 1.1$
RCAL	$129.1^\circ \leq \theta < 177.4^\circ$	$-3.8 < \eta \leq -0.75$

Table 3.1: Polar angle and pseudorapidity coverage of the different ZEUS calorimeter sections

The calorimeter was built up from cells that consisted of alternating layers of 3.3 mm depleted Uranium and 2.6 mm scintillator material. The thickness of the layers had been chosen so that the calorimeter was compensating, meaning that electromagnetic and hadronic showers of equal energy produced the same response, also resulting in the optimal hadronic energy resolution and linearity. Light pulses were collected from each cell with wavelength shifter bars, passed through light guides, and read out with photo-multiplier tubes (PMT) connected to each shifter bar.

The calorimeter cells were arranged into towers with a base area of 20 cm × 20 cm, which were implemented differently in each CAL section as illustrated by figure 3.4: In the FCAL and BCAL each tower was subdivided longitudinally into two hadronic

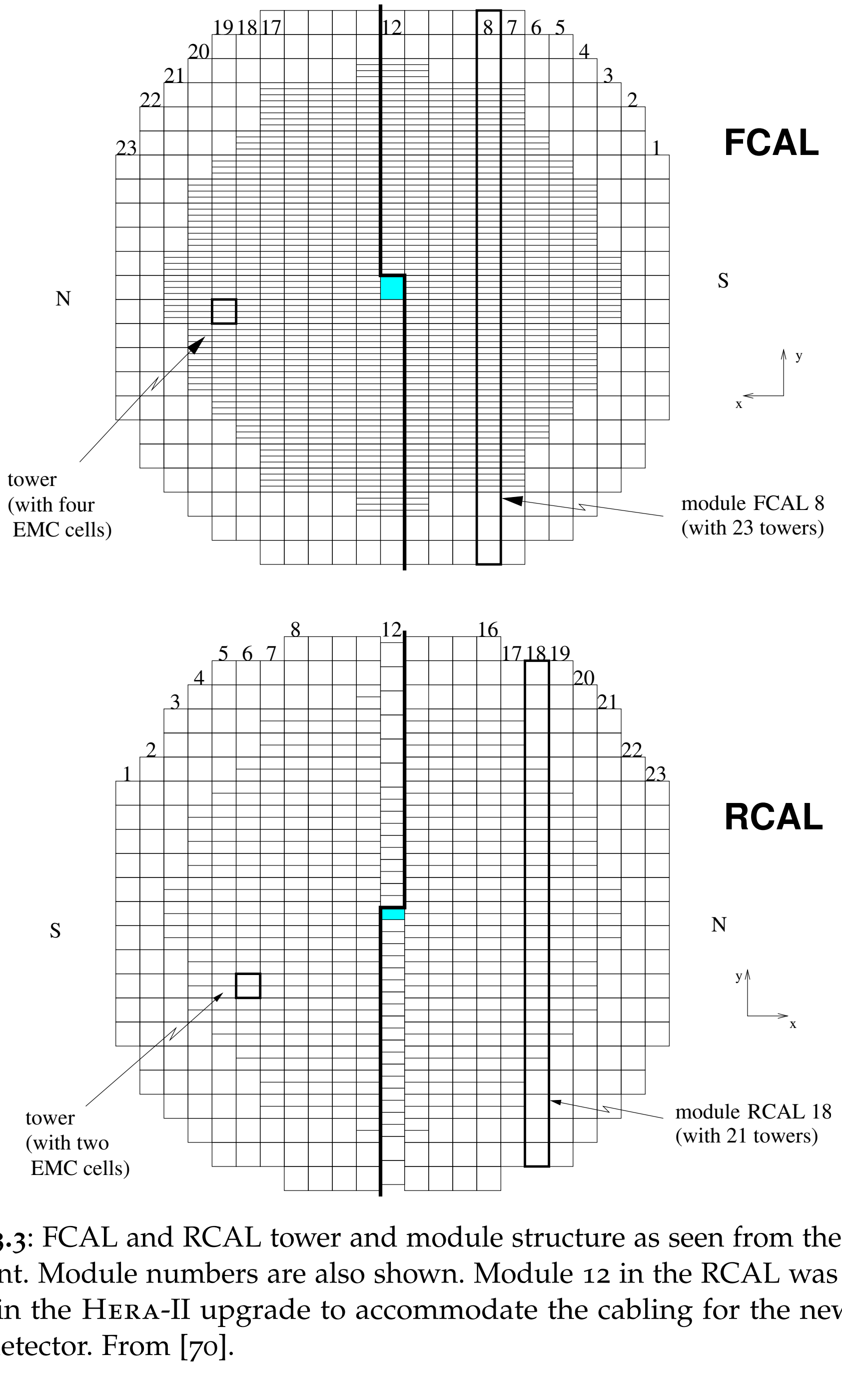

Figure 3.3: FCAL and RCAL tower and module structure as seen from the interaction point. Module numbers are also shown. Module 12 in the RCAL was slightly moved in the HERA-II upgrade to accommodate the cabling for the new micro vertex detector. From [70].

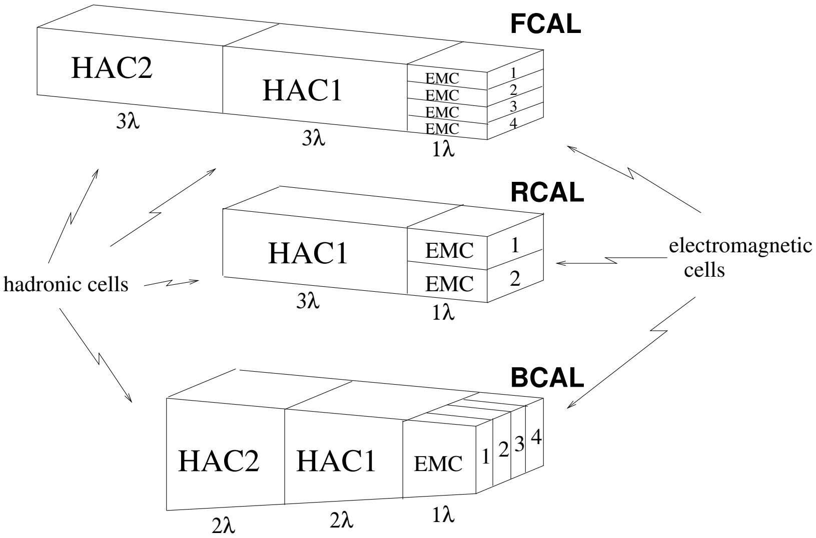

Figure 3.4: Examples for FCAL, BCAL, and RCAL tower structures showing EMC and HAC cells (not to scale). The depths of the cells are indicated in approximate interaction lengths. From [70].

calorimeter (HAC) cells and one electromagnetic calorimeter (EMC) part, which again was transversely divided into four cells with a base area of 5 cm × 20 cm. In the RCAL, the towers consisted of only one hadronic calorimeter cell and of only two electromagnetic calorimeter cells.

The towers were in turn arranged into modules. The RCAL and FCAL each featured 23 modules, while the BCAL was made up of 32 modules. The module and tower structure for the FCAL and RCAL as seen from the interaction point is shown in figure 3.3. In total, there were 5918 cells in the calorimeter.

The resolution of the Zeus calorimeter measured under test beam conditions was found to be $\sigma(E)/E = 35\%/\sqrt{E} \otimes 2\%$ for hadrons and $\sigma(E)/E = 18\%/\sqrt{E} \otimes 1\%$ for electrons, with the energies measured in GeV [63].

Besides allowing a compact and compensating calorimeter design, the usage of uranium as absorber had additional advantages for the long-term monitoring and calibration of the calorimeter. Since a constant amount of radioactively decaying uranium was detected with the scintillators and the PMTs, the resulting measured current provided a natural reference signal. Knowing its nominal value, the original conditions during the test-beam measurements could be restored, e.g. by adjusting the PMT gain. Aside from the remaining electronics calibration, the conversion factor between collected charge and deposited energy known from the test-beam results could in this way be kept constant using in-situ monitoring.

3.2.3. Trigger and Data Acquisition System

At the Hera accelerator, the bunches crossed every 96 ns, corresponding to a frequency of slightly more than 10 MHz. This caused various kinds of physical events to happen at a very high rate, most of which ($\sim$ 100 kHz) were not originating from $e^{\pm}p$ interactions, but from contact of the proton beam with residual gas in the beam pipe, so-called beam gas interactions, and from cosmic rays. Such events are not of interest and are considered *background*. It is the technically challenging task of a trigger system to select as many *ep* physics events as possible while rejecting most of the background and to reduce the event rate down to a level which can be handled by the data acquisition and data recording systems.

The trigger system at Zeus consisted of three levels that subsequently reduced the rate of 10 MHz at which the bunches crossed to about 10 Hz that could be written to tape. Figure 3.5 shows a schematic diagram of the data flow through the Zeus trigger system.

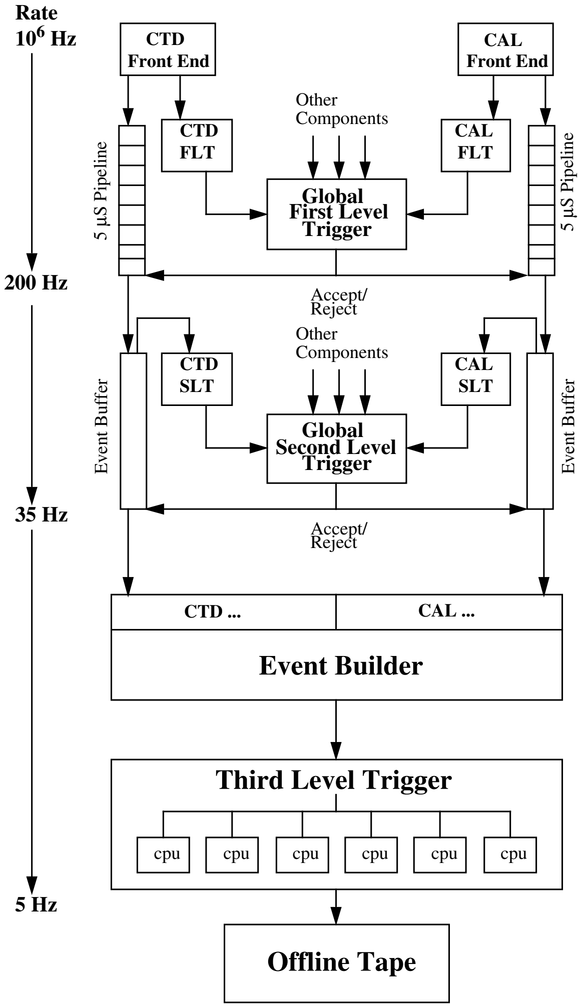

Figure 3.5: Schematic diagram of the data flow through the Zeus trigger and data acquisition system. From [63].

At the first-level trigger (FLT) pipelined memories stored the relevant information from every component of the ZEUS detector for $\sim 5\,\mu\text{s}$. During this time the global first-level trigger (GFLT) had to form a decision on whether or not to accept the event based on information from local FLTs in each component, with only a subset of the full detector information available. The use of the pipelines allowed data-taking at every bunch crossing without any dead time. The FLT was purely hardware-based and was designed to reduce the event rate down to $\sim 1\,\text{kHz}$.

When accepted by the GFLT, the complete information gathered from the components was sent to the relevant component's second-level trigger (SLT) memory buffers. In contrast to the FLT, the second-level trigger was software-based. The resulting flexibility in the architecture, the longer time ($\sim 6000\,\mu\text{s}$) available and the larger amount of information at hand, allowed the employment of more complicated algorithms to make a more informed decision than at the first-level trigger on whether to accept or reject the event. The SLT reduced the event rate to $\sim 100\,\text{Hz}$.

After an SLT-accept signal, the complete detector information was passed on via the event builder to the third-level trigger (TLT). With longer processing time ($\sim 300\,\text{ms}$) available, the TLT was capable of a sophisticated reconstruction of the full event, including the calculation of kinematic variables, identification of the electron candidate, and jet reconstruction. When accepted by the TLT, the event was finally written on tape. The TLT further reduced the event rate until the limit of $\sim 10\,\text{Hz}$ for the data acquisition system was reached.

3.2.4. Luminosity Determination

The luminosity $\mathcal{L}$ is a property of an accelerator that directly relates the cross section σ of a given process to the event rate $\mathcal{N}$ associated with that process,

$$\mathcal{N} = \sigma \cdot \mathcal{L}, \tag{3.1}$$

and is a measure for the rate of particle collisions. A precise knowledge of the luminosity is therefore essential to obtain the correct absolute normalization of the measured cross sections. The luminosity is usually determined by measuring the event rate $\mathcal{N}$ of a well understood process with accurately known cross section. At ZEUS, the rate of photons $\mathcal{N}_\gamma$ from the Bethe-Heitler process $ep \to e'p\gamma$ (Bremsstrahlung) with the cross section σ_{BH} was measured for this purpose at photon scattering angle $\theta_\gamma = 0$ and energy E_γ. The luminosity was then obtained from the formula $\mathcal{L} = \mathcal{N}_\gamma / \sigma_{\text{BH}}$.

Until 2001, the photon detector used was a lead/scintillator sandwich calorimeter [63, 71–74] located about 100 m from the interaction point in the flight direction of the electron beam. The photon detector was later upgraded and extended with a combination of spectrometer system [75] and aerogel Cherenkov counters [76] to improve the energy resolution and to deal with the high synchrotron background radiation introduced by the HERA upgrade described in the following section.

When performing an offline analysis, the more important quantity is the luminosity integrated over time, $L = \int \mathcal{L}(t)\,\mathrm{d}t$. Figure 3.6 shows the integrated luminosities at ZEUS for the years 2002 – 2007. As can be seen, the luminosity increased with each year, reaching a total sum of $406.7\,\text{pb}^{-1}$ in the time frame shown.

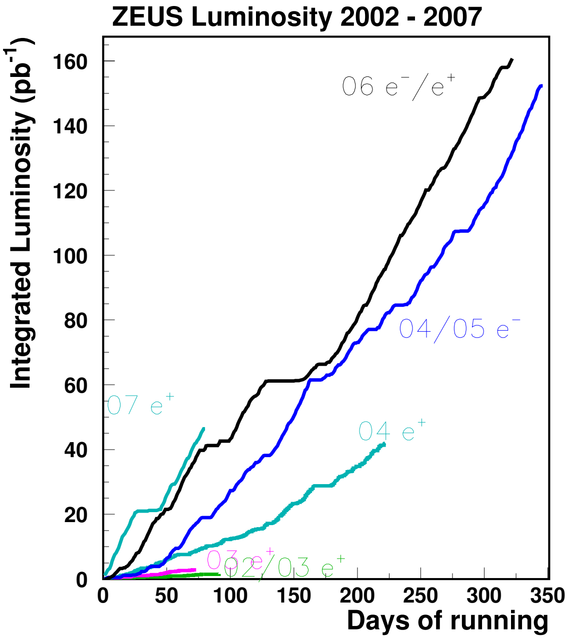

Figure 3.6: Zeus integrated luminosities for the years 2002 – 2007. From [77].

3.3. The HERA Upgrade

Having reached or even exceeded many of Hera's design parameters, it was decided to upgrade the accelerator with regard to the luminosity to aid the research on processes with low cross-sections. Additionally, Hera were to be equipped with spin rotators. In 2000/2001, the collider and its experiments were shut down and upgraded, ending the data taking period started in 1993 that will be referred to in the following as "Hera-I", while the post-upgrade data taking period from 2002/2003 onward will be referred to as "Hera-II". This section will give a brief overview of the technical changes associated with the upgrade. A more detailed description can be found elsewhere [78,79].

In order to achieve the luminosity goal of roughly a factor five higher specific luminosity, the beam sizes before the interaction points had to be reduced down to a third ($118\,\mu\mathrm{m} \times 32\,\mu\mathrm{m}$) of their previous size, while increasing the beam current. This required extensive modifications of the magnet lattice up to $100\,\mathrm{m}$ from the experiments along the beam axis. The most challenging changes involved the focusing magnets in immediate proximity to the interaction points, as they had to be moved even closer toward the detectors, with the superconducting electron magnets then being located in the strongly restricted space inside the detectors.

After the construction work was completed, the resumption of the data taking was delayed by high synchrotron radiation background from the electron beam, caused by the strong magnetic fields of the new magnet configuration around the interaction point. These problems were overcome in an additional shutdown period during 2003. Since then until March 2007, the end of the data taking with a proton energy of

920 GeV, Hera had delivered an integrated luminosity of $556.4\,\mathrm{pb}^{-1}$. In comparison, the total integrated luminosity delivered by Hera during the data taking period of Hera-I was $193.2\,\mathrm{pb}^{-1}$. Figure 3.7 shows the integrated luminosities of both Hera-I and Hera-II, illustrating the increase in luminosity of Hera-II.

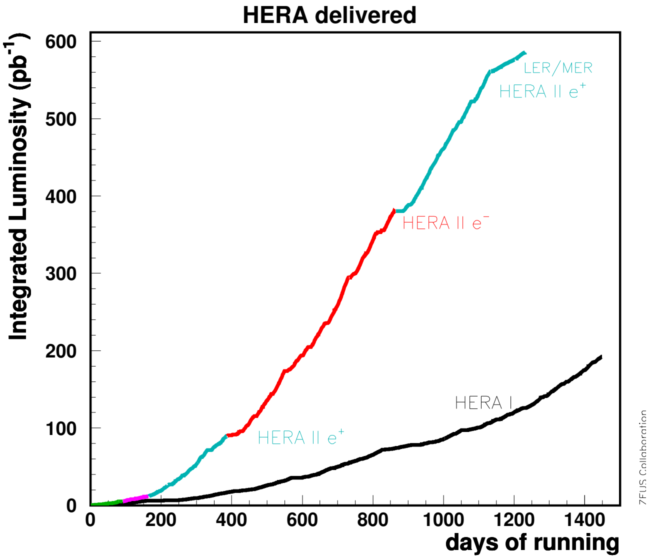

Figure 3.7: Hera delivered integrated luminosities for the data taking periods Hera-I (1993 – 2000) and Hera-II (2002 – 2007). From [77].

4. Event Simulation and Theoretical Predictions

To test and deepen our understanding of the inelastic *ep* scattering process, it is of fundamental importance to compare the measured data with their theoretical predictions. At Hera, such theoretical predictions are commonly provided by perturbative QCD calculations up to a fixed order and by Monte Carlo techniques, which are based on randomly generated distributions of physical observables in accordance with leading-order predictions[1], using approximate methods to generate the hadronic final state.

This chapter will briefly introduce the typical components and functionality of a Monte Carlo simulation, describe the specific generators and Monte Carlo samples used in this analysis, and give an overview of the computer program that provided the next-to-leading order (NLO) calculations.

4.1. Monte Carlo Simulations

Monte Carlo (MC) simulations play an important role in high-energy physics as they offer access to details of the hadronic final state. This makes them an essential tool e.g. for the extraction of relevant physical observables like differential cross-sections from the measured data, for better understanding background contributions, or for studying the detector performance [84].

The simulation typically generates the hadronic final state based upon approximations and model assumptions, implementing only matrix elements up to the first order $\mathcal{O}(\alpha_S)$ and using e.g. emissions by parton showering to simulate higher orders.

At Zeus, the generation of simulated events is typically performed in several distinct steps, involving various programs, which will be introduced below.

The neutral-current DIS Monte Carlo samples for this analysis were generated using the Heracles [85] program. Heracles generates the event kinematics for *ep* interactions and includes a treatment of QED corrections, which are dominated by virtual and real photons radiated from the electron in the initial and final states. Through the Djangoh [86] interface to the programs Lepto [87] and Ariadne [88,89] and using the parton density distributions of Cteq5D [90] as provided by the Pdflib library [39], the hard matrix element is calculated and initial- and final state parton cascades are simulated. The hadronization of the final-state partons into colorless hadrons is performed by the Jetset program.

---

[1] Recently, different techniques have been developed that combine NLO calculations with parton showers [80–82]; but they are currently limited to a number of specific processes, such as $Z+$jet [83].

The programs Lepto, Ariadne, and Jetset and their functionality are explained in more detail in the following.

4.1.1. The ARIADNE and LEPTO Monte Carlo Generators

The Lepto program includes QCD corrections to the leading order electroweak cross-sections determined from exact first order matrix elements from Heracles and higher orders simulated using a parton shower approach based on the Altarelli-Parisi equations [44] in the leading log Q^2 approximation [87]. Using Lepto, quark-parton (QPM) processes and all first order $\mathcal{O}(\alpha_S)$ processes can be simulated, i.e. QCD-Compton (QCDC) and boson-gluon fusion (BGF) processes.

In the Ariadne program on the other hand, only the matrix element for the QCDC process and the parton cascade of the event are implemented. It was therefore used in combination with the Lepto generator which provided the BGF process.

The parton cascade of the Ariadne program is based on the *Color Dipole Model* (CDM) [91–93] which was first implemented for e^+e^- interactions. The CDM treats pairs of color-charged partons as color dipoles which cause gluon emissions, leading to the formation of new dipoles and further emission of gluons.

Since these gluon emissions are not ordered in transverse momentum, the CDM shower evolution of the Ariadne program is BFKL-like, in contrast to the DGLAP approach used in Lepto [89].

4.1.2. Hadronization Using JETSET

In the context of this analysis, the term hadronization is used to describe the combination of fragmentation and subsequent decay of unstable particles until a stable set of final state hadrons is reached.

Fragmentation is the process where the colored partons originating from the hard scattering and the subsequent parton cascade are transformed into colorless hadrons. This occurs at large distances, when confinement sets in. Perturbative QCD breaks down in this regime, and therefore phenomenological models have to be used to describe fragmentation.

In this analysis, the Jetset [94, 95] program was used, which implements the Lund string-fragmentation model [96, 97] and a treatment for the subsequent decays into stable hadrons.

The Lund string-fragmentation model is based on the assumption that the energy stored in a color dipole field between a charge and an anti-charge increases linearly with the separating distance between the charges. This leads to the formation of a "color flux tube" or *string* stretched between both charges. This string extends to typical hadronic sizes ($\approx 1\,\mathrm{fm}$) and has an energy density of $\sim 1\,\mathrm{GeV/fm}$.

When further separating the color charges, the energy stored in the string increases until the string breaks at the point where a new charge/anti-charge pair is created, forming new color dipoles. This process continues until only on-mass-shell hadrons remain [94].

There are also alternative fragmentation models available, for example cluster fragmentation [98] as implemented in the Herwig program [99, 100] or independent fragmentation [21].

4.1.3. Detector Simulation

The stable hadrons resulting from the hadronization process were used as input to the Zeus detector and trigger simulation [63]. Utilizing the Geant [101] package and taking into account geometry, material, and position of detector components, the propagation of particles, their energy loss and decay, multiple-scattering, and the effect of the magnetic field are tracked. After modeling the response and readout of the active detector material, the simulated event is available in the same format as "real" data. This allows to use the Monte Carlo output in the analysis transparently and without modification.

4.1.4. Intermediate Generation Level

An important feature of the Monte Carlo simulation is the access to intermediate steps in the event generation process, distinguished in this analysis as follows:

- The **parton level** corresponds to the stage of simulation after the hard scattering and parton cascade have been calculated;
- the **hadron level** is the stage of the simulation after the formation of hadrons and subsequent decay into stable particles[2], and finally
- the **detector level** is the final stage of the simulation, after the specific detector responses have been simulated and passed through the reconstruction procedures.

4.1.5. Monte Carlo Samples Used in this Analysis

In this analysis, Ariadne was interfaced through Djangoh with Heracles and Lepto for the generation of the central DIS Monte Carlo sample used e.g. for deriving jet-energy corrections and in the unfolding of the cross-sections as described in chapters 7 and 8. For simplicity, this combination of programs will be referred to as just Ariadne.

This sample has been generated with kinematic restrictions on the virtuality of $Q^2 > 4\,\mathrm{GeV}^2$ and on the invariant mass of the hadronic system of $W_X > 5\,\mathrm{GeV}$. QED corrections were provided by the Heracles program.

The following additional Monte Carlo samples were used for specific purposes, and differed in the generator configuration:

- **QED Correction Sample:** Ariadne was used to generate two Monte Carlo samples, one with QED corrections from Heracles and one without. These samples were then used to determine the influence of higher-order QED effects on the cross-sections, as described in chapter 8.3. As only hadron-level information was needed, the samples were not run through the detector simulation.

---

[2] In this analysis, particles are considered "stable" on the hadron level when their lifetime exceeds 10 ps.

- **Hadronization Correction Sample:** To estimate the uncertainty associated with the choice of the hadronization scheme and its specific settings in JETSET, an ARIADNE sample was generated in which specific parameters affecting the hadronization were modified. These parameters determine, for instance, the choice of longitudinal fragmentation function, suppression parameters for pair production in the color field, and decay lengths of particles, but are too numerous to list in detail.

  The tuned settings correspond to the configuration used by the H1 collaboration recently in [7].

- **Photoproduction Background Sample:** The Monte Carlo sample used to estimate the contribution from photoproduction (γp) events to the measured cross-sections was generated with the PYTHIA 6.4 [102] program. The event kinematics were required to satisfy $Q^2 < 1.5\,\mathrm{GeV}^2$ and $y > 0.5$. A sample with $y < 0.5$ was investigated as well, but was found to give no significant contribution to the cross-sections investigated in this analysis.

  The relative normalization of the photoproduction sample to the signal DIS sample was determined by a fit of the γp and ARIADNE samples to the data. This resulted in a lower normalization factor compared to the normalization with respect to the integrated luminosity as calculated by the Monte Carlo simulation. This systematic uncertainty introduced by the normalization of the γp Monte Carlo sample was taken into account and is discussed in chapter 9.

4.2. Fixed-Order Calculations

Parton showers as used in the Monte Carlo simulations offer predictions of soft phenomena and exclusive observables that currently cannot be obtained from fixed-order calculations, but they lack their quantifiable accuracy especially in kinematic regions with small higher-order corrections [103]. The Monte Carlo simulations are therefore less suited for a thorough test of QCD predictions than analytical QCD NLO calculations.

All theoretical predictions for cross sections presented in this analysis were made using the NLOJET++ [104] program. It uses the subtraction method [105] for dealing with the collinear and infra-red divergences. NLOJET++ includes all necessary perturbative corrections in the calculation of the trijet cross-section and can therefore provide QCD predictions for both dijets and trijets of the order $\mathcal{O}(\alpha_S^2)$.

In the calculations, jets were constructed from the outgoing partons using the inclusive k_T algorithm in the Breit frame, as discussed in chapters 2.4 – 2.5.

The calculations were performed using the $\overline{\mathrm{MS}}$ scheme [106] with five active flavors. The renormalization scale, μ_R, and the factorization scale, μ_F, were both set to $\sqrt{(Q^2 + \hat{E}^2_{T,\,\mathrm{B}})/2}$, where $\hat{E}_{T,\,\mathrm{B}}$ denotes either the mean transverse energy of the selected jets (in the case of the inclusive jet cross sections), or alternatively the mean transverse energy of the two hardest jets (in the case of the inclusive dijet and trijet cross-sections) with respect to the Breit frame. Alternative renormalization scales, i.e.

$\mu_R^2 = Q^2$ and $\mu_R^2 = \hat{E}^2_{T,\,\mathrm{B}}$, have also been investigated and are discussed in chapter 10. The value for the strong coupling, α_s, was set to $\alpha_s(M_Z) = 0.118$. For the proton PDFs, the CTEQ6.6 [107] parametrization was used.

After the calculation, the NLO QCD predictions are only valid at the parton level. Through the modeling of the hadronization process by Monte Carlo generators, correction factors can be determined and predictions on hadron level can be assessed. This procedure was used bin-by-bin for all theoretical predictions of cross sections as described in chapter 8.4. The hadronization correction was generally below 15% in each bin.

By using the k_T jet-clustering algorithm, the jet observables are ensured to be infrared safe. However, when imposing symmetric cuts on the transverse jet energy, E_T, of each jet in a dijet system, there are regions of phase space in which the NLO QCD calculations result in unphysical predictions [108, 109]. This behavior occurs when both jets carry balancing E_T at the threshold (i.e. $E^{\mathrm{jet1}}_{T,\,\mathrm{B}} = E^{\mathrm{jet2}}_{T,\,\mathrm{B}} = E^{\mathrm{cut}}_{T,\,\mathrm{B}} = 8\,\mathrm{GeV}$), and are arranged back-to-back with a difference in azimuthal angle $\Delta\phi_{jj,\,\mathrm{B}} \approx \pi$. In this configuration, real soft-gluon emissions are strongly suppressed due to the limited phase space available and thus do not cancel the (negative) virtual soft-gluon contributions to the cross-section.[3] However, cross-sections measured over the remaining part of the phase space are unaffected [108].

Such unphysical behavior of the prediction is expected in any fixed-order calculation and could be solved by using all-orders resummed calculations or non-perturbative approaches. It can also be avoided by either imposing asymmetric cuts on the E_T of the jets, or equivalently by imposing a cut on the invariant mass of the two hardest jets in a dijet system, M_{jj} [108]. For this analysis, the latter approach was chosen, requiring $M_{jj} > 20\,\mathrm{GeV}$ for all dijet and trijet cross-sections.

For identical jet selection criteria, this value for the M_{jj} cut has recently been studied in detail in [110] and found to be safe for most regions of jet phase space.

For purposes of illustration, part of these studies shall be reviewed here:

The critical region of phase space where $E^{\mathrm{jet1}}_{T,\,\mathrm{B}} = E^{\mathrm{jet2}}_{T,\,\mathrm{B}} = 8\,\mathrm{GeV}$ and $\Delta\phi_{jj,\,\mathrm{B}} \approx \pi$ can be identified as function of the observables M_{jj} and η' using the following equations 4.1 – 4.3:

- The absolute value of the center-of-mass scattering angle given by

$$\cos\theta^* = \tanh\eta' \ , \tag{4.1}$$

  where η' corresponds to the average absolute difference in pseudorapidities, $\eta' = \frac{1}{2}|\eta^{\mathrm{jet1}}_{\mathrm{B}} - \eta^{\mathrm{jet2}}_{\mathrm{B}}|$,

- the relation

$$\cosh(\eta^{\mathrm{jet1}}_{\mathrm{B}} - \eta^{\mathrm{jet2}}_{\mathrm{B}}) = \frac{1+\cos^2\theta^*}{1-\cos^2\theta^*} \ \text{, and} \tag{4.2}$$

- the definition for the squared invariant mass of the dijet system,

---

[3] This effect is less pronounced but still present when the two jets carry a E_T at threshold, but are not back-to-back ($0 < \Delta\phi_{jj,\,\mathrm{B}} < \pi$).

$$M_{jj}^2 = 2E_{T,\,\mathrm{B}}^{\mathrm{jet1}} \cdot E_{T,\,\mathrm{B}}^{\mathrm{jet2}} \cdot [\cosh(\eta_{\mathrm{B}}^{\mathrm{jet1}} - \eta_{\mathrm{B}}^{\mathrm{jet2}}) - \cos(\Delta\phi_{jj,\,\mathrm{B}})] \ . \tag{4.3}$$

Figure 4.1 presents the correlation between M_{jj} and η' for Monte Carlo dijet events on hadron level and highlights this specific kinematic configuration as dashed line. Further shown are the kinematic region of $0 < \Delta\phi_{jj,\,\mathrm{B}} < \pi$ with $E_{T,\,\mathrm{B}}^{\mathrm{jet1}} = E_{T,\,\mathrm{B}}^{\mathrm{jet2}} = 8\,\mathrm{GeV}$ as colored area and the M_{jj} cut indicated as horizontal line.

As shown in figure 4.1, the imposed cut of M_{jj} removes most of the phase space region where the NLO QCD prediction becomes unreliable, significantly reducing its influence. However, for values of $\eta' > 0.9$ unsafe kinematic configurations remain that are concentrated in the last bin of the cross-sections $\mathrm{d}\sigma/\,\mathrm{d}\eta'$ ($\eta' > 0.95$). Consequently, the comparison of the measured cross-section with the NLO prediction was omitted in this specific bin.

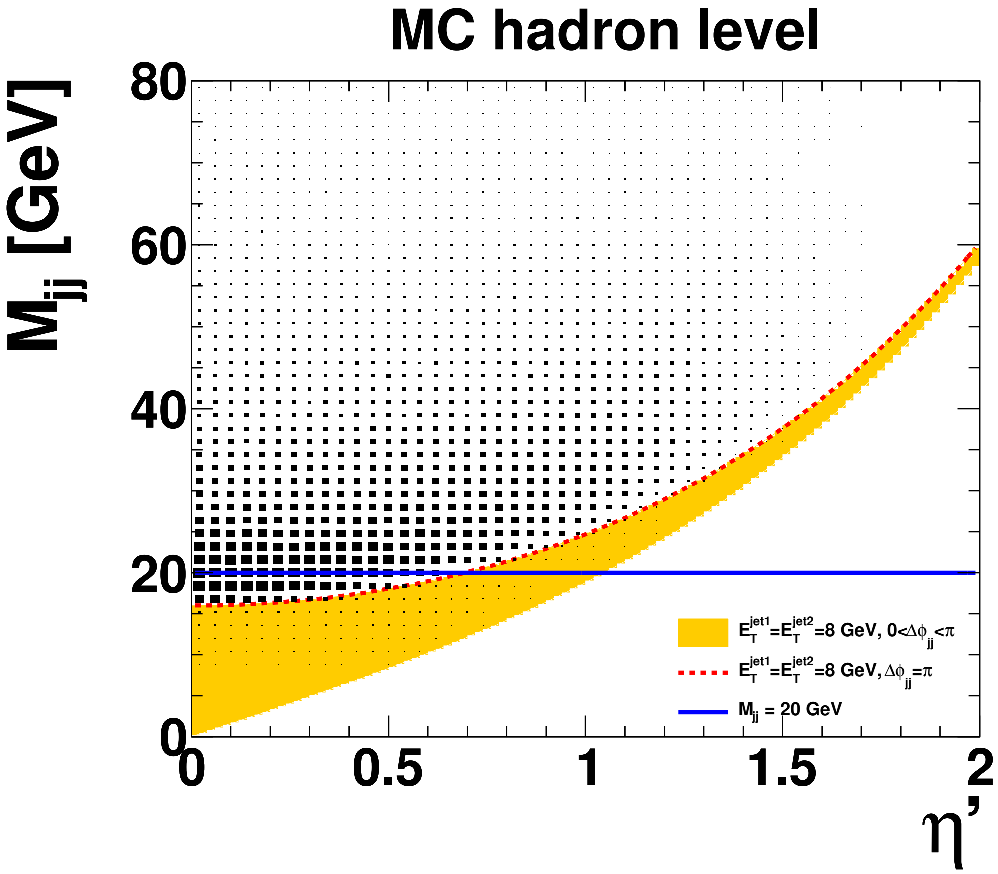

Figure 4.1: Correlation between M_{jj} and η' for hadron-level Monte Carlo dijet events and specific kinematic jet configurations. See text for details.

5. Event Reconstruction

This analysis aims at measuring jet cross-sections in neutral current (NC) deep inelastic scattering (DIS), hence a good reconstruction of both the hadronic final state and the electron is crucial for the precision of the measurement and for background suppression. This chapter describes how the reconstruction is performed and discusses different methods to determine the kinematic variables introduced in chapter 2.1.2 from the scattered electron and the hadronic final state.

5.1. Reconstruction of the Hadronic Final State

For the reconstruction of the hadronic final state two detector components are mainly used: the calorimeter (CAL) and the central tracking detector (CTD). On the one hand the CTD offers superior momentum resolution for particles with low energy and is less sensitive to energy losses in inactive material in front of the calorimeter. The CAL information on the other hand is essential for particles that leave no tracking information and gives better energy resolution for high-energy particles.

It is therefore advantageous to combine the information from both CTD and CAL. At ZEUS this is done in the form of the so-called *energy flow objects* (EFOs). In principle, by using EFOs for the reconstruction of the final state, the resolution of kinematic variables and the one-to-one correspondence between detector-level objects and hadrons can be optimized [111].

However, from 2004 onward the EFO algorithm introduced a systematic effect resulting in double-counting of energy deposits from regions in-between calorimeter sections ("super-crack" regions) in jet analyses [112].

In this analysis, instead of EFOs, the final state was therefore reconstructed from other objects:

- **Calorimeter cells** represent the smallest units of the calorimeter. Only cells were considered that (1) were not associated with the scattered electron candidate, (2) passed noise suppression thresholds[1], and (3) whose signal wasn't caused by a high-voltage discharge. The latter was evaluated by determining the energy difference between the two photomultiplier tubes reading out the respective cell: if it exceeded 90% of the total energy (for cells with more than 1.5 GeV) the cell was ignored.

- **Calorimeter islands** are constructed by merging nearest neighboring cells that fulfill the cuts described above. The islands are then corrected for energy losses in inactive material, for back-splash effects in the calorimeter, and for energy

---

[1] As thresholds were used: 0.05 GeV and 0.1 GeV for electromagnetic calorimeter cells and hadronic cells, respectively.

> loss in the super-crack regions [113]. The positions of the islands were calculated from the energy-weighted sum of the cell positions belonging to the island.

Due to the applied corrections calorimeter islands improve the correspondence between detector level and hadron level. Islands were primarily used in the reconstruction of the kinematic variables while the jets were reconstructed from cells as described below. Through energy corrections presented in chapter 7.1 a good correspondence to the "true" hadron quantities was achieved for cell jets as well.

5.2. Electron Identification

The identification of electrons in the event is crucial in the analysis presented here. The reason being that the presence or absence of the scattered electron is used to discriminate between neutral current DIS, and other processes without electron in the final state such as charged current DIS or events where the scattered electron remains undetected such as photoproduction (γp).

In this analysis, the SINISTRA algorithm is used as the primary electron finder [114]. The algorithm is based on a neural network using information from the calorimeter. It distinguishes between hadrons and electrons based on their showering topology. SINISTRA returns a list of electron candidates and assigns an individual electron probability, $\mathcal{P}_e$, to each one where $\mathcal{P}_e = 0$ corresponds to a hadronic shower and $\mathcal{P}_e = 1$ to an electromagnetic cluster.

Additionally, the EM electron finding algorithm [115,116] was employed to allow the estimation of systematic effects due to the choice of electron identification method. The EM algorithm is based on a detailed parametrization of the electromagnetic response of the ZEUS detector combining CAL and CTD information. It derives an electron probability from a statistical evaluation of each of the parameters used.

In this analysis the electron candidate with the highest probability was assumed to be the scattered electron of the DIS process. Possible background events were suppressed through cuts as described in chapter 6.2, or taken into account by dedicated Monte Carlo samples.

5.3. Kinematic Reconstruction

In neutral current DIS events the ZEUS detector can measure the properties of the scattered electron, such as the azimuthal angle, ϕ_{el}, the polar angle, θ_{el}, and the energy, E'_{el}, as well as properties of the hadronic final state, such as positions and momenta of particles. In principle the knowledge of either the electron or the hadronic final state would be sufficient to reconstruct kinematic variables e.g. the virtuality of the exchanged boson, Q^2, the inelasticity, y, or the fraction of the proton momentum carried by the struck parton, x_{Bj}. Therefore the kinematic variables are overdetermined in neutral current DIS, allowing to employ various reconstruction methods based on either measured quantities or a combination thereof. This also offers the opportunity to cross-check the methods with each other.

The different reconstruction methods exhibit different resolutions and bias, which can also vary in different regions of phase space. Therefore, both resolution and bias have been studied in Monte Carlo for the various methods within the phase space investigated in this analysis. The results of the comparison are shown at the end of this section.

5.3.1. Electron Method

The electron method ("el") [117] uses both the energy E'_{el} and polar angle θ_{el} of the scattered electron to reconstruct y and Q^2,

$$y_{\text{el}} = 1 - \frac{E'_{\text{el}}}{2E_{\text{el}}}(1 - \cos\theta_{\text{el}}) \text{ and} \tag{5.1}$$

$$Q^2_{\text{el}} = 2E_{\text{el}}E'_{\text{el}}(1 + \cos\theta_{\text{el}}), \tag{5.2}$$

where E_{el} is the energy of the beam electron.

Using the interrelation between the kinematic variables introduced in equation 2.4 of chapter 2.1.2,

$$Q^2 = s \cdot x \cdot y, \tag{5.3}$$

with the known center-of-mass energy, $\sqrt{s}$, the value of the Bjorken scaling variable can also be calculated.

The electron method has been shown to be the best choice at low Q^2 [118], and to give the best resolutions for x mainly at high y and for Q^2 over a large kinematic range [119]. However, it is susceptible to initial-state radiation where the electron emits a photon before the interaction [117], effectively reducing the electron energy below the typical beam energy of 27.5 GeV.

5.3.2. Jacquet-Blondel Method

The Jacquet-Blondel ("JB") method [120] is based on momentum conservation and solely relies on the hadronic final state. It can therefore also be employed in certain analyses where no scattered electron is available in the final state as is the case for photoproduction or charged current processes. The kinematic variables are calculated according to

$$y_{\text{JB}} = \frac{1}{2E_{\text{el}}} \sum_h (E_h - p_{z,h}) \text{ and} \tag{5.4}$$

$$Q^2_{\text{JB}} = \frac{1}{1 - y_{\text{JB}}} \left[\left(\sum_h p_{x,h} \right)^2 + \left(\sum_h p_{y,h} \right)^2 \right] , \tag{5.5}$$

where the sums run over all final state objects excluding the electron, and E_h, $p_{x,h}$, $p_{y,h}$, and $p_{z,h}$ are the energy and momentum components of the respective object.

The JB method usually yields a rather bad resolution and a poor measurement of Q^2 compared to other reconstruction methods [117, 121] and is therefore typically not used in neutral-current analyses.

5.3.3. Double-Angle Method

The Double-Angle ("DA") method [117] is based on the polar angles of the electron and of the hadronic final state which are typically measured with high precision:

$$y_{\text{DA}} = \frac{\sin\theta_{\text{el}} \cdot (1 - \cos\gamma_{\text{had}})}{\sin\gamma_{\text{had}} + \sin\theta_{\text{el}} - \sin(\theta_{\text{el}} + \gamma_{\text{had}})} \quad \text{and} \tag{5.6}$$

$$Q^2_{\text{DA}} = \frac{4 \cdot E^2_{\text{el}} \cdot \sin\gamma_{\text{had}}(1 + \cos\theta_{\text{el}})}{\sin\gamma_{\text{had}} + \sin\theta_{\text{el}} - \sin(\theta_{\text{el}} + \gamma_{\text{had}})} \ , \tag{5.7}$$

where γ_{had} corresponds in the leading-order quark-parton model to the scattering angle of the parton. It can be calculated from

$$\cos\gamma_{\text{had}} = \frac{p^2_{T,\,\text{had}} - (\sum_h (E_h - p_{z,h}))^2}{p^2_{T,\,\text{had}} + (\sum_h (E_h - p_{z,h}))^2} \ , \tag{5.8}$$

where $p_{T,\,\text{had}} = (\sum_h p_{x,h})^2 + (\sum_h p_{y,h})^2$ and the sums run over all final state objects excluding the electron. The energy of the scattered electron can be reconstructed with the DA method as

$$E'_{\text{DA}} = \frac{2E_{\text{el}} \sin\gamma_{\text{had}}}{\sin\gamma_{\text{had}} + \sin\theta_{\text{el}} - \sin(\gamma_{\text{had}} + \theta_{\text{el}})} \ . \tag{5.9}$$

Since the DA method is based on angular measurements, it is in first order independent of possible energy losses and thus the absolute energy calibration of the calorimeter [117]. This has been exploited in the energy scale calibration described in chapter 7.1.1. Furthermore, the DA method allows a precise reconstruction over most of the kinematic plane accessible at HERA [117, 121], but degrades in resolution in the low-x low-Q^2 kinematic regime [118, 119]. It has therefore been typically preferred by analyses at high Q^2 [58, 122].

5.3.4. Electron-Σ Method

The electron-Σ method ("eΣ") is also using a combination of information from the electron and from the hadronic final state. It is based on the Σ method [123]:

$$y_\Sigma = \frac{\sum_h (E_h - p_{z,h})}{E - P_z} \ , \text{and} \tag{5.10}$$

$$Q^2_\Sigma = \frac{(E'_{\text{el}} \sin\theta_{\text{el}})^2}{1 - y_\Sigma} \ , \tag{5.11}$$

where $E - p_z \equiv \sum_h (E_h - p_{z,h}) + E'_{\text{el}}(1 - cos\theta_{\text{el}})$. For an ideal detector, $E - P_z$ would be equal to $2E_{\text{el}}$. Since the reconstruction is independent of the energy of the incoming electron beam, it is less influenced by photon radiation in the initial state [123].

In the electron-Σ method, Q^2 is reconstructed using the electron method, y using the Σ method, and x is calculated with equation 5.3.

The eΣ method yields good resolutions over the full kinematic plane, even in the low-x low-Q^2 domain [118, 123]. The method has for example been employed in a recent H1 publication measuring jets at low Q^2 [7] and other neutral-current analyses by the H1 collaboration [124, 125].

5.3.5. Comparison

Using the ARIADNE Monte Carlo sample the different methods were compared regarding their resolution and bias in Q^2, y, and x with respect to the "true" value as given by Monte Carlo.

The sample consists of events that passed the cuts for the inclusive DIS selection as described in the following chapter 6 with one notable exception: all phase-space cuts in y or Q^2 were imposed on the quantities as reconstructed by each respective method.

To estimate the bias and resolution of a reconstruction method, the distributions $(X_{\text{recon}} - X_{\text{true}})/X_{\text{true}}$ (X denotes the respective kinematic variable) were investigated in bins of X_{true}. The resolution was then defined as the standard deviation of the distribution while the bias was defined as the mean. Both were determined by a Gaussian fit to the distribution.

Figure 5.1 shows the results of the study. In most bins of Q^2, y, and x the bias of each method as indicated by the points is quite small and of comparable magnitude. A notable exception is the JB method (and, to a much lesser degree, the DA method) which exhibits a clear bias in x as well as Q^2 while performing well in y. Typically, the electron method gives the smallest bias. These results are compatible with the expectations discussed above.

With respect to the resolution as indicated by the error bars, the differences between the methods are more pronounced. While the JB and DA methods give the worst resolutions especially at low Q^2 and low x, the electron and electron-Σ methods give comparable results, with typically the electron method having slightly better resolution. Again, these results are compatible with the expectations.

Having verified that the electron method yields the best resolution with the smallest bias over most of the investigated phase space, the electron method has consequently been chosen for the reconstruction of all kinematic variables in this analysis and as basis for the boost of all objects to and from the Breit reference frame.

5.4. Summary

Based on the reconstructed objects of the hadronic final state and a correctly identified and well-measured scattered electron, the kinematics of neutral current DIS events can be reconstructed using various methods. The most common reconstruction methods in *ep* analyses, namely the electron method, the Double-Angle method, the Jacquet-Blondel method, and the electron-Σ method, were presented and compared with respect to their resolution and bias.

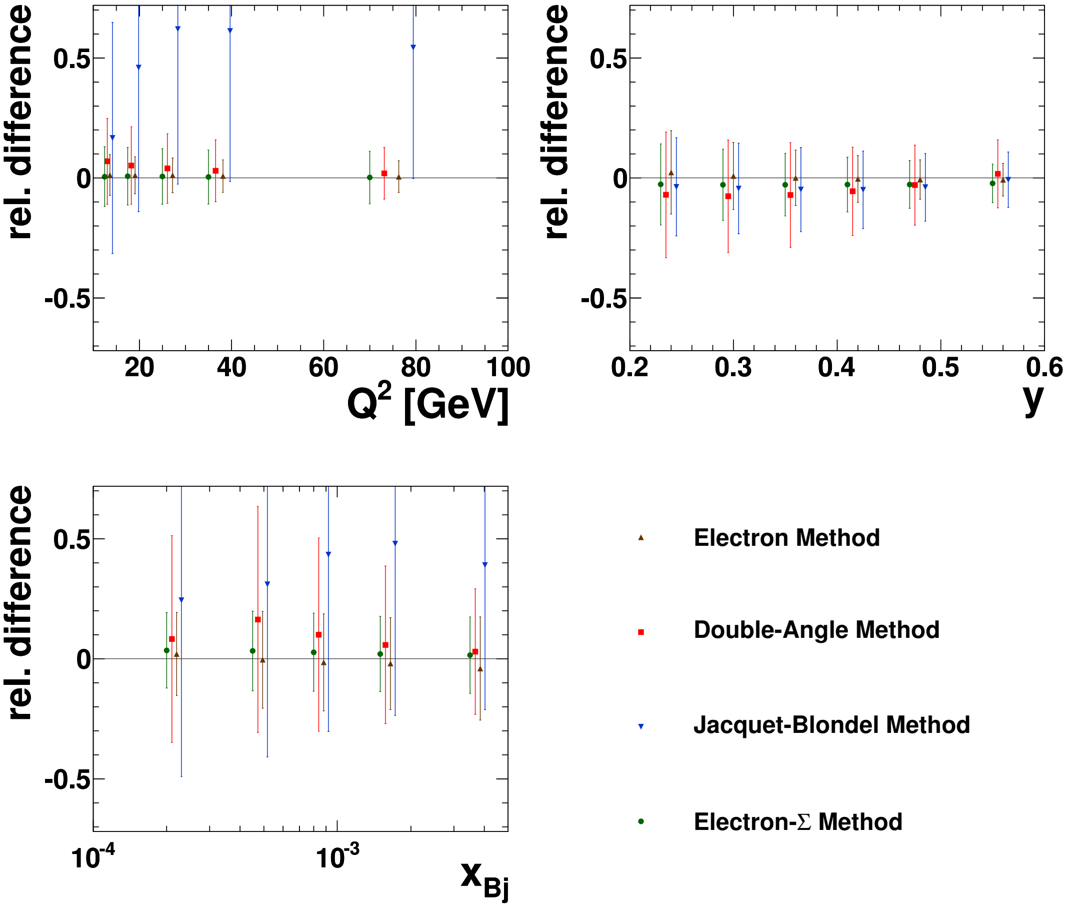

Figure 5.1: Comparison of resolutions and biases for different reconstruction methods as function of the generated quantity. The values were determined from a Gaussian fit to the distributions of the relative difference $(X_{\text{recon}} - X_{\text{true}})/X_{\text{true}}$ in Monte Carlo events for the reconstructed variable X, where for the resolution (error bar) σ and for the bias (marker position) the mean from the Gaussian fit are used. The points were drawn with different horizontal offsets to enhance visibility.

The electron method yields the best resolution and the smallest bias in the kinematic range investigated in this measurement and thus has been employed for this analysis.

6. Event and Jet Selection

This analysis aims at studying events in deep inelastic scattering at low photon virtualities i.e. in the region of $10 < Q^2 < 100\,\mathrm{GeV}$. In this chapter, both the online and offline selection criteria are described and motivated, that have been used to define the corresponding inclusive DIS sample and to remove background events. The online selection consists of requirements on data quality and on the trigger chain, while the offline selection is realized through cuts on reconstructed kinematic event variables and, at a later stage, a selection on the jets reconstructed from final-state objects.

The data sample used in this analysis has been recorded with the ZEUS detector during the years 2004 – 2007; it corresponds to an integrated luminosity of $296.0\,\mathrm{pb}^{-1}$.

6.1. Data Sample and Data Quality

The full data sample is divided into three distinct *running periods* listed in table 6.1.

Period	Lepton	Luminosity
2004 – 2005	e^-	$133.6\,\mathrm{pb}^{-1}$
2006	e^-	$53.0\,\mathrm{pb}^{-1}$
2006 – 2007	e^+	$109.5\,\mathrm{pb}^{-1}$
HERA-II		$296.0\,\mathrm{pb}^{-1}$

Table 6.1: Data samples used in this analysis with corresponding integrated luminosities.

Each period is further divided into intervals of stable data-taking conditions called *runs*. For each run the status of all detector components is recorded and marked offline according to various criteria [126]. The verdict of this DQM-routine is expressed as an integer; For this analysis only runs were considered that were flagged with 1 ("good"). Furthermore, specific runs were removed which exhibit an incorrect threshold setting in certain first level trigger slots also used in this analysis [127]. The final list of runs is a subset of the one considered for [122].

Trigger Selection

The trigger chain imposed by this analysis requires the detection of an electron candidate in the event as a necessary characteristic for neutral current (NC) processes and the essential ingredient for the offline reconstruction of the event kinematics.

As discussed in chapter 3.2.3 the ZEUS trigger system is structured in three different levels for an efficient data taking with a minimum dead-time and a minimal amount of background events. For an event to be accepted for this analysis, it had to pass on each level a specific set of trigger conditions. These conditions were expressed through combinations of trigger bits of which at least one had to be active[1].

On the first trigger level ("FLT"), the event rate that results from the short bunch crossing time of 96 ns is too high for a full read out of all calorimeter data. Nevertheless, the ZEUS trigger system is capable of triggering on the number of isolated electrons[2] using limited calorimeter information [128] where the isolation criterion reduces the background rate from hadrons. **FLT 30** and **FLT 36** are examples of trigger bits whose logic is primarily based on an isolated electron in the RCAL. FLT 36 additionally requires a "loose track veto" which will be discussed in more detail below. Both triggers are required by this analysis on the first trigger level.

On the second trigger level ("SLT") the bit **SLT SPP01** was required.[3] It ensures a well-reconstructed electron and hadronic final state by requiring a energy-longitudinal momentum imbalance of $E - p_z > 30\,\mathrm{GeV}$, a certain energy deposit found in at least one of the calorimeter sections, and an energy above 5 GeV in the isolated electron cluster. Also, SLT SPP01 implies that at least one of eleven FLT bits including 30 and 36 are set.

On the third trigger level ("TLT") the bit **TLT SPP02** was required. It adds a box cut on the electron position around the beam pipe of $|x_{el}|, |y_{el}| > 12\,\mathrm{cm}$, a cut on the electron energy of $E_{el} > 4\,\mathrm{GeV}$ and an upper cut on $E - p_z < 100\,\mathrm{GeV}$. The second level bit SLT SPP01 described above is already implicitly considered by TLT SPP02.

For the data taking periods after 2005 TLT SPP02 has been prescaled. Therefore additional TLT trigger bits were also considered for all later periods: **SPP09**, **HFL17**, and **HPP31**. These are neutral current DIS triggers with similar requirements as SPP02. HFL17 and HPP31 further demand loose restrictions on tracks, though.

Furthermore, one of the data summary tape ("DST") bits 49, 56, or 89 was required[4]. These directly correspond to TLT bits SPP02, SPP09, and HFL17, respectively.

Trigger Efficiencies

The first level trigger does not necessarily register all events that it should, leading to inefficiencies of the trigger chain. Such inefficiencies would result in an underestimation of the measured cross-section *if* this inefficiency was not also reproduced by the simulation.

The correct simulation of the trigger behavior can be verified by cross checking the reference data sample using a *monitor sample* selected with an independent ("orthogonal") trigger in addition to the offline DIS selection criteria introduced in the following section 6.2. The efficiency of the trigger is then defined as

---

[1] This corresponds to a logical `OR`.

[2] At the FLT stage, an isolated electron is defined as a single or group of up to four CAL supertowers with electromagnetic energy deposit, surrounded by "quiet" supertowers (and additional logic for CAL boundary regions and noise suppression) [128].

[3] Historically, all SLT and TLT bits are named according to the physics group they were originally intended for. For example, SPP is the abbreviation for "soft photoproduction".

[4] Except for data taking periods before 2006, were the DST bit 49 was required to be active.

$$\epsilon^{\text{ref}}_{\text{mon}} = \frac{N^{\text{ref}\wedge\text{mon}}}{N^{\text{mon}}} \,, \tag{6.1}$$

where $N^{\text{ref}\wedge\text{mon}}$ is the number of events triggered by requiring both the reference and the monitor trigger and N_{mon} is the number of events inclusively selected by the monitor trigger.

The FLT efficiency of the data sample used in this analysis has been investigated in two steps. First, the isolated electron-finding efficiency is studied. Next, the track veto efficiency as imposed by FLT 36 was estimated by using FLT 30 as monitor trigger.

Isolated Electron-Finding Efficiency

To study the isolated electron-finding efficiency on which both reference FLT bits 30 and 36 rely, monitor triggers have been used that primarily require total energy deposits in the calorimeter.

FLT bit	Requirements
40	$E^{\text{CAL}}_{\text{EMC, FLT}} > 20\,\text{GeV}$
41	$E^{\text{CAL}}_{T,\,\text{FLT}} > 30\,\text{GeV}$
43	$E^{\text{CAL}}_{T,\,\text{FLT}} > 15\,\text{GeV}$ and good track

Table 6.2: Requirements of the monitor FLT bits used in the evaluation of the isolated electron-finding efficiency

Table 6.2 lists the conditions that the monitor trigger bits 40, 41, and 43 impose, where $E^{\text{CAL}}_{\text{EMC, FLT}}$ and $E^{\text{CAL}}_{T,\,\text{FLT}}$ are the total electromagnetic and transverse energy deposits in the calorimeter, respectively. Due to the high-energy requirements the monitor sample is only a sub-sample of the reference sample. This is illustrated in figure 6.1 which shows the number of events selected inclusively by either the monitor or the reference triggers, or by requiring both to be active. After the inclusive DIS selection introduced in the following section 6.2, only about one third of the total reference sample has also been triggered by the monitor triggers. This number increases to about two thirds after jet selection due to the imposed cut on the transverse energy of the jets.

Thus the chosen monitor triggers still provide a meaningful way for evaluating the trigger efficiency for a substantial part of the data sample. The efficiency defined by equation 6.1 is shown in figure 6.2 for both the inclusive DIS and the jet selection as function of Q^2, $\cos\gamma_{\text{had}}$, and $E^{\text{CAL}}_{T,\,\text{FLT}}$ as used in the FLT trigger decision algorithm. The distributions show the overall efficiency to be almost equal to one, the only exception being the lowest bins in Q^2 where it drops to ~ 0.98. This is most likely due to the difficulty of finding isolated electrons very close to the beam pipe. In these few Q^2 bins the efficiency as determined in the Monte Carlo simulation also deviates by $\sim 1.5\%$ from the one measured in data.

The fact that the trigger efficiency as function of $E^{\text{CAL}}_{T,\,\text{FLT}}$ does neither drop at low energies nor exhibit differences between data and the Monte Carlo simulation makes it reasonable to assume that the efficiencies determined by the set of monitor triggers requiring high energies are sensible.

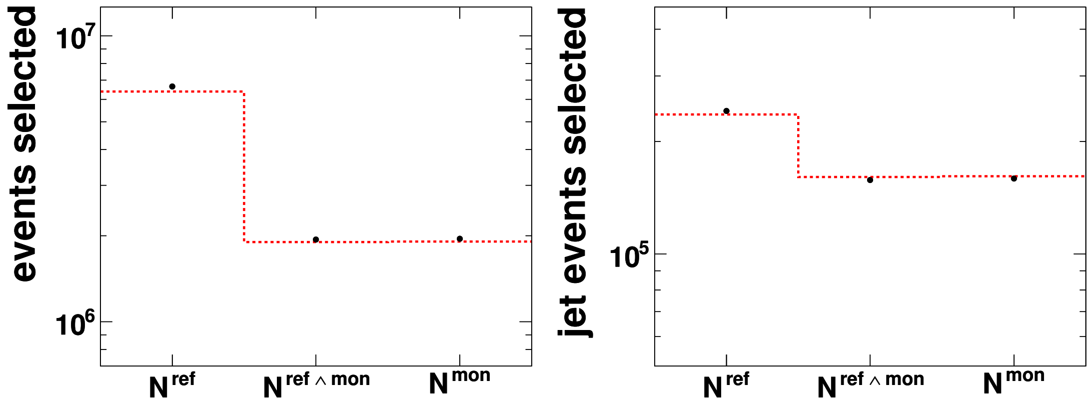

Figure 6.1: Number of events selected inclusively by reference (N^{ref}) or monitor (N^{mon}) trigger sets or by requiring both ($N^{\mathrm{ref}\wedge\mathrm{mon}}$) for the inclusive DIS sample (left) and the inclusive jet sample (right) for data (points) and DIS Monte Carlo simulation (dashed line).

Overall, the isolated electron-finding efficiency of the FLT triggers was found to be close to one and to be reasonably described by the Monte Carlo simulation.

Track Veto Efficiency

Because FLT 36 and FLT 43 have the loose track veto requirement in common, the monitor trigger set as defined in table 6.2 is not completely orthogonal. The efficiency of the track veto must therefore be evaluated separately.

The "loose track veto" imposed by FLT 36 is based upon information from the CTD. Due to restricted processing time at the first level trigger stage the full resolution of the CTD cannot be exploited. Instead the CTD-FLT uses a time difference measurement to provide a fast determination of the z-coordinate for each hit with an average resolution of 4.4 cm [130]. From the number of tracks fitted to the vertex of the ep interaction as function of the total number of tracks, the event is classified at trigger time as shown in figure 6.3. The loose track veto is defined to rejects all events classified with "2".

To test the efficiency of this veto and whether or not it is described well by the Monte Carlo simulation, FLT 30 was used as monitor trigger and compared to FLT 30 with an additional (offline) imposed track veto. Figure 6.4 shows the thus determined efficiency as function of Q^2, $\cos\gamma_{\mathrm{had}}$, and y both after the DIS and the jet selection. The value of the efficiency is in general above 0.9 in data, but typically 2.5 – 3.5% higher in the Monte Carlo simulation. The ratio between data and Monte Carlo simulation is almost flat except for a slight slope visible especially in y and $\cos\gamma_{\mathrm{had}}$.

The effect of the incorrect simulation of the track veto efficiency on the final data sample is reduced by the fact that only a subset of the events are exclusively triggered by FLT 36. This is illustrated by figure 6.5 from which follows that approximately 30% of the total number of selected events is only triggered by FLT 36. The maximum effect

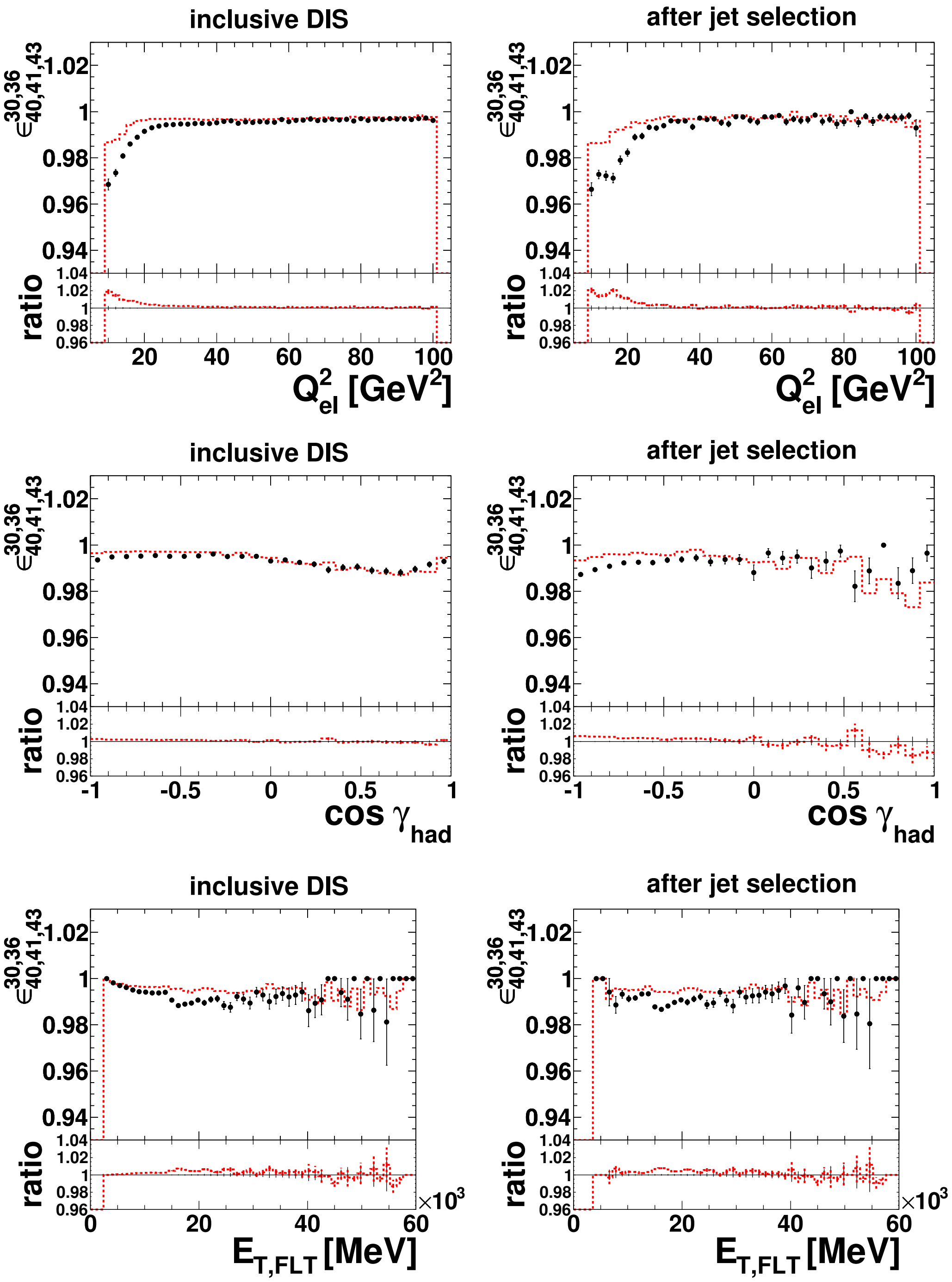

Figure 6.2: The trigger efficiency for FLT bits 30 and 36 determined in a monitor sample triggered by FLT bits 40, 41, and 43 as function of different variables for both data (points) and DIS Monte Carlo simulation (dashed line). Left hand side shows efficiencies after the inclusive DIS selection, right hand side after the inclusive jet selection.

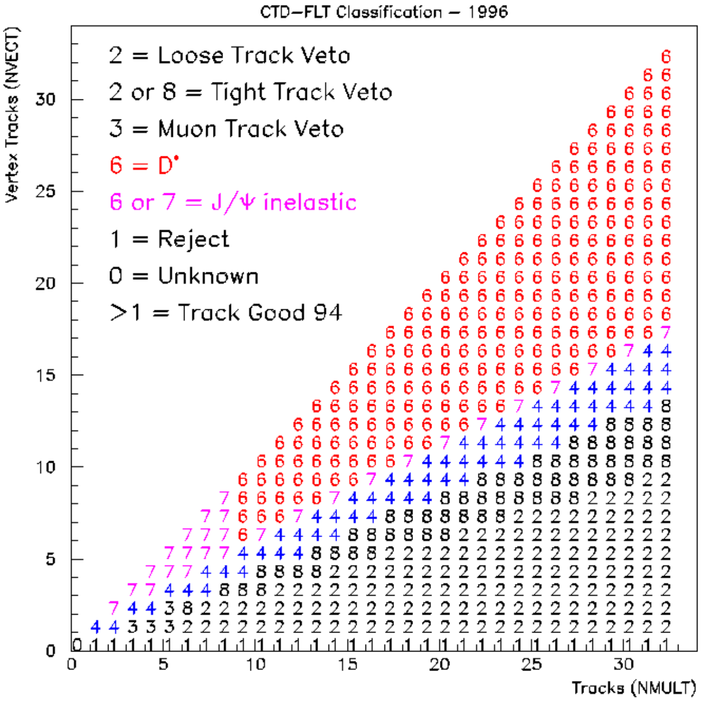

Figure 6.3: Definition of CTD-FLT classification: total number of tracks and vertex-fitted tracks from CTD-FLT. Taken from [129].

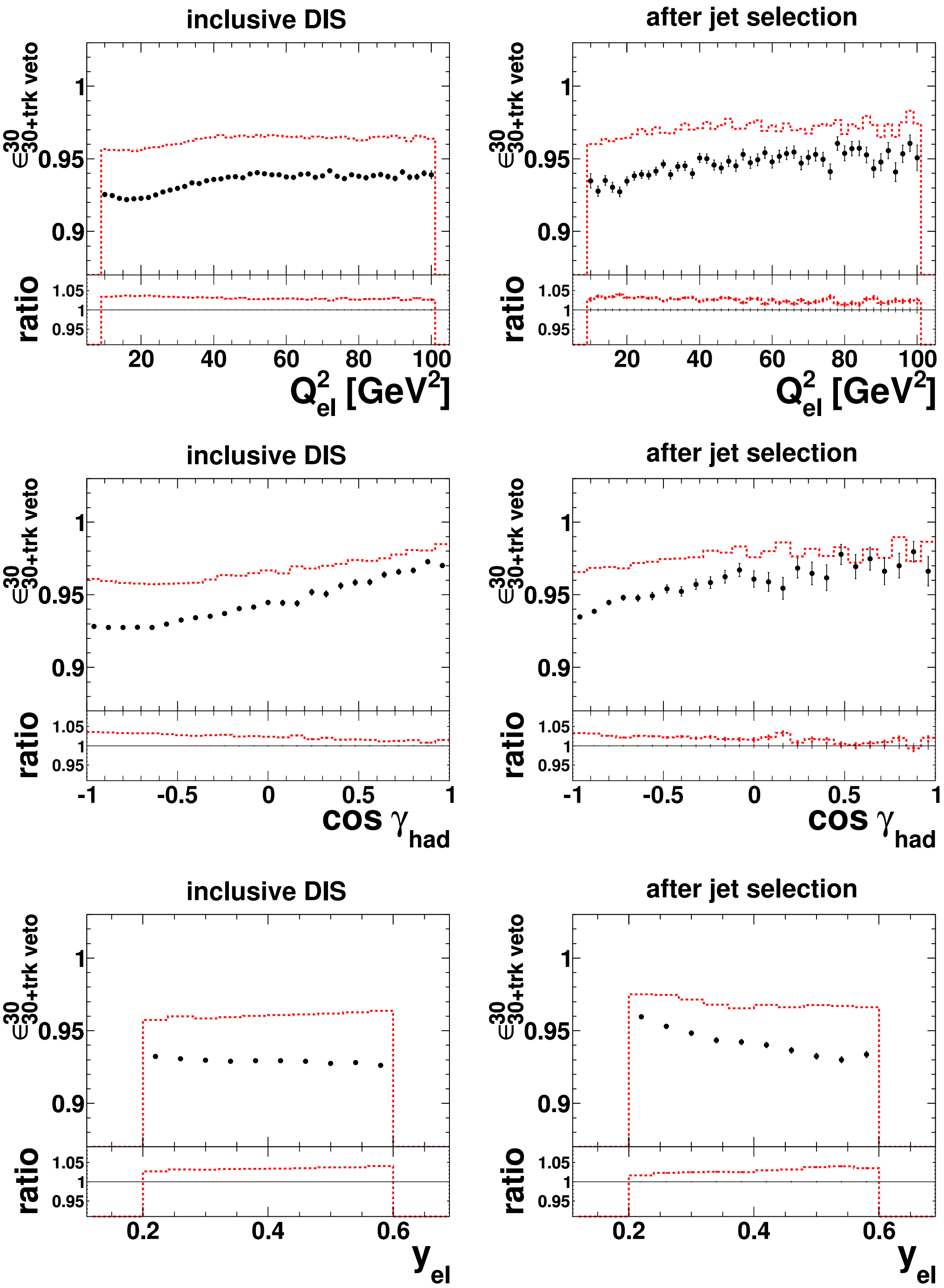

Figure 6.4: The veto efficiency used for FLT bit 36 determined in a monitor sample triggered by FLT bit 30 as function of different variables for both data (points) and DIS Monte Carlo simulation (dashed line). Left hand side shows efficiencies after the inclusive DIS selection, right hand side after the inclusive jet selection.

on the final data sample can thus be estimated to be in the order of 1%. A correction procedure for this remaining difference is discussed in chapter 7.3.

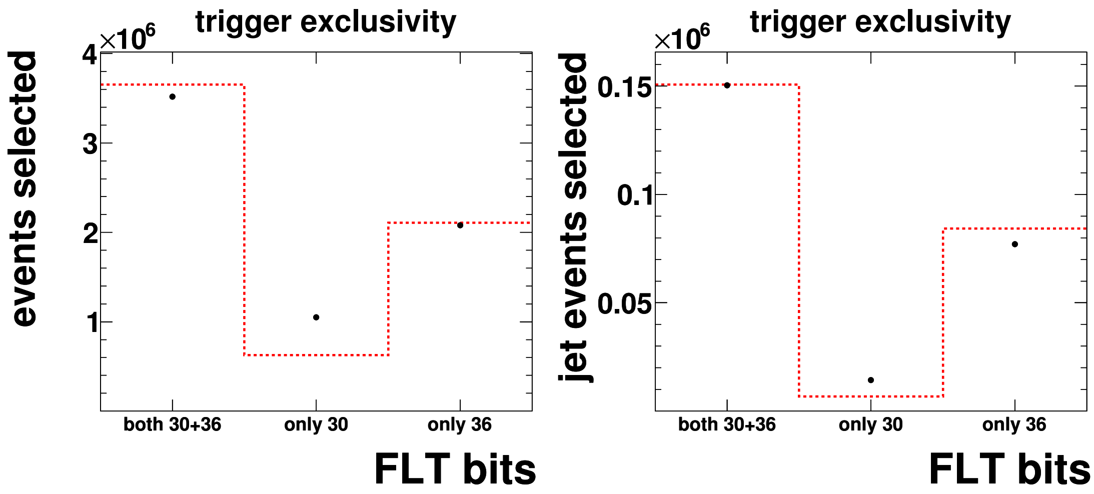

Figure 6.5: Number of events selected as function of the active FLT triggers: both FLT 30 *and* 36, only 30, and only 36 for the inclusive DIS sample (left) and the inclusive jet sample (right). Shown are data (points) and the DIS Monte Carlo simulation (dashed line).

6.2. Inclusive DIS Event Selection

After events passed the online selection criteria described in the previous sections, additional offline requirements are imposed. These consist of the *phase space cuts* which select the kinematic region to be studied and *cleaning cuts* which are performed for technical reasons, for background suppression, and to increase the purity of the data sample.

The dominant background in the investigated phase space are photoproduction (γp) events where the scattered electron escaped into the beam pipe and, at the same time, another particle (typically a π^0) is misidentified as electron.

To estimate the influence of this background, a photoproduction Monte Carlo sample was used. Figures 6.6 – 6.9 illustrate the cuts described below by comparing data with the DIS Monte Carlo sample, the γp Monte Carlo sample, and the sum of the two for various variables on which cuts were imposed. The distribution is always shown without the respective cut applied thus extending beyond the region considered in this analysis. The cuts are indicated in the figures by a vertical line.

6.2.1. Phase Space

The phase space selection consists of cuts on the kinematic variables Q^2 and y reconstructed via the Electron method as discussed in chapter 5.3.1.

- **Photon virtuality**, $10 < Q^2_{\mathrm{el}} < 100\,\mathrm{GeV}^2$: selects deep inelastic processes with low momentum transfer. The corresponding distribution is shown in figure 6.6a. Below a value of $Q^2 \approx 8\,\mathrm{GeV}^2$ the fraction of photoproduction events rises while the description of the data by the Monte Carlo simulation degrades, in part motivating the lower cut on Q^2.

- **Inelasticity**, $0.2 < y_{\mathrm{el}} < 0.6$: the lower cut on y suppresses events with hadronic activity in the forward direction at low transverse momentum. Additionally, it restricts the phase space to a region where the Electron method yields a good resolution. The upper cut on y ensures a well reconstructed Electron and suppresses photoproduction background as demonstrated in figure 6.6b.

The Monte Carlo simulation describes the data very reasonably over the full investigated phase space as shown in figure 6.6.

6.2.2. Cleaning Cuts

Cleaning cuts are imposed on the DIS sample for detector-related reasons, for the suppression of backgrounds, and to increase the purity of the data sample.

Based on offline selection criteria applied in recent ZEUS publications [122, 131] the following cuts were applied in this analysis:

- **Longitudinal vertex position**, $|z_{vtx}| < 30\,\mathrm{cm}$: the *ep* interaction can occur anywhere along the length of the overlapping electron and proton bunches, leading to an approximately Gaussian-shaped central part of the z-vertex distribution as

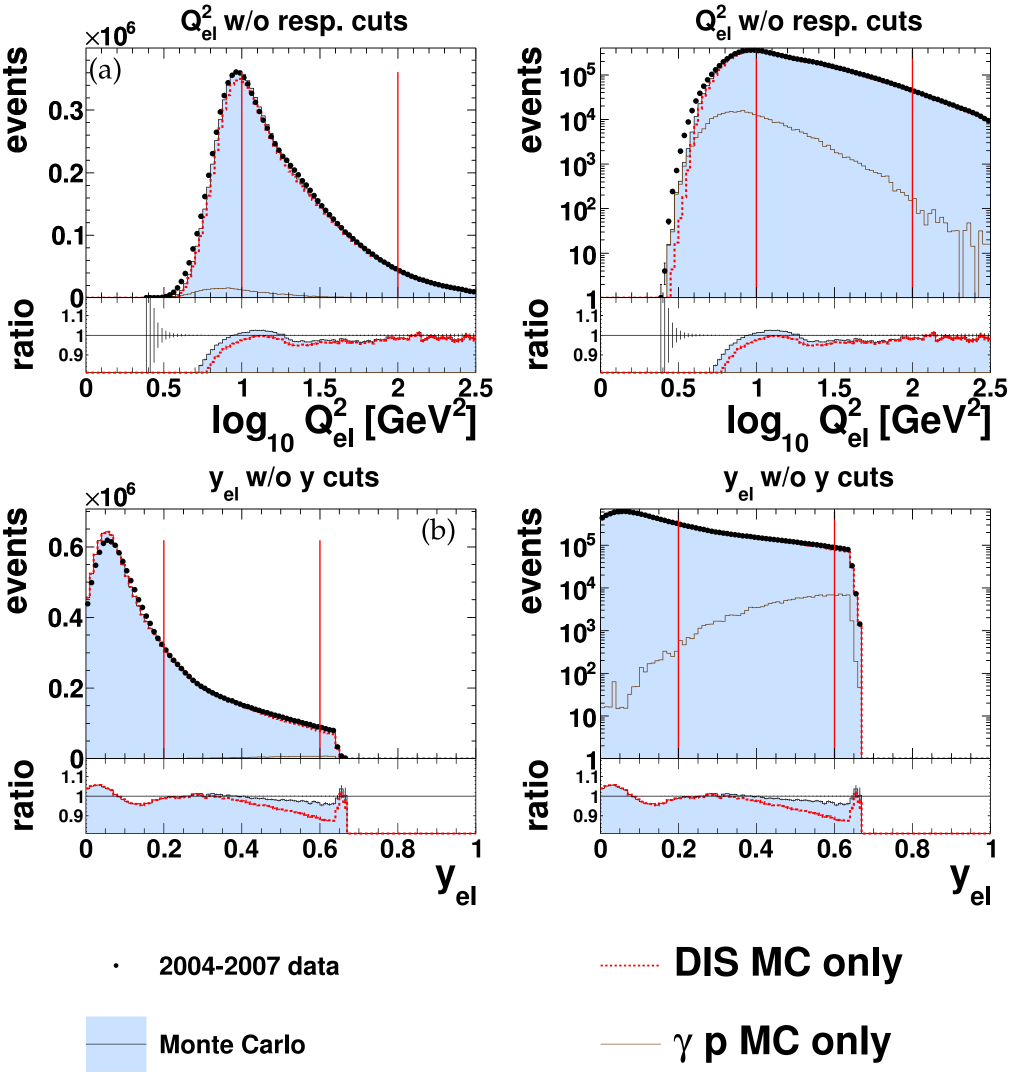

Figure 6.6: Control distributions illustrating the phase-space cuts for the offline event selection (solid vertical lines). The Monte Carlo sample has been normalized to the luminosity of the data. Shown are data (points) and the sum of Monte Carlo samples (shaded area), as well as its individual contributions, DIS (dashed line) and γp (solid line). The lower part shows the ratio to data where vertical lines indicate the statistical uncertainty of the respective sample. The Monte Carlo events were reweighted as function of the longitudinal vertex position and were corrected for the previously observed deviation in trigger efficiency, as described in chapter 7.

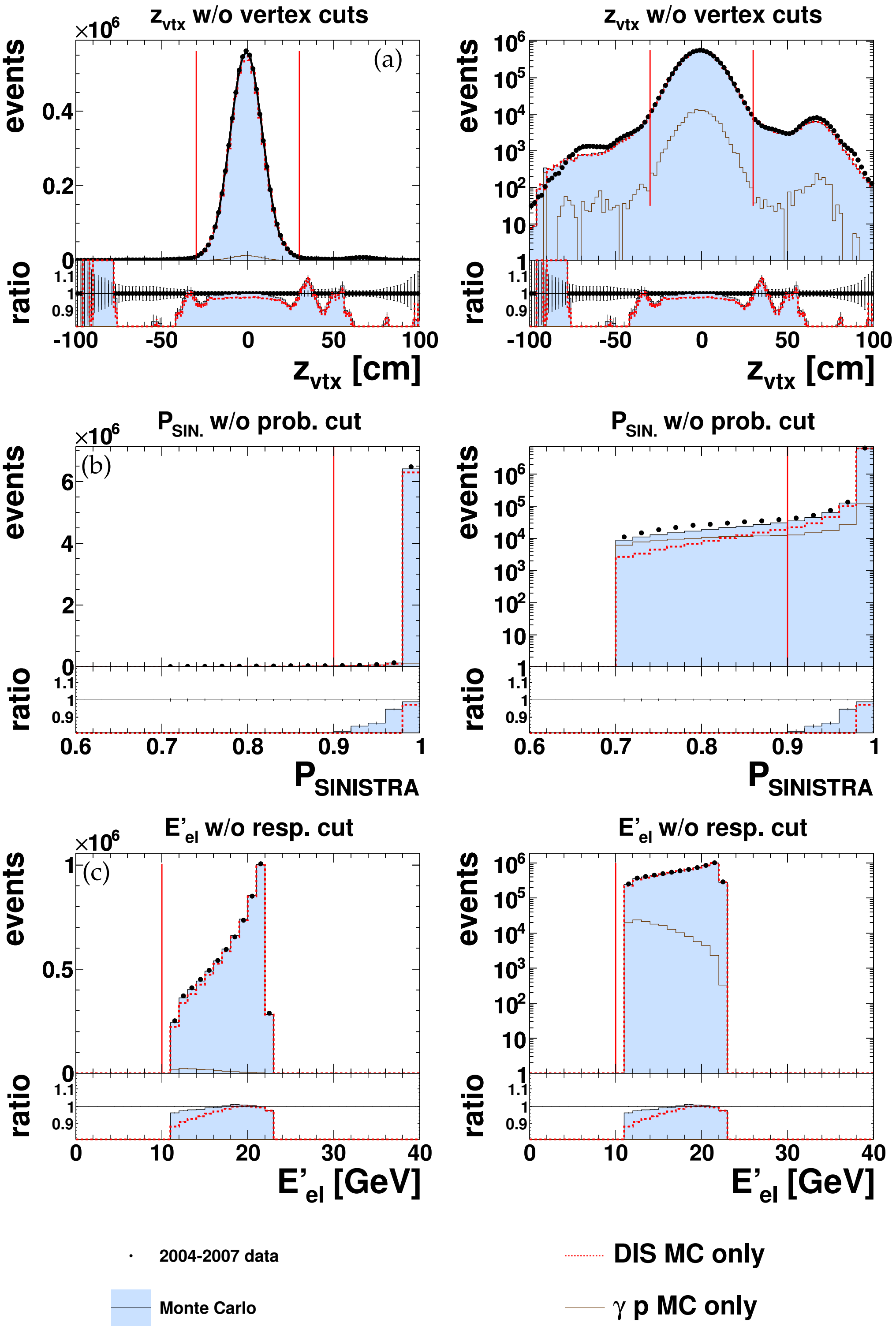

Figure 6.7: Control distributions illustrating the cleaning cuts for the offline event selection. For details see the caption to figure 6.6.

shown in figure 6.7a.[5]. The collision of nominal with neighboring bunches forms the so-called satellite peaks. Furthermore, beam-gas events can originate from any point along the z-axis. To reduce the influence of events with a displaced vertex, a cut of $|z_{vtx}| < 30\,\text{cm}$ is imposed, corresponding to $\sim \pm 3\sigma$ of the central peak.

The Monte Carlo simulation describes the data well in the region of the central peak but fails to fully characterize the satellite peaks. Still, the statistically relevant regions are reasonably described.

- **Electron reconstruction**: Since the electron is essential for the derivation of the kinematics, several selection criteria were applied to ensure a well reconstructed electron in the event:
    - **Probability**: the electron candidate as identified by the SINISTRA algorithm was required to have a probability of $\mathcal{P}_{\text{SINISTRA}} > 0.9$. Figure 6.7b shows the corresponding distribution. The fraction of photoproduction background events where e.g. a photon resulting from neutral pion decay was misidentified as electron, can be seen to rise toward lower values of $\mathcal{P}_{\text{SINISTRA}}$ thus motivating the imposed cut. Due to requirements already applied when preparing the data samples, no events with a probability below 0.7 are seen.
    - **Electron energy**: requiring an electron energy of $E'_{\text{el}} > 10\,\text{GeV}$ suppresses photoproduction background events as indicated in figure 6.7c where the background increases for lower electron energies. Furthermore, the electron finding and trigger efficiencies are higher in this region of the electron energy. An explicit cut on E'_{el} is barely needed in the phase space investigated in this analysis though, as the upper cut on y is roughly equivalent to $E'_{\text{el}} > 10\,\text{GeV}$.
    - **Isolation**: to suppress events where a hadronic jet is overlapping with the scattered electron, the hadronic energy inside a cone around the electron candidate was required to be less than 10% of the total energy deposited within. The cone was defined with a radius of 0.7 in the pseudorapidity-azimuthal plane around the electron direction. As demonstrated in figure 6.8a, this cut only effects a relatively small percentage of events.
    - **Position**: to measure the full energy of the electron it is important that the electron cluster is fully contained within the calorimeter. The entry position of the electron in the calorimeter was therefore required to be outside of (a) regions close to the beam pipe[6], (b) a part of the RCAL where the depth was reduced due to the cooling pipe for the solenoid ("chimney")[7], and (c) regions in-between calorimeter sections ("super-crack" regions)[8].

---

[5] The distributions shown have been reweighted in the Monte Carlo simulation as function of the z-vertex as will be motivated and discussed in chapter 7.

[6] $R > 18\,\text{cm}$, where $R = \sqrt{x^2_{\text{elect.}} + y^2_{\text{elect.}}}$ with $x_{\text{elect.}}$ and $y_{\text{elect.}}$ denoting the scattered electron position in the RCAL.

[7] Cut applied if $z_{\text{elect.}} < -148\,\text{cm}$ and $y_{\text{elect.}} > 90\,\text{cm}$ and $-14 < x_{\text{elect.}} < 12\,\text{cm}$.

[8] Cut applied if $-104 < z_{\text{elect.}} < -98.5\,\text{cm}$ or if $164 < z_{\text{elect.}} < 174\,\text{cm}$ where $z_{\text{elect.}}$ denotes the longitudinal position of the scattered electron.

Additionally, for specific run ranges in the 2006 – 2007 period the electron candidate was required *not* to be located inside one specific RCAL inner ring cell[9] with known inefficiencies [132].

Figure 6.8b shows the number of events as function of the distance to the beam pipe ("radius") and indicates the respective cut. The steep rise of the distribution up to a maximum at $\sim 27\,\mathrm{cm}$ is the result of the lower kinematic cut on Q^2_{el} already removing many events at small angles with the beam pipe, thus reducing the impact of the cut.

- The **energy-longitudinal momentum balance** is defined by

$$E - p_z = (E_{\mathrm{had}} - p_{z,\,\mathrm{had}}) + (E_{\mathrm{el}} - p_{z,\,\mathrm{el}}) \ , \tag{6.2}$$

where E denotes the energy and p_z the longitudinal momentum component of the hadronic system and the electron, respectively. In the initial state with $E_{\mathrm{el}} = -p_{z,\,\mathrm{el}} = 27.5\,\mathrm{GeV}$ and $E_{\mathrm{had}} = p_{z,\,\mathrm{had}} = 920\,\mathrm{GeV}$, the longitudinal momentum balance is equal to two times the electron beam energy or $\approx 55\,\mathrm{GeV}$. Energy-momentum conservation requires the same $E - p_z$ in the final state. However, the finite detector resolution and radiative processes affect the value of $E - p_z$.

A specific feature of the quantity $E - p_z$ is that undetected particles of the proton remnant have only a small impact on its value, while particles escaping undetected in the direction of the electron beam, for example from photoproduction processes (electron) or caused by initial state radiation (photon), reduce the value of $E - p_z$ by two times the energy of the undetected particle. These types of events can therefore be suppressed by a lower cut of $E - p_z > 42\,\mathrm{GeV}$.

Beam-gas interactions on the other hand can also lead to higher values of $E - p_z$ and were suppressed by an upper cut of $E - p_z < 65\,\mathrm{GeV}$.

The number of events as function of $E - p_z$ is shown in figure 6.9a. The Monte Carlo distribution exhibits a small shift toward higher values of $E - p_z$ with respect to the data.

- **Transverse momentum balance**: the transverse momenta of the hadronic system and of the electron were required to satisfy $p_{T,\,\mathrm{had}}/p_{T,\,\mathrm{el}} > 0.3$. In neutral current events the ratio is expected to be close to one as the hadronic system is balanced by the scattered electron. This cut removes events where the p_T of the hadronic system is much smaller than that of the electron. This occurs, for example, in charged current events where a photon in the hadronic final state is misidentified as electron resulting in an unbalanced p_T with respect to the remaining hadronic system.

Figure 6.9b shows the number of selected events as function of the transverse momentum balance. The distribution exhibits the expected peak close to $p_{T,\,\mathrm{had}}/p_{T,\,\mathrm{el}} \approx 1$. The position of the peak is well described by the Monte

---

[9] Affected cell: $7.515 < x_{\mathrm{elect.}} < 31.845\,\mathrm{cm}$ and $7.9 < y_{\mathrm{elect.}} < 31.9\,\mathrm{cm}$ with the scattered electron position in x and y directions in the RCAL; affected run ranges: 59600 – 60780, 61350 – 61580, and 61800 – 63000.

Carlo simulation, but the width of the distribution is predicted to be larger by the simulation than is seen in data.

- **Number of tracks**: To remove events typically not well described by the Monte Carlo simulation, at least one "good" track was required. A "good" track was defined as having $p_T > 0.2\,\mathrm{GeV}$, having been fitted to the primary vertex and having passed at least three CTD superlayers.

- **Elastic QED-Compton scattering**: in elastic Compton scattering, the proton does not dissociate and remains in the beam pipe, resulting in the detection of two electromagnetic clusters with balancing p_T. As these events are not well described by the Monte Carlo simulation, events were rejected if a second electron candidate was found with a probability assigned by SINISTRA of greater than 0.9, with an azimuthal separation between the candidates of $\Delta\phi > 3$, a ratio of transverse momenta of the two candidates between 0.8 and 1.2, and no calorimeter energy beside the two EM clusters of more than $3\,\mathrm{GeV}$.

The overall description of the data by the Monte Carlo simulation, as shown in figures 6.6 – 6.9, is reasonable in most of the statistically relevant regions of the distributions discussed above. The absolute normalization of the data is correctly reflected in the simulation within approximately $(2-3)\%$, while individual features are typically reproduced within an additional $(1-2)\%$. Notable exceptions are the $E - p_z$ and the $p_{T,\,\mathrm{had}}/p_{T,\,\mathrm{el}}$ distributions.

Possible systematic effects on the measurement introduced by the imposed cuts will be discussed in detail in chapter 9.1.

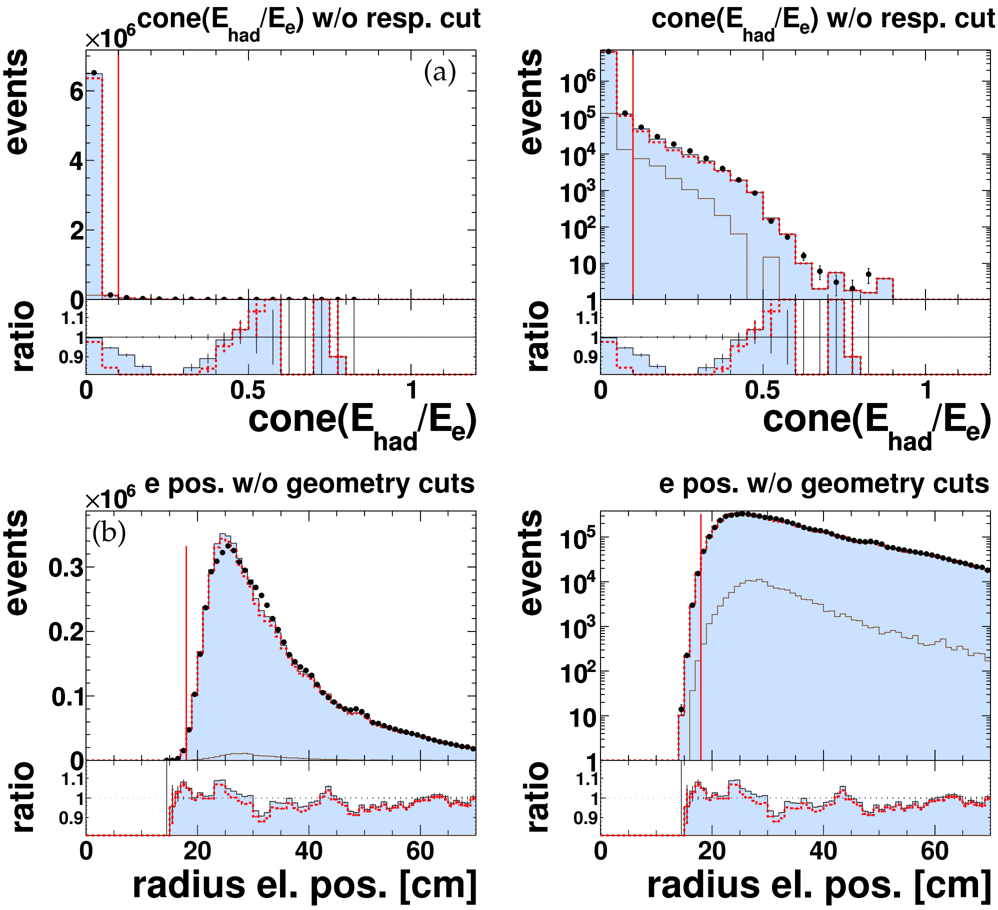

Figure 6.8: Control distributions illustrating the cleaning cuts for the offline event selection. For details see caption and legend to figure 6.6.

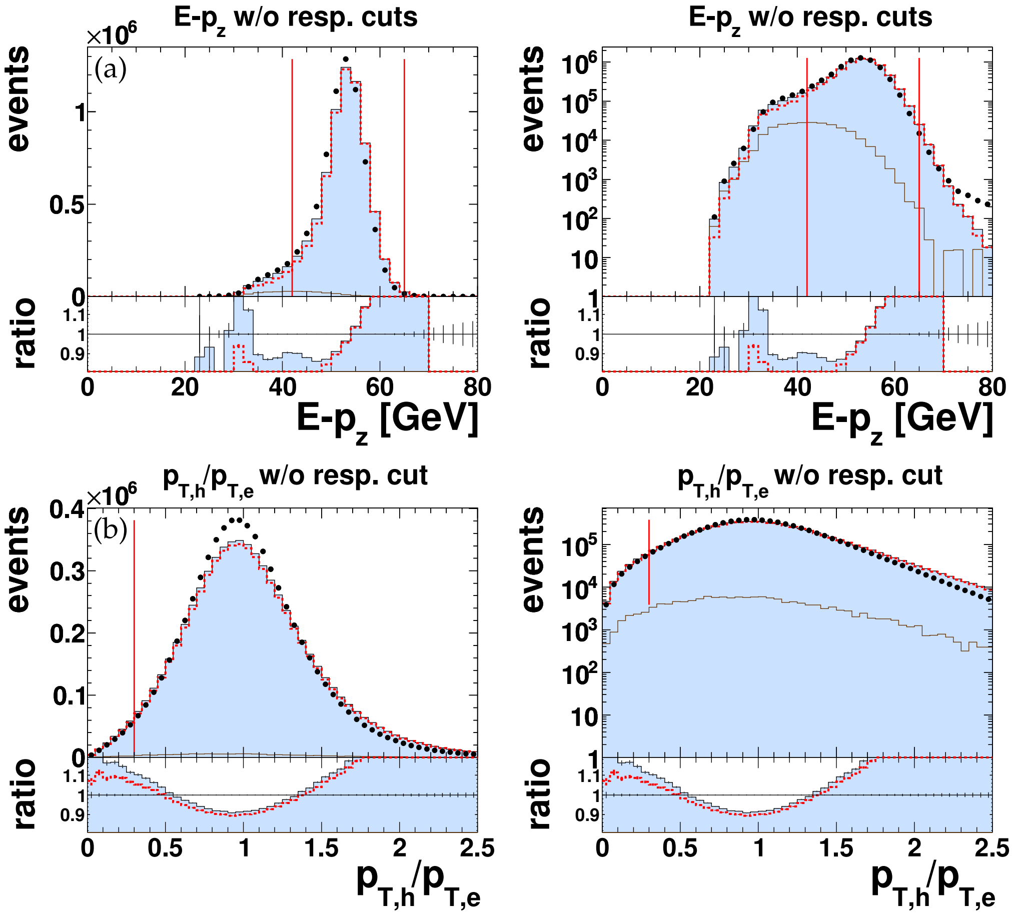

Figure 6.9: Control distributions illustrating the cleaning cuts for the offline event selection. For details see caption and legend to figure 6.6.

6.3. Jet Sample Selection

As explained in chapter 2.4, jets were reconstructed using the longitudinally invariant k_T cluster algorithm on calorimeter cells[10] in the Breit reference frame. The four-vectors of the jets were afterwards boosted back to the laboratory ("lab") frame.

To ensure well-reconstructed jets and a high-purity sample, cleaning cuts were first imposed on the jet sample:

- **Far backward jet**: In the case of initial-state radiation where a photon is emitted close to the electron beam direction, the photon can be misidentified as a jet. Thus, events were rejected in which a jet with a pseudorapidity in the laboratory frame, η_{lab}, below -2 with a transverse momentum in the Breit frame, $E_{T,\,\mathrm{Breit}}$, above 5 GeV was found.
- **Electron-Jet isolation:** to ensure a well-isolated electron the distance ΔR between each jet and the electron candidate as defined by

  $$\Delta R = \sqrt{(\eta^{\mathrm{jet}}_{\mathrm{lab}} - \eta^{\mathrm{el}}_{\mathrm{lab}})^2 + (\phi^{\mathrm{jet}}_{\mathrm{lab}} - \phi^{\mathrm{el}}_{\mathrm{lab}})^2}\ , \tag{6.3}$$

  was examined, where ϕ and η are the azimuthal angles and the pseudorapidities of the jet and the electron, respectively. Only events were accepted where no jet exhibited $\Delta R < 1$.
- **Low transverse momentum**: to assure well-reconstructed jets with minimal relative scale uncertainty, a lower cut on the transverse momentum in the laboratory frame, $E_{T,\,\mathrm{lab}}$, of 3 GeV was imposed.

After the above cleaning cuts were applied, the following phase-space requirements were imposed:

- **Transverse momentum**: each jet was required to feature a transverse momentum in the Breit frame of at least $E_{T,\,\mathrm{Breit}} > 8\,\mathrm{GeV}$.
- **Pseudorapidity**: each jet was required to be inside the pseudorapidity interval in the laboratory frame of $-1 < \eta_{\mathrm{lab}} < 2.5$.

The *inclusive jet sample* consists of all events with one or more jets. For the *dijet sample* and *trijet sample* only events were considered that feature at least two and three jets, respectively, and that fulfill the following additional criterion:

- **Invariant dijet mass**: the invariant dijet mass, M_{jj}, determined from the *two hardest jets* in the event meeting the other selection criteria, was required to be greater than 20 GeV.

The cut on M_{jj} was introduced to keep clear of unphysical behavior of the NLO QCD predictions due to infrared cut-offs as detailed in chapter 4.2.

The resulting trijet sample is a subset of the dijet sample.

---

[10] For details, refer to chapter 5.1.

6.4. Background and Diffractive Events in the Inclusive DIS and Jet Samples

In the inclusive DIS data sample, events are present that result from processes neither considered by the NLO QCD prediction nor by the Monte Carlo simulation used in this analysis.

These processes include

- *diffractive processes* where the photon interacts with the proton to form two hadronic final state systems separated by a large gap in rapidity [133], and
- *photoproduction processes* where a quasi-real photon is exchanged and the electron is scattered at very low angles thus escaping undetected into the beam pipe.

Diffraction also occurs in DIS but is not described by the NLO QCD prediction. Its effect on the total cross-section is therefore estimated in this section. Contributions to the cross-sections from photoproduction (γp) events, on the other hand, were considered background and have been corrected for using a dedicated γp Monte Carlo sample as described below.

To differentiate between diffractive events and non-diffractive events in DIS, the presence of a large rapidity gap can be used. A measure for this rapidity gap is η_{max}, the maximum pseudorapidity of the most forward going calorimeter condensate with an energy above 400 MeV. For η_{max} values smaller than 2.5 the diffractive background becomes dominant [134].

Figure 6.10 shows the η_{max} distributions after the inclusive DIS and the inclusive jet selections. While with approximately 6.6% there is a sizable contribution of events with $\eta_{\mathrm{max}} < 2.5$ in the inclusive DIS sample, this type of event is suppressed down to $\sim 1.5\%$ in the jet sample. These numbers can only serve as an upper estimate of the diffractive contribution though, as these candidates for diffractive processes have not been investigated further.

The background due to photoproduction processes has been studied using a dedicated γp Monte Carlo sample on which the same selection criteria as described above were imposed. This sample is shown e.g. in figures 6.6 – 6.9 for various distributions of the inclusive DIS sample as solid dark line.

Both the DIS and the γp Monte Carlo samples were normalized to their respective luminosities. After the inclusive DIS selection is performed approximately 2.5% of the total number of selected Monte Carlo events come from the photoproduction sample.

This number is significantly reduced after the inclusive jet selection, after which only $\approx (0.5 \pm 0.2)\%$ photoproduction events remain.[11] This suppression in the jet sample is mainly due to the requirements on the transverse energies of the jets since the E_T^{jet} distributions are more steeply falling in the γp sample compared to the DIS Monte Carlo simulation.[12]

---

[11] The uncertainty on the fraction of photoproduction events in the jet sample has been estimated from the statistics of the sample only.

[12] See chapter 8 for details.

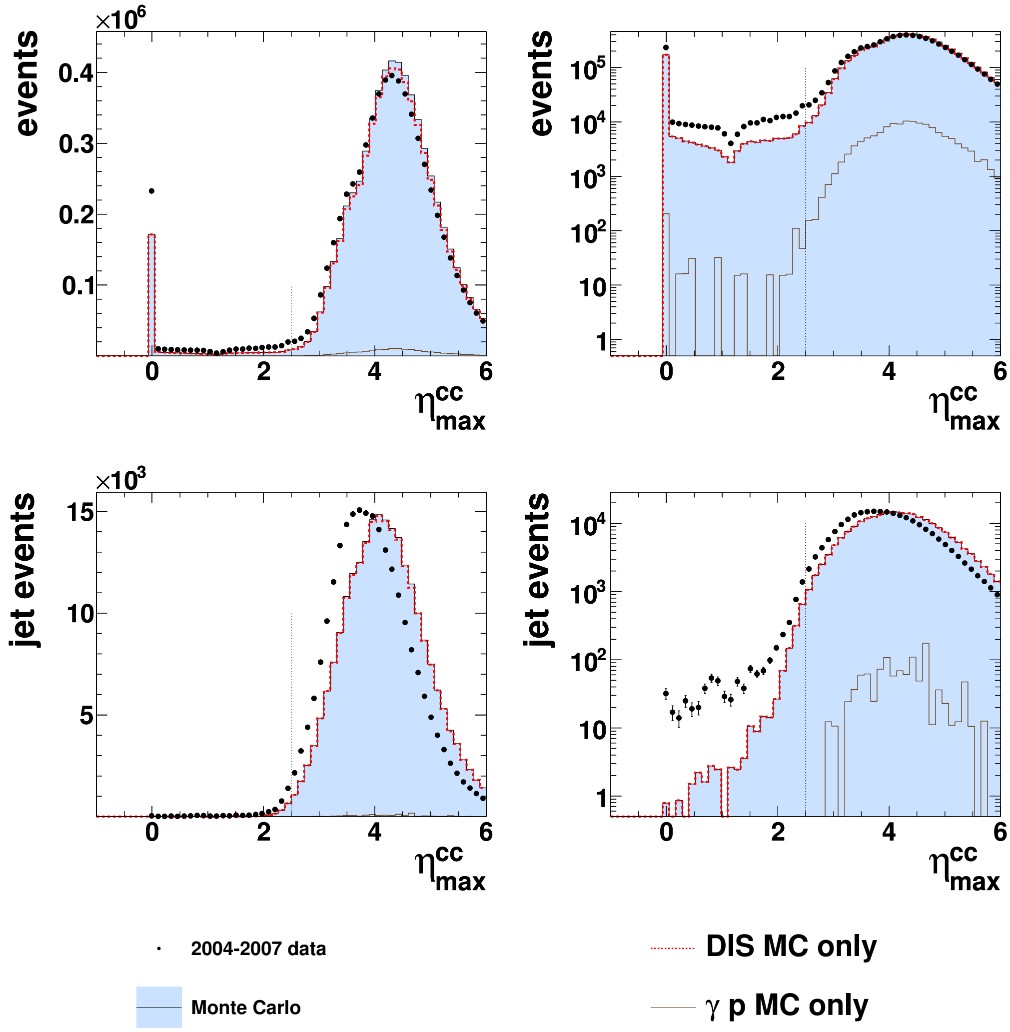

Figure 6.10: $\eta_{\max}$ distributions for the inclusive DIS sample (top) and the inclusive jet sample (bottom) in linear (left) and logarithmic scale (right). The vertical dotted lines indicate $\eta_{\max} = 2.5$.

By using the sum of the two Monte Carlo samples in the unfolding of the data as described in chapter 8, the data have been corrected for background events from photoproduction processes.

The systematic effects introduced by the estimation of the photoproduction background contribution to the sample will be discussed in chapter 9.1.

6.5. Summary

The online and offline criteria used to select events in DIS and subsequently the jet samples have been presented. Table 6.3 shows an overview of the number of selected events in each data-taking period for each data sample.

Period	Lepton	Selected events in sample			
		inclusive DIS	inclusive jets	dijets	trijets
2004 – 2005	e^-	3,099,556	112,354	30,977	1,892
2006	e^-	1,203,488	44,295	11,996	712
2006 – 2007	e^+	2,346,267	85,069	23,532	1,451
HERA-II		6,649,311	241,718	66,505	4,055

Table 6.3: Number of selected events in the inclusive DIS, inclusive jet, dijet, and trijet samples.

The final data sample will be discussed in more detail in chapter 8, after jet energy corrections and reweighting procedures have been introduced in chapter 7.

7. Corrections and Reweighting

A precise cross-section measurement with a realistic evaluation of the associated uncertainties requires both a good understanding of the detector and an accurate simulation of its response. As the jet energy is commonly the dominant source of uncertainty in jet cross-section measurements at Zeus [122, 135, 136], two studies were performed to improve its reconstruction and simulation.

In the first study correction factors were derived to ensure a correct description of the calorimeter hadronic energy scale in the simulation by balancing the transverse momentum of the electron with that of the hadronic final state in specifically selected neutral current DIS events.

The second study aims at compensating for inactive material in the detector which typically leads to an underestimation of the reconstructed jet energy. Correction factors are derived by taking advantage of the generated hadronic final state together with the full detector simulation available in Monte Carlo simulations. Both studies are described in detail in the first part of this chapter.

As will be explained in chapter 8, the Monte Carlo simulation is used to derive the cross-sections. An important prerequisite for the use of the simulation is the adequate agreement between the output of the simulation and the measured detector information. The second half of this chapter presents studies performed with the aim of re-adjusting the simulated detector output to improve its agreement with the data.

7.1. Jet Corrections

This section presents two studies, the first performed in order to calibrate the hadronic energy scale of the simulation, the second to correct the reconstructed jets for energy losses in both data and the Monte Carlo simulation. Both use a similar approach as described in [110, 137].

For Zeus jet cross-section measurements one of the most important aspects in the simulation of the detector output is the correct description of the hadronic energy scale of the calorimeter. It has been shown that energy scale uncertainties of $\pm(3-5)\%$ lead to uncertainties of the cross-section measurement in the order of $\pm(10-20)\%$ [138, 139]. These uncertainties can be significantly improved among others by correcting deviations in the absolute hadronic energy scale of data and the Monte Carlo simulation as shown by more recent publications [122, 136, 137, 139, 140].

After the hadronic energy scale in the simulation has been calibrated, the reconstructed jets can be further corrected for energy losses: Monte Carlo simulations allow to directly compare the jets reconstructed from simulated calorimeter information with the "true" jets composed of the final state hadrons. As shown later in this chapter one observes that the transverse energy of a jet in the calorimeter, E_T^{CAL}, is reduced by up to 20% compared to the E_T^{had} for the jet on hadron level[1]. This is mainly caused by inactive material in front of the calorimeter but also by contributions from other effects [141].

7.1.1. Hadronic Energy Scale Calibration

For this analysis the hadronic energy scale has been adjusted by exploiting energy and momentum conservation between the electron and the hadronic final state. Assuming a perfect calibration and no energy losses the ratio of the respective transverse energies should be equal to one:

$$r_T = \frac{E_T^{\text{hadr.}}}{E_T^{\text{elec.}}} = 1 \tag{7.1}$$

In reality r_T deviates from unity due to energy absorbed in inactive material, neutrinos from hadronic decays escaping the detector, or miscalibration. Nevertheless, these effects are assumed to be correctly described in Monte Carlo simulation so that

$$C_{\text{scale}} = \frac{\langle r_T^{\text{data}} \rangle}{\langle r_T^{\text{MC}} \rangle} \overset{!}{=} 1 \ , \tag{7.2}$$

where $\langle r_T \rangle$ denotes the mean ratio of the transverse energies of the hadronic final state and the scattered electron. Any deviation of C_{scale} from one indicates that the energy scales in the simulation are shifted with respect to the data. In the context of this study, the energy scale of the electron reconstructed with the DA method is assumed to be correctly described by the simulation, thus leaving a difference in hadronic calorimeter scale as cause for $C_{\text{scale}} \neq 1$.

The calibration of the hadronic energy scale is performed by first measuring C_{scale} as function of η_{lab}. C_{scale} is then applied in the main analysis as a multiplicative correction factor to the energy of all Monte Carlo jets.

For practical reasons $E_T^{\text{hadr.}}$ is approximated by the transverse jet energy, E_T^{jet}, which is a legitimate approach as long as the hadronic activity is concentrated in one jet. As this is not always the case we introduce a cut-off transverse energy for other jets which was set at 4 GeV and will be later shown to have little systematic effect on the corrections.[2]

For this study the electron energy has been determined using the Double-Angle method as described in section 5.3.3. The advantage of this method is that it is in first approximation independent of the absolute scale of the energy measurement.

In order to investigate the energy scale over the full studied η_{lab} range, the event sample was selected with $Q^2 > 125\,\text{GeV}^2$ and without any cuts on y. This loosened the angular restrictions imposed on the reconstructed electron with respect to the main analysis, but also required a different choice of trigger compared to the event selection described in chapter 6. To summarize all modifications with respect to the main analysis:

- high-Q^2 sample (no y cut, $Q^2 > 125\,\text{GeV}^2$);

---

[1] For a definition of the different levels distinguished in the simulation see 4.1.4.

[2] It should be noted though that allowing additional low-E_T jets causes $r_T < 1$.

- trigger chain replaced by a high-Q^2 trigger chain;[3]
- jets clustered in the laboratory frame;
- one jet with $E_{T,\,\mathrm{lab}} > 10\,\mathrm{GeV}$;
- no other jet with $E_{T,\,\mathrm{lab}}$ greater than $4\,\mathrm{GeV}$.

Figure 7.1 shows control distributions for this high-Q^2 data sample. The distributions demonstrate good agreement between data and the simulation for kinematic variables reconstructed with the Double-Angle method and jet variables.

Deriving the correction factors

Figure 7.2 shows the ratio of transverse energies, r_T, for one bin in pseudorapidity for both data and MC. The distributions are roughly Gaussian in shape with a mean value close to but not quite equal to one. From the ratio of $\langle r_T \rangle$ of data over the Monte Carlo sample one can determine $C_{\mathrm{scale}} \approx 1.014$ which corresponds to a shift of the MC relative to the data of $\sim 1.4\%$ towards smaller values.

The result of the measurement of $\langle r_T \rangle$ for all bins in η_{lab} as well as bins in E_T^{jet} is shown in figure 7.3. It demonstrates that $\langle r_T \rangle \geq 0.95$ in all bins except in the lowest E_T^{jet} bin where it drops to ≈ 0.90. This behavior can be expected as the relative amount of hadronic energy absorbed in dead material is higher for low-E_T jets. The calorimeter response is generally described *in shape* by the Monte Carlo simulation over the full E_T^{jet}-range.

This can be studied in more detail in figure 7.4 where the ratio of means, $\langle r_T^{\mathrm{data}} \rangle / \langle r_T^{\mathrm{MC}} \rangle$, is shown in the same bins of E_T^{jet} and η. The figure demonstrates that the Monte Carlo simulation describes the energy scale of the data within approximately 3% with only a constant offset, thus motivating the correction of the energy scale in the Monte Carlo simulation.

The dashed line in figure 7.4 indicates the values of $C_{\mathrm{scale}}(\eta)$ that were determined for each η bin independent of E_T^{jet}. These values range from 0.995 to 1.015 and thus correspond to energy scale corrections of up to 1.5%.

Results of the calibration

Figure 7.5 shows the ratio $\langle r_T^{\mathrm{data}} \rangle / \langle r_T^{\mathrm{MC}} \rangle$ after the energy scale correction factors have been applied. The results demonstrate the successful application of the correction procedure. The Monte Carlo simulation describes the data within $\sim 1\%$. This is compatible with previous estimations of the hadronic energy scale uncertainty [122] for jets with $E_{T,\,\mathrm{lab}} > 10\,\mathrm{GeV}$.

However, for a conclusive evaluation of the remaining hadronic energy scale uncertainty further independent studies are advised. This has been recently investigated in [110, 122], resulting in uncertainties of the hadronic energy scale of $\pm 3\%$ for jets with transverse momenta below $10\,\mathrm{GeV}$ and $\pm 1\%$ for jets with $E_{T,\,\mathrm{lab}} > 10\,\mathrm{GeV}$.

---

[3] *FLT*: bits 40, 43, 50; *SLT*: SPP bits 1,4,7,9; *TLT*: DIS bit 03; *DST*: bit 12; entire chain is described in detail in [110].

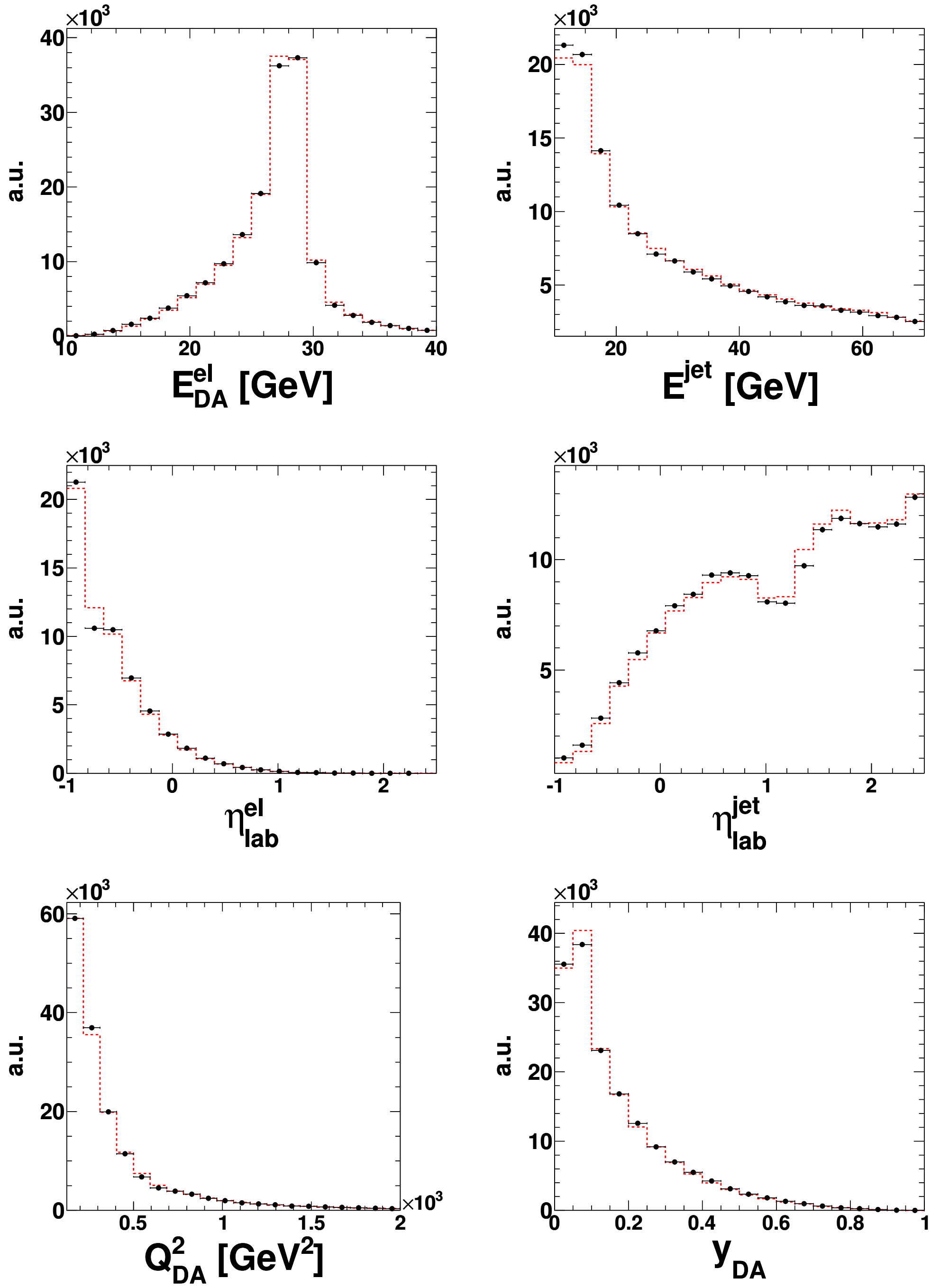

Figure 7.1: Control distributions for the high-Q^2 data sample used in the calibration of the hadronic energy scale. Shown are data (points) for all HERA-II data taking periods and the corresponding ARIADNE sample (dashed line). The Monte Carlo sample has been area normalized to the data.

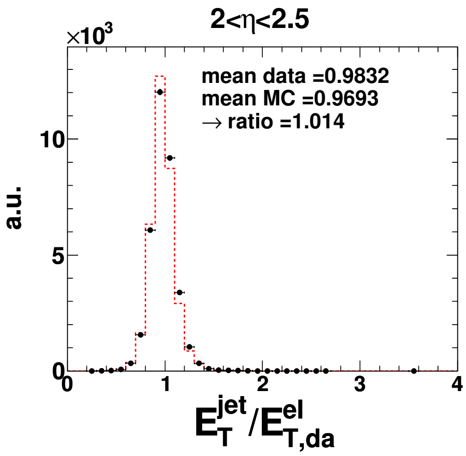

Figure 7.2: Ratio r_T of the transverse energies of the jet and the reconstructed electron for the η bin of $2 < \eta_{\text{lab}} < 2.5$. Shown are data of 2006/2007e^+ and the corresponding Monte Carlo simulation.

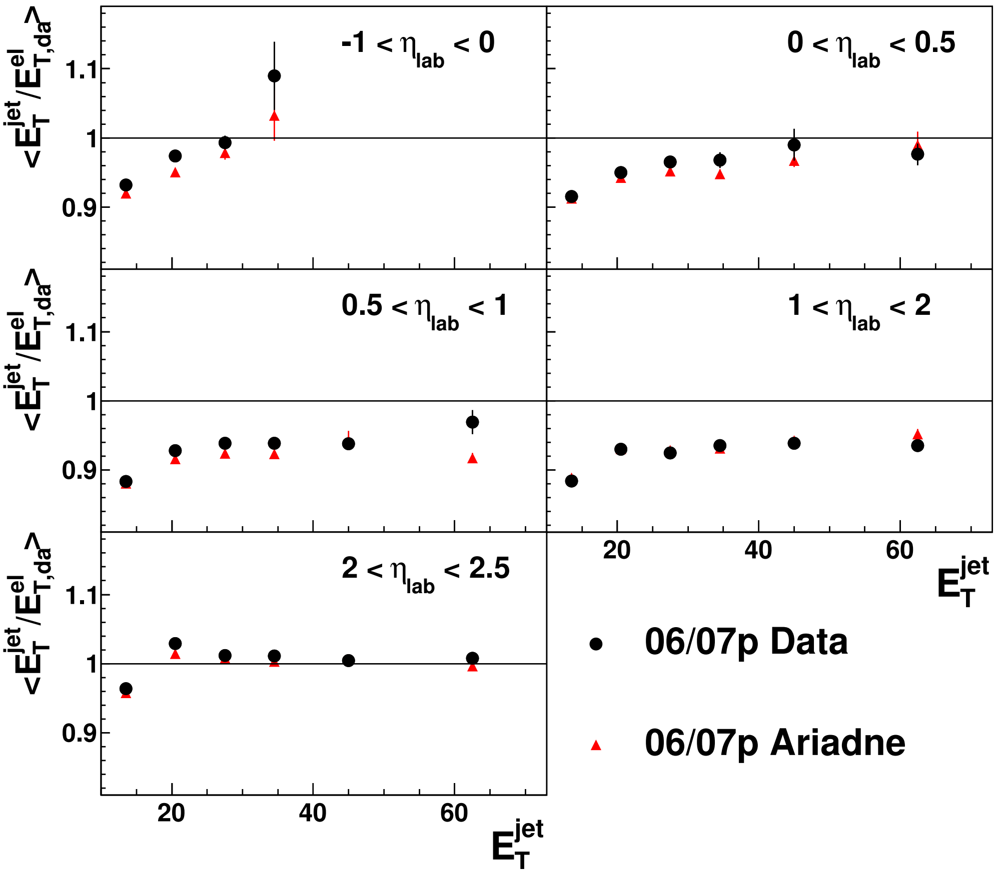

Figure 7.3: The mean ratio $\langle r_T \rangle$ of the transverse energies of the jet and the reconstructed electron in bins of η_{lab} and E_T^{jet}.

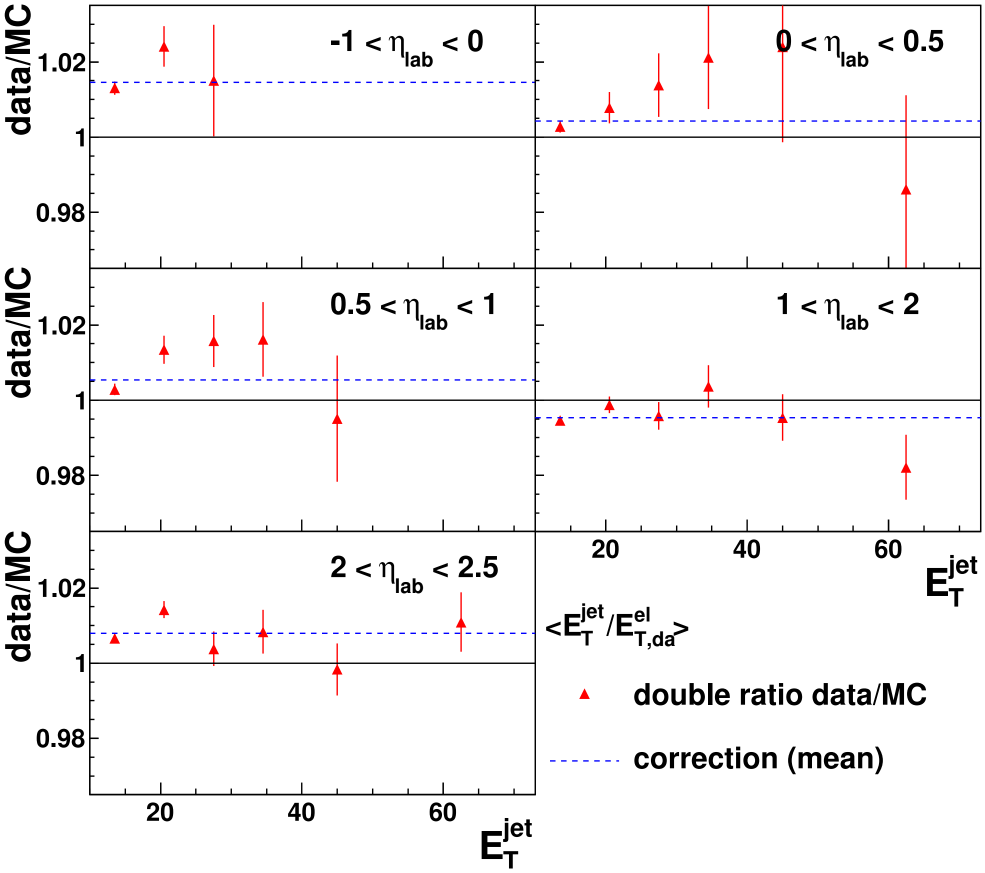

Figure 7.4: The double ratio data/MC for the mean transverse energies of the jet and the reconstructed electron in bins of η_{lab} and E_T^{jet}. The dashed line indicates the correction factor for each η bin.

These remaining uncertainties have been taken into account as systematic uncertainties as will be discussed in detail in chapter 9.1.

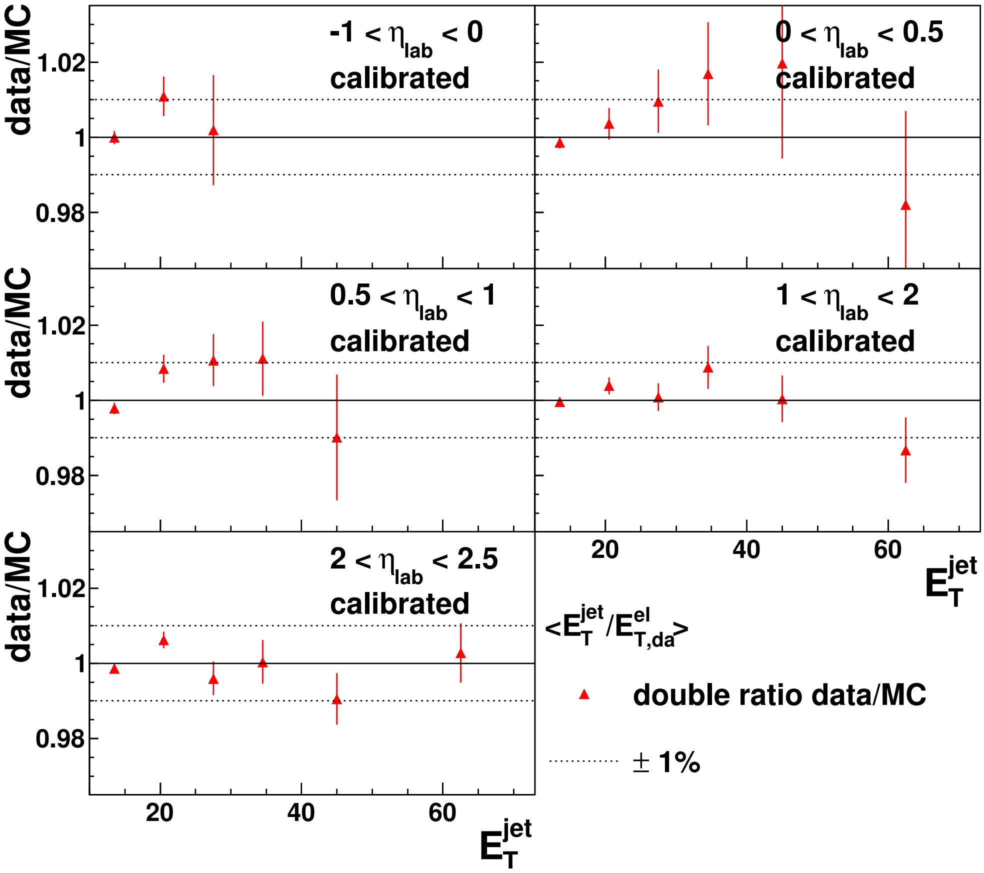

Figure 7.5: *After calibration*: double ratio data/MC for the mean transverse energies of the jet and the reconstructed electron in bins of η_{lab} and E_T^{jet}.

The determination of the correction factors C_{scale} might yield an additional systematic uncertainty. This has been investigated by varying the lower E_T cutoff parameter for additional jets used in this study. As figure 7.6 shows for one bin of η_{lab}, the correction factor never changes by more than 0.3%. Any systematic uncertainty is therefore covered by the remaining uncertainty on the hadronic energy scale of 3% (1%).

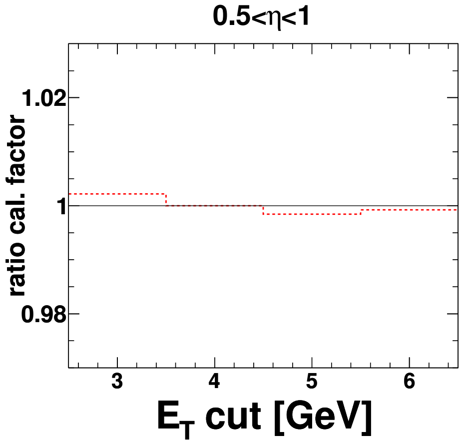

Figure 7.6: Relative variation of the scale calibration factors for one η bin derived for different values of the E_T^{jets} cut for additional jets. The reference value is derived for a cut of $E_T^{\text{jets}} < 4\,\text{GeV}$.

7.1.2. Jet Energy Correction

When reconstructing the energy of a jet in the detector, various effects influence the measurement, such as inactive material between the interaction point and the calorimeter, noise, inefficiencies, inhomogeneities and other effects.

This analysis exploits the detector simulation available in the Monte Carlo simulation to correct the reconstructed energy of the jets on average to the value of the jets reconstructed from hadrons [110, 122, 142]. The correction factors C_E are a function of the uncorrected transverse jet energy E_T^{det} as reconstructed from calorimeter cells and of the pseudorapidity η of the jet,

$$C_E(\langle E_T^{\text{det}} \rangle, \eta) \cdot \langle E_T^{\text{det}} \rangle \approx \langle E_T^{\text{had}} \rangle \tag{7.3}$$

where E_T^{had} denotes the transverse jet energy from hadrons with all quantities determined with respect to the laboratory reference frame. The corrections are applied to all reconstructed jets in both data and the Monte Carlo simulation as a multiplicative factor to the jet energy after the previously described scale calibration has been applied.

To derive the correction function C_E a sample of Monte Carlo events based on the inclusive jet selection described in chapter 6.3 was used. The selection was altered slightly for this study:

- only events were considered that passed the DIS selection on both hadron and detector level and featured at least one jet on each level with $-1 < \eta_{\text{lab}} < 2.5$ and $E_T^{\text{lab}} > 3\,\text{GeV}$;
- jets are only accepted in pairs on hadron and detector level which are required to be "matched" in the η-ϕ plane. That is, the distance $r_{\text{had}}^{\text{det}}$ between all possible pairs of jets was calculated according to $r_{\text{had}}^{\text{det}} = \left[(\eta_{\text{lab}}^{\text{had}} - \eta_{\text{lab}}^{\text{det}})^2 + (\phi_{\text{lab}}^{\text{had}} - \phi_{\text{lab}}^{\text{det}})^2 \right]^{\frac{1}{2}}$, with all those pairs of jets being selected as "matched" that satisfied $r_{\text{had}}^{\text{det}} < 0.5$ starting from the smallest distance found.

All matched pairs of jets were used to measure E_T^{det} in bins of both E_T^{had} and η as shown exemplarily in figure 7.7 for two regions of E_T^{had}. All quantities were measured in the laboratory frame. From these distributions the mean transverse energy on detector level, $\langle E_T^{\text{det}} \rangle$, was determined: either by a Gaussian fit as shown on the left of figure 7.7 for E_T^{had} bins with $E_T^{\text{had}} < 9\,\text{GeV}$ or by calculating the numeric mean for higher E_T^{had} bins. The former approach was chosen to avoid a bias in $\langle E_T^{\text{det}} \rangle$ caused by removing part of the smeared-out distribution through the lower E_T^{det} cleaning cut.

In high E_T bins on the other hand, the fit suffers from a lack of statistics and was therefore replaced by a numeric mean. At $E_T^{\text{had}} = 9\,\text{GeV}$ where the methods are merged both yield comparable results.

After thus determining $\langle E_T^{\text{det}} \rangle$ the mean on hadron level for each bin of E_T^{had} was also measured to correct the bin center of $\langle E_T^{\text{had}} \rangle$.

Now $\langle E_T^{\text{det}} \rangle$ can be expressed as function of $\langle E_T^{\text{had}} \rangle$ as shown in figure 7.8 for 14 regions of the pseudorapidity of the jets. The figure illustrates the reduced measured transverse jet energy in the detector compared to the E_T of the hadron level jet. $\langle E_T^{\text{det}} \rangle$ is typically smaller by $\sim 15\%$ with the exception of the higher η-bins where the

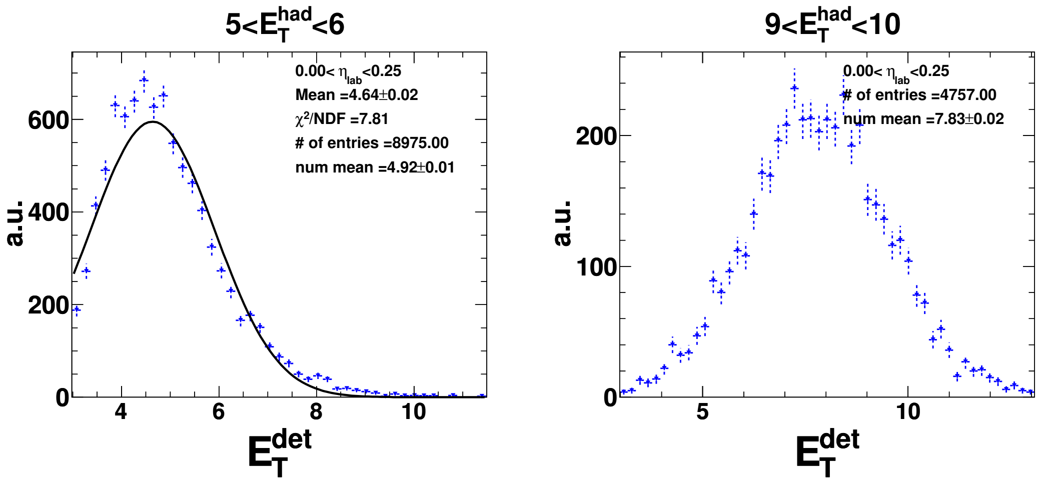

Figure 7.7: Exemplarily reconstructed E_T^{det} for jets in the laboratory frame for two different regions of hadron level E_T^{had} of the same η_{lab} region for the 04/05e MC simulation. The solid line is the result of a Gaussian fit to the distributions. The mean of the distribution is either determined by the Gaussian fit ("mean") or by a numerical calculation ("num mean").

difference is less pronounced. The dependence of $\langle E_T^{\mathrm{det}} \rangle$ on $\langle E_T^{\mathrm{had}} \rangle$ is typically linear for $\langle E_T^{\mathrm{had}} \rangle > 10\,\mathrm{GeV}$.

The correction factors were now derived in two steps for each η bin:

1. The $\langle E_T^{\mathrm{det}} \rangle$ graphs of figure 7.8 were fitted by a function composed of two parts: a second order polynomial for $\langle E_T^{\mathrm{had}} \rangle < 10\,\mathrm{GeV}$ and a linear function for values above 10 GeV with the boundary condition of both parts being merged at the crossover point

$$f_\eta(E_T^{\mathrm{had}}) = \begin{cases} a_0 + a_1 \cdot E_T^{\mathrm{had}} + a_2 \cdot (E_T^{\mathrm{had}})^2, & \text{if } E_T^{\mathrm{had}} \leq 10\,\mathrm{GeV} \\ b_0 \cdot \left(E_T^{\mathrm{had}} - k_{\mathrm{cut}}\right) + f_\eta(k_{\mathrm{cut}}), & \text{if } E_T^{\mathrm{had}} > 10\,\mathrm{GeV}, \end{cases} \tag{7.4}$$

   where $k_{\mathrm{cut}} = 10\,\mathrm{GeV}$.

2. As the correction factors must be applicable with only detector information available, the inverse function to equation 7.4, $f^{-1}(E_T^{\mathrm{det}})$ is determined analytically. The correction factors can then be calculated for each η-region from

$$C_E(E_T^{\mathrm{det}}, \eta) = \frac{f_\eta^{-1}(E_T^{\mathrm{det}})}{E_T^{\mathrm{det}}} \quad . \tag{7.5}$$

Results of the correction

The correction factors as defined by equation 7.5 were applied to all reconstructed jets in both data and the Monte Carlo simulation but only to those that already fulfilled

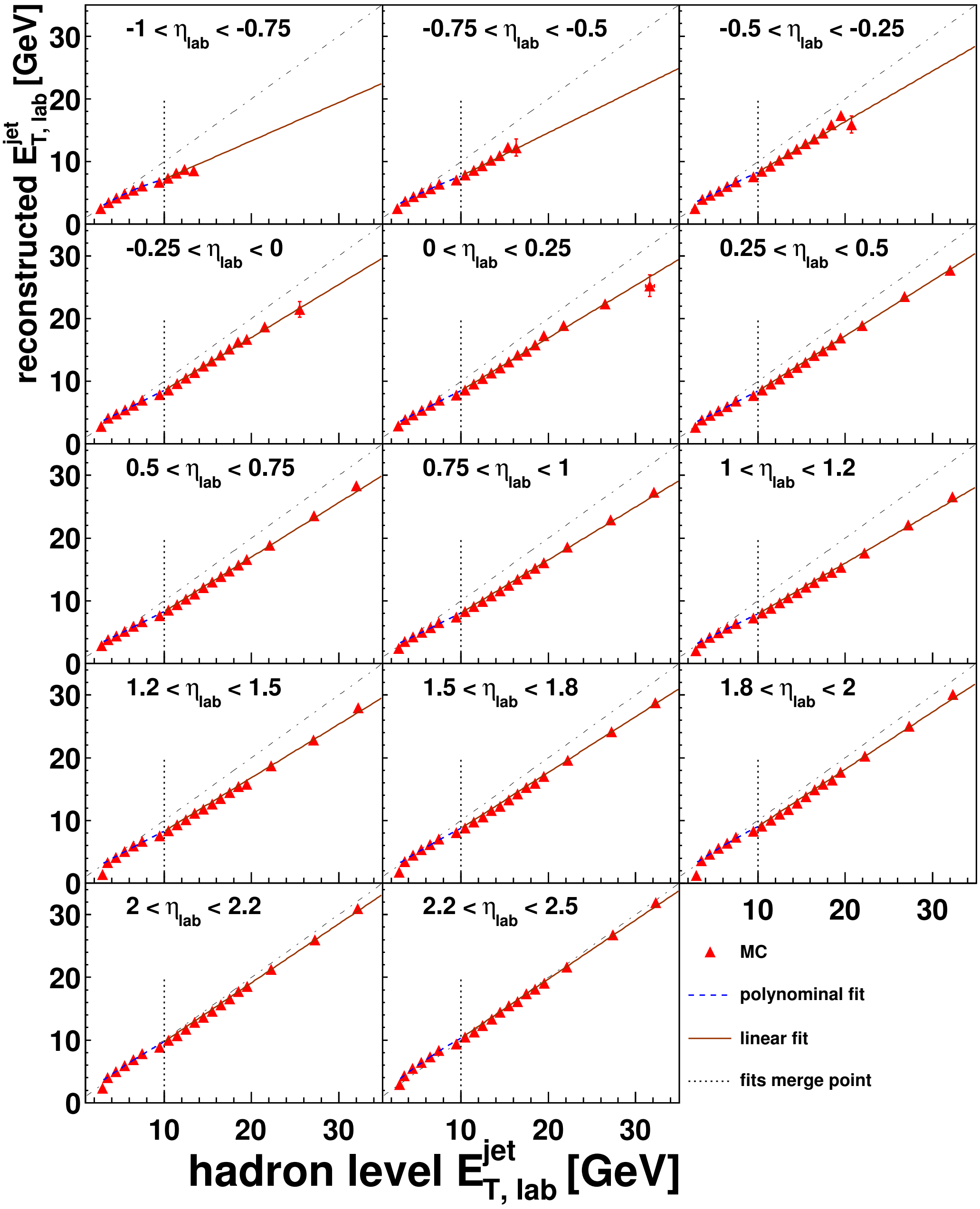

Figure 7.8: Reconstructed mean E_T^{det} for laboratory jets as function of mean hadron level E_T^{had} (shown for the 2004/2005e^- MC). The x-axis range has been limited for easier comparison. The dashed and the solid lines are the results of different fits to the distribution. The vertical dotted line indicates where the fits were merged while the diagonal dashed-dotted line guides the eye.

$E_{T,\text{lab}} > 3\,\text{GeV}$. Figure 7.9 shows the relative difference of the mean transverse energies on detector and hadron level before and after the jet energy correction has been applied. The graphs illustrate the improvement achieved by the correction over the full range of pseudorapidity. The remaining difference in E_T between the two level is always below 5% and typically in the order of 2% or less.

Therefore, the correction procedure has been shown to archive $\langle E_{T,\,\text{corr.}}^{\text{det}} \rangle \approx \langle E_T^{\text{had}} \rangle$ successfully.

The only noteworthy exceptions of the observed improvement are the first bins in E_T^{had} where the difference is much larger. This is caused by the combination of a prior lower E_T cutoff with a subsequent correction factor $C_E > 1$ for the jet energy resulting in a depopulation of this particular E_T bin. The resulting low statistics of this bin lead to an unreliable fit when determining $\langle E_T^{\text{det}} \rangle$. This particular bin should therefore be interpreted with caution. This problem occurs only when verifying the correct application of the correction and does not effect the analysis.

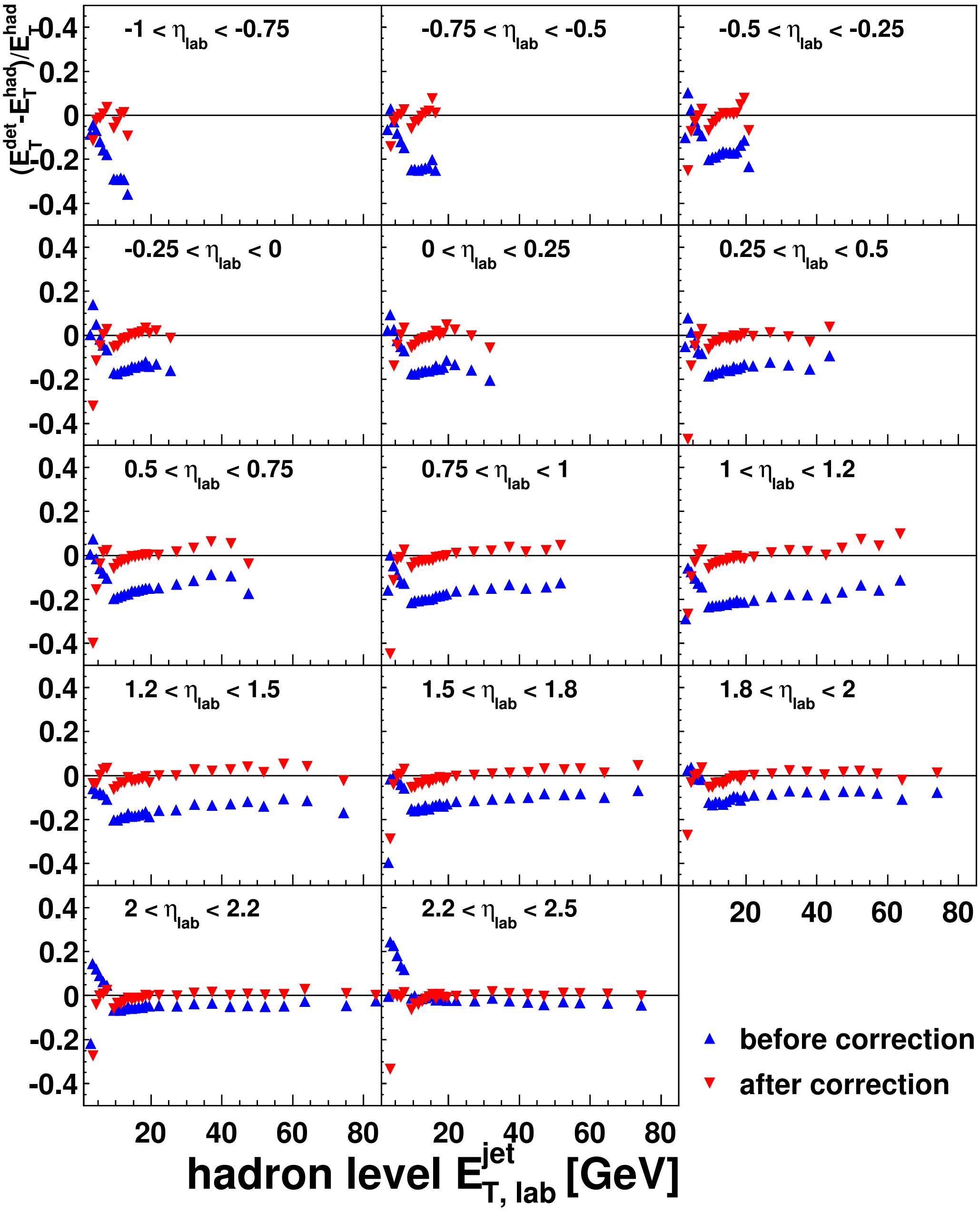

Figure 7.9: Relative difference of reconstructed mean transverse jet energy, $E_T^{\rm det}$, to mean hadron level $E_T^{\rm had}$ for laboratory jets as function of mean hadron level E_T (shown for the 2004/2005e^- MC). The blue up-pointing triangles show values before correction while the red down-pointing triangles indicate the results after applying the correction factors.

7.2. Monte Carlo Reweighting

In high energy physics one of the main purposes of the Monte Carlo simulation is to allow the correction of measured cross-sections for detector effects as will be discussed in detail in chapter 8. However for the unfolding of the data to be reliable, the output of the simulation must be checked against what is actually measured in the detector. Only if the Monte Carlo simulation correctly describes the data in all variables crucial to the specific analysis, it can be trusted to deliver the right corrections.

Unfortunately this is not always the case, mainly due to incomplete and/or incorrect

1. detector simulation, or
2. modeling of underlying physics processes.

Ideally such differences between data and the Monte Carlo simulation are resolved by the improvements brought about by the constant work being done in both respects (e.g. [143, 144]). As these are complex tasks this approach is often not feasible in the context of an analysis.

In cases where the observed differences arise from inadequate models in the Monte Carlo simulation there is also a more practical approach that still allows to use the Monte Carlo simulation as tool for data unfolding: *reweighting* the Monte Carlo samples to resemble the data more closely. This approach works by assigning each simulated event a weight as function of an event property e.g. a kinematic variable. This weight is chosen such that the sum of all Monte Carlo events adequately describes the data distribution with respect to the chosen property. It is important for a reliable reweighting to assure that the selected property is available for every event generated. It therefore should not rely on any reconstruction i.e. should be based on Monte Carlo *true* information.

The reweighting can be considered successful if the data are well described by the Monte Carlo simulation in *all* important variables.

For this analysis the Monte Carlo samples have been reweighted in three properties as described in the following. The final applied weight was calculated by multiplying all individual weights.

7.2.1. Reweighting of the Longitudinal Vertex Distribution

A correct reproduction of the measured longitudinal vertex distribution, z_{vtx}, by the Monte Carlo simulation is important as the vertex position enters in the reconstruction of the kinematic variables. Furthermore, since a cleaning cut on z_{vtx} is part of the DIS event selection, deviations of the simulation from the data in z_{vtx} also enter in the overall normalization of the measurement.

The expected shape of the z_{vtx} distribution is determined by the HERA collider timing and the length of the electron and proton bunches. The interaction can occur anywhere along the length of the overlapping bunches, leading to the approximately Gaussian-shaped central part of the distribution. The collision of nominal with neighboring bunches forms the so-called *satellite peaks* on both sides of the central peak.

While for the data taking periods 2004–2006 the description of the longitudinal vertex distribution was found to be sufficient this was no longer the case for 2006/2007e^+ as figure 7.10 demonstrates. These larger differences in the later running period have already been observed by previous studies [145]. For this data sample a reweighting procedure as function of the Monte Carlo true vertex information, $z_{\mathrm{vtx}}^{\mathrm{true}}$, has therefore been applied. The weights used in this analysis have been recently determined for [122]. They were derived by a fit of $g_{\mathrm{data}}/g_{\mathrm{MC}}$ to the bin-by-bin ratio of data over the Monte Carlo simulation as function of z_{vtx} where each g is a sum of four Gaussians. The function parameters resulting from the minimization procedure then give the weights for each event as function of z_{vtx}. Details to this procedure can be found in [110].

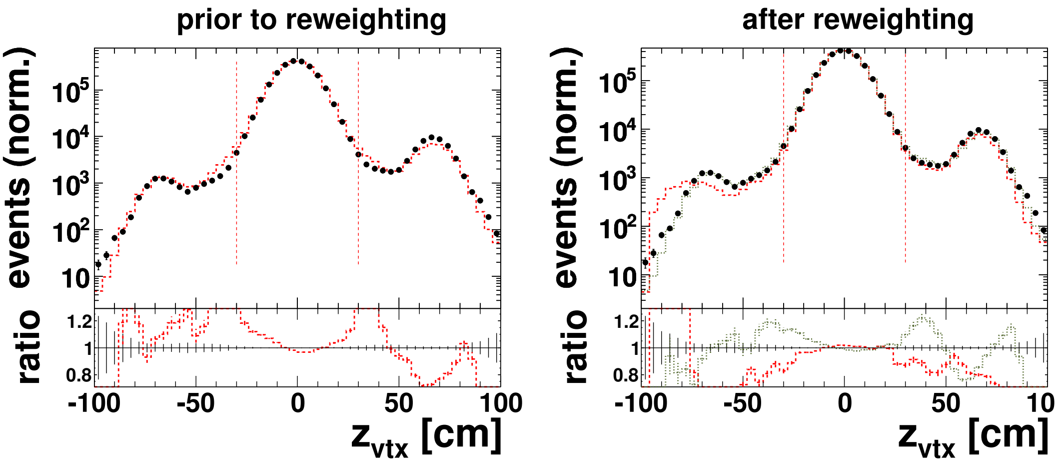

Figure 7.10: The longitudinal vertex distributions for 2006/2007e^+ data and DIS Monte Carlo simulation before (left) and after reweighting (right). Two reweighting schemes were used (dashed/dotted lines). Vertical lines in the ratio indicate the statistical uncertainty of the respective sample.

Figure 7.10 shows the DIS sample for data (points) and the Monte Carlo simulation (dashed line) as function of z_{vtx} for the running period of 2006/2007e^+ both with and without applied vertex reweighting. After reweighting the description of the data is improved, most significantly so in the region of the central peak. The satellite peaks are still not fully reproduced though.

An alternative reweighting procedure recently developed [146] has therefore been investigated as well. Details of the method can be found in [147, 148]. The resulting reweighted Monte Carlo sample is shown in figure 7.10 as dotted line. Using this method both the satellite peaks and the central region are described better than without reweighting. However, the central region is not described as well as with as with the previously described reweighting method.

Thus the previous method has been employed as reference reweighting scheme with the alternative method only being used in the evaluation of the systematic uncertainty as discussed in chapter 9.1.

7.2.2. Reweighting of the Jet Samples

After the inclusive jet selection some of the kinematic and jet variables were not sufficiently well described by ARIADNE making the usefulness of the MC for unfolding doubtful. Figure 7.11 demonstrates the observed differences for some of the affected variables.

The Monte Carlo simulation shows more events at low Q^2 as well as more jet activity at high $E_{T,\,\mathrm{Breit}}$ values and in the forward region than seen in data. The y distribution on the other hand exhibits only a small shift toward higher values of y. In x_{Bj} the difference is again more pronounced, especially at low values of x_{Bj}.

To improve the description of the data by the Monte Carlo simulation the jet samples have been reweighted in two steps.

Reweighting jets in inelasticity and virtuality

As a first step the Monte Carlo jet events were reweighted in the kinematic variables Q^2 and y simultaneously. To derive the necessary weights the two-dimensional distribution of the detector level quantities y_{el} versus $\log_{10} Q^2_{\mathrm{el}}$ has been measured. The ratio of data over the Monte Carlo simulation was then fitted with

$$\begin{aligned} w_1(\log_{10} Q^2_{\mathrm{el}}, y_{\mathrm{el}}) = a_0 + a_1 \cdot \log_{10} Q^2_{\mathrm{el}} + a_2 \cdot y_{\mathrm{el}} \\ + a_3 \cdot (\log_{10} Q^2_{\mathrm{el}})^2 + a_4 \cdot y^2_{\mathrm{el}} \ . \end{aligned} \tag{7.6}$$

With the parameters determined by the result of the minimization procedure the function $w_1(\log_{10} Q^2_{\mathrm{true}}, y_{\mathrm{true}})$ then gives the event weights as function of the Monte Carlo *true* information. The weights are then applied in the Monte Carlo simulation for both detector and hadron level.

To further improve the results of the reweighting, the above procedure was repeated once more. The weights derived in the second iteration were again applied as multiplicative factor.

Figure 7.12 shows the relative difference between data and the Monte Carlo simulation as function of $\log_{10} Q^2$ and y before and after the reweighting. The latter plot demonstrates the considerable reduction of deviations between the Monte Carlo simulation and the data in both variables.

Reweighting jets in pseudorapidity and transverse energy

As can be seen in figure 7.11 not only the kinematic but also the jet variables are not well described by ARIADNE. These distributions are not notably improved by the previous reweighting. Hence making further reweighting steps necessary.

Jet variables pose an additional difficulty when used as reweighting property, as not necessarily every event contains a jet as defined by the jet selection criteria on both detector and hadron level. This problem can be mitigated by searching for the hardest jet on hadron level without imposing any cuts on it's properties. This practically ensures one valid hadron level jet for every single event from which a weight can then be determined.

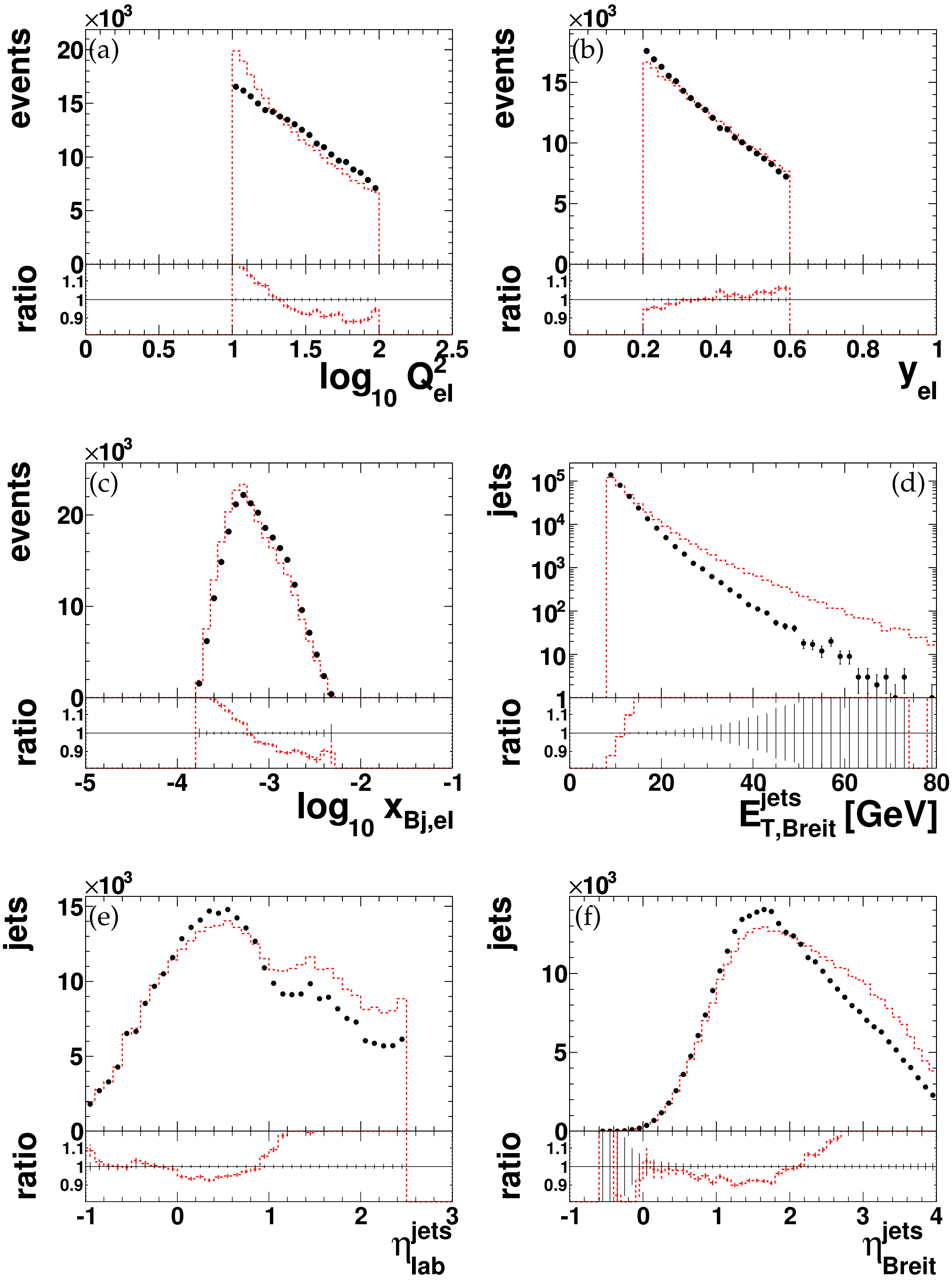

Figure 7.11: Event and jet variables after inclusive jet selection *before reweighting*. Shown are data (points) and DIS Monte Carlo simulation (dotted line). The Monte Carlo sample has been normalized to the integral of the data distributions. The reweighted distributions are shown and discussed in chapter 8.1.

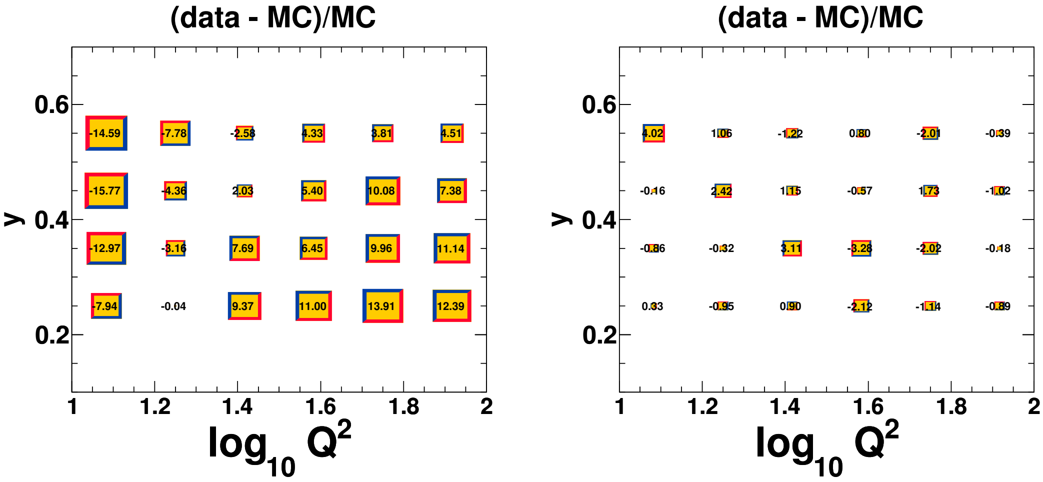

Figure 7.12: The relative difference in percent between data and the Monte Carlo simulation indicated by both value and box size after the inclusive jet selection in bins of y and $\log_{10} Q^2$ before reweighting (left) and after the second reweighting iteration (right).

By fitting the detector-level ratio of Monte Carlo simulation over data as function of properties of the hardest jet, one can derive the parameters necessary to calculate the weights from the hadron level jet, similar to the procedure described in the previous section 7.2.2.

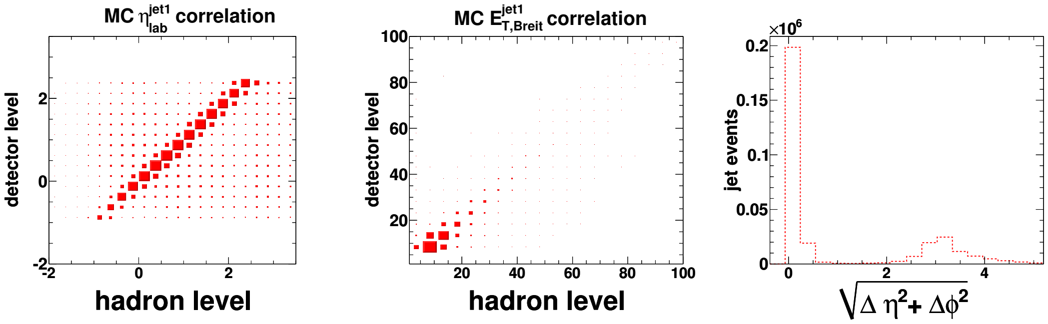

Figure 7.13: Correlation between hardest jet on hadron level and the hardest jet reconstructed on detector level as function of η_{lab} and $E_{T,\,\text{Breit}}$, as well as the difference between the two in the $\eta\phi$-plane.

Figure 7.13 demonstrates the correlation between the hardest jet on detector level and the hardest jet on hadron level as function of the pseudorapidity, $\eta^{\text{jet1}}_{\text{lab}}$, the transverse energy, $E^{\text{jet1}}_{T,\,\text{Breit}}$, and by the difference between the two in the η-ϕ plane. A strong correlation typically corresponds to a matching[4] of the jets on both levels. This is important for consistency in the reweighting, since the weights are derived on detector

---

[4] See section 7.1.2 for the definition of *matched* jets.

level but applied according to hadron level quantities.

Especially the $\Delta\eta\phi$ distribution shows that the hardest jet is matched on both levels in more than 80% of all events. Furthermore, it was experimentally found that every single jet event selected on detector level also featured a jet found on hadron level using the above described loosened definition.

Reweighting in both both variables $\eta_{\text{lab}}^{\text{jet1}}$ and $E_{T,\text{ Breit}}^{\text{jet1}}$ is therefore feasible.

The weights were derived in a similar fashion as described in the previous section 7.2.2. First $E_{T,\text{ Breit}}^{\text{jet1}}$ versus $\eta_{\text{lab}}^{\text{jet1}}$ was measured as 2D distribution. Then the ratio Monte Carlo simulation over data was fitted with a function w_2 defined as

$$\begin{aligned} w_2(\eta_{\text{lab}}^{\text{jet1}}, E_{T,\text{ Breit}}^{\text{jet1}}) = a_0 + a_1 \cdot \eta_{\text{lab}}^{\text{jet1}} + a_2 \cdot E_{T,\text{ Breit}}^{\text{jet1}} \\ + a_3 \cdot (\eta_{\text{lab}}^{\text{jet1}})^2 + a_4 \cdot (E_{T,\text{ Breit}}^{\text{jet1}})^2 + a_5 \cdot (E_{T,\text{ Breit}}^{\text{jet1}})^3 \ . \end{aligned} \tag{7.7}$$

The weights were then given by $w_2(\eta_{\text{lab, true}}^{\text{jet1}}, E_{T,\text{Br.,true}}^{\text{jet1}})$ and applied on an event-by-event basis to both detector and hadron level in all Monte Carlo events of the jet sample.

To further improve the results of the reweighting, the above procedure was repeated once more. The weights derived in the second iteration were again applied as multiplicative factor.

Figure 7.14 shows the relative difference between data and the Monte Carlo simulation before and after reweighting. Although the distributions improve considerably this is not immediately apparent as the deviations also increase in some statistically less significant bins. The most important change is in low-$E_{T,\text{ Breit}}$ and low- η_{lab} bins as well as in the mid-$E_{T,\text{ Breit}}$ and high-η_{lab} region where the difference is diminished.

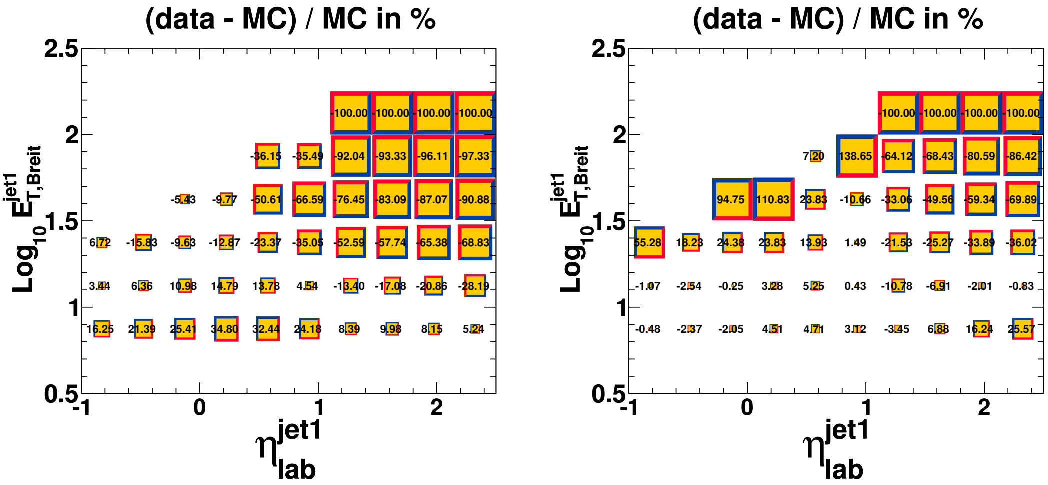

Figure 7.14: The relative difference in percent between data and the Monte Carlo simulation indicated by value and relative box size after the inclusive jet selection in bins of η_{lab} and $E_{T,\text{ Breit}}$ of the hardest jet before reweighting (left) and after the second reweighting iteration (right).

For a final conclusive test of the combined reweighting efforts please refer to chapter 8.1 where control distributions of all essential kinematic and jet variables are shown and discussed.

7.3. Trigger Efficiency

As seen in chapter 6.1, the efficiency of the "loose track veto" in the first level trigger differed in the Monte Carlo simulation from the data. Any such deviation directly influences the acceptance corrections, as the Monte Carlo simulation would predict either a smaller or higher number of events lost due to the trigger efficiency.

To adjust the Monte Carlo simulation to accurately describe the track veto efficiency of the data, the following correction procedure has been applied.

1. As discussed in chapter 6.1, the efficiency ratio data over the Monte Carlo sample, $\epsilon^{\text{veto}}_{\text{data}}/\epsilon^{\text{veto}}_{\text{MC}}$, has been determined as function of y_{el} (shown in figure 7.15);
2. the ratio was then fitted with a linear function $f_{\text{veto}}(y_{\text{el}}) = a_0 + a_1 \cdot y_{\text{el}}$;
3. for all Monte Carlo events exclusively triggered by FLT 36 which imposes said track veto, a uniformly-distributed random number p_0 between 0 and 1 has been determined. If $p_0 > f_{\text{veto}}(y_{\text{el}})$ then the event was considered *not* to be triggered.

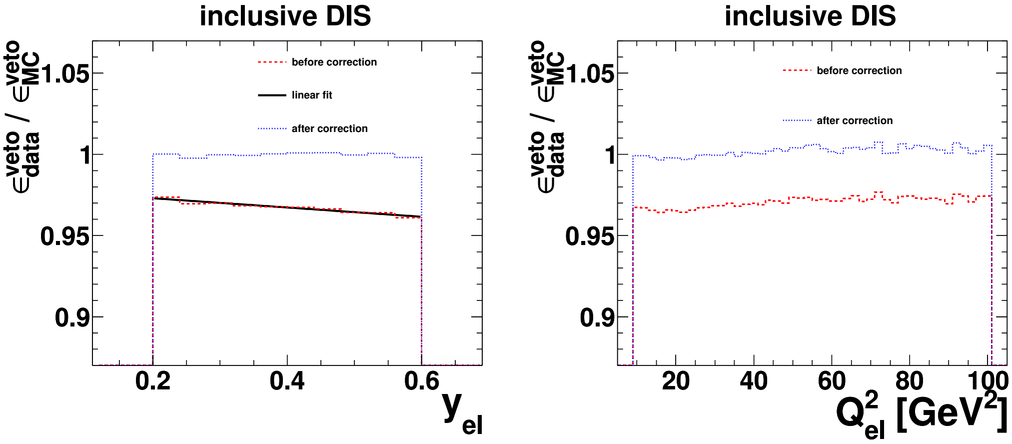

Figure 7.15: The ratio for the FLT track veto efficiencies of data over the Monte Carlo simulation before (dashed line) and after (dotted line) applied corrections as function of y_{el} (left) and Q^2_{el} (right).

The correction has been applied to all data taking periods separately. The result of the procedure can be seen in figure 7.15. After adjusting the efficiency of the Monte Carlo simulation, the ratio to data is approximately equal to one and nearly flat both as function of y and Q^2.

The systematic influence of the trigger efficiency correction is discussed in chapter 9.1.

7.4. Summary and Conclusions

Precise cross-section measurements and control of the systematics require both a well-understood detector and its accurate simulation. In this chapter studies were presented addressing both issues.

First the calibration and correction of the hadronic energy measured in the calorimeter have been demonstrated. The result are reconstructed jets whose energy is on average consistent with that of the hadrons entering the calorimeter. From remaining differences in the energy scale of data and the Monte Carlo simulation the uncertainty on the hadronic energy scale was estimated to be 1% for jets with $E_{T,\,\mathrm{lab}} > 10\,\mathrm{GeV}$ which is comparable to previous studies. For jets with lower $E_{T,\,\mathrm{lab}}$ values, the uncertainty was taken to be 3% as used by recent ZEUS publications [122].

Secondly studies were performed with the aim of re-adjusting the simulated detector output so that it bears sufficiently close resemblance to the data. This was shown to be the case for all variables in which the Monte Carlo simulation has been reweighted. Furthermore, the trigger efficiency in the Monte Carlo simulation has been modified to correspond to the data. The following chapter now will discuss the final data sample in detail and will show the overall good agreement of the simulation with the data achieved through the corrections.

8. Unfolding of the Data

In order to test a given theory by comparing its predictions with experimentally determined results in a meaningful way, both have to meet on common ground so to speak: the data have to be adjusted for influences caused by the experimental conditions while the theory has to be modified for any phenomenological aspects it might lack. These corrections also allow to directly compare experimental results from different experiments, a crucial prerequisite e.g. for the inclusion of the data in fits determining the parton-density distributions.

In high-energy physics, the process of correcting measured cross-sections for effects of finite resolution and limited detector acceptance is commonly referred to as "unfolding" of the data. The subject matter of unfolding is a very complex one, belonging mathematically to the domain of *inverse problems* [149].

In this analysis, using the Monte Carlo simulation, the data have been unfolded to the hadron level, which is the stage of the simulation after the formation of hadrons and subsequent decay into stable particles. Consequently, the NLO QCD predictions required corrections for the non-perturbative hadronization of the final state partons. The data were also separately corrected for higher-order QED effects.

In contrast to the corrections discussed in the previous chapter, the corrections presented here are not applied to single jets or on an event-by-event basis, but are instead carried out *bin-by-bin* on the cross-sections.

As the determination of the corrections is based on the Monte Carlo simulations, it is crucial that they correctly describe the data in all relevant observables. This is investigated in detail in the first part of this chapter where the final data samples are compared to the Monte Carlo simulation.

The procedures to derive each of the above mentioned corrections are then presented in the second part of this chapter.

8.1. Final Data Sample

In this section, the inclusive DIS sample as defined by the online and offline selection criteria detailed in chapter 6.2 and the jet sub-samples defined by additional cuts imposed on the hadronic final state as discussed in chapter 6.3 are investigated separately.

For each sample it must be verified that the Monte Carlo simulation correctly describes the measured data. This is achieved by comparing the Monte Carlo simulation with the data in quantities related to all important aspects of this analysis: detection of the scattered electron, reconstruction of the hadronic final state, and measurement of the observables intended for cross-section determination.

As described in chapter 6 the Monte Carlo simulated data set consists of two distinct samples shown individually and as a sum in the control distributions: an ARIADNE DIS sample and a PYTHIA sample used to estimate the photoproduction background.

All quantities are shown after the corrections described in chapter 7 have been applied.

8.1.1. Inclusive DIS Sample

The Monte Carlo samples have already been compared to some extent with the data for the inclusive selection when the individual selection criteria were discussed in chapter 6. The overall absolute normalization to the integrated luminosity of the data was found to be adequate. The Monte Carlo simulation usually described the data within 4% in the statistically relevant bins.

This can also be observed in figure 8.1 which summarizes the phase space defined by the variables Q^2, x and y. Also shown in the figure are the angular distribution of the hadronic system, γ_{had}, and that of the electron given by the azimuthal and polar angles, ϕ_{el} and θ_{el}. Perhaps contrary to the usual expectation, the ϕ_{el} distribution exhibits fluctuations and most strikingly a suppression of events with $\phi_{\text{el}} \approx 1$. While the former is caused by inhomogeneities of the calorimeter such as cell edges and gaps in-between cells, the latter is the result of the cleaning cuts imposed on the electron position in the RCAL, mainly by removing events of certain runs in the 2006 – 2007 data sample where the electron candidate is located in a specific inner ring cell of the RCAL.[1]

In all variables, the description by the Monte Carlo simulation is very reasonable. The contributions from photoproduction events are mostly concentrated at low Q^2, low $\cos \gamma_{\text{had}}$, and high y.

In section 6.2.2 it was found that neither the longitudinal momentum balance, $E - p_z$, nor the transverse momentum balance of the electron and the hadronic system, $p_{T,\,\text{had}} / p_{T,\,\text{el}}$, were particularly well reproduced by the Monte Carlo simulation. Figure 8.2 investigates this observation in more detail by showing the individual components from the electron and the hadronic final state.

Figures 8.2a and 8.2b display the number of selected events as function of the transverse momenta of the electron and of the hadronic system, respectively. The $p_{T,\,\text{el}}$ distribution exhibits both a steep rise at $\sim 2\,\text{GeV}$ and a sharp drop at $\sim 9\,\text{GeV}$. Both features are a direct result of the imposed Q^2 cuts. The $p_{T,\,\text{had}}$ distribution on the other hand features a much broader shape, and, in contrast to $p_{T,\,\text{el}}$, is not as well described by the Monte Carlo simulation. Especially for high values of $p_{T,\,\text{had}}$, the Monte Carlo simulation assumes more events than seen in data.

Similarly, the quantity $E - p_z$ is also better reproduced by the Monte Carlo simulation for the electron, shown in figure 8.2c, than for the hadronic system shown in figure 8.2d.

Nevertheless, since the overall description of the inclusive DIS data by the Monte Carlo simulation is reasonable, and the transverse momentum spectrum of the hadronic final state has been specifically adjusted in the jet samples[2], the observed discrepancies are acceptable.

---

[1] See chapter 6.2.2 for details.

[2] See the reweighting procedure described in chapter 7.2.2.

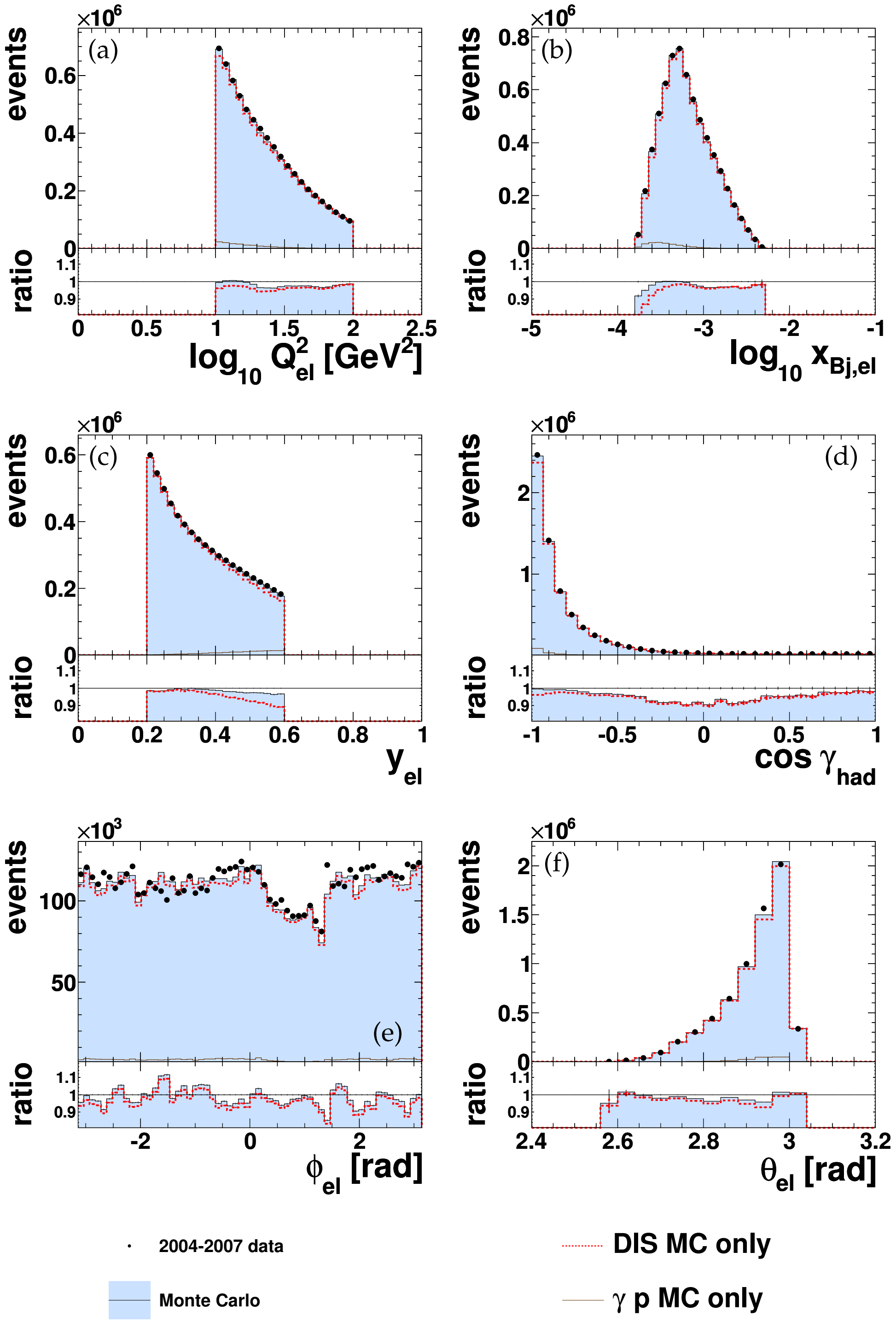

Figure 8.1: Event variables after the inclusive DIS selection. Shown are data (points), the sum of the Monte Carlo samples (shaded area), as well as its DIS (dotted line) and γp (solid line) contributions. The Monte Carlo sample has been normalized to the integrated luminosity of the data. For additional control plots of the inclusive DIS sample see figures 6.6 – 6.9.

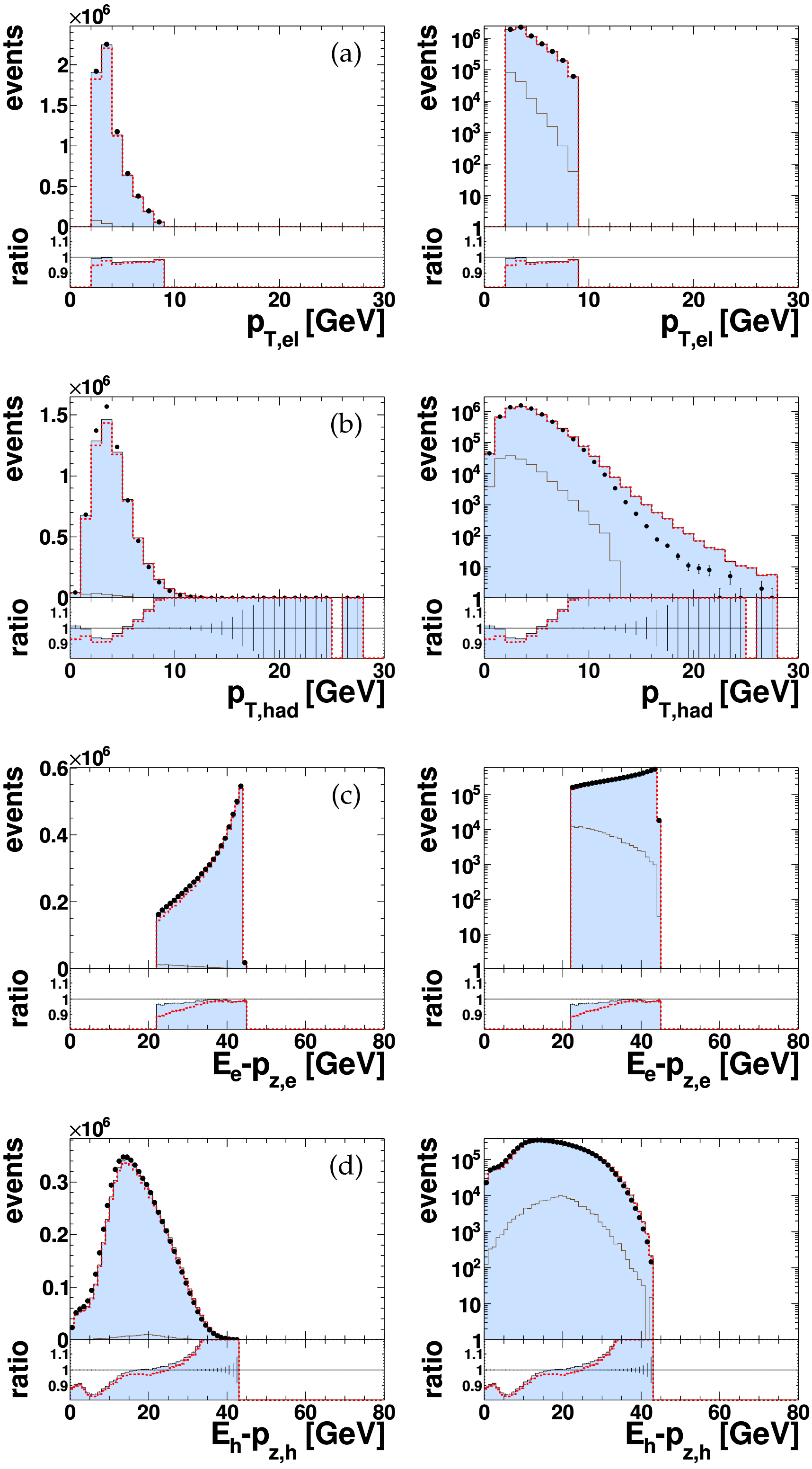

Figure 8.2: Event variables after the inclusive DIS selection in linear and logarithmic scale. For details, see the text as well as the caption and the legend to figure 8.1.

8.1.2. Jet Samples

Inclusive jet sample

The inclusive jet sample consists of all events that passed the inclusive DIS selection cuts and that feature at least one jet satisfying the criteria described in section 6.3.

Figure 8.3 shows control distributions for event variables after the inclusive jet selection with the corrections introduced in chapter 7 already applied. Since the Monte Carlo simulations are based on leading-order predictions, they cannot provide the correct normalization for the jet samples. All distributions shown in this section are therefore normalized to the integrated *number of jet-events* in the data. For the inclusive jet sample this corresponded to a normalization factor of ~ 0.77 relative to the luminosity normalization factor[3].

Compared to the distributions of the inclusive DIS sample, the most striking difference is a change in shape of the Q^2 distribution, and, to a lesser extent, of the y and x distributions as well. In Q^2, the relative amount of events with higher Q^2 values increases, resulting in a more gradually falling distribution. This is caused by the selection of jets with transverse momenta above 8 GeV, which become more prevalent at higher values of Q^2. Overall, the Monte Carlo simulation is in very good agreement with the data.

Figure 8.4 shows control plots for jet quantities: the number of jets per event, the distribution of jets in the azimuthal angle, ϕ, the pseudorapidity, η, and the transverse energy, E_T. The latter quantities, η and E_T, are shown in both the laboratory and Breit reference frames.

Figure 8.4a illustrates the final inclusive jet sample size: a total of $\sim 242,000$ events feature one or more jets, while $\sim 67,000$ events have two or more jets. The pseudorapidity distribution shown in figure 8.4c illustrates that most jets are reconstructed in the forward-facing part of the BCAL with approximately $1/3$ found in the FCAL. Each jet typically carries a transverse energy of less than 20 GeV but can reach values of E_T of up to ~ 70 GeV for either reference frame as demonstrated in figure 8.4f.

As illustrated by the distributions shown in figures 8.3 and 8.4, the Monte Carlo simulation gives an overall reasonable description of the data after the inclusive jet selection and the reweighting have been applied. Compared to figure 7.11 which shows key distributions before the reweighting, the description of the data by the Monte Carlo simulation improved significantly in all variables investigated.

However, the jet multiplicity, certain regions of η, and the E_T spectrum of the jets above 25 GeV still exhibit deviations between the distributions of the Monte Carlo simulation and of the data. Possible systematic uncertainties introduced by this remaining deviation have been taken into account and will be discussed in chapter 9.1.

The fact that the Monte Carlo simulation does not fully describe the jet multiplicity observed in the data results in a small offset in the chosen normalization of the simulation in all distributions measured in number of jets instead of number of events. This can be seen for instance in figure 8.4b showing the number of jets as function of ϕ.

---

[3] The normalization factor is in principle affected by the corrections and reweighting introduced in section 7, but has been found to only change marginally for the inclusive jet sample.

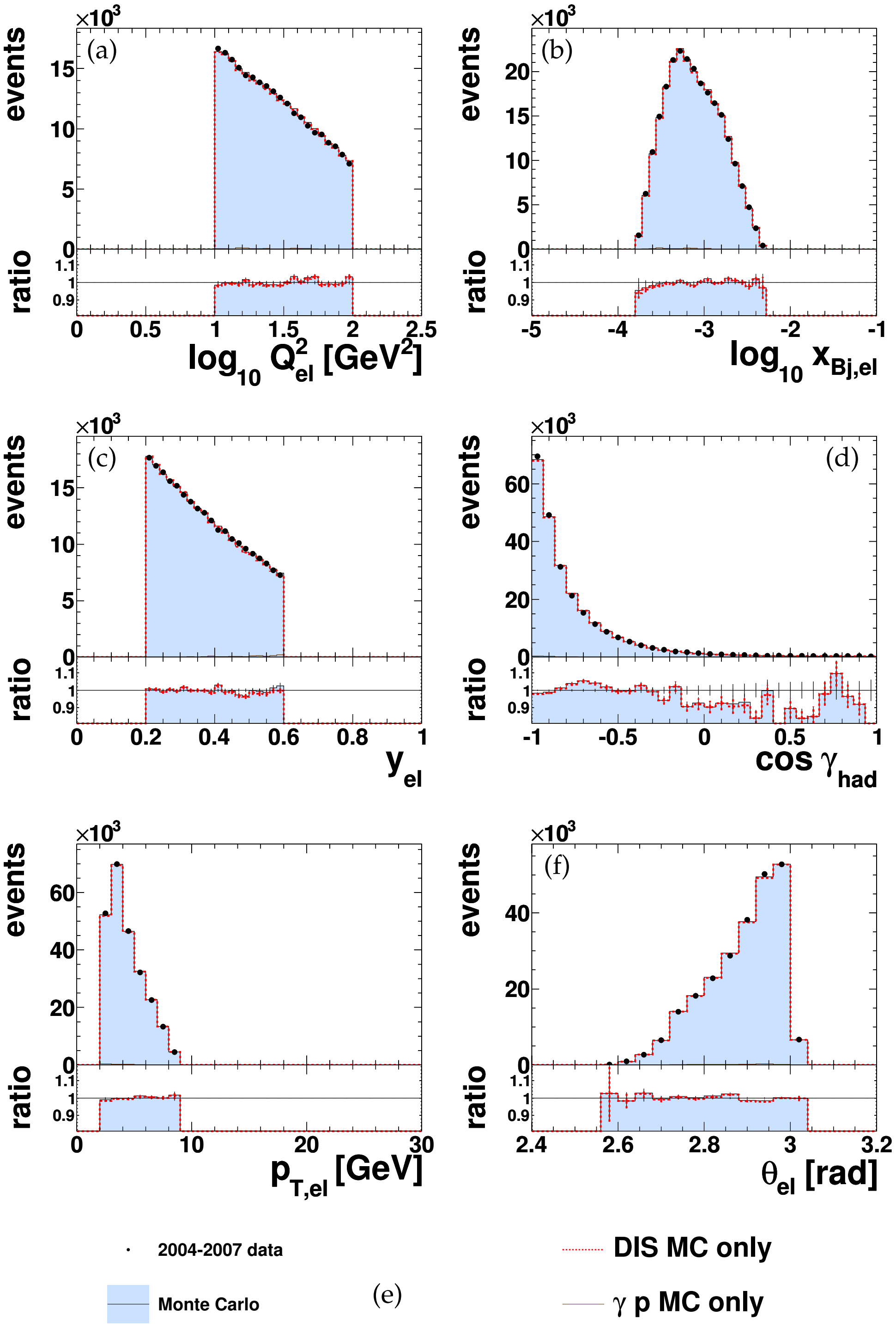

Figure 8.3: Event variables after inclusive jet selection. Shown are data (points), the summed Monte Carlo samples (shaded area), as well as its DIS (dotted line) and γp (solid line) contributions. The Monte Carlo sample has been normalized to the *number of jet-events* the data.

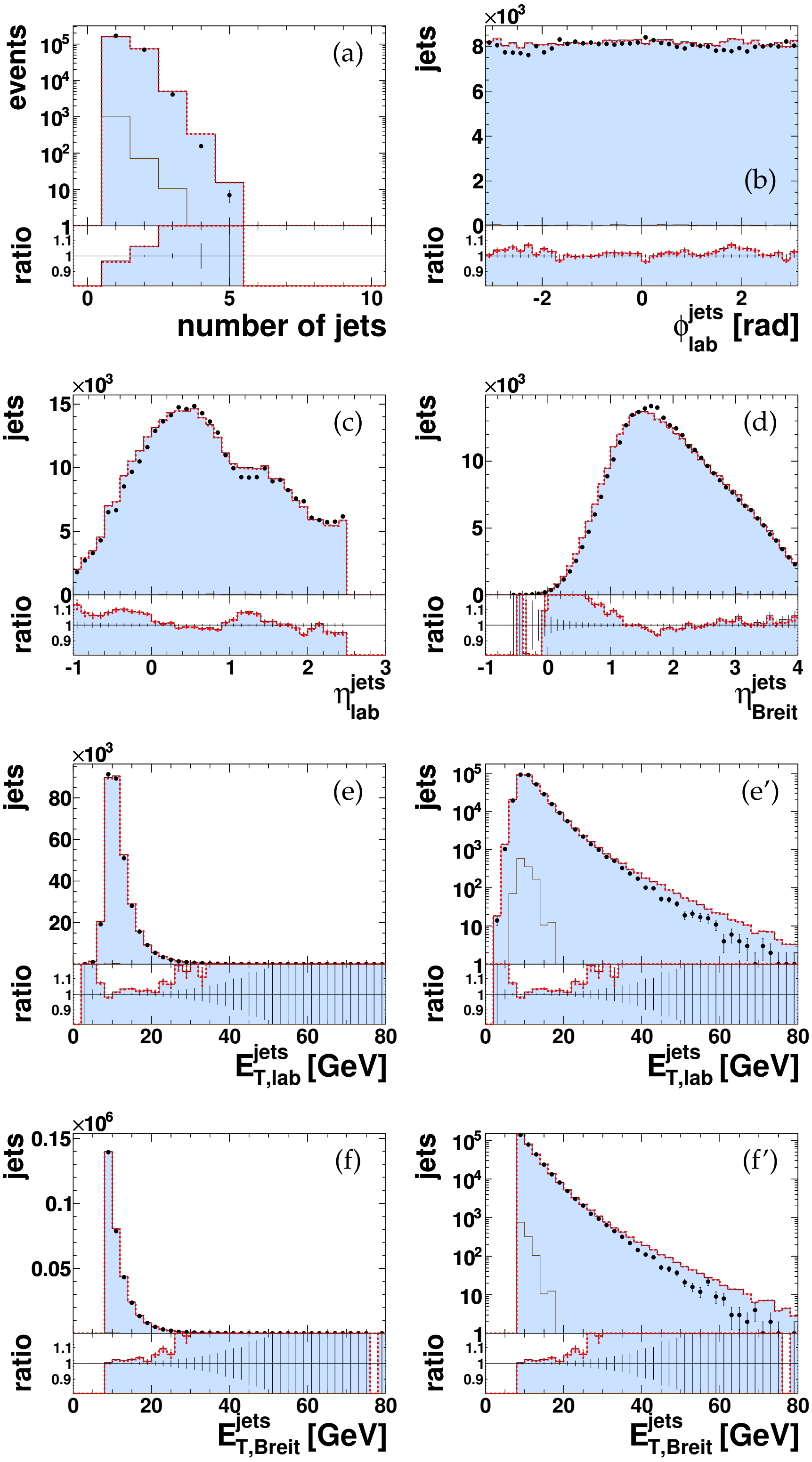

Figure 8.4: Inclusive jet variables after jet selection. For details see caption to figure 8.3.

Inclusive dijet sample

The inclusive dijet sample consists of all selected DIS events with at least two or more jets satisfying the selection criteria introduced in chapter 6.3.

Figure 8.5 shows the pseudorapidity and transverse momentum distributions of the jets in the inclusive dijet sample in both the laboratory and the Breit reference frame. Compared to the inclusive jet sample, the dijet sample is slightly enriched in jets in the forward η_{lab} region and in jets with high transverse momentum, an effect which is caused by the additional E_T requirement on the second jet.

In figure 8.6, distributions are shown which are specific to the dijet system: the invariant dijet mass, M_{jj}, the momentum fraction of the parton entering into the hard process, ξ, the absolute difference in pseudorapidities in the Breit frame, η', the difference in azimuthal angle, $\Delta\phi_{\text{lab}}$, the difference in pseudorapidities in the laboratory frame, $\Delta\eta_{\text{lab}}$, the difference in transverse energies, $\Delta E_{T,\,\text{Breit}}$, and the center-of-mass scattering angle, $\cos\theta^*$.

Overall, most distributions are reasonably well described by the Monte Carlo simulation. However, compared to the inclusive jet sample, the η_{lab} distribution, shown in figure 8.5a, appears to be slightly shifted in the Monte Carlo simulation with respect to the data, resulting in a degraded description. This deviation is most likely the cause for the differences seen in $\Delta\eta_{\text{lab}}$. The Monte Carlo simulation does not quite reproduce the η' distribution either, but still gives an acceptable result.

Similar to the observation made for the inclusive jet sample, the Monte Carlo simulation also yields more events at higher values of $E_{T,\,\text{Breit}}$ in the transverse jet energy distribution than found in the data.

Inclusive trijet sample

The inclusive trijet sample consists of events featuring at least three or more jets that satisfy all inclusive DIS and jet selection cuts. In the full HERA-II data sample, $\sim 4,000$ events have been found matching this criterion.

Figure 8.7 shows control plots for the inclusive trijet sample. The most striking differences with respect to the dijet sample are the increased jet activity in the forward η_{lab} region and, to a lesser extent, a broadening of the M_{jj} peak.

Within the (arguably high) statistical uncertainty, the Monte Carlo simulation describes the sample quite reasonably. The most striking deviation from the data is again in the E_T spectra, even though it is not as pronounced as in the other jet samples.

8.1.3. Jet Energy Resolution

To estimate the energy resolution of the jets, a separate study has been performed on the high-Q^2 sample defined for the derivation of the calibration factors for the hadronic energy scale as described in chapter 7.1.1.

In single-jet events, the average ratio of transverse energies of the jet and the scattered electron was measured in bins of both $E^{\text{jet}}_{T,\,\text{lab}}$ and $\eta^{\text{jet}}_{\text{lab}}$ of the jet. The resulting distributions are similar to the example depicted in figure 7.2. The width of these E_T

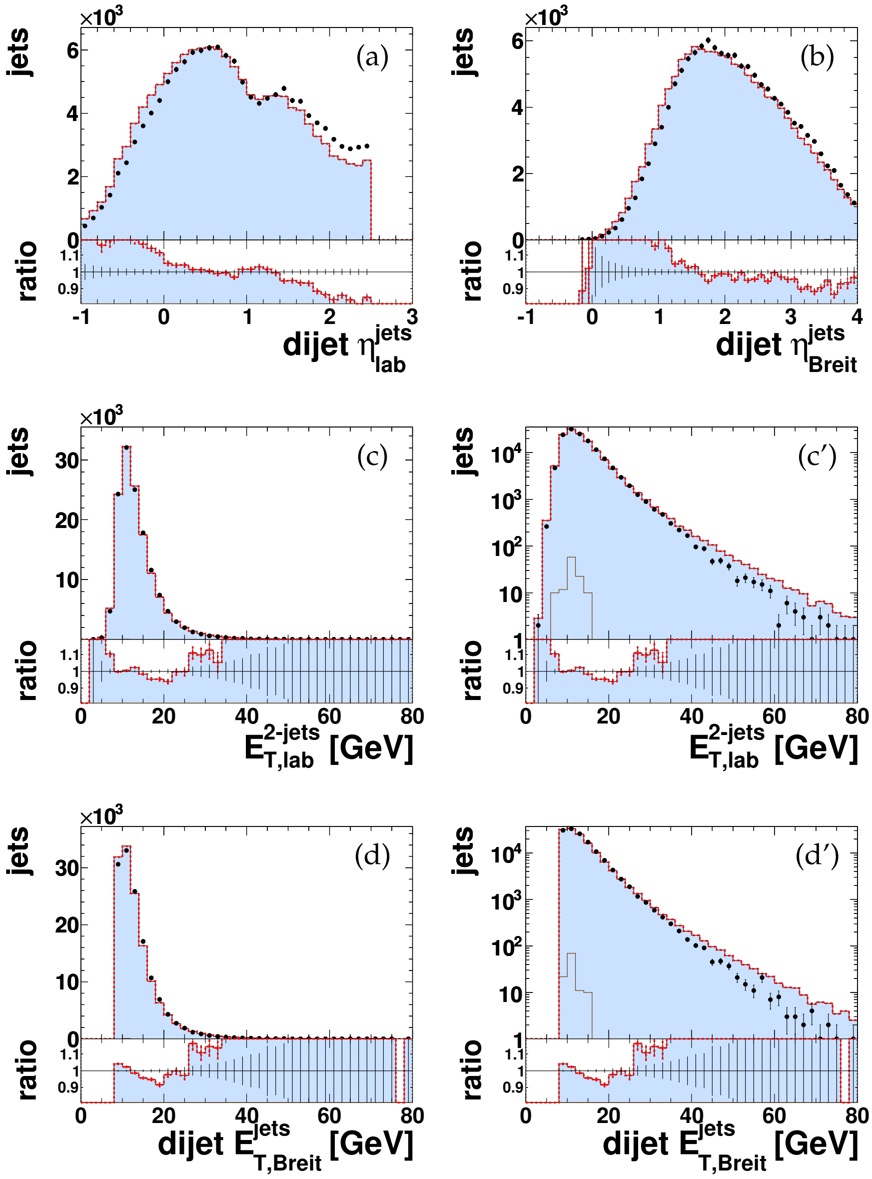

Figure 8.5: Jet variables after the inclusive dijet selection. For details see caption to figure 8.3.

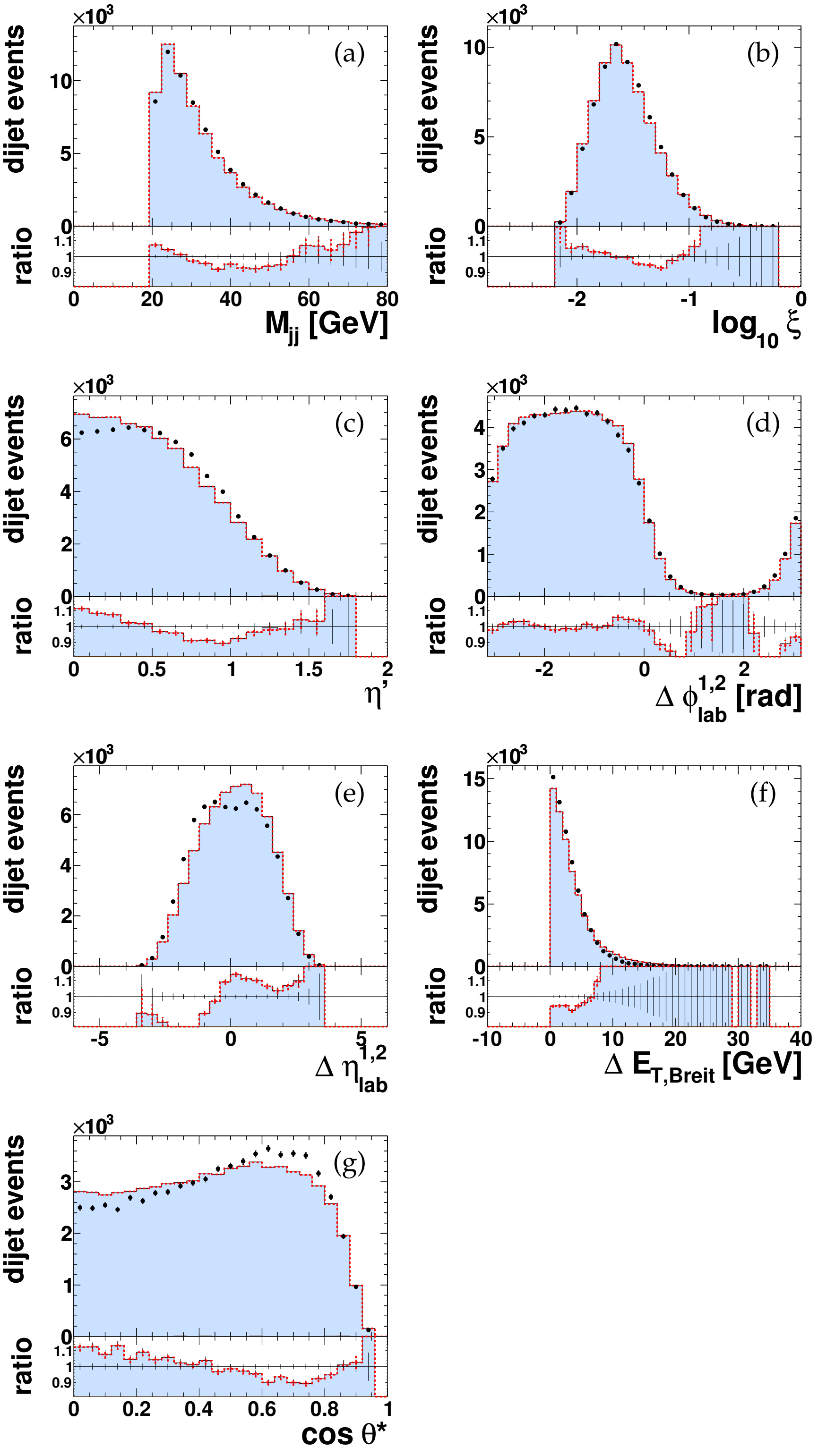

Figure 8.6: Control distributions after dijet selection. For details see caption to figure 8.3.

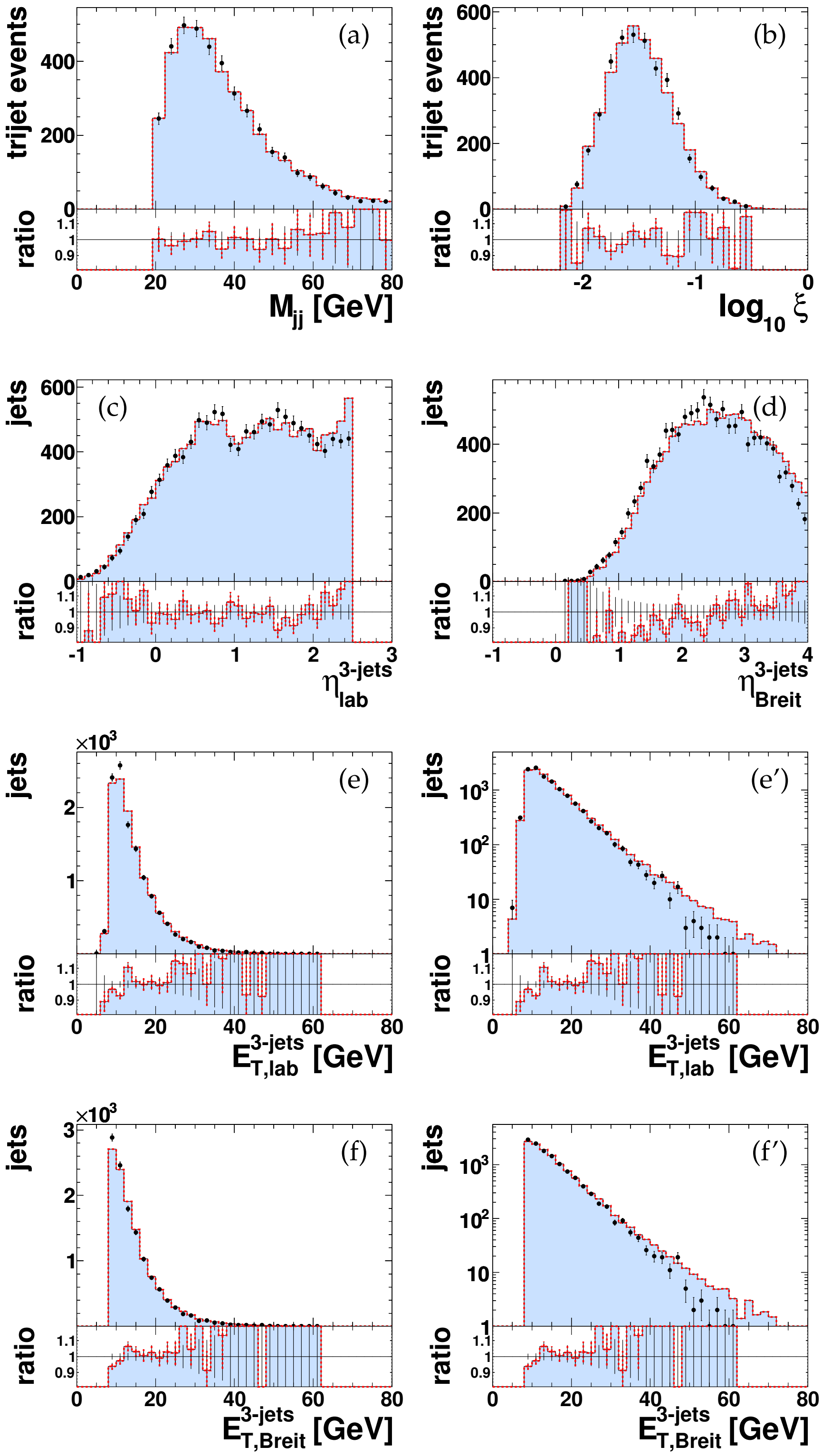

Figure 8.7: Control distributions after trijet selection. For details see caption to figure 8.3.

ratio distributions is directly correlated with the resolutions of the underlying energy measurements of the scattered electron and of the jet.

Assuming that the jet-energy determination dominates the width of the E_T ratio distribution, the resolution can be estimated from a Gaussian fit to the E_T ratio distribution, with a standard deviation corresponding to the jet energy resolution.

Figure 8.8 shows the thus determined relative jet energy resolution as function of the transverse energy of the jet in bins of $\eta_{\mathrm{lab}}^{\mathrm{jet}}$. The resolution is in all bins better than 0.15 and even below 0.10 for jets with E_T values above $\sim 30\,\mathrm{GeV}$. This is compatible with previous studies on jet resolutions in Hera-II data [110].

The Monte Carlo simulation reproduces the resolution seen in data within the statistical uncertainties.

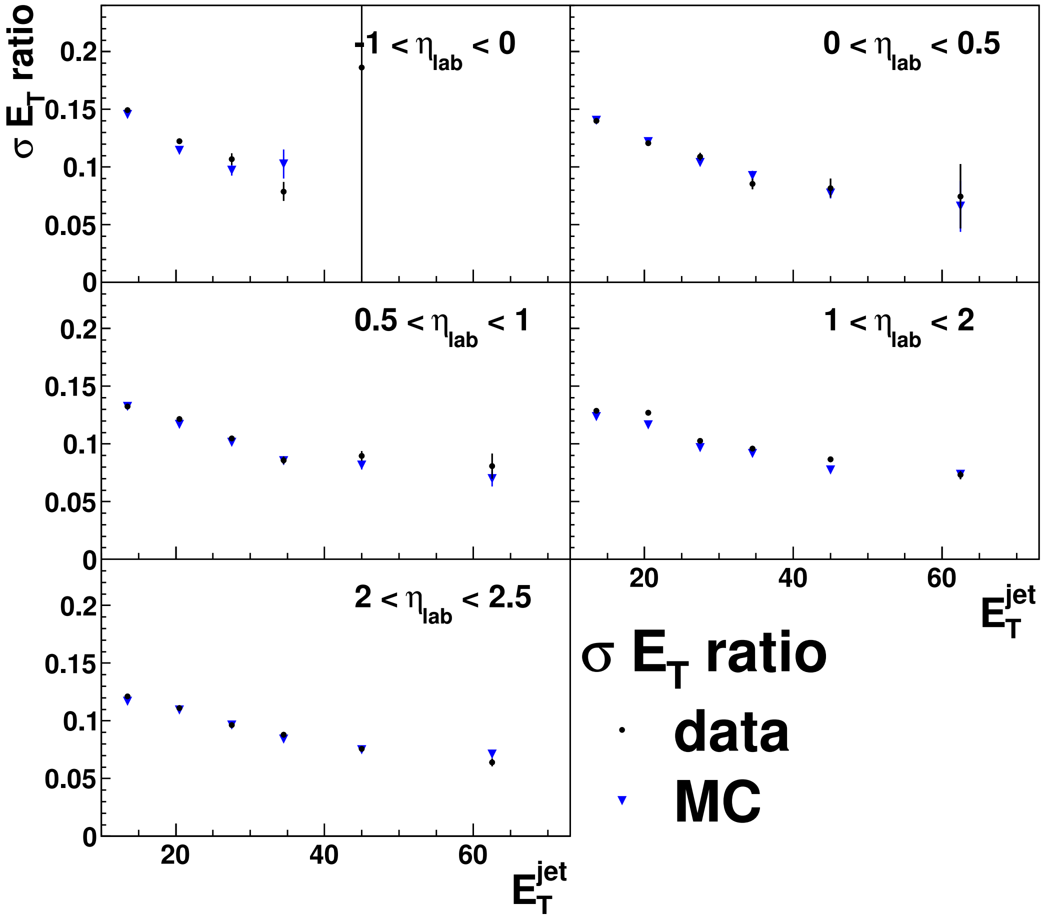

Figure 8.8: The relative jet energy resolution as function of the transverse jet energy for different bins of η_{lab}. The resolution was determined as one standard deviation of a Gaussian fitted to the E_T ratio of the jet and the scattered electron in specifically selected single jet events. See the text for details.

8.2. Acceptance Correction

When a physical quantity such as a cross-section is measured, it cannot be directly compared to theoretical predictions or even measurements from other detectors. This is due to the fact that any given detector is imperfect and that such imperfections lead to a deviation of the measured quantity from the underlying true hadronic parameter. The main reasons for this difference are

- inefficiencies, e.g. from the cuts, from the trigger, and from energy losses in the calorimeter,
- impurities in the online and offline selection of the data sample, and
- limited resolution and bias of the detector.

Due to these effects, instead of the cross-section on hadron level, $\sigma_{\text{had}}(x)$, dependent on the physically relevant variable x, a distorted distribution $\sigma_{\text{det}}(y)$ of variable y is measured, where y may significantly differ from x [149].

The relation between σ_{det} and σ_{had} can be expressed as a convolution of $\sigma_{\text{had}}(x)$ with an a-priori unknown detector acceptance function, $A(x,y)$,

$$\sigma_{\text{had}}(x) \otimes A(x,y) = \sigma_{\text{det}}(y) \quad . \tag{8.1}$$

Through modeling the detector response in the Monte Carlo simulation, the acceptance function $A(x,y)$ can be estimated, and its inverse, the acceptance correction A^{-1}, can be determined. The process of determining and applying the acceptance correction A^{-1} to the detector-level distribution to access the underlying hadron-level cross-section is referred to as the *unfolding* of the cross-section.

Unfolding is a very complex problem, especially due to the limited detector resolution causing a smearing of the underlying $\sigma_{\text{had}}(x)$ distribution. Any fluctuations and uncertainties on the measured distribution $\sigma_{\text{det}}(y)$ can therefore lead to large effects in the resulting determination of $\sigma_{\text{had}}(x)$, making the solution to the unfolding process unstable [149].

There are several statistical approaches[4] toward unfolding in high-energy physics, including *regularized unfolding* [151], *iterative methods* [152], and *correcting-factors methods* [153]. Typically, the different procedures vary significantly in their complexity, in the variance of their solution, and in their bias toward the Monte Carlo model used in the unfolding process [150].

This analysis uses the *bin-by-bin* method, a variant of the correcting-factors method that is widely used in high-energy physics (see references [7, 58, 154, 155], for example) for its relative simplicity. A major drawback of the bin-by-bin method is its reliance on the underlying Monte Carlo *true* information, resulting in bias toward this distribution [150]. This behavior has therefore to be taken into account by the systematic uncertainty.

---

[4] An overview is given in [150].

With this method, the number of measured events, N_i^{had}, on hadron level in bin i of a physical quantity x is given by

$$N_i^{\text{had}} = A_i^{-1} \cdot N_i^{\text{det}} \tag{8.2}$$

and the acceptance correction for bin i can be calculated directly from the Monte Carlo simulation through

$$A_i^{-1} = \frac{N_{i,\,\text{MC}}^{\text{had}}}{N_{i,\,\text{MC}}^{\text{det}}}, \tag{8.3}$$

where $N_{i,\,\text{MC}}^{\text{det/had}}$ are the numbers of entries in bin i on detector level and hadron level, respectively, as determined from the Monte Carlo simulation. Two useful quantities in the determination of the acceptance correction are the *efficiency* and the *purity*. The efficiency of the i-th bin, ϵ_i, is defined as the fraction of all events generated in bin i which are also detected in bin i,

$$\epsilon_i = \frac{N_i^{\text{had}\,\wedge\,\text{det}}}{N_i^{\text{had}}}, \tag{8.4}$$

where $N_i^{\text{had}\,\wedge\,\text{det}}$ is the number of events in bin i measured on both levels. The efficiency is a measure for losses of events on detector level into other bins or migrations out of the measurement range. The purity, $\mathcal{P}_i$, on the other hand is defined as the fraction of events detected in bin i that were also generated in that bin,

$$\mathcal{P}_i = \frac{N_i^{\text{had}\,\wedge\,\text{det}}}{N_i^{\text{det}}} \quad . \tag{8.5}$$

Therefore, the purity of a bin is a measure for the number of events that migrated into the bin from other bins. From the definitions of the purity and the efficiency and from equation 8.3 follows

$$A_i^{-1} = \frac{\mathcal{P}_i}{\epsilon_i} \quad . \tag{8.6}$$

For a perfect detector, both purity and efficiency would satisfy $\mathcal{P}_i = \epsilon_i = 1$, leading to a perfect measurement of the hadron-level distribution. However, in the presence of detector deficiencies with resulting migrations, the values of both are also affected by the shape of the distribution of the underlying physical quantity.

Both the purity and the efficiency can be visualized in a *migration matrix*, as shown in figure 8.9 for cross-sections $\mathrm{d}\sigma/\,\mathrm{d}Q^2$, $\mathrm{d}\sigma/\,\mathrm{d}\eta_{\text{lab}}$ and $\mathrm{d}\sigma/\,\mathrm{d}p_T$ of the inclusive jet sample. Each event is put into an element mn of the matrix, where m is the number of the bin in which the event was generated and n the bin number of the bin in which it was measured on detector level. All the events generated and measured in the same bin on both levels ($m = n$) form the diagonal of the matrix. Events outside the diagonal ($m \neq n$) have migrated from the bin they were generated in. If an event is found in a bin on one level, but not measured or generated in any bin of the other level, it is filled into the 0th column or row respectively. This might happen if the event did not pass the selection cuts on one level, if the binning range does not cover the full phase space, or in studies of multi-differential cross-sections if migrations into bins of other distributions occur.

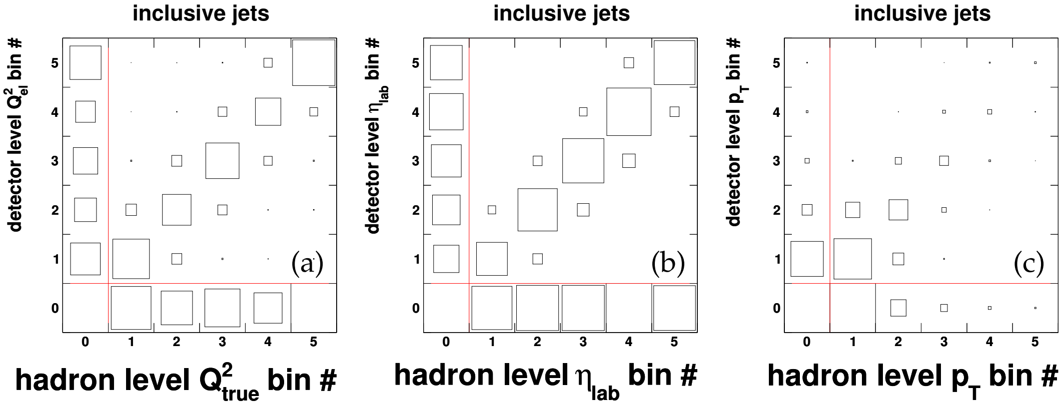

Figure 8.9: Migration matrices for selected inclusive jet cross sections for the 2004 – 2005 e^- data taking period.

From a migration matrix, M, the purity and efficiency of a bin i can be calculated directly. From equations 8.4 and 8.5 it follows that

$$\epsilon_i = \frac{M_{ii}}{\sum_n M_{in}} \tag{8.7}$$

and

$$\mathcal{P}_i = \frac{M_{ii}}{\sum_m M_{mi}} \ , \tag{8.8}$$

where M_{mn} is the value of the m-th column in the n-th row.

The statistical uncertainty for each quantity can then be calculated using

$$\Delta\epsilon_i = \sqrt{\frac{(1-\epsilon_i)\cdot\epsilon_i}{\sum_m M_{mi}}} \ , \tag{8.9}$$

$$\Delta\mathcal{P}_i = \sqrt{\frac{(1-\mathcal{P}_i)\cdot\mathcal{P}_i}{\sum_n M_{in}}} \ \text{, and} \tag{8.10}$$

$$\Delta A_i^{-1} = \sqrt{\frac{\sum_m M_{mi}}{(\sum_n M_{in})^3}\cdot\left[\sum_m M_{mi} + \sum_n M_{in} - 2\cdot M_{ii}\right]} \ . \tag{8.11}$$

Figure 8.10 shows the purities and efficiencies for the selected cross-sections of the inclusive jet and the dijet samples[5]. Typical values for this analysis are $\epsilon \approx (30-60)\%$ and $\mathcal{P} \approx (45-65)\%$. The efficiency and purity are usually poor in the kinematic region of low p_T in the inclusive jet sample and low $\langle p_T \rangle$ in the case of the dijet and trijet

---

[5] For the purities, efficiencies and correction factors of cross-sections omitted here see appendix A.

samples (see fig. 8.10c and 8.10f). Generally, the trijet sample exhibits reduced purities and efficiencies compared to the other jet samples.

The best values for the purity and efficiency are consequently for high p_T and high $\langle p_T \rangle$ in the inclusive and dijet samples, respectively, where both reach values of up to $\sim 65\%$, resulting in correction factors close to unity.

Cross-sections were only measured in bins where the luminosity-weighted average of the purity over all data-taking periods was above 30% and that of the efficiency was better than 25%. Otherwise the bin was omitted in the cross-section figures and marked as such in the cross-section tables in appendix B.

Typically, the correction factors are in the region of 1 – 1.5 and nearly constant for each cross-section, except for the dijet cross-sections as functions of ξ and $\langle p_T \rangle$ where the correction factors become smaller for higher values of ξ and $\langle p_T \rangle$, respectively. For these bins, the statistical uncertainty on the acceptance correction factors becomes noticeable.

8.3. QED Corrections

To take contributions from higher-order QED processes such as initial and final state radiation or the running of α_{em} into account, the cross-sections have been corrected by exploiting the modeling of QED effects found in the Monte Carlo simulation.

For this purpose, two separate Ariadne Monte Carlo samples have been generated. Based on otherwise identical settings, one sample included the simulation of QED effects[6] while the other did not.

Using these two samples, the effects of higher-order QED contributions on the cross-sections as function of quantity x can be determined as

$$C_i^{\mathrm{QED}} = \frac{\sigma_i^{\mathrm{w/o\ QED}}}{\sigma_i^{\mathrm{QED}}} \,, \tag{8.12}$$

where σ_i^{QED} and $\sigma_i^{\mathrm{w/o\ QED}}$ denote the cross-sections as functions of x in bin i with and without simulated QED effects, respectively. The correction factors C_i^{QED} are then applied to the data.

Figure 8.11 shows the QED correction factors for selected inclusive and dijet cross-sections. Typical values for the correction are 0.95 – 0.98 with only small variations between cross-section bins.

Since the luminosity of both Monte Carlo samples used in the determination of the QED-correction factors was very high, the statistical uncertainty on the correction was much smaller than that of the data and is therefore negligible.

---

[6] As described in chapter 4.1, the default Monte Carlo samples were generated with the simulation of higher-order QED processes included.

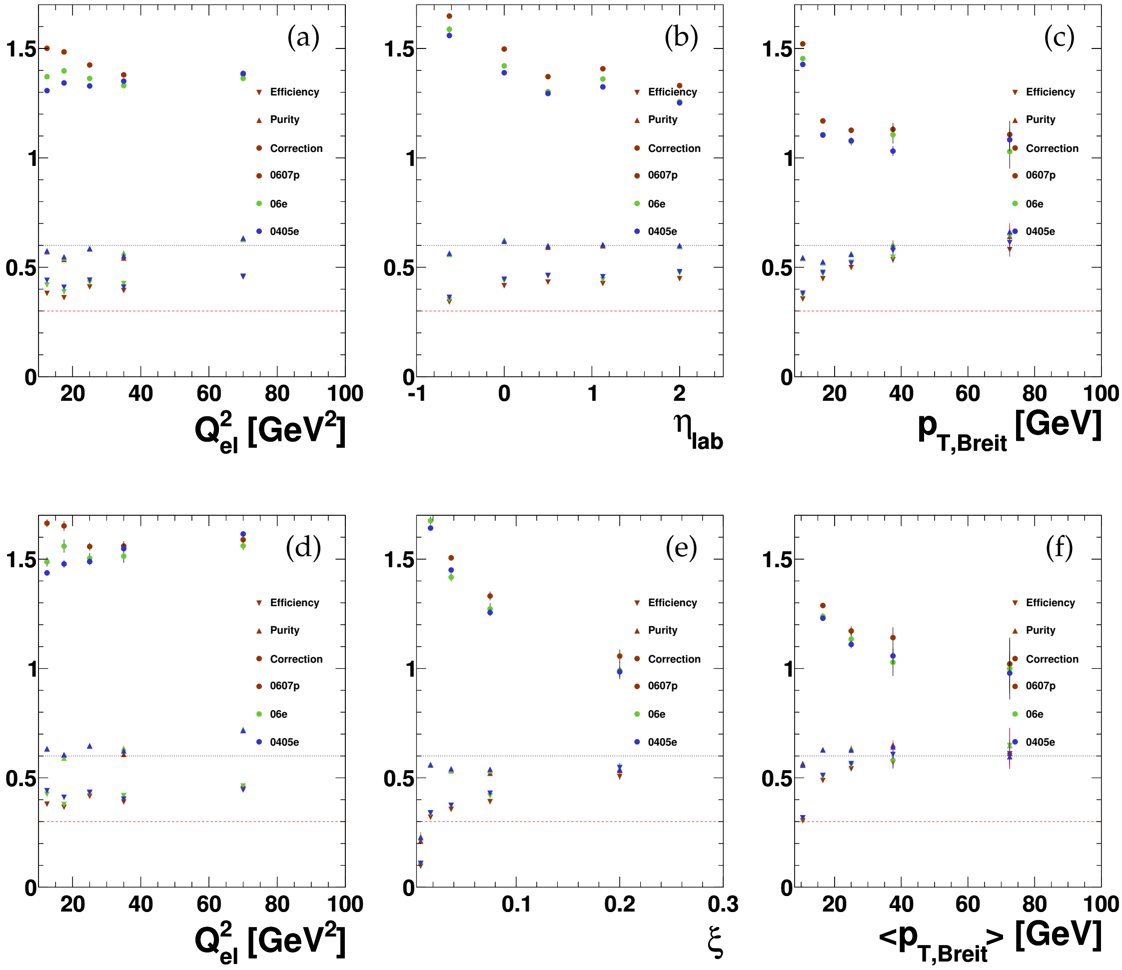

Figure 8.10: Purities (up-pointing triangles), efficiencies (down-pointing triangles), and acceptance correction factors (circles) for selected inclusive jet cross-sections (top) and dijet cross-sections (bottom). The different data taking periods are shown with different colors. To guide the eye, horizontal lines mark values of 0.6 and 0.3 .

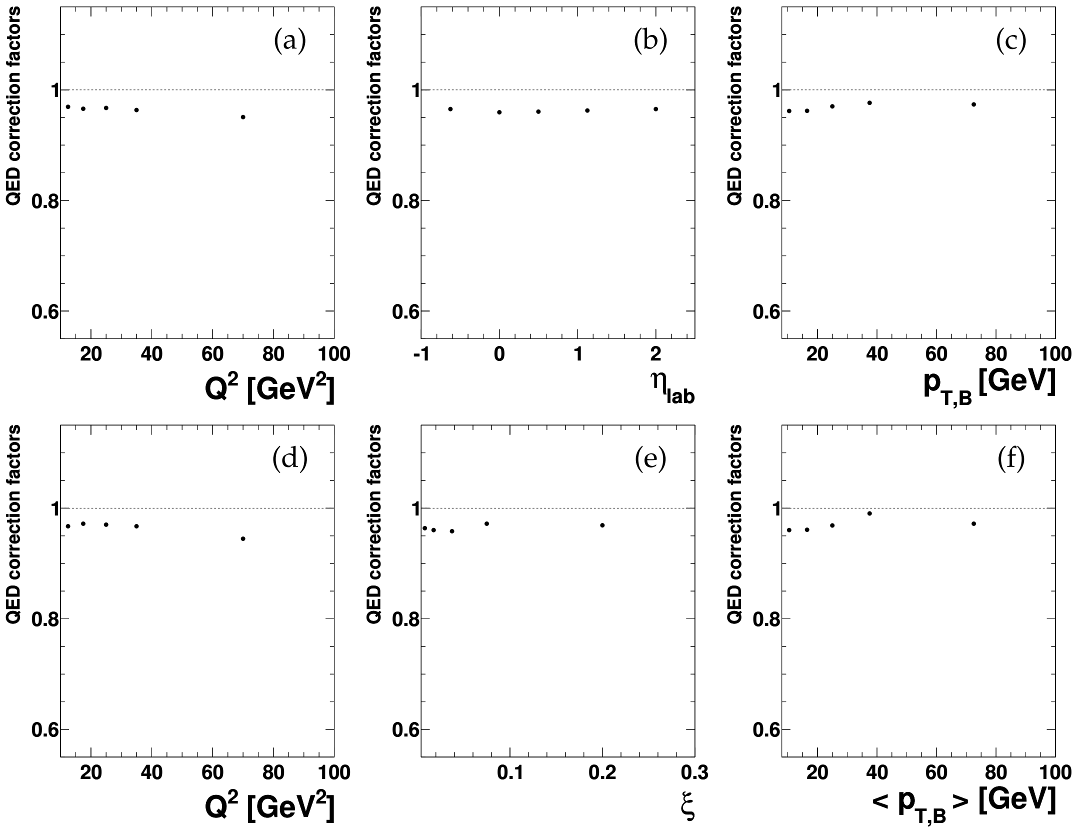

Figure 8.11: QED correction factors for selected inclusive jet cross sections (top) and dijet cross-sections (bottom).

8.4. Hadronization Correction

In order to compare measured cross-sections with perturbative QCD predictions, the theory has to be corrected for non-perturbative effects.

Using predictions from fragmentation models implemented in the Monte Carlo simulation, the non-perturbative hadronization of the final state partons can be approximated and applied as correction to the NLO calculations [156]. The correction factors account for changes in the final state topology caused by the hadronization and the subsequent migration effects.

For each cross-section of an observable x the hadronization correction can be determined using

$$C_i^{\text{hadr.}} = \frac{N_i^{\text{had}}}{N_i^{\text{par}}} \ , \tag{8.13}$$

where N_i^{had} and N_i^{par} are the number of events generated in bin i on hadron level and parton level, respectively.

Two distinct Ariadne Monte Carlo samples were used in the calculation of the hadronization correction factors, which differed in their tuning with respect to the hadronization model as described in chapter 4.1.5. The average value of the two was used as the correction factor, while the uncertainty was estimated as half the difference between both generators.

Figure 8.12 shows the resulting factors for selected inclusive and dijet cross-sections. Typical values are in the range of 0.85 – 0.95. The largest variation in the correction factors can be seen in the distribution for the η_{lab} cross-sections, while the largest uncertainties arise in the distribution for the $p_{T,\,\text{Breit}}$ cross-sections.

All correction factors are listed in the cross-section tables presented in appendix B.

8.5. Summary: Cross-Section Determination

The Monte Carlo simulation has been shown to describe the data reasonably well in the kinematic region investigated in this analysis. It is therefore suited to be used in the determination of the acceptance correction factors, A_i^{-1}. The data were unfolded through bin-by-bin multiplication with the correction factors, performed separately for each data taking period, i.e. for bin i of a cross-section as function of quantity x,

$$\left(\frac{\mathrm{d}\sigma}{\mathrm{d}x}\right)_i = \left(\sum_{p=04/05}^{06/07} A_{p,i}^{-1} \cdot N_i^p\right) \cdot \frac{1}{L} \cdot C_i^{\text{QED}} \ , \tag{8.14}$$

where the sum runs over all data taking periods p, L denotes the integrated luminosity of the samples, and C_i^{QED} is the correction factor for higher-order QED effects. N_i denotes the number of events, or rather jets in the case of the inclusive jet sample, measured in bin i.

The statistical uncertainty on the cross-section was determined by error propagation of the uncorrelated uncertainties $\Delta N_i^p \mathrel{\widehat{=}} \sqrt{N_i^p}$ and $\Delta A_{p,i}^{-1}$ as previously defined. Both

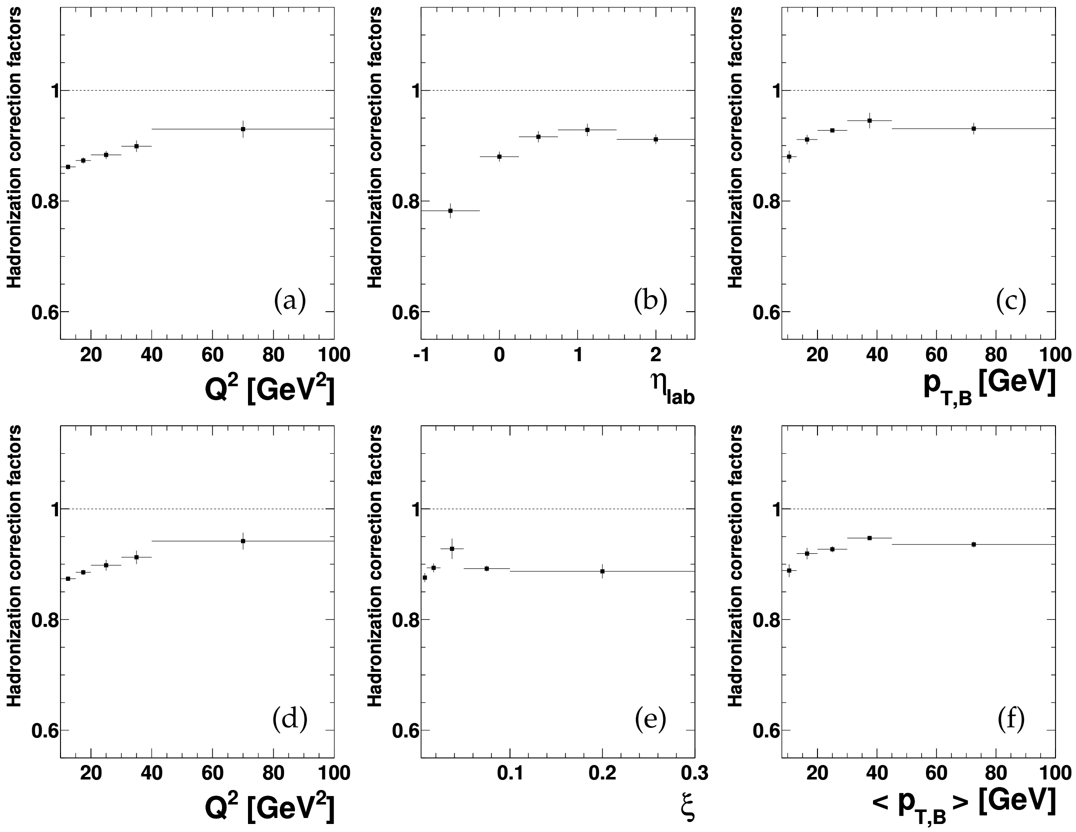

Figure 8.12: Hadronization correction factors for selected inclusive jet cross sections (top) and dijet cross-sections (bottom).

contributions are listed separately in the cross-section tables in appendix B. Typically, the statistical uncertainties on the acceptance correction are smaller but of the same order of magnitude as the statistical uncertainty of N_i^p.

Other sources of uncertainties are discussed in detail in the following chapter.

9. Estimation of Systematic Uncertainties

Aside from statistical uncertainties caused by the limited size of the data sample and of the MC samples used for corrections, every measurement is typically also affected by systematic uncertainties.

In this analysis, sources of systematic experimental uncertainties that have been investigated include model-dependent assumptions in the unfolding of the data, the limited knowledge of the absolute energy scales of the detector, background contributions from photoproduction processes and the choice of cleaning cuts in the event selection.

Similarly, the theoretical predictions are affected by the choice of renormalization and factorization scales, by the uncertainty of the PDF set, and by an uncertainty arising from the hadronization correction procedure.

In this chapter, the methods are described that have been used to estimate the effects of each of these sources of uncertainty on the measurement or prediction of the cross-sections, respectively.

9.1. Experimental Uncertainties

In the unfolding of the cross-sections, as described in the previous chapter, the Monte Carlo simulation is assumed (a) to give a valid approximation of the underlying physics processes, (b) to correctly simulate the response of the detector, and consequently (c) to correctly model migrations of events between measured cross-section bins as well as migrations of events into and out of the selected data sample. Each of these assumptions is associated with a certain systematic uncertainty that has to be taken into account.

Since (c) is reflected in the previously investigated reproduction of the data distributions by the Monte Carlo simulation, the uncertainty arising from deviations can be estimated by revising the reweighting and correction procedures for the Monte Carlo simulation that were introduced in chapter 7.2.

Similarly, the uncertainties associated with (b) can be assessed by studying the influence of a modified event selection on the cross-sections by varying the cleaning cuts described in chapter 6.2.2 within the resolution of the respective variables the cuts are imposed on.

On the other hand, the uncertainties arising from (a), the model dependence of the simulation, are typically estimated in Zeus studies by exchanging the Monte Carlo generator with one based on different model assumptions. In this analysis, a different approach was chosen; based on the fact, that the transverse energy spectrum of the jets is strongly dependent on the underlying model, a specific reweighting scheme was devised to determine the sensitivity of the measured cross-sections to variations in this spectrum.

Generally, the impact of each source of systematic uncertainty on the measured cross-sections is evaluated by studying the effect an appropriate modification to the analysis has on the measurement. Therefore, in bin i of a cross-section σ measured as function of quantity x, the uncertainty associated with s is calculated as

$$\Delta_i^s = \left(\frac{\mathrm{d}\sigma}{\mathrm{d}x}\right)_i - \left(\frac{\mathrm{d}\sigma'_s}{\mathrm{d}x}\right)_i \tag{9.1}$$

where σ'_s denotes the cross-section resulting from the systematically modified measurement.

The total systematic uncertainty in each bin is calculated by adding the individual uncorrelated contributions of the same sign in quadrature, a procedure that usually results in asymmetric uncertainties. However, where stated in the text, the systematic uncertainties were *symmetrized* for specific sources, i.e. equally contributed to both positive and negative total systematic uncertainties.

The jet energy scale uncertainty is not added to the total systematic uncertainty and instead is displayed separately, as it is assumed to be fully correlated across bins.

The following sources of systematic uncertainty have been investigated:

- **Acceptance and Monte Carlo corrections:** In chapter 7, correction procedures were introduced that re-adjusted the Monte Carlo simulation in various aspects to reproduce the data more closely. Both the correction procedure itself as well as the remaining deficiencies of the simulation give rise to systematic uncertainties in the acceptance corrections.

  - *Reweighting of the jet samples:* The jet samples have been reweighted in two steps, first, as function of Q^2_{el} and y_{el}, and second as function of the transverse energy in the Breit frame, $E^{\mathrm{jet1}}_{T,\,\mathrm{Breit}}$, and of the pseudorapidity in the laboratory system, $\eta^{\mathrm{jet1}}_{\mathrm{lab}}$, of the hardest jet found in the event. Each of these reweighting steps was performed in two consecutive iterations.

    The improvement in the description of the data gained by the second reweighting iteration is illustrated by figure 9.1. Shown are, exemplarily, the transverse jet energy, jet pseudorapidity, and jet multiplicity as predicted by the Monte Carlo simulation after each reweighting iteration. Especially the second reweighting significantly improves the description of the data in the jet multiplicity and at low values of E_T, while deviations from the data in the tail of the E_T distribution remain. However, the description of the η_{lab} distribution is somewhat degraded in the very forward and backward regions by the second reweighting iteration.

    The systematic uncertainty associated with the reweighting of the Monte Carlo simulation was estimated by limiting the reweighting to the first iteration in each of the steps described above, shown as dotted line the figure. The resulting systematic uncertainties were typically in the order of $\pm(0.5 - 2)\%$ and were symmetrized.

- *Estimation of the model dependence and remaining deviations of the Monte Carlo simulation from the data:* In chapter 8.1.2, the Monte Carlo simulation was shown to generally give a sufficient description of the data. However, for transverse energies above 25 GeV the ARIADNE Monte Carlo simulation predicts significantly more jets than measured.

  This behavior of the ARIADNE Monte Carlo simulation in the prediction of the transverse jet energy spectrum has been observed before [157] and is strongly dependent on the underlying model used in the simulation and its parameters.

  Therefore variations of the E_T spectrum of the jets were studied in order to estimate the systematic uncertainty introduced by the choice of model parameters in the simulation and the observed difference in the E_T spectrum with respect to the data.

  The associated systematic uncertainty was estimated by replacing the second iteration of the reweighting in $(E^{\mathrm{jet1}}_{T,\,\mathrm{Breit}}, \eta^{\mathrm{jet1}}_{\mathrm{lab}})$ with a reweighting only in the transverse energy of the leading jet. The event weights were determined, similarly to the procedure described in chapter 7.2.2, by fitting the ratio of the Monte Carlo simulation over the data as function of $E^{\mathrm{jet1}}_{T,\,\mathrm{Breit}}$ with a third-order polynomial.

  Figure 9.1a shows the number of jets as function of the transverse jet energy for data and two differently reweighted Monte Carlo samples: one only E_T reweighted in the 2nd iteration (dotted-dashed), and the other using the default reweighting scheme (dashed). After the specific reweighting of $E^{\mathrm{jet1}}_{T,\,\mathrm{Breit}}$, the transverse jet energy spectrum is very well described by the Monte Carlo simulation, even up to $E_{T,\,\mathrm{Breit}}$ values of 70 GeV. This also resulted in an improvement of the description of the jet multiplicity as shown in figure 9.1a. The newly reweighted Monte Carlo sample reproduces the data in other quantities as well, but overall gives a slightly worse description than achieved with the default reweighting scheme.

  The resulting uncertainty from this variation of the transverse energy spectrum is typically below 2% in most cross-section bins but increases in the cross-sections as function of $E_{T,\,\mathrm{Breit}}$ for higher values of E_T to up to 10%. Similarly, the uncertainty on the dijet cross-sections as functions of ξ and M_{jj} increases from values below 1% to up to 7% for higher values of ξ and M_{jj}, respectively.

  The thus determined uncertainties were again symmetrized.

- *Reweighting of the longitudinal vertex distributions:* Of the two different reweighting schemes for the z_{vtx} distributions presented in chapter 7.2.1, one has been used as default in the unfolding of the cross-sections [110], while the second was used to estimate the systematic uncertainty introduced by the choice [147, 148].

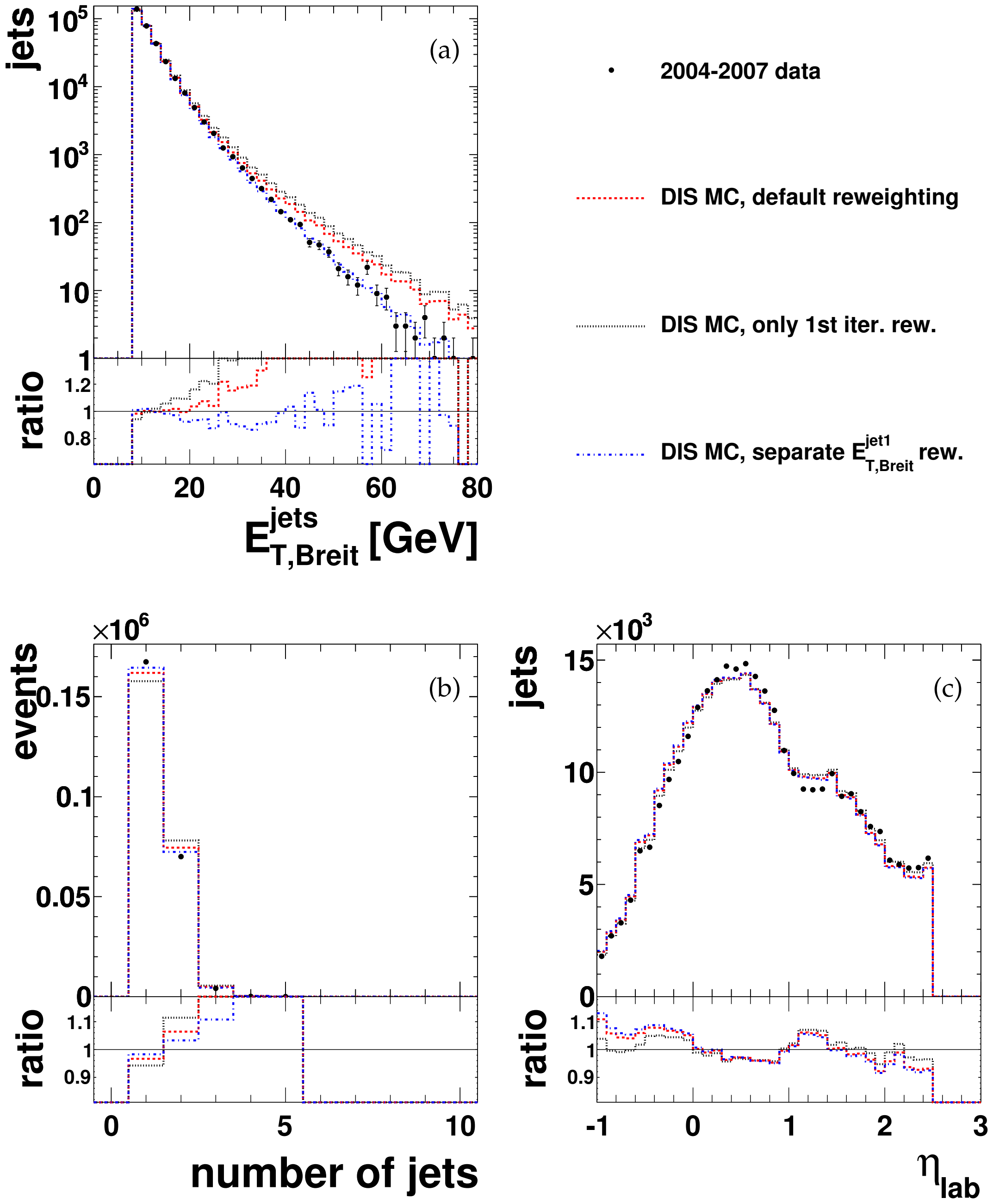

Figure 9.1: Transverse jet energy in the Breit frame, the jet multiplicity, and the jet pseudorapidity in the laboratory frame for data (points) and for Ariadne Monte Carlo samples with the default reweighting scheme as described in chapter 7.2.2 (dashed line), with reweighting limited to the first iterations (dotted line), and with an alternative E_T-focused reweighting scheme (dashed-dotted line). See the text for details.

Exchanging one z_{vtx} reweighting scheme for the other typically resulted in a systematic uncertainty of less than 0.2%.

- *Correcting the trigger efficiency:* As described in chapter 7.3, to correct the difference in trigger efficiency observed between data and Monte Carlo simulation, a correction function was derived by a fit to the efficiency ratio data over Monte Carlo simulation as function of y_{el}.

  To estimate the systematic uncertainty introduced by the fit and the choice of distribution, the correction was alternatively derived by fitting the efficiency ratio as function of Q^2_{el}. The resulting uncertainty on the measured cross-sections was typically in the order of 0.1% or less.

- **Cleaning cuts:** The cleaning cuts imposed on the jet samples were varied by amounts corresponding to the resolution of the respective quantities from their original values introduced in chapters 6.2.2 and 6.3 in both data and in the Monte Carlo simulation to estimate the systematic uncertainties associated with the choice of the imposed cut values.

  Table 9.1 summarizes the applied variation to each cut and the typical effect it had on the measured cross-section. Typically, the systematic uncertainties introduced by the cleaning cuts are well below 1% in all cross-section bins, with the exception of the uncertainties associated with the cuts on the energy-longitudinal momentum balance which extend up to 2%. The sensitivity to the specific value at which the $E - p_z$ spectrum is cut is most probably due to the shift of the Monte Carlo simulation in the $E - p_z$ distribution with respect to the data, as shown in figure 6.9 on page 60.

Cut imposed on	**Variation**	**Typical unc.** $\pm$[%]
longitudinal vertex position	$\pm 4\,\text{cm}$	< 0.2
scattered electron energy	$\pm 0.5\%$	$\ll 0.01$
radius of e position in RCAL	$\pm 1\,\text{cm}$	0.2
energy-longitudinal momentum balance	$\pm 2\,\text{GeV}$	$0.5 \ldots 2$
transverse momentum balance	± 0.02	< 0.1
hadronic energy fraction in e cone	$\pm 1\%$	< 0.1
transverse jet energy in lab. frame	$+1.5\,\text{GeV}$	< 0.05

Table 9.1: Imposed cleaning cuts, their variations used to estimate the associated uncorrelated systematic uncertainties, and typically resulting values of uncertainty.

- **Photoproduction background:** The amount of photoproduction (γp) background was estimated using a dedicated Monte Carlo sample. The normalization of this sample was determined by a fit of the γp and the signal DIS samples to data distributions after the inclusive DIS selection. This resulted in a lower value compared to the normalization with respect to the integrated luminosity as given by the Monte Carlo simulation.

  The thus determined relative normalization factor between the DIS and the γp Monte Carlo samples was also used for the jet samples.

To account for uncertainties introduced by the normalization of the background MC sample, the normalization factor was increased by a factor of 3. The resulting uncertainties on the measured cross-sections were typically smaller than 0.5% but increased up to 1.7% in low x_{Bj} and low Q^2 bins. The uncertainties were symmetrized for all cross-sections.

- **Electron identification:** In this analysis, the SINISTRA algorithm is used as the primary electron finder.[1] To estimate the systematic uncertainty introduced by this choice, the EM electron finding algorithm was employed instead. The resulting uncertainties were typically in the order of $(0.5-3)\%$ but could reach values of up to 5.5% in the highest bin for the inclusive jet cross-sections as function of E_T.

- **Hadronic energy scale:** The absolute hadronic energy scale is commonly the dominant source of uncertainty in jet cross-section measurements at ZEUS and has been discussed in detail in chapter 7.1.1. After the calibration of the hadronic energy scale, the remaining uncertainty was estimated to be ±3% for jets with transverse momenta below 10 GeV and ±1% for jets with $E_{T,\,\mathrm{lab}} > 10\,\mathrm{GeV}$ [110, 122].

  The corresponding systematic uncertainty on the cross-sections was determined by varying the energy of the jets in the Monte Carlo simulation, once increasing the energy and once lowering it by the above stated percentages.

  The resulting uncertainties were typically in the order of $(4-8)\%$ for the inclusive jet cross-sections. Due to the additional cuts on the hadronic system imposed on the dijet and trijet cross-sections, the typical uncertainties increase to $(4-10)\%$ and $(6-13)\%$, respectively.

  Since the uncertainty on the absolute hadronic energy scale is assumed to be fully correlated across cross-section bins, it is shown separately in the plots and in the cross-section tables in appendix B.

- **Electromagnetic energy scale:** The uncertainty on the absolute electromagnetic energy scale can be studied in a similar manner as presented in chapter 7.1.1 for the hadronic energy scale: by using the energy of the scattered electron as reconstructed by the Double-Angle method as reference for E'_{el}, exploiting the fact that the Double-Angle method is based on angular measurements and is thus in first order independent of the absolute energy calibration of the calorimeter.

  Figure 9.2 shows the difference between data and the Monte Carlo simulation in the energy scale for the scattered electron to be less than 1% over the full Q^2 range investigated in this analysis. This result is compatible with previous studies [158].

  The uncertainty on the absolute electromagnetic energy scale was therefore estimated as ±1% and was propagated to the cross-sections by varying the energy of the scattered electron in the Monte Carlo simulation by ±1%.

---

[1] For details on the electron identification algorithms see chapter 5.2.

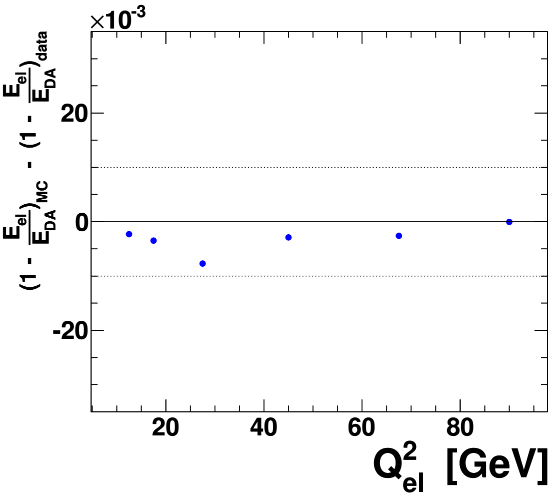

Figure 9.2: Difference between data and the Monte Carlo simulation in the energy scale for scattered electrons as a function of Q^2. Dotted lines at ±1% are shown to guide the eye.

The resulting systematic uncertainty on the cross-sections was typically in the order of $(1-3)\%$.

In addition to the systematic uncertainties discussed above, the measured integrated luminosity introduces an overall normalization uncertainty of 2.6% on all measured cross-sections.[2] This uncertainty was included neither in the plots nor in the cross-section tables in the appendix.

9.2. Theoretical Uncertainties

The following sources of uncertainty have been considered in the calculation of the NLO QCD predictions:

- **Parton-density functions:** The uncertainty of the predicted cross-sections due to their dependence on the proton PDFs was estimated by repeating the calculations using 44 additional PDF sets provided by the CTEQ6.6 group [107].

  The resulting uncertainty on the cross-sections was typically in the order of ±4% but increased to up to ±8% at high values of jet E_T.

- **Strong coupling constant:** The uncertainty due to the choice of $\alpha_S(m_Z)$ was assessed with special CTEQ6.6 PDF sets with values of $\alpha_S(m_Z) = 0.114$ and $\alpha_S(m_Z) = 0.122$ [107]. The difference of the resulting predictions with respect

---

[2] Recent re-evaluations of the systematic uncertainty associated with the luminosity measurement reduce the uncertainty for the full HERA-II data taking period to 1.8% [159]. The involved correction of the integrated luminosity was not carried out in this analysis, therefore the established value of 2.6% is cited.

to the central cross-section prediction (based on $\alpha_S(m_Z) = 0.118$) was scaled by 1/4 in accordance to current estimates of the uncertainties on $\alpha_S(m_Z)$ of ~ 0.001 [160, 161].

The resulting uncertainty on the predicted cross-sections was typically in the order of 3% but increased to ~ 5% for the trijet cross-sections due to their $\mathcal{O}(\alpha_S^2)$ dependence in NLO on the strong coupling constant.

- **Factorization scale:** The uncertainty on the cross-section prediction due to the choice of factorization scale, μ_F, was determined by varying the factorization scale by a factor in the arbitrary range 0.5 to 2 [7].

  The resulting uncertainty on the cross-sections was typically in the order of ±3% but increased to up to ±5% in cross-section bins with high values of jet E_T or low values of x_{Bj}.

- **Renormalization scale:** Similarly, the uncertainty on the cross-section prediction due to the choice of renormalization scale, μ_R, was determined by varying the renormalization scale by a factor in the arbitrary range 0.5 to 2 [7].

  The resulting uncertainty on the cross-sections was typically in the range of ±10 to ±30% and dominated the overall uncertainty on the NLO QCD predictions.

- **Hadronization correction:** Two distinct ARIADNE Monte Carlo samples were used in the calculation of the hadronization correction factors, which differed in their tuning with respect to the hadronization model.[3] The average value of the two was used as the correction factor, while the uncertainty was estimated as half the spread between both samples.

  The uncertainty on the cross-sections due to the hadronization correction was typically in the order of $\pm(3-5)\%$

Figure 9.3 shows the theoretical uncertainties for the inclusive jet and the dijet cross-sections as function of Q^2. The choice of renormalization scale is clearly the dominant source of uncertainty for the NLO QCD predictions. The associated uncertainties are asymmetric with respect to the central value and decrease with higher values of Q^2. Both observations also apply to the uncertainties due to the choice of μ_F which generally yields the smallest theoretical uncertainty.

9.3. Summary

In this chapter, various sources of systematic uncertainty affecting either the measurement or the theoretical calculations have been discussed and their effect on the cross-sections has been estimated.

For the NLO QCD calculations by far the dominant source of uncertainty is the choice of renormalization scale. This indicates the importance of missing higher orders for the prediction.

---

[3] For details, see chapter 4.1.5.

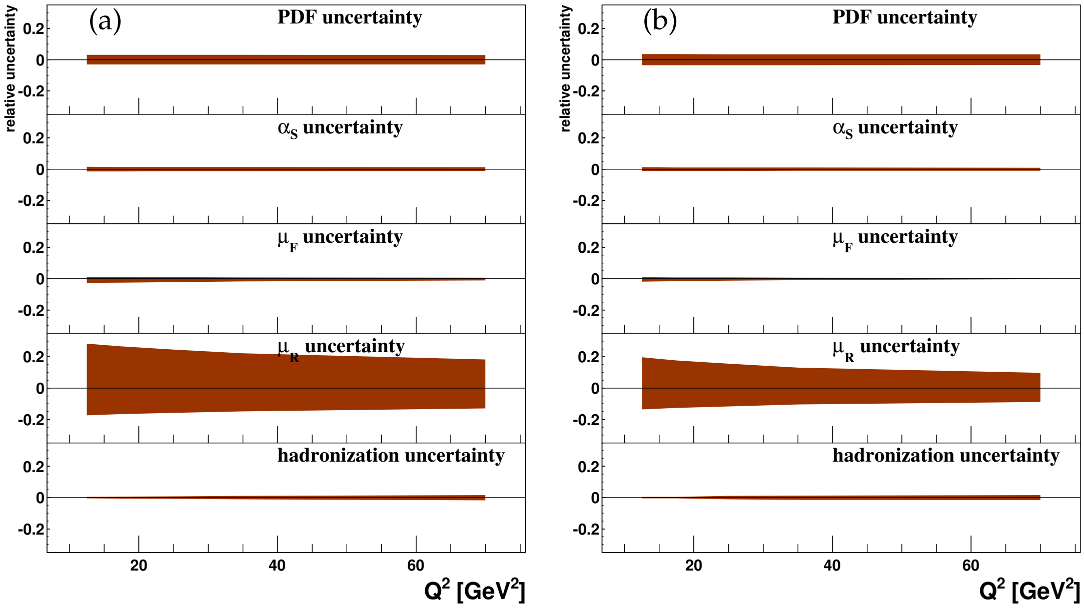

Figure 9.3: Theoretical uncertainties due to the choice of PDF, the factorization scale, μ_F, the renormalization scale, μ_R, and the hadronization correction for cross section predictions as function of Q^2 for inclusive jets (left) and dijets (right).

On the experimental side, the dominant source of uncertainty is the absolute hadronic energy scale, which is correlated across cross-section bins and therefore shown separately in the plots. Other large contributions to the systematic uncertainty arise from the inability of the underlying Monte Carlo model to fully reproduce the transverse jet energy spectrum of the data.

Table 9.3 summarizes the experimental sources of uncertainty considered and the variations used to estimate the associated uncertainties.

Source of systematic uncertainty	**Remarks/Variation**
Acceptance and Monte Carlo corrections	*applied to MC only*
Reweighting of the jet samples	alternative weights
Model dependence	reweighting of $E_{T,\,\mathrm{Breit}}^{\mathrm{jet1}}$
Trigger efficiency corrections	alt. correction function
z_{vtx} reweighting	alternative weights
Cleaning cuts on	*applied to data and MC*
longitudinal vertex position	$\pm 4\,\mathrm{cm}$
scattered electron energy	$\pm 0.5\%$
radius of e position in RCAL	$\pm 1\,\mathrm{cm}$
energy-longitudinal momentum balance	$\pm 2\,\mathrm{GeV}$
transverse momentum balance	± 0.02
hadronic energy fraction in e cone	$\pm 1\%$
transverse jet energy in lab. frame	$+1.5\,\mathrm{GeV}$
Energy scales	*applied to MC only*
Hadronic-energy scale	$\pm 3\%$ for $E_{T,\,\mathrm{lab}}^{\mathrm{jet}} < 10\,\mathrm{GeV}$ and $\pm 1\%$ for $E_{T,\,\mathrm{lab}}^{\mathrm{jet}} > 10\,\mathrm{GeV}$
Electromagnetic-energy scale	$\pm 1\%$
Other sources	
Photoproduction background	γp MC normalization $\times 3$
Electron identification	EM-algorithm *in data and MC*

Table 9.2: Summary of the experimental sources of systematic uncertainty and the variation used to estimate their impact on the cross-section measurements.

10. Results

The cross-sections presented in this chapter were measured using the 2004 – 2007 ZEUS data sample (HERA-II) after applying the DIS and jet selection criteria as described in the previous chapter 6, restricting the kinematic region to $10 < Q^2 < 100\,\mathrm{GeV}^2$ and $0.2 < y < 0.6$. The jets were clustered with the inclusive k_T algorithm in the Breit frame and were required to be in the pseudorapidity range of $-1 < \eta_{\mathrm{lab}} < 2.5$ in the laboratory frame with a transverse momentum[1]in the Breit frame, $p_{T,\mathrm{B}}$, of at least $8\,\mathrm{GeV}$. The dijet and trijet samples were additionally required to feature an invariant dijet mass of the two hardest jets of at least $20\,\mathrm{GeV}$.

After a brief review of the studied observables, the measured cross-sections will be presented, starting with the cross-sections for inclusive jet production and followed by the cross-sections for inclusive dijet and trijet production.

The future combination of selected cross-sections with corresponding measurements from the H1 experiment is discussed at the end of this chapter.

The observations made in the following sections are summarized and further discussed in chapter 11.

10.1. Observables

In the inclusive jet sample, differential cross-sections with respect to the virtuality, Q^2, the jet pseudorapidity in the laboratory frame, η_{lab}, the jet transverse momentum in the Breit frame, $p_{T,\mathrm{B}}$, and the Bjorken-scaling variable, x_{Bj} were measured.

The double-differential inclusive-jet cross-sections were measured in five regions of Q^2 as functions of η_{lab}, $p_{T,\mathrm{B}}$, and x_{Bj}. The cross-section as functions of $p_{T,\mathrm{B}}$ was also measured double-differentially in three bins of η_{lab}.

For the inclusive-jet cross-sections, each *jet* that satisfied the selection requirements entered into the measured distributions.

In the inclusive dijet sample, differential cross-sections were measured as functions of Q^2, the invariant dijet mass, M_{jj}, the absolute difference in pseudorapidity between the dijets in the Breit frame, η', the mean transverse momentum in the Breit frame of the dijets, $\langle p_{T,\mathrm{B}} \rangle$, and the proton's momentum fraction entering into the hard scattering, ξ. The cross-sections with respect to $\langle p_{T,\mathrm{B}} \rangle$ and ξ were also measured double-differentially in five bins of Q^2.

In the inclusive trijet sample, differential cross-sections were measured as functions of Q^2, the invariant dijet mass of the two hardest jets, M_{jj}, and the mean transverse momentum in the Breit frame of the two hardest jets, $\langle p_{T,\mathrm{B}} \rangle$. The latter were also measured double-differentially in five bins of Q^2.

---

[1] The jets considered throughout this analysis are massless, i.e. $E_T^{\mathrm{jet}} \mathrel{\widehat{=}} p_T^{\mathrm{jet}}$.

For the cross-sections of inclusive dijet (trijet) production, each *event* that featured at least two (three) jets satisfying the selection criteria entered into the above distributions.

The data are presented in the figures as dots with the statistical uncertainties shown as inner error bars, and the quadratic sum of the statistical and the systematic uncertainties shown outer error bars. The uncertainty arising from the jet energy scale is assumed to be fully correlated across bins and is therefore shown separately as shaded band.

The data have been corrected for limited detector acceptance, efficiency, and resolution as well as for QED radiation effects and the running of α_{em} as discussed in chapter 8.

The next-to-leading order (NLO) QCD predictions have been calculated with scales of $\mu_F^2 = \mu_R^2 = (Q^2 + \hat{E}_{T,\mathrm{B}}^2)/2$, where $\hat{E}_{T,\mathrm{B}}^2$ denotes either the mean transverse energy of the jets (for the inclusive jet cross-sections) or the mean transverse energy of the two hardest jets (dijet and trijet cross-sections) with respect to the Breit frame. The predictions were corrected for hadronization effects and are shown as dashed line with their associated uncertainties displayed as shaded area.

For all cross-sections the ratio to NLO is shown either underneath the cross-sections or in a separate figure in the case of the double-differential cross-sections.

Appendix B contains tables detailing the numerical values for all cross-sections presented in this chapter, together with statistical, uncorrelated systematic, and jet-energy scale uncertainties, as well as QED and hadronization correction factors.

10.2. Inclusive Jet Cross Sections

Figure 10.1 shows the cross-section $\mathrm{d}\sigma/\,\mathrm{d}Q^2$ and the corresponding NLO QCD predictions for inclusive jet production. Over the investigated Q^2 range, the measured cross-section drops by approximately one order of magnitude.

The NLO prediction generally agrees with the data, but has a tendency to be below the data. This difference is still well within the uncertainties of data and theory, though.

While the uncertainty on the data is dominated by the uncertainty associated with the jet energy scale, the total experimental uncertainty is still much smaller than the total theoretical uncertainty, especially at values of Q^2 below $40\,\mathrm{GeV}^2$ where the uncertainty on the NLO calculation becomes larger than 20%. In this region, the renormalization scale uncertainty, which dominates the theoretical uncertainty, becomes very large.

This is demonstrated by NLO calculations performed at $\mu_R^2 = Q^2$ and $\mu_R^2 = \bar{E}_{T,\mathrm{B}}^2$ shown in figure 10.1 as solid and dotted lines, respectively. Since typically $E_{T,B}^2 > Q^2$ in most of the phase space investigated in this analysis, $\mu_R^2 = \bar{E}_{T,\mathrm{B}}^2$ usually provides a harder scale and $\mu_R^2 = Q^2$ a much softer scale than $\mu_R^2 = (Q^2 + \bar{E}_{T,\mathrm{B}}^2)/2$, the scale at which the central NLO was calculated.

The resulting predictions are compatible at $Q^2 > 40\,\mathrm{GeV}^2$, but they differ significantly at lower values of Q^2 where the NLO calculation at $\mu_R^2 = Q^2$ predicts cross-sections $\sim 30\%$ larger than the predictions using the other investigated scales.

Figure 10.1 suggests that the data favor a softer renormalization scale. This observation does not lead to any obvious conclusions, however, as (a) the better description of

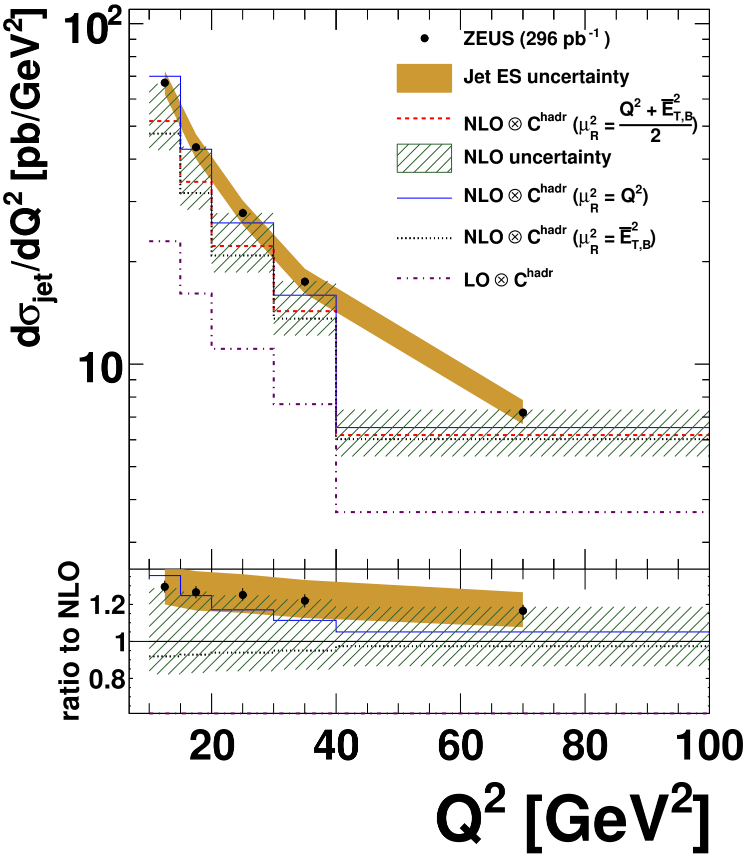

Figure 10.1: Measured inclusive jet cross-section $d\sigma / dQ^2$ compared with NLO QCD predictions (dashed line) shown with their associated uncertainties (shaded area). Additionally, NLO QCD predictions with varied renormalization scale (solid and dotted lines) as well as LO QCD calculations (dash-dotted line) are shown for comparison. The data (dots) are presented with statistical (inner bars), and statistical and systematic uncertainties added in quadrature (outer bar) along with the jet energy scale uncertainty (shaded band). The ratio to the NLO QCD prediction is shown at the bottom of the figure.

the data by the NLO calculations at $\mu_R^2 = Q^2$ could be purely accidental, especially considering the larger scale uncertainty associated with this choice of scale [6, 162]; (b) the large theoretical uncertainties due to the renormalization scale dependence already demonstrate the impact of missing higher orders in the calculation; and (c) other effects could also play a role such as a resolved photon structure [163–165] or possibly the onset of BFKL dynamics.

Such large renormalization scale uncertainties are often accompanied by large differences between the next-to-leading order and the leading-order (LO) predictions, typically expressed in form of a k factor,

$$k \equiv \frac{\sigma_{\mathrm{NLO}}}{\sigma_{\mathrm{LO}}} \ . \tag{10.1}$$

Assuming that the relative correction to the cross-section decreases with higher orders of the perturbative series, the k factor is a measure of the stability of the prediction [162]. Values of the k factor close to unity are then an indication that only small contributions can be expected from the next-to-next-to-leading order (NNLO) term.[2] The k factors can also be used in the normalization of LO cross-section predictions, e.g. from parton showers [166, 167].

For the cross-section as function of Q^2, the LO prediction[3] is shown in figure 10.1 as well. While at LO the QCD prediction roughly predicts the shape of the measured cross-sections, the normalization is off by approximately a factor 3. The k factors are also quite large with values greater than 2 for the lowest Q^2 bin.[4] They decrease to about 1.75 for the highest Q^2 values, corresponding with the smaller scale dependence of the NLO prediction seen in these bins. These values are compatible with previous observations in similar kinematic regimes [4, 6, 162].

The scale dependence is further investigated in figure 10.2 where the measured cross-section $\mathrm{d}\sigma/\,\mathrm{d}\eta_{\mathrm{lab}}$ is presented and compared to NLO predictions.

The cross-section as function of η_{lab} is largest in the region $0.25 < \eta_{\mathrm{lab}} < 0.75$ and drops by $\sim 50\%$ in both bins of smallest η_{lab} values (the electron beam or "backward" direction) and bins of largest η_{lab} values (proton beam or "forward" direction).

Within the uncertainties, which are dominated by the theoretical uncertainties, the NLO prediction agrees with the measured data up to $\eta_{\mathrm{lab}} = 0.75$. For increasing values of η_{lab} the data rise above the prediction with a measured value $\sim 60\%$ larger than the NLO prediction in the most forward η_{lab} bin. With $\sim 35\%$, the uncertainty on the NLO is also largest in this bin. Akin to the theoretical uncertainty, the k factors increase as function of η_{lab} as well, from ≈ 1.5 in the lowest bin up to values of ≈ 3.75 in the most forward bin.

A similar behavior of the NLO has been observed before in studies of forward jets in neutral current DIS at low Q^2, where jets were investigated in the pseudorapidity ranges of 1.7 to 2.8 [168] and 2 to 4.3 [169]. Here, the NLO predictions were found to be lower than the data by as much as a factor two, most prominently at low values of x.

---

[2] The precise value of the k factor also depends on other variables though, such as the choice of renormalization and factorization scales and the PDF sets used in the calculations.

[3] The LO prediction has been calculated with the CTEQ6L LO-PDF set [107] and using scales of $\mu_F^2 = \mu_R^2 = (Q^2 + \bar{E}_{T,\mathrm{B}}^2)/2$.

[4] Please note that the ratio plot presented at the bottom of the figure shows $k^{-1} \mathrel{\widehat{=}} \sigma_{\mathrm{LO}}/\sigma_{\mathrm{NLO}}$.

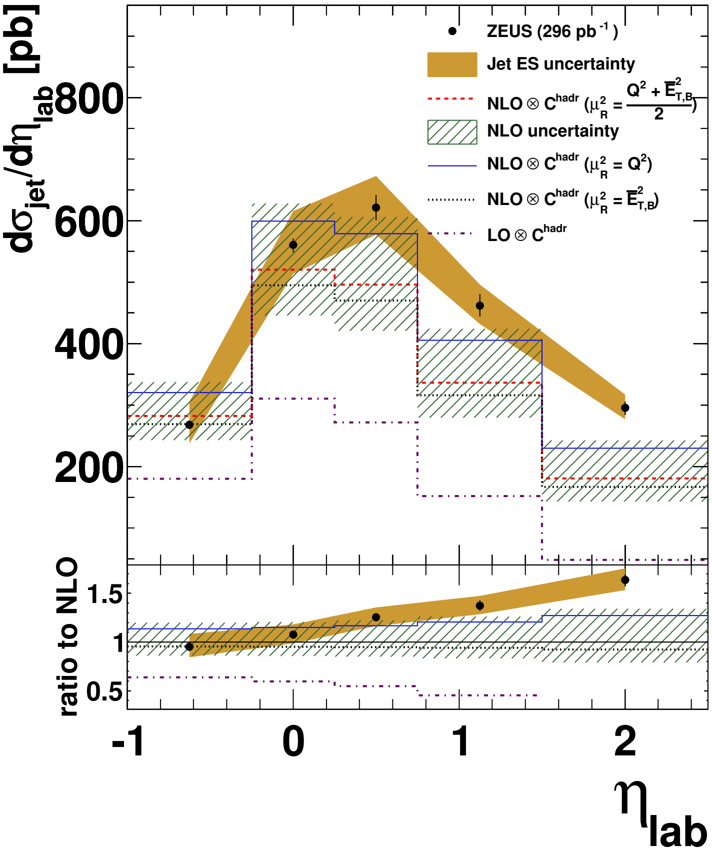

Figure 10.2: Measured inclusive jet cross-section $d\sigma/\,d\eta_{lab}$ compared with NLO QCD predictions. See text and caption to figure 10.1 for details.

In [168], DGLAP-based models ascribing a partonic structure to the exchanged virtual photon gave an improved description of the data; however, remaining deviations were interpreted as possible evidence of BFKL-like parton dynamics.

Figure 10.2 shows that of the NLO calculations at the alternative renormalization scales investigated, none correctly predicts the shape of the $d\sigma / d\eta_{\mathrm{lab}}$ cross-section. It is important to note though, that the NLO calculation effectively becomes a leading-order prediction at large values of η_{lab} and fixed values of Q^2 and y, since the LO contribution is suppressed [170]. This underlines the importance of higher-order calculations for this kinematic regime.

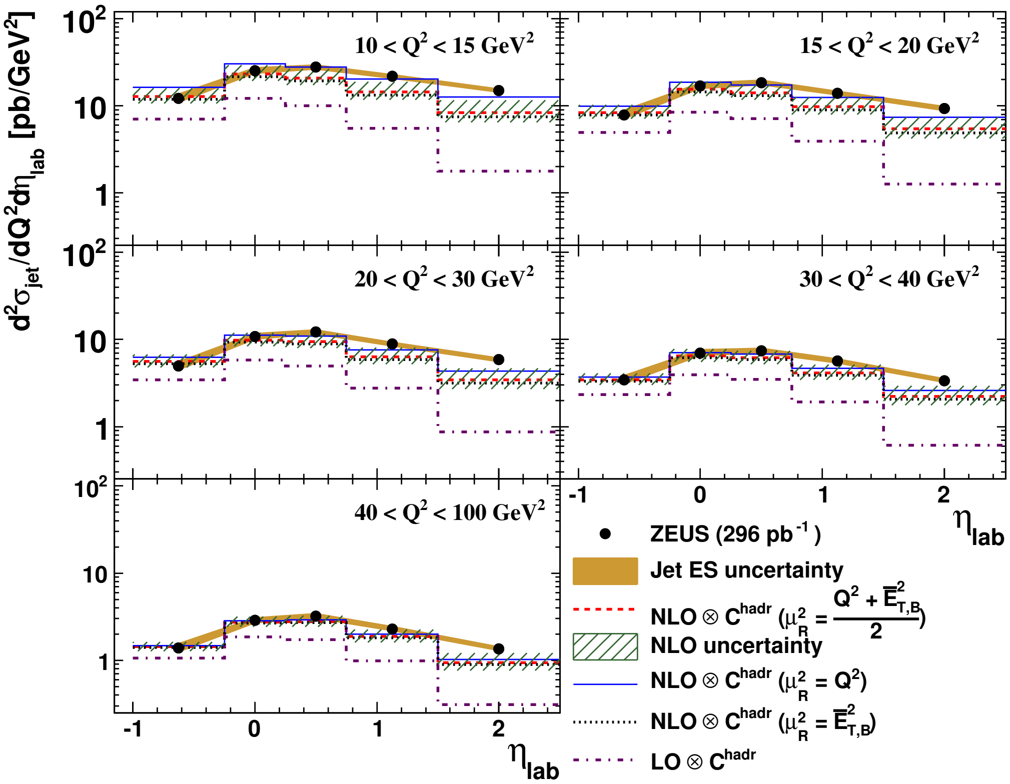

Figure 10.3: Measured double-differential inclusive jet cross-section $d^2\sigma / d\eta_{\mathrm{lab}}\, dQ^2$ compared with NLO QCD predictions. The ratio to the prediction is shown in fig. 10.4. See text and caption to figure 10.1 for details.

Figures 10.3 and 10.4 show the cross-section double-differentially as function of η_{lab} and Q^2 and its ratio to the NLO QCD prediction, respectively. While the measured cross-sections in each η_{lab} bin drop by approximately one order of magnitude over the studied Q^2 range, the shape of the $d\sigma / d\eta_{\mathrm{lab}}$ distribution does not change significantly.

The NLO calculations predict the data best and most precisely in the highest Q^2 region, where, except for the most forward η_{lab} bin, the data are within the theoretical uncertainty and the difference between the predictions at the various studied renormalization scales is almost negligible. In the highest η_{lab} bin, the measured cross-section is

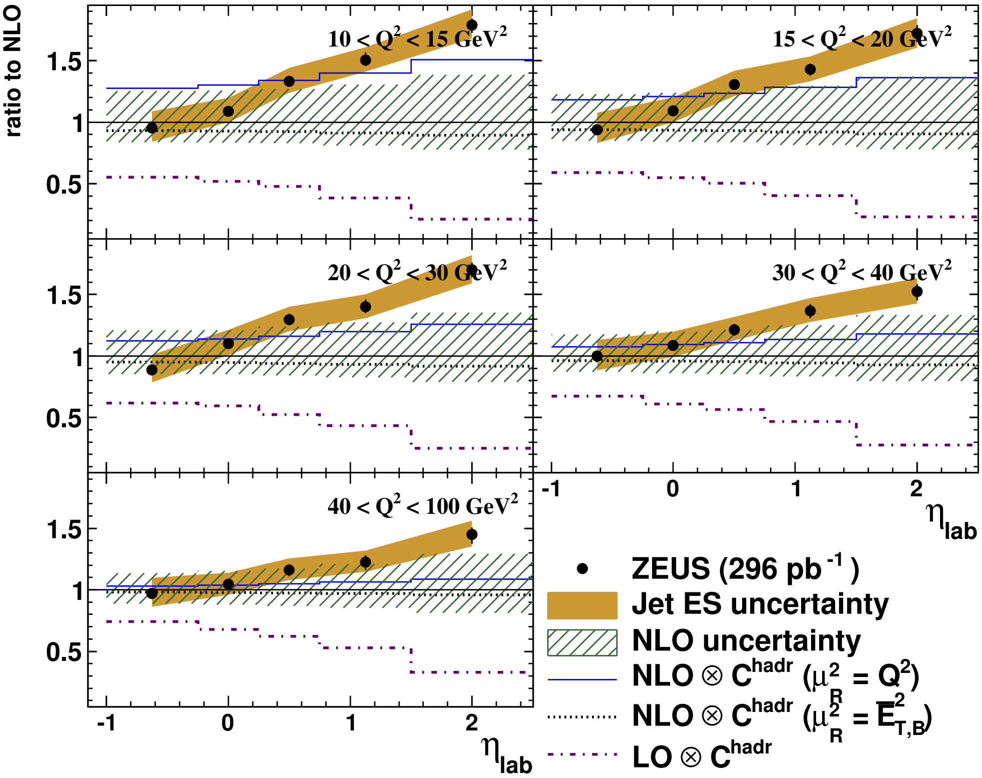

Figure 10.4: Ratio of double-differential cross-section $d^2\sigma / d\eta_{lab}\, dQ^2$ to the NLO QCD predictions. For the cross-sections and details, see fig. 10.3.

still ∼ 50% larger than predicted by the NLO, though.

At lower values of Q^2, the NLO calculation becomes more dependent on the choice of renormalization scale, which affects both normalization and shape of the resulting predictions. This is again most striking in the highest η_{lab} bin, where also the ratio between LO and NLO is largest. Here, the k factor reaches a value of ≈ 5 in the lowest Q^2 region.

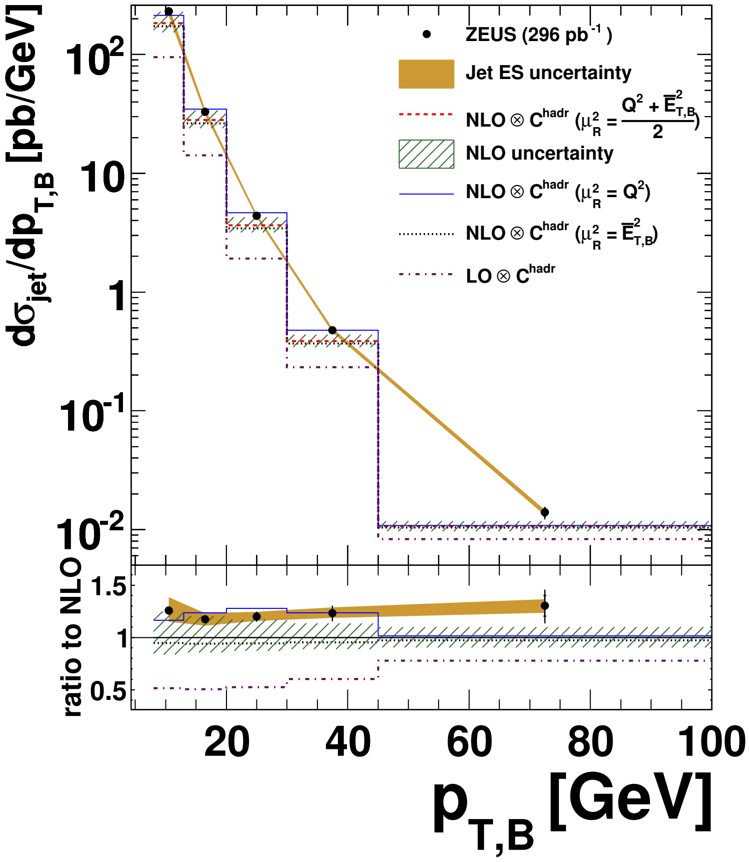

Figure 10.5: Measured inclusive jet cross-section $d\sigma/\,dp_{T,\mathrm{B}}$ compared with NLO QCD predictions. See text and caption to figure 10.1 for details.

Figure 10.5 presents the cross-section as function of $p_{T,\mathrm{B}}$. Over the investigated $p_{T,\mathrm{B}}$ range the cross-section drops by over four orders of magnitude. The NLO calculations predict the shape of the measured cross-section rather well. Even though the absolute values are approximately 25% below the data's, the theoretical prediction still agrees with the measurement within the uncertainties.

At values of $p_{T,\mathrm{B}}$ lower than 45 GeV, the uncertainty on the NLO prediction is significantly larger than that of the data. In this region, the renormalization scale dependence of the calculations is very notable. Also, the k factors exhibit large values of ∼ 2, which are reduced down to ∼ 1.3 toward higher values of $p_{T,\mathrm{B}}$ in conjunction with a decrease of the overall renormalization scale dependence.

In the highest $p_{T,\mathrm{B}}$ bin, the statistical uncertainty on the data becomes significant.

Here, the total statistical and uncorrelated systematic uncertainty dominate the experimental uncertainty over the jet energy scale uncertainty. In this region, the precision of the data is similar to that of the perturbative QCD prediction.

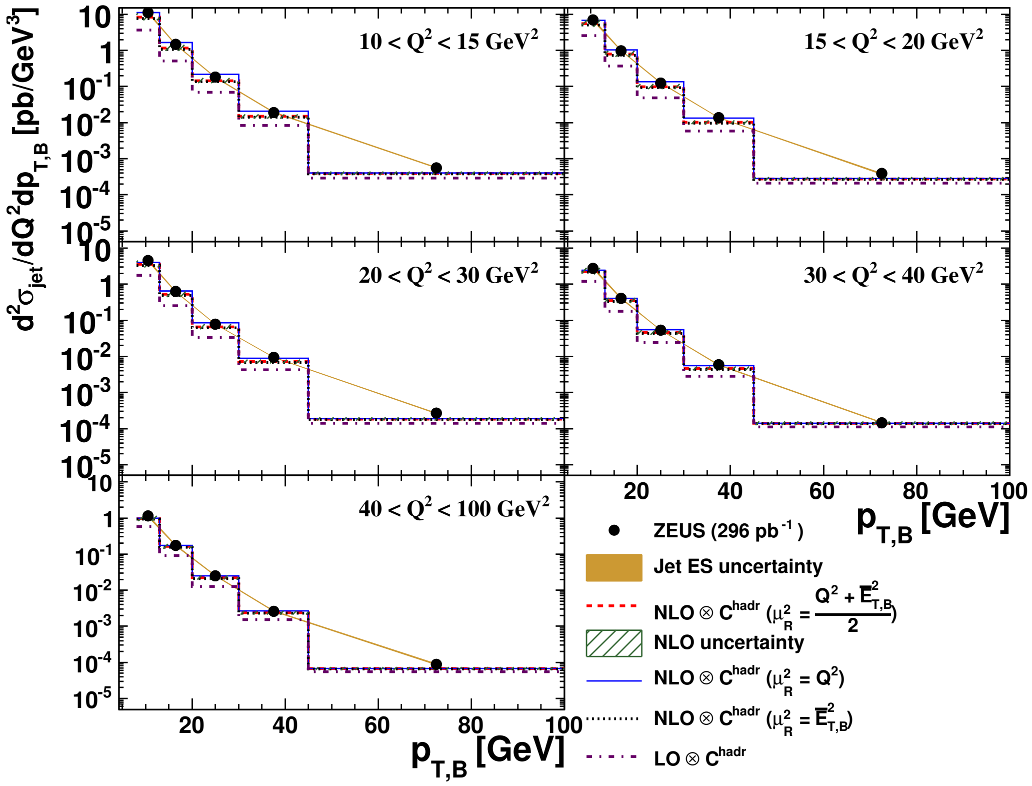

Figure 10.6: Measured double-differential inclusive jet cross-section $d^2\sigma/\,dp_{T,B}\,dQ^2$ compared with NLO QCD predictions. The ratio to the prediction is shown in fig. 10.7. See text and caption to figure 10.1 for details.

The Q^2 dependence of $d\sigma/\,dp_{T,B}$ is investigated in figures 10.6 and 10.7, which present the cross-section double-differentially as function of $p_{T,B}$ and Q^2 and its ratios to the NLO prediction. While the cross-section in the lowest $p_{T,B}$ bin drops over the investigated Q^2 range by one order of magnitude, the decrease in higher $p_{T,B}$ bins is less pronounced, therefore increasing the relative contribution to the cross-section from these bins.

Overall, the NLO calculations correctly predict the measured cross-sections within the uncertainties. The theoretical uncertainty is largest at low values of $p_{T,B}$ and Q^2, where the choice of renormalization scale also has the largest influence on the predictions. Generally, setting the renormalization scale to $\sqrt{Q^2}$ gives a better agreement with the data, with the exception of the region $10 < Q^2 < 15\,\mathrm{GeV}^2$ where the resulting prediction is significantly larger than the measured cross-sections.

The experimental uncertainty on the measurement is typically smaller than that on the perturbative QCD calculation for $p_{T,B}$ values smaller than 30 GeV. At larger

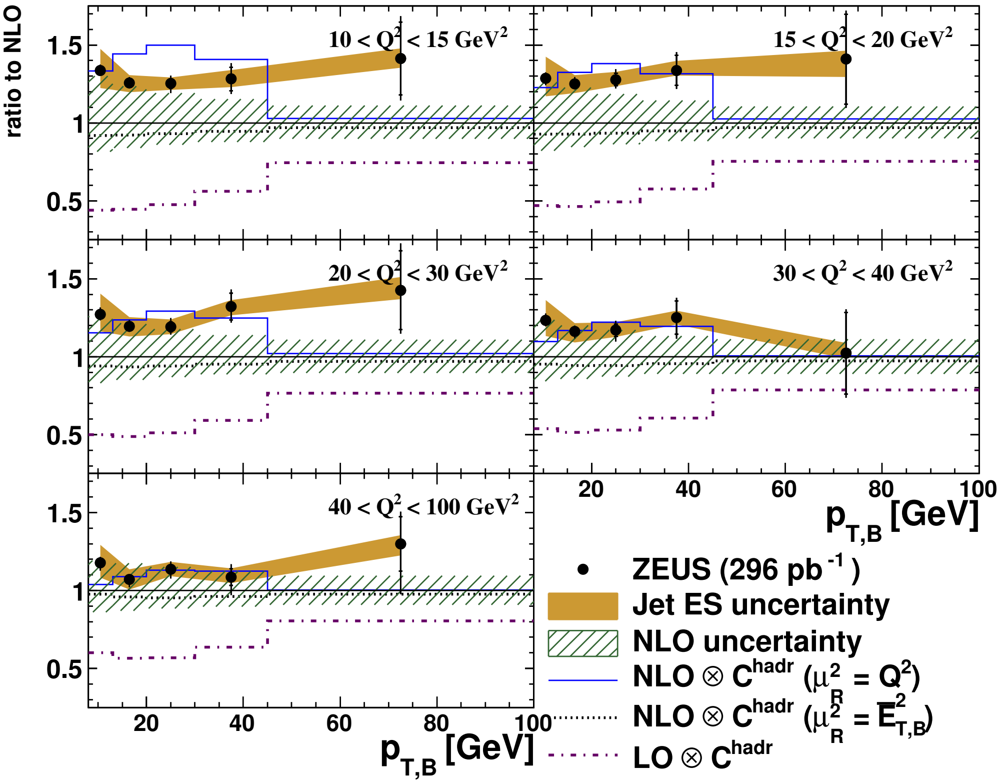

Figure 10.7: Ratio of double-differential cross-section $\mathrm{d}\sigma^2/\,\mathrm{d}p_{T,\mathrm{B}}\,\mathrm{d}Q^2$ to the NLO QCD predictions. For the cross-sections and details, see fig. 10.6.

values of $p_{T,\mathrm{B}}$, the limited statistics of the data sample and of the Monte Carlo sample used in the unfolding become dominant, and are considerably larger than the NLO uncertainty in the highest $p_{T,\mathrm{B}}$ bin.

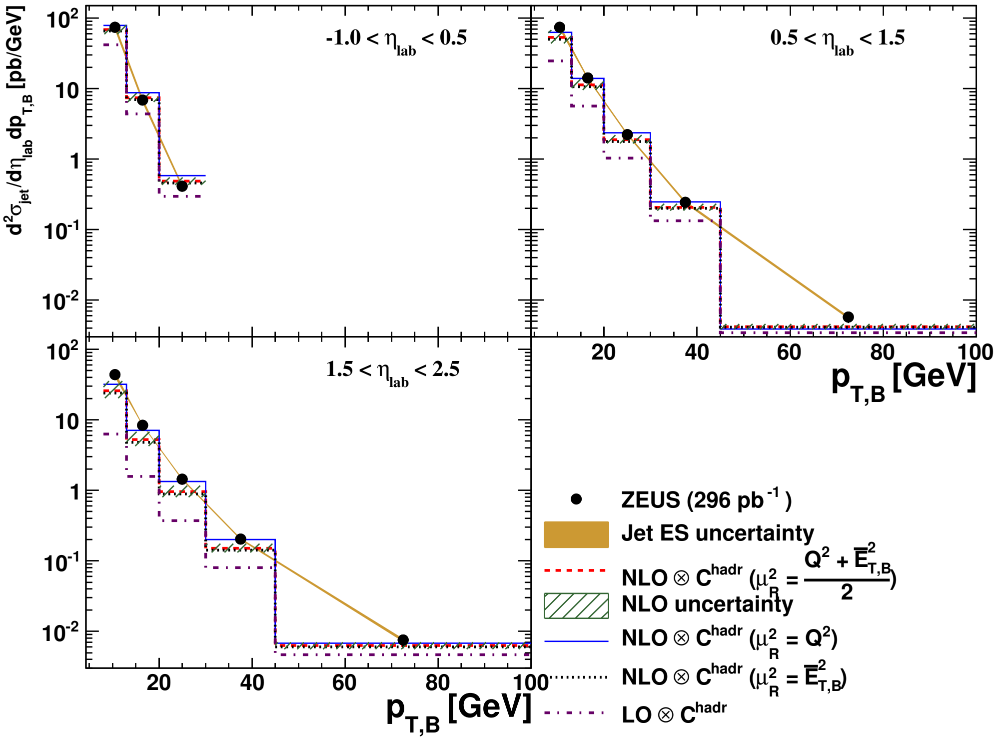

Figure 10.8: Measured double-differential inclusive jet cross-section $d^2\sigma/\,dp_{T,\mathrm{B}}\,d\eta_{\mathrm{lab}}$ compared with NLO QCD predictions. The ratio to the prediction is shown in fig. 10.9. See text and caption to figure 10.1 for details.

The cross-section $d\sigma/\,dp_{T,\mathrm{B}}$ is further studied in figures 10.8 and 10.9, where the cross-section and its ratio to the NLO prediction, respectively, are presented double-differentially as function of $p_{T,\mathrm{B}}$ and η_{lab}. Most notably, the cross-section at low $p_{T,\mathrm{B}}$ decreases toward the forward regions in η_{lab}, while the cross-section of the two highest $p_{T,\mathrm{B}}$ bins increases.

Within the uncertainties, the NLO prediction agrees with the data in the lower two η_{lab} regions, although the data already tend to be above the perturbative QCD calculations in the central region. In the most forward η_{lab} bin, the NLO predicts cross-sections which are at $p_{T,\mathrm{B}} < 30\,\mathrm{GeV}$ more than 50% below the results of the measurement. In this region, the NLO calculations exhibit uncertainties of up to 40% and a strong renormalization scale dependence. This coincides with very large k factor values of up to 4.

The results obtained for the differential and double-differential cross-sections as function of $p_{T,\mathrm{B}}$ can be compared in some regions of Q^2 with previous H1 publications, which studied inclusive jets at low values of Q^2 [6,7]. The observations are generally

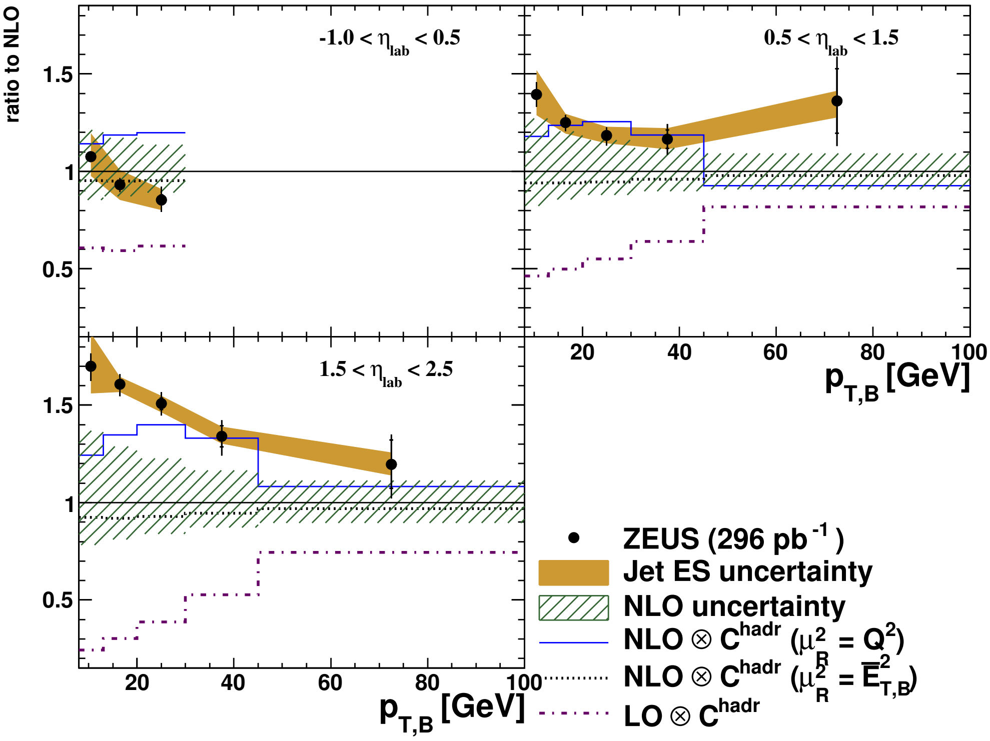

Figure 10.9: Ratio of double-differential cross-section $d^2\,\sigma/\,dp_{T,B}\,d\eta_{lab}$ to the NLO QCD predictions. For the cross-sections and details, see fig. 10.8.

compatible when taking into account differences in phase space and scales used in the calculation of the NLO.

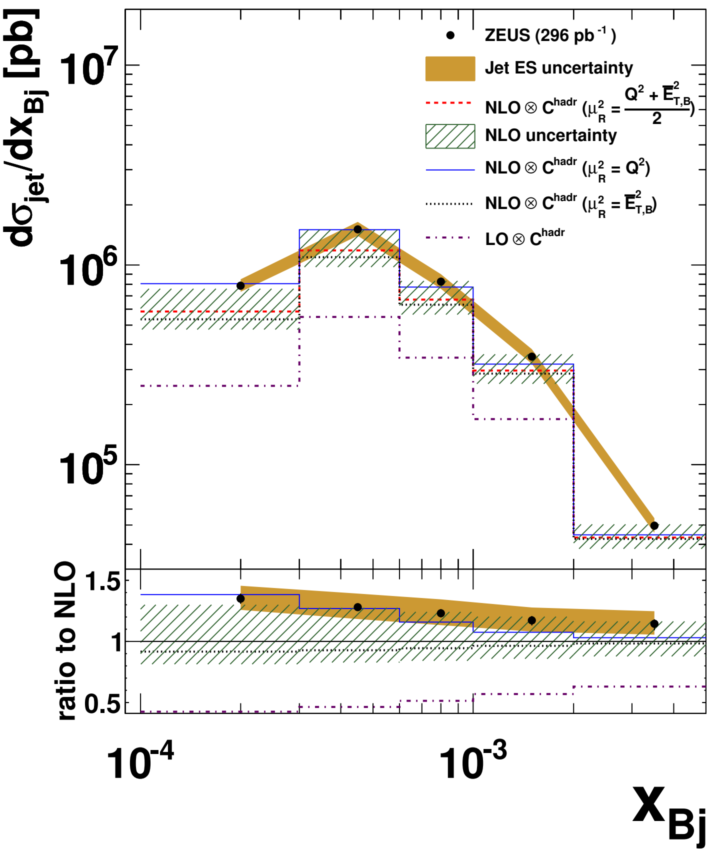

Figure 10.10: Measured inclusive jet cross-section $d\sigma/\,dx_{Bj}$ compared with NLO QCD predictions. See text and caption to figure 10.1 for details.

Finally, figure 10.10 presents the cross-section measured with respect to x_{Bj}. The measurement extends down to values of $x_{Bj} = 10^{-4}$ and up to $x_{Bj} = 5 \cdot 10^{-3}$. The cross-section peaks around $x_{Bj} \approx 5 \cdot 10^{-4}$. At low values of x_{Bj} the cross-section is expected to rise due to the increase of the gluon density[5]; however, this is suppressed by the transverse momentum requirements imposed on the jets together with the lower Q^2 cut.

Within the uncertainties, the NLO prediction describes the measurement, although the data tend to be above the theory. At low x_{Bj} the NLO calculation exhibits large uncertainties and a strong renormalization scale dependence. Also in this region, the data favor a softer renormalization scale.

Figures 10.11 and 10.12 investigate the Q^2 dependence of the cross-section $d\sigma/\,dx_{Bj}$ by presenting the cross-section and its ratio to the NLO prediction, respectively, double-differentially as function of x_{Bj} and Q^2.

---

[5] See for example figure 2.5 in chapter 2.2.2, showing the parton density functions for $Q^2 = 10\,\mathrm{GeV}^2$.

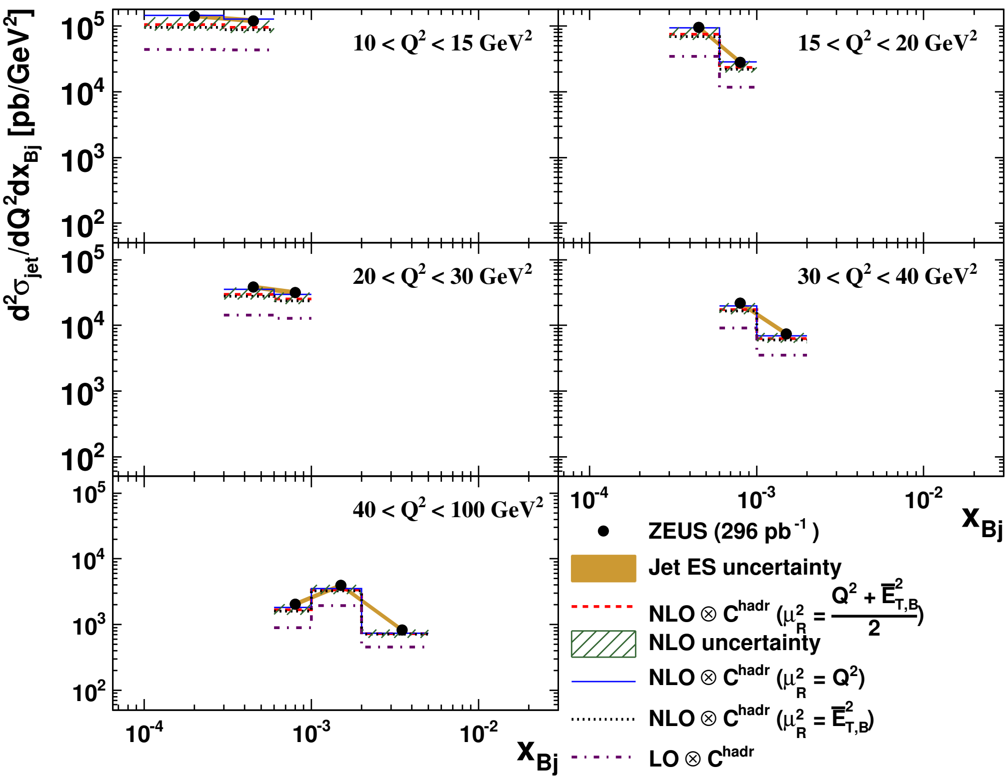

Figure 10.11: Measured double-differential inclusive jet cross-section $d^2\sigma/ dx_{Bj}\, dQ^2$ compared with NLO QCD predictions. The ratio to the prediction is shown in fig. 10.12. See text and caption to figure 10.1 for details.

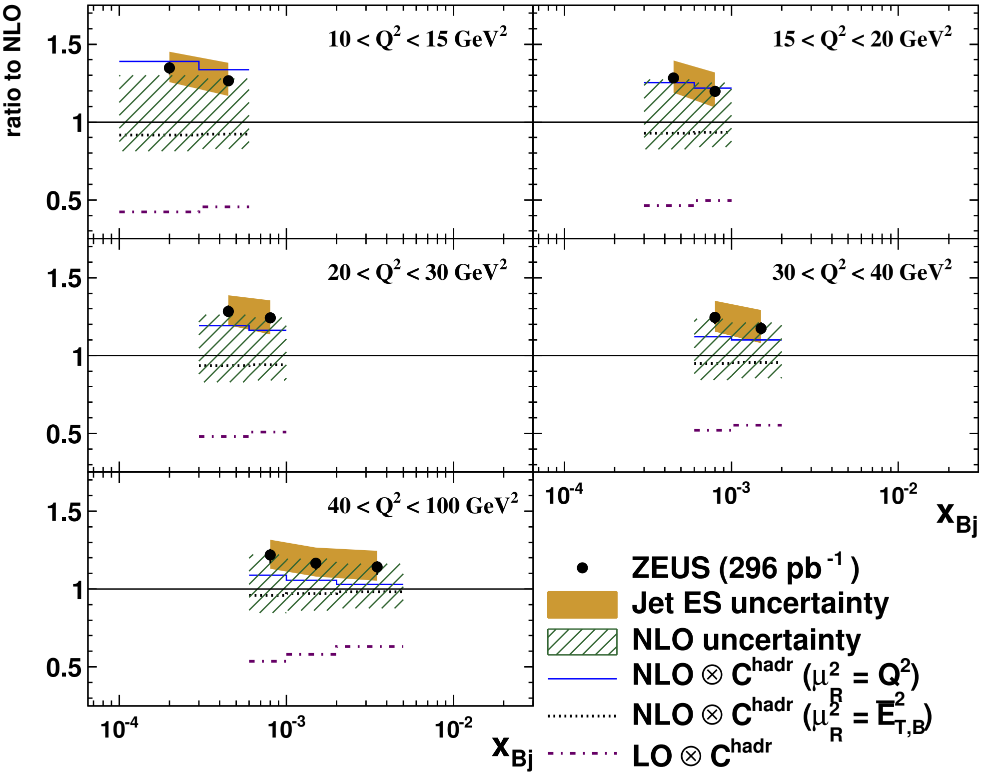

Figure 10.12: Ratio of double-differential cross-section $\mathrm{d}^2\sigma/\,\mathrm{d}x_{\mathrm{Bj}}\,\mathrm{d}Q^2$ to the NLO QCD predictions. For the cross-sections and details, see fig. 10.11.

As x_{Bj} and Q^2 are directly proportional for a given value of y, the cross-section as function of x_{Bj} strongly depends on the Q^2 region. The lowest x_{Bj} bin was only measurable in the region $10 < Q^2 < 15\,\mathrm{GeV}^2$ while the highest x_{Bj} bin was only accessible at the highest Q^2 values.

Overall, the NLO calculation describes the data within the uncertainties but predicts somewhat lower values than measured. Using a softer renormalization scale at $\mu_R^2 = Q^2$ matches the data more accurately, especially at low Q^2 and low x values. In this region, the theoretical uncertainties are much larger than that of the data.

10.3. Dijet Cross Sections

In this section, cross-sections measured in inclusive dijet production are presented.

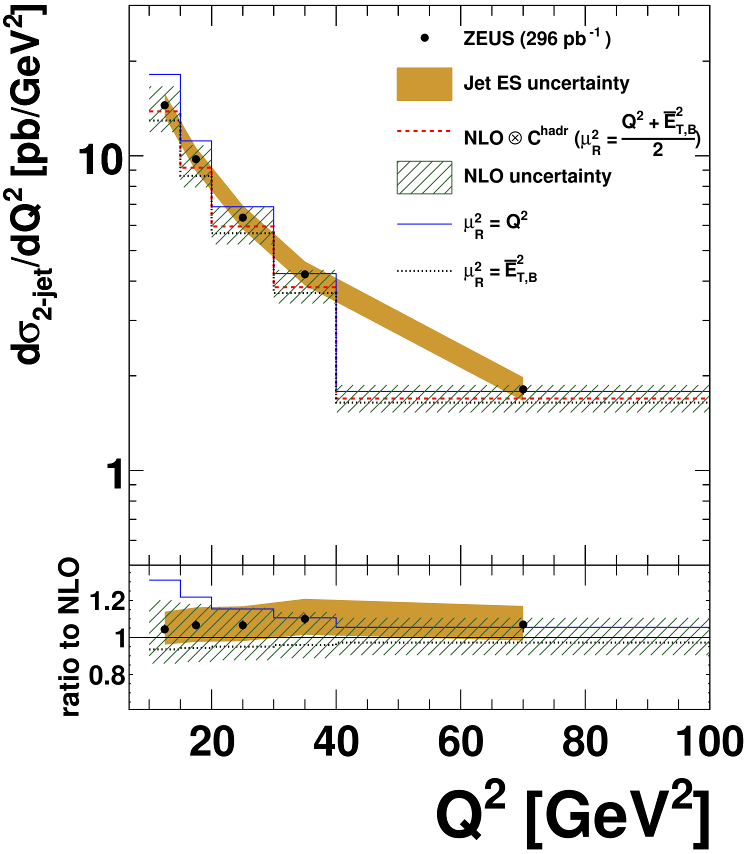

Figure 10.13: Measured inclusive dijet cross-section $d\sigma/\,dQ^2$ compared with NLO QCD predictions. See text and caption to figure 10.1 for details.

Figure 10.13 shows the cross-section as function of Q^2. Over the range investigated, the cross-section falls by approximately one order of magnitude. Since the definition of the cross-sections for *dijet* production differs[6] from that of the cross-sections for

---

[6] In the cross-sections for inclusive jet production each jet is counted toward the cross-sections, instead

inclusive jet production, the absolute cross-section values cannot be compared directly; but with respect to the shape, the cross-section as function of Q^2 for inclusive jet production exhibits a slightly steeper slope. This is the result of the additional transverse momentum requirements imposed on the dijet sample, since jets with high $p_{T,\mathrm{B}}$ become more prevalent at higher values of Q^2.

The NLO calculations describe the data well over the full investigated Q^2 range. The theoretical uncertainty is of similar magnitude as the experimental uncertainty, except for the lowest Q^2 bins, where the NLO uncertainty dominates. In this region, the prediction at the softer renormalization scale, $\mu_R^2 = Q^2$, deviates over 30% from the other predictions. The harder scale, $\mu_R^2 = \bar{E}_{T,\mathrm{B}}^2$, on the other hand only differs by $\sim 5\%$.

The theoretical uncertainty is generally smaller by 5 – 10% compared to the respective cross-section for inclusive jet production, while the experimental uncertainty is of similar magnitude. This is again a consequence of the additional transverse jet momentum and invariant mass requirements imposed on the dijet sample, suppressing softer processes.

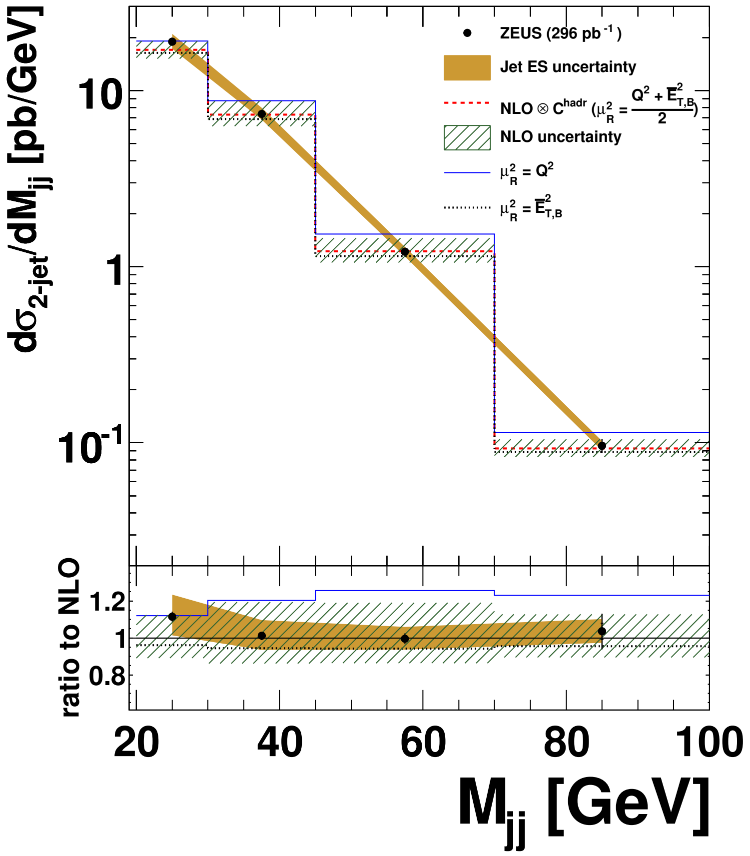

Figure 10.14: Measured inclusive dijet cross-section $d\sigma/\,dM_{jj}$ compared with NLO QCD predictions. See text and caption to figure 10.1 for details.

---

of only each dijet (trijet) event as for the inclusive dijet (trijet) cross-sections.

Figure 10.14 presents the cross-section as function of M_{jj} for inclusive dijet production. The cross-section extends to M_{jj} values of up to 100 GeV while decreasing over one order of magnitude.

The NLO prediction agrees well with the data. The theoretical uncertainty is significantly larger than the experimental uncertainty in the region of $30 < M_{jj} < 70\,\text{GeV}$ and of similar magnitude otherwise. Using $\mu_R^2 = Q^2$ the prediction differs by more than 20% from the central NLO calculation for $M_{jj} > 30\,\text{GeV}$ and is clearly disfavored by the data.

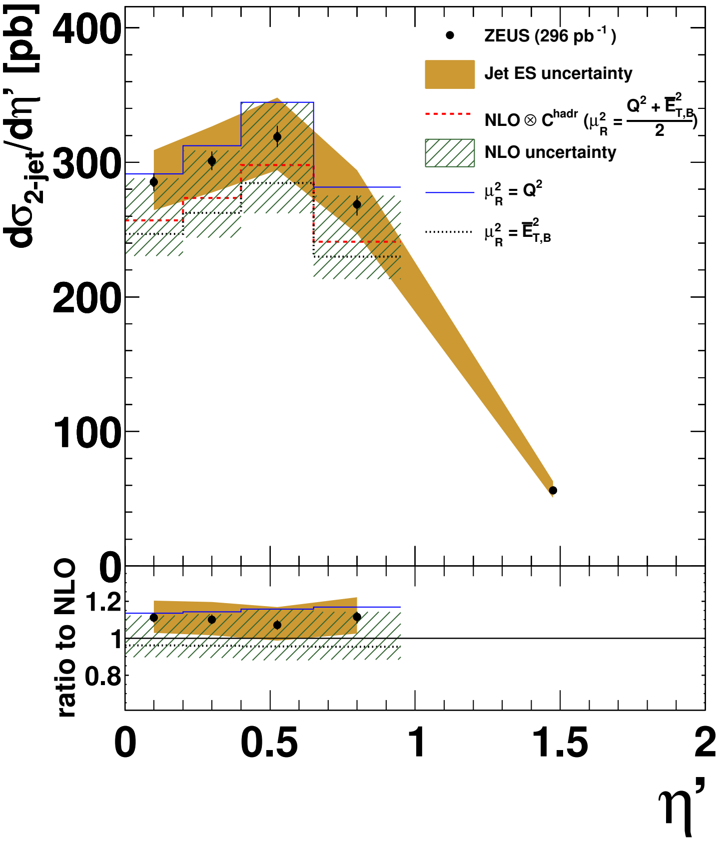

Figure 10.15: Measured inclusive dijet cross-section $d\sigma/\,d\eta'$ compared with NLO QCD predictions. No predictions are shown for the highest bin in η' due to the sensitivity of the NLO to infrared cut-offs in this region, as discussed in chapter 4.2. See text and caption to figure 10.1 for details.

Figure 10.15 presents the cross-section as function of the absolute difference in pseudorapidity between the dijets in the Breit frame, η'. The cross-section peaks around $\eta' \approx 0.5$ and drops by a factor of ~ 6 toward the highest η' bin. For the latter bin, no predictions are shown due to the sensitivity of the NLO results to infrared cut-offs in this region, as discussed in chapter 4.2.

In the remaining η' bins, the data agree well with the NLO prediction. The relative theoretical uncertainty remains nearly constant over the η' range and is larger than that of the data.

For the cross-section as function of η', the choice of renormalization scale mainly affects the normalization of the prediction.

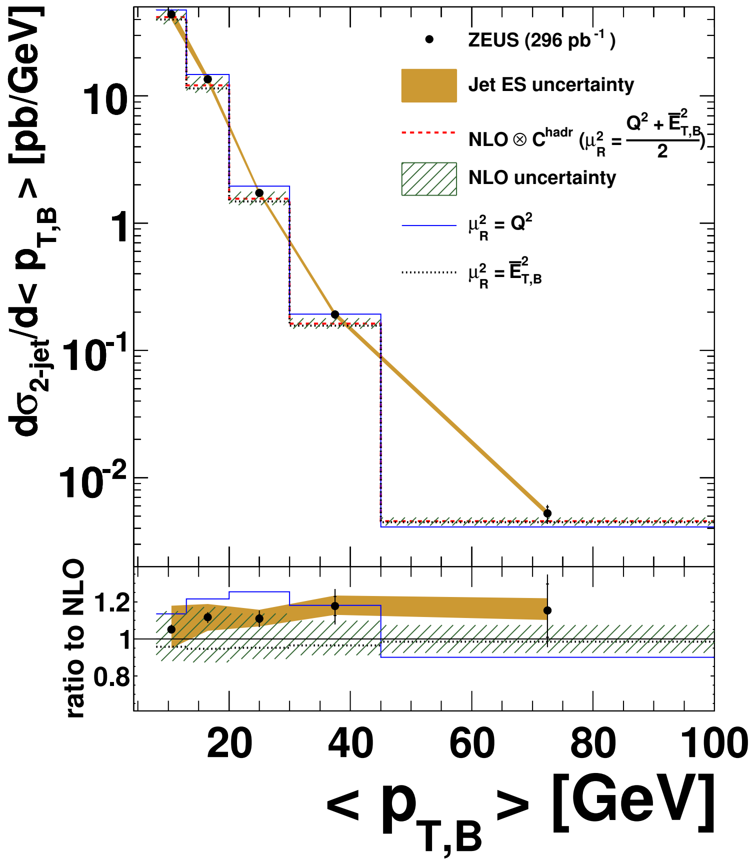

Figure 10.16: Measured inclusive dijet cross-section $d\sigma/\,d\langle p_{T,B}\rangle$ compared with NLO QCD predictions. See text and caption to figure 10.1 for details.

The cross-section as function of $\langle p_{T,B}\rangle$ is shown in figure 10.16. The cross-section extends to values of $\langle p_{T,B}\rangle$ of up to 100 GeV toward which it drops by almost four orders of magnitude.

The data are well described the NLO predictions over the full $\langle p_{T,B}\rangle$ range. The theoretical prediction is associated with an uncertainty of typically between 10 and 15% and exhibits the largest renormalization scale dependence in the region of $13 < \langle p_{T,B}\rangle < 45$ GeV.

The experimental uncertainty is largest at high values of $\langle p_{T,B}\rangle$ (dominated by statistical uncertainties) and in the lowest $\langle p_{T,B}\rangle$ bin (dominated by the uncertainty on the hadronic jet energy scale). In the region of $13 < \langle p_{T,B}\rangle < 30$ GeV the experimental uncertainty is significantly smaller than the theoretical uncertainty.

The Q^2 dependence of the cross-section as function of $\langle p_{T,B}\rangle$ is investigated in figures 10.17 and 10.18 presenting the double-differential cross-section $d^2\,\sigma/\,d\langle p_{T,B}\rangle Q^2$ and its ratio to the NLO prediction, respectively. The cross-section distributions do not

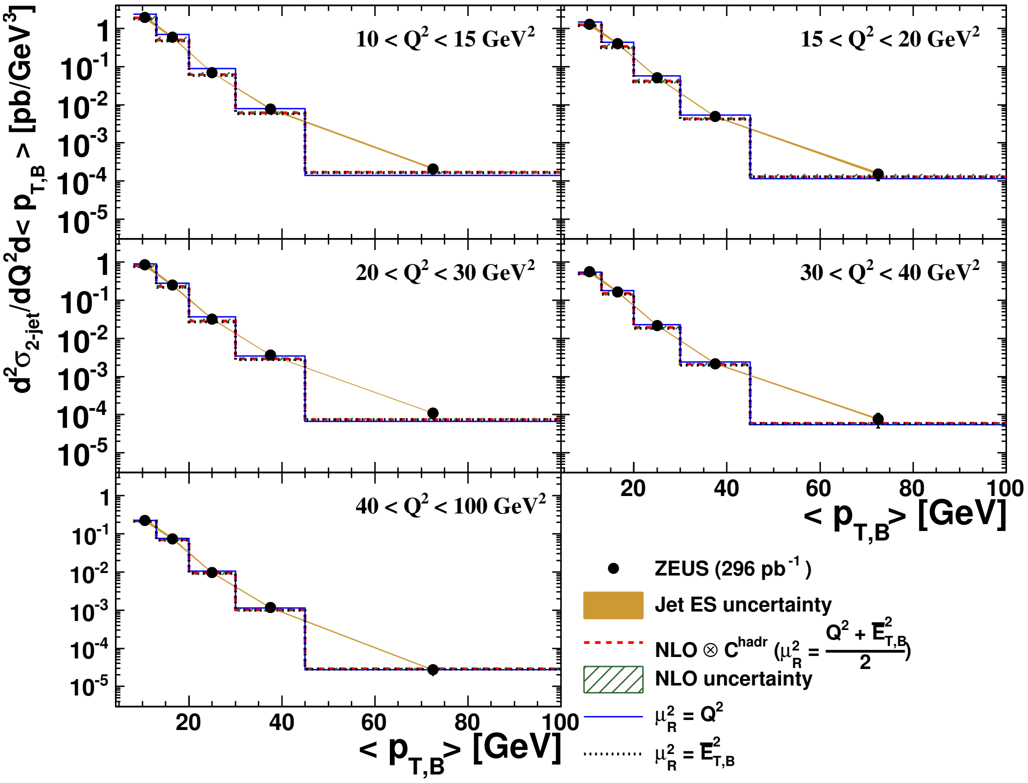

Figure 10.17: Measured double-differential inclusive dijet cross-section $\mathrm{d}^2\sigma/\,\mathrm{d}\langle p_{T,\mathrm{B}}\rangle\,\mathrm{d}Q^2$ compared with NLO QCD predictions. The ratio to the prediction is shown in fig. 10.18. See text and caption to figure 10.1 for details.

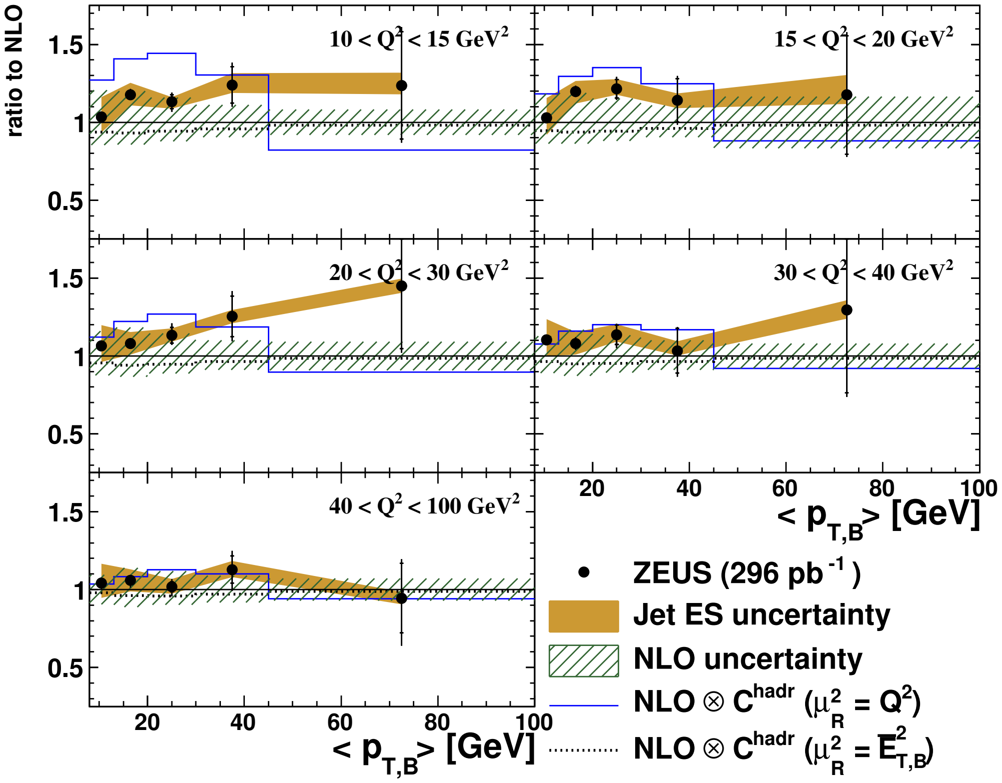

Figure 10.18: Ratio of double-differential inclusive dijet cross-section $d^2\sigma / d\langle p_{T,B}\rangle \, dQ^2$ to the NLO QCD predictions. For the cross-sections and details, see fig. 10.17.

change significantly in shape over the studied Q^2 range, except for a slight decrease in slope with higher values of Q^2.

The NLO calculations predict the measured cross-sections over the full $\langle p_{T,\mathrm{B}} \rangle$ spectrum in all investigated regions of Q^2.

The theoretical uncertainty is typically of the order of 10% and only increases to $\sim$ 20% at the lower regions of Q^2. At low values of both Q^2 and $\langle p_{T,\mathrm{B}} \rangle$ the NLO calculation exhibits the largest dependence on the renormalization scale. The fact, that the calculations at $\mu_R^2 = Q^2$ deviate from the central predictions significantly beyond the range given by the theoretical uncertainty, suggests that the uncertainty on the choice of renormalization scale is underestimated in this region.

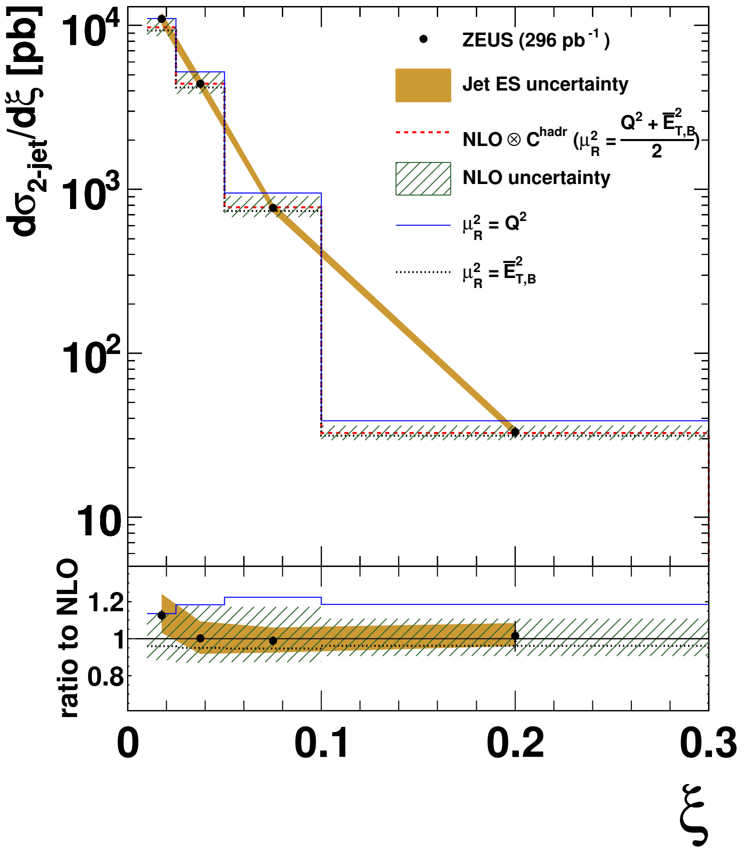

Figure 10.19: Measured inclusive dijet cross-section $d\sigma/\,d\xi$ compared with NLO QCD predictions. See text and caption to figure 10.1 for details.

In figure 10.19, the cross-section as function of ξ is presented. The cross-section distribution drops over two orders of magnitude over the investigated ξ range. In all bins, the data are well described by the NLO prediction.

Except for the highest bin in ξ, the experimental uncertainty is smaller than that of the theoretical prediction. Generally, the data disfavor the renormalization scale of $\sqrt{Q^2}$.

The dependence of the cross-section $d\sigma/\,d\xi$ on Q^2 is investigated in more detail in

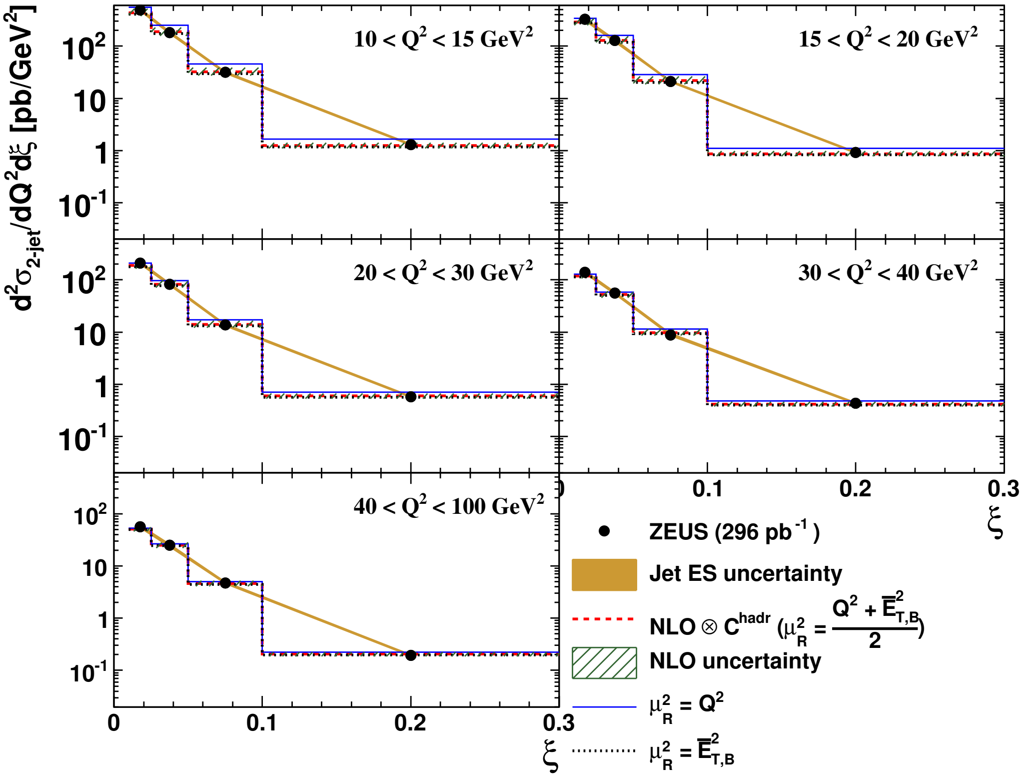

Figure 10.20: Measured double-differential inclusive dijet cross-section $d^2\sigma/d\xi\,dQ^2$ compared with NLO QCD predictions. The ratio to the prediction is shown in fig. 10.21. See text and caption to figure 10.1 for details.

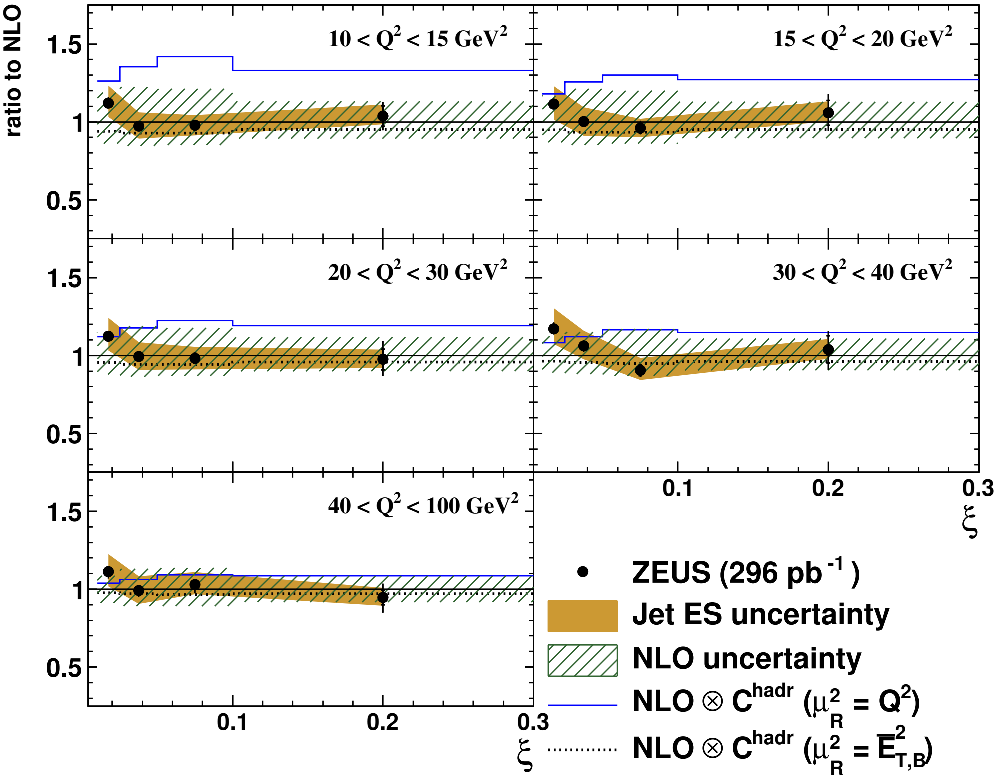

Figure 10.21: Ratio of double-differential inclusive dijet cross-section $d^2\sigma/\,d\xi\,dQ^2$ to the NLO QCD predictions. For the cross-sections and details, see fig. 10.20.

figures 10.20 and 10.21, presenting in different the double-differential cross-section as function of ξ and Q^2 and its ratio to the NLO prediction, respectively. Overall, the shapes of the cross-section distributions do not change significantly with increasing Q^2 values, although the slopes become slightly less steep.

The NLO calculations correctly predict the measured cross-sections within the uncertainties over the full Q^2 and ξ ranges. In the region of $Q^2 < 40\,\mathrm{GeV}^2$ the experimental uncertainties are typically smaller than the theoretical uncertainties with the exception of the highest ξ bin, where the statistical uncertainty on the data become significant.

Similarly to the previous observations, the NLO calculations at different renormalization scales show the largest deviations at low Q^2, where the differences are again not fully covered by the theoretical uncertainty.

10.4. Trijet Cross Sections

In this section, the cross-sections measured in inclusive trijet production are presented.

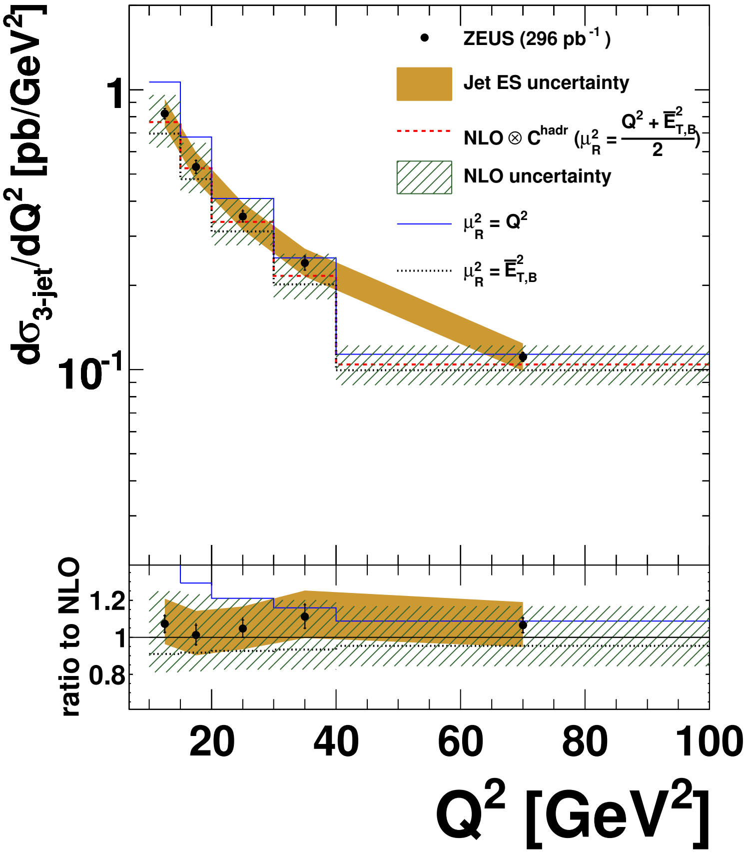

Figure 10.22: Measured inclusive trijet cross-section $\mathrm{d}\sigma/\,\mathrm{d}Q^2$ compared with NLO QCD predictions. See text and caption to figure 10.1 for details.

Figure 10.22 shows the cross-section $\mathrm{d}\sigma/\,\mathrm{d}Q^2$. Over the investigated Q^2 range the cross-section falls by almost one order of magnitude. Compared to the cross-section measured in inclusive dijet production, the trijet cross-section is reduced by more than one order of magnitude.

The NLO prediction describes the data well for all studied values of Q^2. The theoretical uncertainty is in the order of 20% and thus in all bins larger than the experimental uncertainty. The choice of renormalization scale most strongly affects the low-Q^2 region. Here, the softer scale choice of $\sqrt{Q^2}$ leads to $\sim$ 40% larger cross-section predictions and does not give a good description of the data.

The experimental uncertainty, on the other hand, is dominated by the jet energy scale uncertainty which is typically of the order of ±12% and therefore $\sim$ 3% larger than observed for the dijet cross-section.

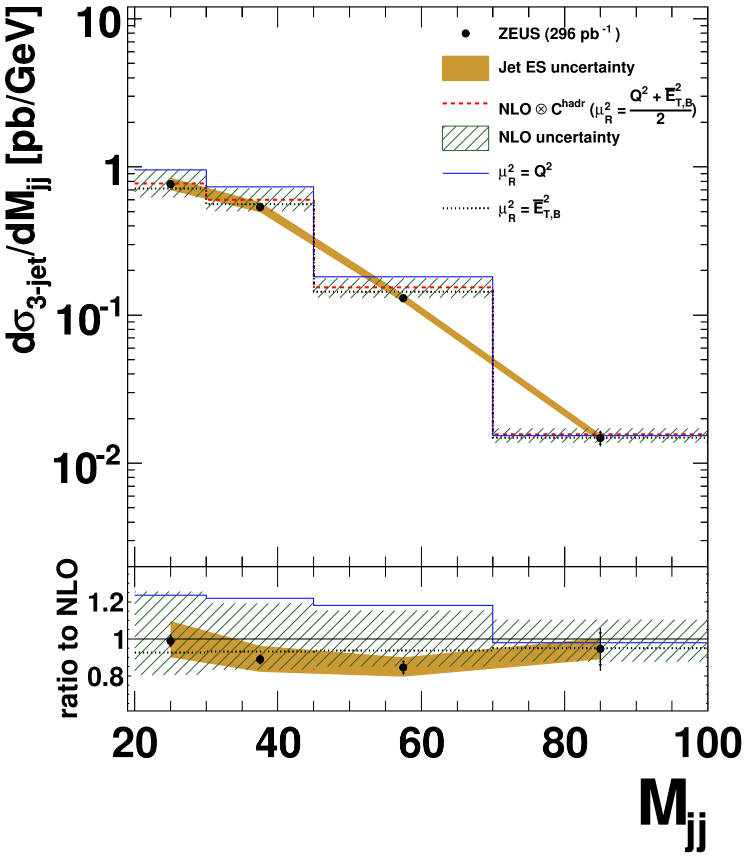

Figure 10.23: Measured inclusive trijet cross-section $d\sigma/\,dM_{jj}$ compared with NLO QCD predictions. See text and caption to figure 10.1 for details.

The cross-section as function of M_{jj} is presented in figure 10.23. The cross-section drops by almost two orders of magnitude over the measured M_{jj} range, but the distribution exhibits a less steep slope compared to the cross-section measured in inclusive dijet production.

The NLO calculations give a good prediction of the measured data. Except for the highest M_{jj} bin, where the statistical uncertainty of the measurement dominates, the theoretical uncertainty is significantly larger than the experimental uncertainty. As previously observed for other trijet cross-sections, the data are better described by the predictions at the harder renormalization scales.

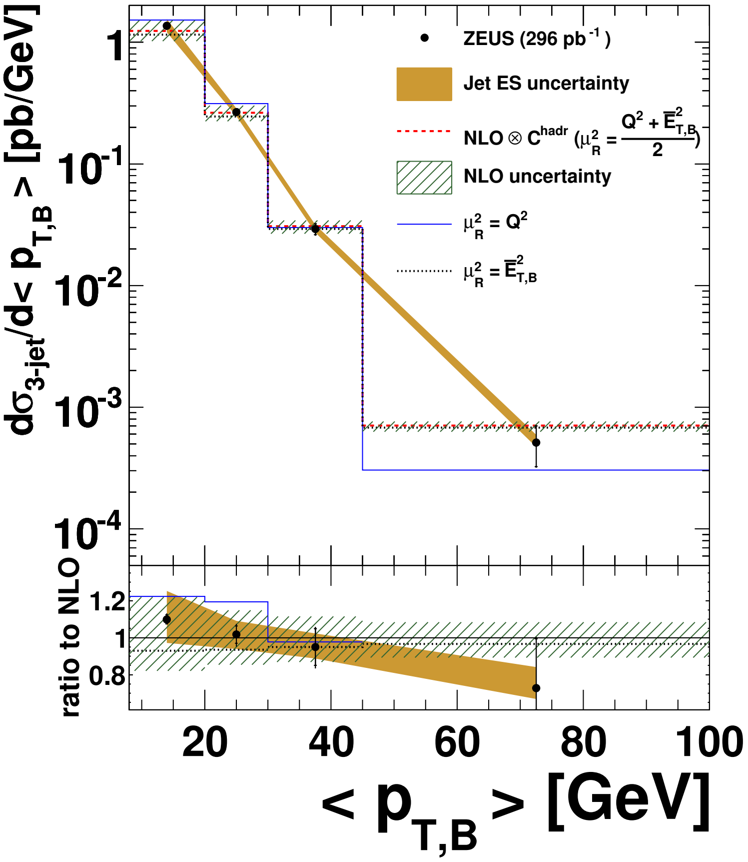

Figure 10.24: Measured inclusive trijet cross-section $d\sigma/\, d\langle p_{T,\mathrm{B}}\rangle$ compared with NLO QCD predictions. See text and caption to figure 10.1 for details.

In figure 10.24, the cross-section as function of $\langle p_{T,\mathrm{B}}\rangle$ is presented. The measurement extends to high values of $\langle p_{T,\mathrm{B}}\rangle$ of up to 100 GeV and toward these drops over three orders of magnitude.

The experimental uncertainty is dominated by the statistical uncertainty at $\langle p_{T,\mathrm{B}}\rangle >$ 30 GeV and by the large jet energy scale uncertainty of $^{+14.5\%}_{-11.0\%}$ at lower values of $\langle p_{T,\mathrm{B}}\rangle$. However, for the lower two $\langle p_{T,\mathrm{B}}\rangle$ bins, the theoretical uncertainty is still larger at $\sim \pm 20\%$.

Within these uncertainties, the NLO calculations describe the data.

Figures 10.25 and 10.26 present the double-differential cross-section as function of $\langle p_{T,\mathrm{B}}\rangle$ and Q^2 and its ratio to the NLO prediction, respectively.

In all but the lowest $\langle p_{T,\mathrm{B}}\rangle$ bin, the uncertainty on the data is dominated by the statistical uncertainty. However, for $\langle p_{T,\mathrm{B}}\rangle < 30$ GeV the uncertainty of the measurement is typically smaller than that on the theory. Within the uncertainties, the NLO calculation predicts the measured cross-sections well.

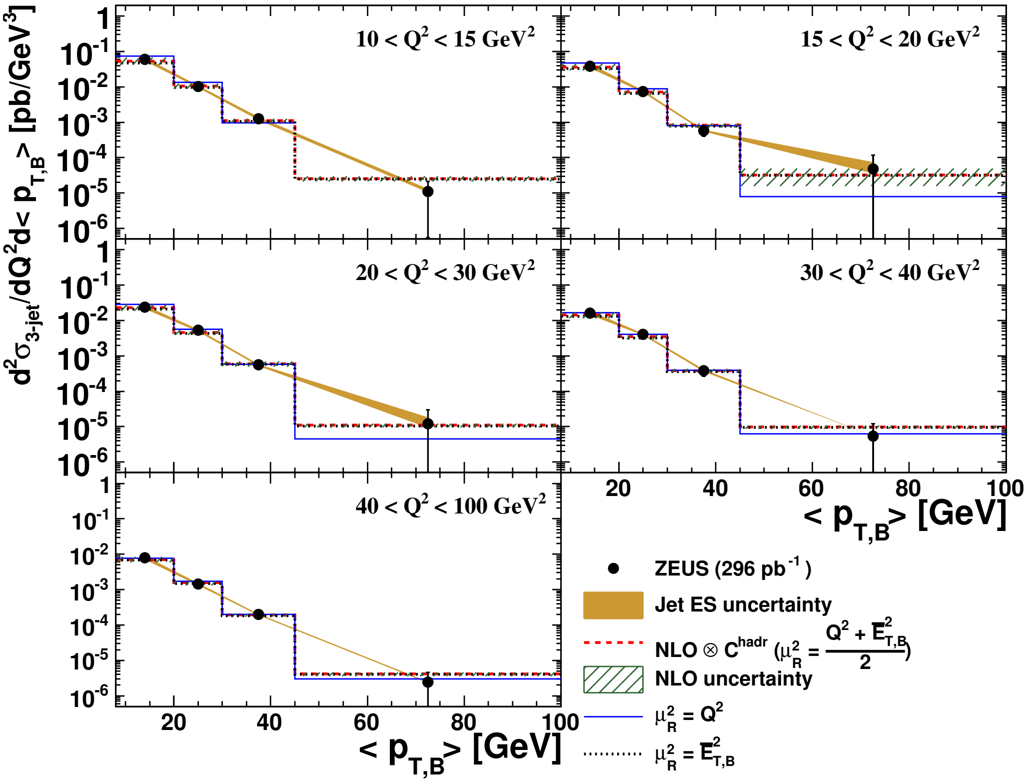

Figure 10.25: Measured double-differential inclusive trijet cross-section $d^2\sigma / d\langle p_{T,B}\rangle \, dQ^2$ compared with NLO QCD predictions. The ratio to the prediction is shown in fig. 10.26. See text and caption to figure 10.1 for details.

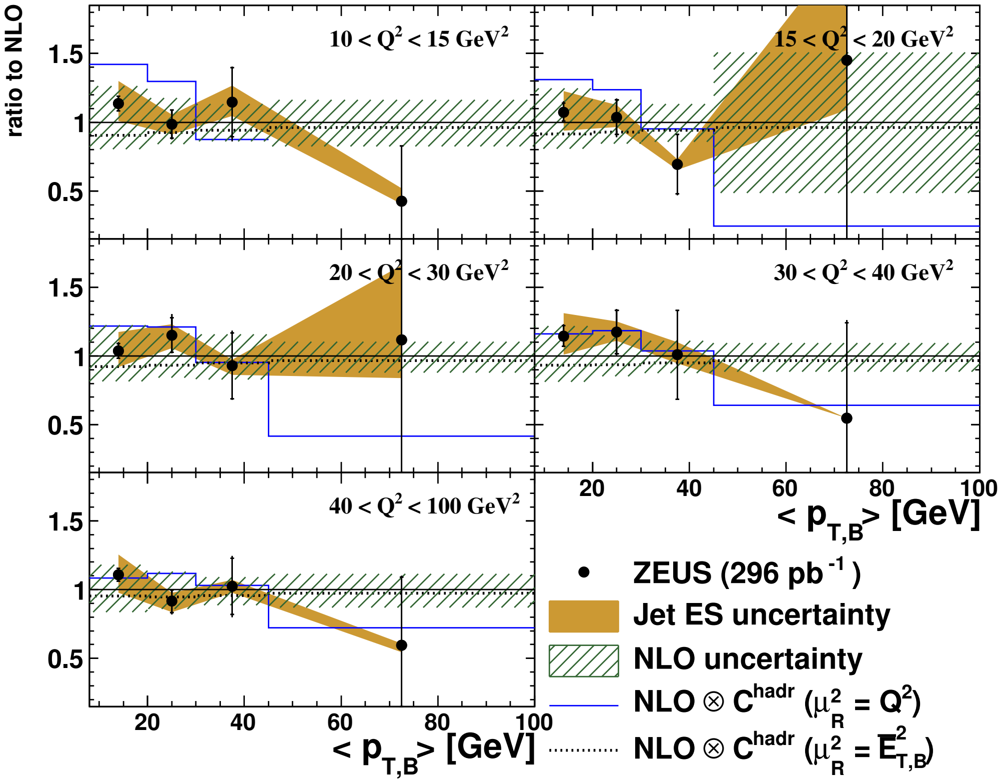

Figure 10.26: Ratio of double-differential inclusive trijet cross-section $d^2\sigma / d\langle p_{T,B}\rangle \, dQ^2$ to the NLO QCD predictions. For the cross-sections and details, see fig. 10.25.

10.5. H1 and ZEUS Combination Activities

In recent years, both the H1 and the Zeus collaborations together published several measurements that exploited the *ep* data samples of both experiments [41, 171, 172]. This section summarizes these combination activities and describes the strategy that was chosen for the future combination of this analysis and the corresponding H1 measurement.

Generally, combinations of H1 and Zeus results allow more accurate measurements with higher statistics, and, due to the different detectors and reconstruction methods, also the possible reduction of systematic uncertainties. Furthermore, they provide the opportunity for a model-independent check of the data consistency.

The method used so far for the combination of the cross-sections is an averaging procedure based on a χ^2 minimization, introduced in [173, 174], that takes statistical uncertainties as well as correlated and uncorrelated systematic uncertainties into account.

The combination can become more complicated if the cross-sections were not measured in identical phase space regions within compatible binning, requiring e.g. the extrapolation to a common phase-space grid [41] and thus the introduction of further theoretical uncertainties.

To avoid such difficulties in the future combination of the results presented in this analysis with their corresponding H1 measurements, a common phase space, the observables to be measured, and a suitable cross-section binning were defined early on in the analysis. This applies so far to all single-differential cross-sections shown in the previous sections of this chapter (and will possibly also include the cross-sections in regions of Q^2).

The combination of the H1 and Zeus low-Q^2 jet measurements will therefore be simplified and will require neither modifications of the analyses nor large phase-space extrapolations.

11. Summary and Conclusions

At HERA, jet cross-sections have been measured for many years, and have been used e.g. to extract values of α_s [4–9] or as input to NLO QCD fits to determine the proton PDFs [10], where they had a significant impact on the uncertainty on the gluon contribution. Furthermore, the sensitivity of the jet data to the hard QCD process has been used for stringent tests of perturbative QCD predictions in many regions of phase space.

Typically, in neutral current (NC) deep inelastic scattering (DIS) with high four-momentum transfers[1] the measured jet cross-sections were found to be accurately predicted by next-to-leading (NLO) calculations [11, 122].

The region of low virtualities on the other hand, which is especially interesting as input to QCD PDF fits due to its sensitivity to the gluon density [11], proves to be more complicated. In this region, the NLO calculations show a strong dependence on the choice of the renormalization scale [4, 6, 7, 12], which is commonly associated with a physical hard scale such as the virtuality, the invariant mass, or the transverse energy of jets. The fact, that a priori no preferred scale can be discerned, and the typical "softness" of the physical scales, result in large theoretical uncertainties in the kinematic region of low virtualities.

Within the uncertainties, the NLO prediction has been found to describe the data [6, 7]. However, in specific regions of phase space, previous studies showed considerable deviations, especially for jets toward the proton beam direction [6, 168, 169] and in observables of angular jet correlations [12, 175].

In this work, jet cross-sections were measured for inclusive jet, inclusive dijet, and inclusive trijet production at low virtualities in the range of $10 < Q^2 < 100\,\mathrm{GeV}^2$.

The data analyzed were recorded with the ZEUS detector in the years 2004 – 2007 corresponding to an integrated luminosity of $296\,\mathrm{pb}^{-1}$. The presented analysis is the first jet analysis at such low values of Q^2 to exploit the full HERA-II ZEUS data set, and as such is performed at significant higher luminosities than previous publications [7, 12].

Events in neutral current DIS were selected in the above stated Q^2 region for an inelasticity of $0.2 < y < 0.6$. The jets were reconstructed in the Breit frame, where the virtual boson and the proton collide head on. The jets were required to carry a transverse momentum in the Breit frame of $p_{T,\mathrm{B}} > 8\,\mathrm{GeV}$ and to have a pseudorapidity in the laboratory frame in the range of $-1 < \eta_{\mathrm{lab}} < 2.5$. For the dijet and trijet samples, an additional requirement was imposed on the invariant dijet mass of $M_{jj} > 20\,\mathrm{GeV}$ to avoid phase space regions where the fixed order calculations are sensitive to infrared divergences.

---

[1] At HERA, *high* (*low*) typically refers to virtualities of the exchanged boson above (below) values of $Q^2 \approx 100\,\mathrm{GeV}^2$.

With fewer imposed phase-space requirements, the cross-sections for inclusive jet production are measured in an extended phase space compared to the dijet and trijet samples. They were presented as function of Q^2, and single-differentially as well as double-differentially in regions of Q^2 as function of the Bjorken scaling variable (x_{Bj}), $p_{T,\mathrm{B}}$, and η_{lab}.

Overall, the NLO calculations correctly predict the measured cross-sections within the uncertainties in all studied quantities and over most of the investigated regions of phase space, except in the pseudorapidity region close to the proton beam direction ("forward" region) where the prediction is considerably below the data. As mentioned above, this has already been previously observed [6, 168, 169] and can be expected, as the NLO calculation effectively becomes a leading-order prediction in this region [170].

The uncertainty on the NLO prediction, dominated by the uncertainty associated with the choice of the renormalization scale, is typically larger than the experimental uncertainty, which is for the most part dominated by the uncertainty of the jet energy scale.

In the low-Q^2, low-$p_{T,\mathrm{B}}$, or forward-η_{lab} regions, the theoretical uncertainty is especially large (up to 40%), as demonstrated by large NLO corrections to the leading-order (LO) prediction with k factors of up to ~ 5. These correction factors were usually in the order of ~ 2 and decreased for higher values of Q^2 and $p_{T,\mathrm{B}}$.

In particular at low values of Q^2, x, or $p_{T,\mathrm{B}}$, a tendency of the NLO prediction to be below the data was observed and investigated further by comparing the measured cross-sections with NLO calculations at either harder or softer renormalization scales. For inclusive jet production, the data were typically found to favor the softer scale of $\mu_R^2 = Q^2$.

This observation does not lead to any clear conclusions, however, as the better description of the data by the NLO calculations at $\mu_R^2 = Q^2$ could be purely accidental. Furthermore, the large k factors in this kinematic region support the assumption, that considerable contributions from higher orders missing in the NLO calculations can be expected. On the other hand, the deviation with respect to the data could be also caused by other effects not considered in the NLO calculation such as a resolved photon structure [163–165] or possibly the onset of BFKL dynamics.

Where the results can be easily related to previous measurements, they are generally compatible with previous H1 publications, which studied inclusive jets at low values of Q^2 [6, 7].

The cross-sections for dijet production were presented as function of Q^2, the invariant dijet mass, M_{jj}, the absolute difference in pseudorapidity in the Breit frame between the two jets, η', the mean transverse momentum in the Breit frame of the dijets, $\langle p_{T,\mathrm{B}} \rangle$, and the parton momentum entering into the hard scattering, ξ. The cross-sections with respect to $\langle p_{T,\mathrm{B}} \rangle$ and ξ were also measured double-differentially in five bins of Q^2.

In all studied quantities and over the full investigated ranges, the measured cross-sections are well described by the NLO predictions. The relative uncertainty on the prediction is reduced with respect to the cross-sections for inclusive jet production, but is still larger than the experimental uncertainty in most cross-section bins.

Finally, the cross-sections for inclusive trijet production were presented as function of Q^2, as well as M_{jj} and $\langle p_{T,\mathrm{B}} \rangle$ defined with respect to the two hardest jets of the event.

The NLO calculations give a good prediction of the measured cross-sections in all studied observables and over the full investigated ranges. The theoretical uncertainty is typically larger than the experimental uncertainty, except at high Q^2 and $\langle p_{T,\mathrm{B}} \rangle$ values. Here, the experimental uncertainty becomes large due to the higher statistical uncertainty and the stronger dependence on the absolute hadronic jet energy scale.

Conclusions and Outlook

The measured jet cross-sections presented in this analysis offer a thorough test of NLO QCD predictions for values of Q^2 in the region of $10 < Q^2 < 100\,\mathrm{GeV}^2$.

On the one hand, the overall agreement found between the theoretical predictions and the experimental results illustrates the capability of perturbative QCD to describe measurements over a wide range of phase space. On the other hand, the observed discrepancies, the large NLO corrections, and the uncertainty associated with the specific choice of the (unphysical) renormalization scale indicate the importance of including higher orders of the perturbative expansion in the calculations [12, 175].

Thanks to the precision of the presented measurement, the data are expected to give a stringent test of future next-to-next-leading order (NNLO) predictions, predictions implementing BFKL dynamics, or calculations including a treatment of resolved photons.

Such NNLO calculations will be necessary to fully exploit the sensitivity of the low Q^2 jet data in QCD PDF fits and fits to extract values of α_s [4, 7]. In the former, the presented jet cross-sections are assumed to have an impact especially on the gluon density at low x values [11].

The precision of the data and their impact on above mentioned fits is expected to be further improved by a combination of the measured cross-sections of the H1 and ZEUS experiments. In the case of the presented analysis, the strategy for the future combination has been significantly simplified by an agreement on the phase space, the observables, and the binning of the cross-sections.

Part II.

Radiation Damage Studies for Silicon Sensors for the XFEL

12. Introduction

Planed to be operational in 2015 the European **X**-ray **F**ree-**E**lectron **L**aser (XFEL) will set new standards in brilliance for X-ray sources. With laser pulses of the order of 10 fs duration at wavelengths of about 0.1 nm the XFEL will open up new possibilities for many fields of research such as the analysis of single bio-molecules, the recording of chemical reactions, and the investigation of extreme states of matter.

Experiments at the XFEL pose unprecedented requirements to the detectors in terms of radiation tolerance: integrated fluxes of up to 10^{16}[12 keV photons/ cm^2], corresponding to approximately 10^9 Gy in SiO_2, are expected. As the threshold for bulk damage is 300 keV, only surface damage is expected: build-up of charges inside the oxide and of energy states ("traps") at the Si-SiO_2 interface.[1] While both effects will change the field distribution, which is relevant for the device stability, the latter will also result in an increase of the dark current, which impacts the read-out electronics and may result in an increase of the noise.

The aim of this study is to investigate the behavior of silicon sensors at high doses with the help of test structures and to determine the relevant parameters for device simulations and thus allowing to reliably predict the sensor performance as function of dose. The work is part of the detector R&D for the European X-Ray Free-Electron-Laser.

This part[2] of the thesis is organized as follows: The irradiation facility at HASYLAB and the irradiation procedure are presented in chapter 13. Chapter 14 gives an overview of the investigated test-structures, the experimental techniques used and the implemented model calculations. The results of the measurements are then presented in chapter 15 and discussed as well as summarized in chapter 16.

---

[1] See for example [176–180].

[2] This part is based to some extend on previously published articles by the author [181, 182].

13. Irradiation Procedure

In this chapter, an overview of the irradiation facility set up at beamline F3/F4 at HASYLAB is given, after the specific properties of the synchrotron beam and the procedure used for the determination of the dose have been presented.

13.1. HASYLAB at DORIS

The **Ha**mburg **Sy**nchrotron Radiation **Lab**oratory (HASYLAB) provides beamtime and support for the light sources available at DESY. One of these light sources is DORIS[1], a ring accelerator for electrons or positrons. Operated since 1974 and initially used in parallel for particle physics experiments and research with synchrotron radiation, DORIS was upgraded in 1993 ("DORIS-III") and serves as dedicated synchrotron radiation source since.

DORIS stores electrons or positrons at energies of 4.45 GeV and initial beam currents of up to 140 mA. Synchrotron radiation is generated by 1.22 T bending magnets at a critical photon energy of $E_c = 16\,\text{keV}$, as well as by wigglers and undulators.

Beamlines F3 and F4 at HASYLAB

The beamlines F3 and F4 at HASYLAB provide a white photon beam from a bending magnet. As shown in figure 13.1 the typical photon energy at the detector is $E_\gamma \approx 10\,\text{keV}$ with a full width half maximum of $\approx 13\,\text{keV}$. The spectrum was calculated using the SPEKTRA [183,184] program, taking into account the absorption[2] by materials and gases[3] in the path of the beam before reaching the sample [186].

The spatial beam intensity was measured at F4 from the photo current of a silicon pad sensor. Using the irradiation setup detailed in the following section, the sensor was placed behind a collimator with an opening of $0.1 \times 0.1\,\text{mm}^2$ and was moved in 0.1 mm steps, thus scanning the x-y plane perpendicular to the beam direction. The result is presented in figure 13.2.

In the horizontal direction, the photon beam is $\sim 5\,\text{mm}$ wide and approximately constant in intensity. The latter is to be expected, as the positrons emit synchrotron radiation of the same intensity at every point of their flight path through the magnetic field of the bending magnet.

In the vertical direction, on the other hand, the photon beam intensity is determined by the spatial distribution of the positrons in the DORIS beam. The vertical photon

---

[1] **Do**ppel-**Ri**ng-**S**peicher

[2] The attenuation coefficients were taken from [185].

[3] At beamline F3 absorbers consisted of: a 50 µm Al Window, a 250 µm Be Window, 20 cm of nitrogen, and a 25 µm capton window; and at beamline F4 of: a 400 µm Be Window, 10 cm of helium, a $\sim$ 30 µm Al window, 18 cm of helium, and a 25 µm capton window.

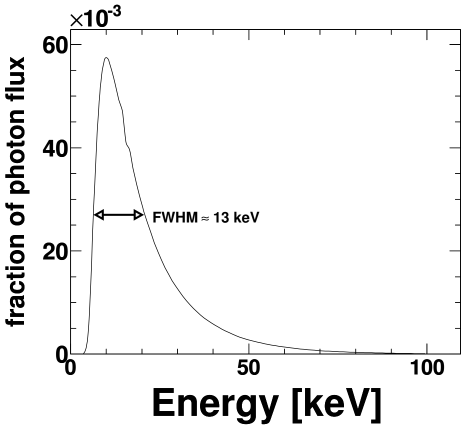

Figure 13.1: Theoretical beam spectrum at the detector for beamline F3. The spectrum has been calculated from the synchrotron spectrum and the absorbers.

beam cross section shown in figure 13.2c is Gaussian-like in shape, with a $\sim 2\,\mathrm{mm}$ wide peak of near-constant intensity. At a vertical position of $y \approx -3\,\mathrm{mm}$, the intensity drops sharply. This was caused by misaligned opening slits installed at F4, that blocked part of the beam despite being in their maximal "open" position. This did not affect our setup, however, as the vertical beam width was still sufficiently large.

13.2. Dose Determination

Based on a normalized photon spectrum such as shown in figure 13.1, the absolute dose with respect to the SiO_2 of a test structure can be determined by measuring the photo current, I_{photo}, of a planar silicon diode in the beam.

From I_{photo} and the energy necessary to create electron-hole pairs in the silicon bulk, the total energy deposited in the photo cell can be calculated. Using the photon spectrum of figure 13.1 and the energy-dependent attenuation of Si [185], the absolute photon flux at the detector can be calculated for a given I_{photo}. The dose rate, d, can then be calculated from this absolute photon flux and the attenuation of SiO_2.

In our specific case, with the SiO_2 widths of the gate-controlled diodes introduced in the next chapter, the calculated photon spectrum[4] for beamline F3, and the beam area with approximately constant intensity of $0.5 \times 0.2\,\mathrm{cm}^2$ found at beamlines F3 and F4, the dose rate as function of the photo current corresponds to

$$d(I_{\mathrm{photo}}) = I_{\mathrm{photo}} \cdot 6.8 \cdot 10^5\,\frac{\mathrm{Gy}}{\mathrm{s\,A}} \ . \qquad (13.1)$$

---

[4] Since the details of the materials in the F4 beamline were not documented at the time, the spectrum of beamline F3 was used instead; a difference of 20 µm in the thickness of the Al window being the major change, the systematic uncertainty introduced on the deposited dose at F4 is estimated as less than 10%. This estimate is supported by studies of the influence of 0.1 mm Al absorber plates in front of the photo cell on the measured photo current. Since the dose range investigated covers 6 orders of magnitude, this uncertainty on the absolute dose is negligible.

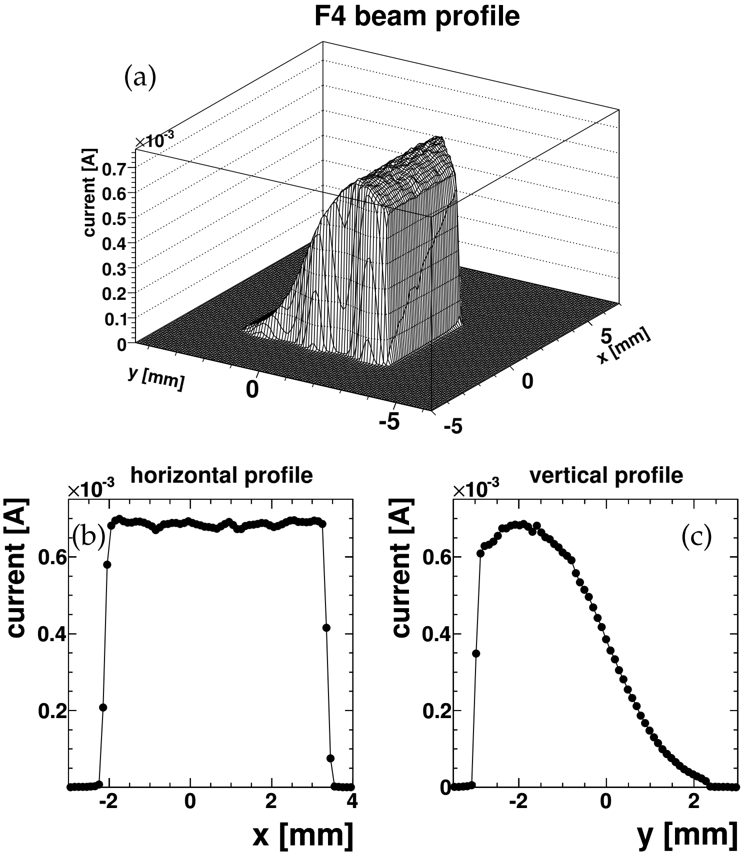

Figure 13.2: Beam profile at Hasylab beamline F4: measured photo current at different *x*-*y*-positions using a small collimator opening of $0.1 \times 0.1\,\mathrm{mm}^2$ at a Doris current of $105\,\mathrm{mA}$. Shown are the 2D profile (*top*) and horizontal and vertical cross sections (*bottom*). The measured values have been corrected for the drop of the Doris current over the time of the measurement.

In order to ensure a homogeneous dose rate over the full irradiated area, the test structures can be moved vertically through the full beam, thus smoothing the vertical beam profile. In the study presented here, this procedure is referred to as *beam scanning technique*.

To calculate the respective dose for one scan, the vertical beam intensity was measured in steps of 0.5 mm with a collimator opening of the same vertical width. Horizontally, the collimator was centered on the beam and opened to 5 mm. From the measured photo current, the dose rate at each position could be calculated similarly to equation 13.1. With a vertical motor speed of $1/8\,\mathrm{mm\,s^{-1}}$ and a resulting exposure time of 4 s per step, the total dose for each step can be calculated. For a full beam scan over the range of 8 mm and at a reference Doris current of $I^{\mathrm{ref}}_{\mathrm{DORIS}} = 112\,\mathrm{mA}$, the integrated dose of

$$D_{\mathrm{scan}}(I^{\mathrm{ref}}_{\mathrm{DORIS}}) = 6.1\,\mathrm{MGy} \ , \tag{13.2}$$

was determined with respect to the SiO_2 of the gate-controlled diodes.

Since the photon flux at the detector is directly proportional to I_{DORIS}, equation 13.2 can be easily adjusted to give the dose for a scan at arbitrary I_{DORIS},

$$D_{\mathrm{scan}}(I_{\mathrm{DORIS}}) = 6.1\,\mathrm{MGy} \cdot \frac{I_{\mathrm{DORIS}}}{I^{\mathrm{ref}}_{\mathrm{DORIS}}} \ , \tag{13.3}$$

where $I^{\mathrm{ref}}_{\mathrm{DORIS}} = 112\,\mathrm{mA}$.

13.3. Irradiation Facility and Procedure

For this study an irradiation facility has been set up at the beamline F3 at Hasylab [148, 186] that was later moved to beamline F4. The setup is illustrated in figure 13.3: It consists of a Ta chopper, with which the dose rate can be varied within $0.5 - 150\,\mathrm{kGy\,s^{-1}}$, a manually adjustable *x*-*y* collimator to precisely define the field of irradiation and a sample holder, which allows easy exchange of samples, up to 4 biasing lines and temperature control through liquid cooling in the range of 10 to 30° C.

The test structures themselves are glued and bonded to a ceramic substrate, depicted in the top left of figure 13.3, thus making the exchange and handling of the structures easier and safer.

As the set-up is mounted on a *x*-*y*-*z*-table, larger areas can be irradiated by computer controlled scanning. An pneumatic beam shutter, installed close to the exit window of the beam pipe, allows a precise definition of the exposure time and can be controlled via software.

To verify the efficiency of the liquid cooling system, the temperature during irradiation with active cooling at 20° C was studied using a PT-100 element and a Keithley 2700 instrument. The PT-100 element was attached on top of a Si test sample in close proximity to the beam spot. The measurement was once performed while reducing the dose rate to 5% using the chopper, and once at full dose rate.

The result is presented in figure 13.3. The figure demonstrates that the temperature at the detector never exceeds 36° C at the full dose rate. Using the chopper, the

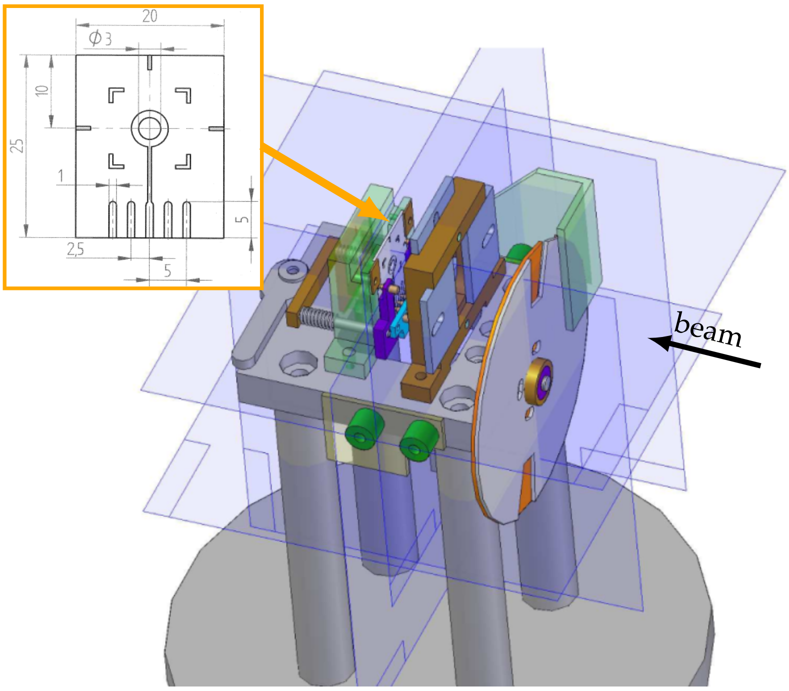

Figure 13.3: Setup of the irradiation facility. Elements, ordered in the beam direction: chopper, collimator, and sample holder with cooling and spring mechanism, allowing easy mounting of the ceramic substrates with test structures (shown separately in the top left).

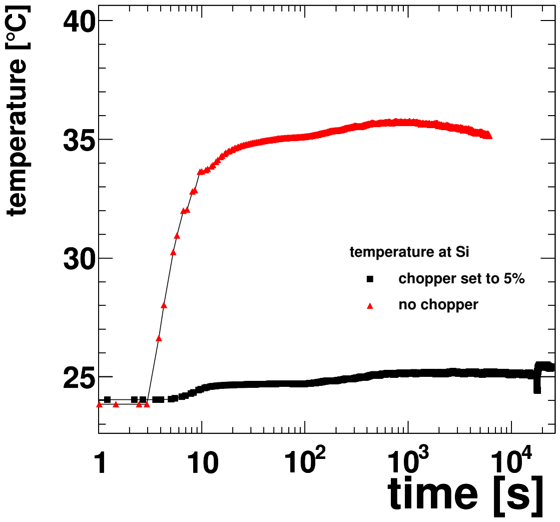

Figure 13.4: Temperature measured on Si test structure during irradiation in close proximity to the beam spot with active liquid cooling at 20° C, once with reduced dose rate (triangles) and once at full dose rate (squares). See the text for details.

overall temperature increase amounts to only $\approx 3^\circ$ C. Please note, however, that the measurements were not performed simultaneously. This explains the small offset in both time and initial temperature between the two curves. The point of temperature increase corresponds closely to the time when the pneumatic beam shutter was opened. The "jump" around $2 \cdot 10^4$ s in the measurement with chopper corresponds to a short break during which the Doris beam was refilled. The following increase in temperature illustrates the dependence on the Doris current.

14. Test-Structures and Measurement Techniques

This chapter introduces the investigated test-structures, the gate-controlled diode, and gives an overview over the employed measurement techniques. In the last section, model calculations for the capacitance characteristics of a MOS (Metal-Oxide-Silicon) device are presented and compared to measured data.

14.1. Gate-Controlled Diodes

Gate-controlled diodes, as first introduced in [187], have been chosen as test-structures for this study. They are especially suited as they allow the measurement of both diode and MOS characteristics using one structure. Fig. 14.1 shows the gate-controlled diodes used for the study and sketches the measurement techniques used:

- C/V (Capacitance-Voltage) on the MOS capacitor realized by gate rings 2 and 3,
- I/V_{gate} (Current-Voltage) on gate ring 1 and the diode,
- TDRC (Thermally Depolarization Relaxation Current) on gate rings 2 and 3.

The gate-controlled diodes that were used in this study are part of a test field that is included in the mask set designed by the Rose collaboration [188]. This mask layout has been implemented in the wafer design of the first Atlas pixel sensor prototype [189] to be used for radiation hardness studies.

The diodes have been fabricated on a 285 µm thick n-doped Si-substrate of $\rho \approx 3.4\,\mathrm{k\Omega cm}$ and a crystal orientation of $\langle 111 \rangle$ with a central p^+-doped diode and five surrounding aluminum gate rings on top of a $\sim 400\,\mathrm{nm}$ isolation layer consisting of $SiO_2 + Si_3N_4$. The structures have a total diameter of 1.5 mm while the central diode has a diameter of 1 mm.

For this analysis, 18 gate-controlled diodes were irradiated in three irradiation campaigns[1] during 2007 – 2008. In the first campaign, four devices were exposed to up to 1 MGy in several steps at the beam line F3 at Hasylab [148, 186]. Next, five gate-controlled diodes were irradiated in several steps to up to 1 GGy. During this irradiation campaign, the setup was moved from beam line F3 to F4 [148]. In the last irradiation campaign, nine gate-controlled diodes were exposed in multiple steps to doses in the range of 0.25 – 25 MGy. This irradiation was performed at beam line F4 using the beam scanning technique described in chapter 13.3.

---

[1] The author only participated in the later two irradiation campaigns.

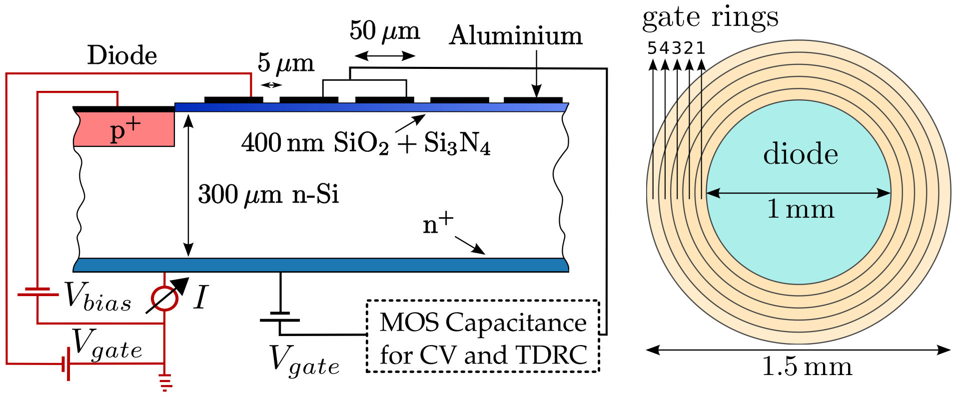

Figure 14.1: Schematic drawings of the gate-controlled diode: cross section with measurement techniques (*left*) and top view (*right*).

After the irradiation of the gate-controlled diodes, C/V and I/V measurements were performed in the laboratory within four hours of the irradiation. For the last irradiation campaign, the time between beam exposure and measurement was significantly reduced, and the gate-controlled diodes were otherwise stored at $-30°$ C to prevent annealing effects occurring at room temperature. The devices used in the last campaign were also studied in TDRC measurements and with respect to their properties after temperature induced annealing.

All employed measurement techniques are described in more detail in the following section.

14.2. Measurement Techniques

14.2.1. Capacitance versus Voltage (C/V) Measurements

In this analysis, the *C/V measurements* were performed using the HP 4284A capacitance bridge[2]. The bridge measures the admittance Y, respectively the impedance $Z = Y^{-1}$, of a device as function of the voltage V_{gate} by modulating V_{gate} with a small-signal variation of frequency f_{AC} and amplitude V_{AC}. By associating the device with a equivalent parallel circuit[3] of a capacitance C_{p} and a resistor R_{p}, the admittance can be expressed as $Y = G + j2\pi f_{\text{AC}} C_{\text{p}}$, where the real part, $G = 1/R_{\text{p}}$, denotes the *conductance* and the imaginary part divided by $2\pi f_{\text{AC}}$ provides the (parallel) *capacitance*.

Figure 14.2 shows an example of a C/V and G/V measurement on an unirradiated sample at four different frequencies[4] with $V_{\text{AC}} = 0.05\,\text{V}$.

---

[2] The HP 4284A bridge was later replaced by an Agilent 4980A; for more details regarding the electrical setup for the C/V and I/V measurements, see [190].

[3] An alternative representation is a equivalent serial circuit of a serial capacitance C_{s} and a resistor R_{s}; both are equivalent representation of the complex values measured and can be transformed from one to another [191].

[4] The frequency is continuously being switched between the different values while the gate voltage is ramped up, therefore allowing to measure the curves at all frequencies in one go.

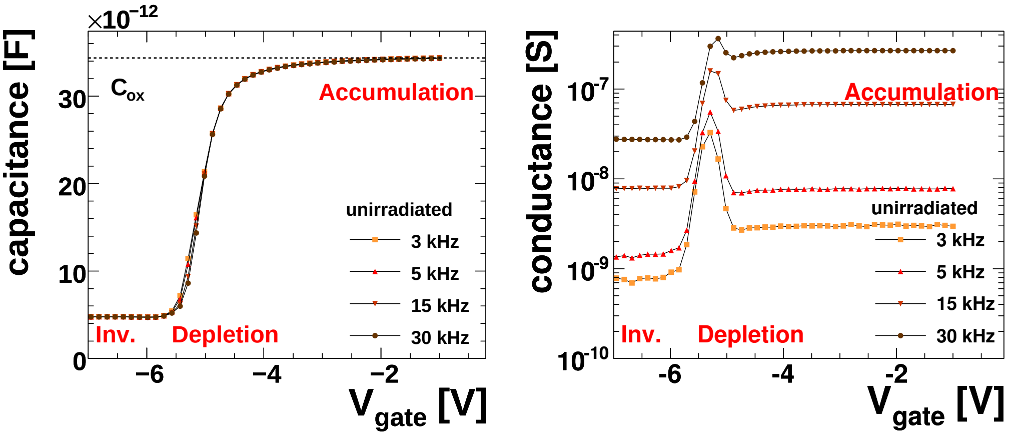

Figure 14.2: Example for a C/V measurement: capacitance (*left*) and conductance (*right*) of an unirradiated gate-controlled diode at different frequencies.

With increasing the negative voltage applied to the second and third gate rings the Si-SiO_2 interface below the rings undergoes three different biasing conditions resulting in the characteristic shape of the C/V and G/V curves: *accumulation*, *depletion*, and *inversion*. These are illustrated in figure 14.3 and will be described in the following for the C/V measurement.

The MOS capacitor is said to be under accumulation conditions as long as the net electric field at the Si-SiO_2 interface is positive, resulting in electrons accumulating at the surface. The measured capacitance in this case is equal to the oxide capacitance, C_{ox}, which is determined by the capacitor formed by the metal gates and the non-depleted silicon with the oxide as dielectric.

The measured capacitance does not change with the gate voltage until the *flat-band voltage*, V_{fb}, is approached. When exceeded the net electric field at the surface becomes negative. It then pushes away electrons thus creating a region depleted of mobile charge carriers underneath the gates. This condition is called depletion. The depleted region acts as capacitor in series to the oxide capacitor therefore reducing the total measured capacitance.

The depletion region grows with increasing gate voltage until inversion is reached where the strong negative field causes holes to form a thin positively charged inversion layer underneath the gates. This charged layer effectively shields the depleted region from any further increase of the field. The measured capacitance therefore does not change anymore with increasing gate voltage.

Besides the bias applied to the gate the net electric field at the surface also depends on fixed charges present in the oxide bulk, N_{ox}, and charged energy states at the interface, N_{it}. Both cause a shift of the measured curve relative to the ideal C/V curve. Additionally, the interface states introduce a frequency dependence into the C/V measurements [193]: As the states differ in the time needed to charge and discharge, some are not "fast" enough to follow the applied small-signal voltage variation at frequency f_0, and therefore do not influence the measured capacitance $C(f_0)$. As

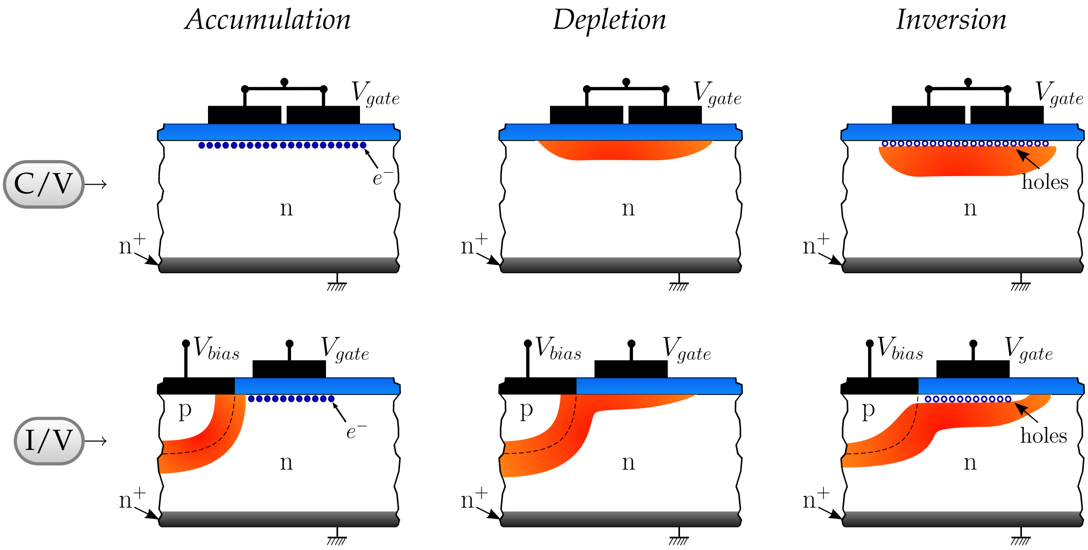

Figure 14.3: Charge distributions under accumulation, depletion, and inversion conditions for C/V measurements (*top*) and I/V measurements (*bottom*). The red colored areas indicate a region depleted of charge carriers. After [192].

shown in figure 14.2 for unirradiated samples the frequency dependence of the C/V curve is small indicating the presence of relatively few interface states.

14.2.2. Current versus Voltage (I/V) Measurements

Another measurement technique sensitive to the number of interface states is the *I/V measurement*: the current through the diode is measured versus the voltage V_{gate} applied to the first gate ring while a constant bias is applied between the diode and the backside contact. Figure 14.1 shows an illustration of the setup and figure 14.4 shows an example of the resulting I/V curve for different V_{bias} values.

Since in I/V measurements the voltage applied the gate ring is varied, the same biasing conditions as in C/V measurements occur: With increasing negative voltage on the first gate ring the area underneath the gate goes from accumulation to depletion and finally into inversion as illustrated in figure 14.3.

In accumulation, only a small volume generation current from the depletion region of the pn-junction is measured. But in the case of depletion the measured current changes significantly: When the depleted region underneath the first gate ring merges with the depleted part of the pn-junction of the diode, the volume generation current slightly increases in relation to the width of the depleted region. More importantly though, the accompanying electric field transfers free charge carriers generated at the Si-SiO_2 interface to the diode where they are measured in addition to the volume generation current. This current is referred to as *surface generation current*[5], I_{surf} [192]

---

[5] There are different names used in the literature: surface generation current, interface current, or oxide current.

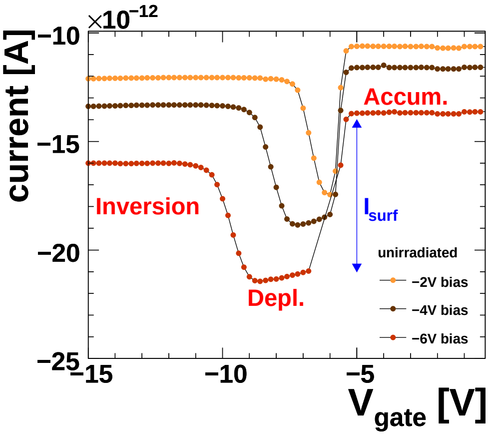

Figure 14.4: Example for an I/V measurement of an unirradiated gate-controlled diode at different bias voltages.

and can be expressed as

$$I_{\text{surf}} = q_e n_{\text{i}} S_0 A_{\text{gate}} \quad , \tag{14.1}$$

with n_{i} denoting the intrinsic charge carrier density, A_{ox} the oxide area underneath the gates, and S_0 the interface recombination velocity [187, 194]. For a *uniform distribution* of interface states, S_0 can be written as

$$S_0 = \sigma v_{\text{th}} \pi k_{\text{B}} T D_{\text{it}} \quad , \tag{14.2}$$

where σ is the effective capture cross-section, v_{th} the thermal velocity of the minority carriers, T the absolute Temperature, and D_{it} the density of interface states.

When inversion is reached the interface is isolated from the field region through a thin inversion layer, therefore terminating I_{surf}. Consequently, the measured current drops to the value seen in accumulation plus the small volume generation current from the depleted region under the gate ring.

Through the surface current, the I/V measurement is therefore sensitive to the number and energy in the bandgap of interface states. Through equation 14.2 the surface current is also directly dependent on the temperature; hence, all measurements were performed in a temperature controlled environment at an average temperature of 21° C with less than 1° C deviation.

14.2.3. Thermally Depolarization Relaxation Current (TDRC) Measurements

The third measurement technique, *TDRC measurements* [195], allows to directly determine the density of interface states: the gate-controlled diode is first cooled to 30 K while biased at zero gate voltage (accumulation), thus filling all interface states with electrons. Then V_{gate} is applied to the second and third gate rings and the sample is heated up with the constant rate of 0.183 K/s while the current from the discharge of the filled states is measured as function of the temperature.

The measurement is performed for values of V_{gate} between -20 and -100 V. From the TDRC spectrum the density of interface states, D_{it}, as function of the energy distance from the conduction band, $E_c - E_t$, is obtained. Fig. 14.5 shows the results of such a measurement for a sample irradiated[6] to 5 MGy and annealed for 60 minutes at 80° C.

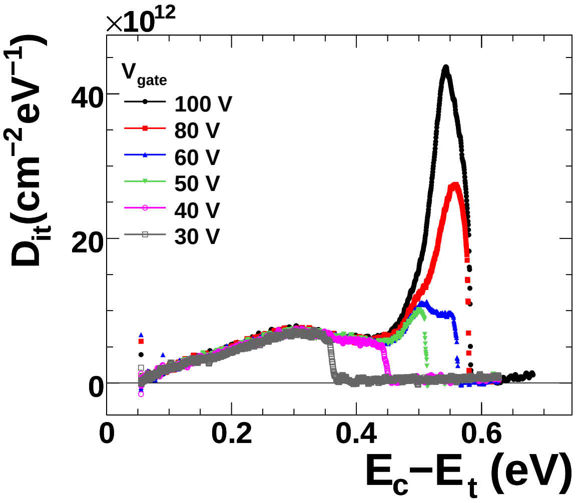

Figure 14.5: D_{it} versus position in band gap as function of the energy distance from the conduction band, measured on a 5 MGy sample after annealing for 60 m at 80° C with different values for V_{gate}. The flat-band voltage as determined from a C/V measurement at 10 kHz is $V_{\mathrm{fb}} \approx 45$ V.

The data show up to which energy in the band gap the interface states are filled as function of the gate voltage V_{gate}. Up to approximately 0.45 eV the value derived for the interface state density D_{it} is independent of the gate voltage, whereas at higher gate voltages a significant increase of D_{it} is observed. This can be interpreted as evidence for the presence of near-interfacial oxide traps that can exchange charges with the Si, i.e. *border traps* [196–199], introduced by irradiation. These will be discussed in more detail in the next chapter.

14.3. Model of the MOS Capacitance

As mentioned in the previous sections, all of the employed measurement techniques are, to varying degree, sensitive to microscopic properties of the Si-SiO$_2$ interface.

In case of the C/V measurement, the capacitance as function of the gate voltage is influenced by the number of fixed oxide charges, N_{ox}, and the number of interface states, N_{it}, as well as their density distribution in the band gap, $D_{\mathrm{it}}(E_t)$. Using model calculations of the capacitance, these parameters can be assessed and their effect on the measurement can be studied.

---

[6] The TDRC signal for an unirradiated gate-controlled diode is below the noise-level.

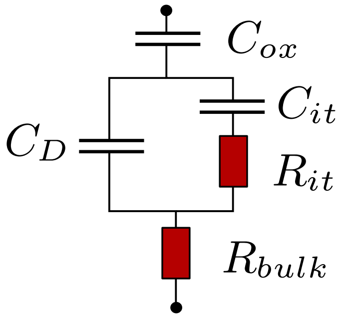

Figure 14.6: Equivalent circuit for a MOS capacitance in depletion. See text for details.

For this purpose, model calculations for the high-frequency capacitance as function of gate voltage of an n-doped MOS capacitor were implemented, building on the method described in [193] and modifications by I. Pintilie based on [200].

In the model calculations, the MOS device is approximated by an equivalent circuit as illustrated in figure 14.3 for the depletion case. Here, the semiconductor depletion-layer capacitance, C_D, is parallel to C_it and R_it, which model the charge storage and the energy loss through capture and emission in interface states, respectively, with a interface state lifetime of $\tau = R_\mathrm{it} \cdot C_\mathrm{it}$. This parallel circuit is in series with the oxide capacitance, C_ox, and the n-bulk resistor, R_bulk.

To model the capacitance as function of gate voltage, C_D and C_it have to be calculated, while C_ox and R_bulk are constants determined by the material and geometry of the device and can be measured directly.

It is convenient to calculate C_D and C_it in terms of the dimensionless surface potential v_s, defined by the surface potential (also referred to as *total band bending*), $\psi_\mathrm{s} = v_\mathrm{s} \cdot \frac{k_\mathrm{B}T}{q_e}$, which denotes the total potential difference between the silicon surface and the bulk, as indicated in figure 14.7a. Another potential needed is the bulk potential, ϕ_B, defined as the potential deep in the silicon bulk.

The gate voltage, V_gate, a reference necessary for the comparison with experimental values, will later be calculated as function of the surface potential.

The charge conditions as depicted in figure 14.7 can be differentiated with regards to the surface potential ψ_s, as listed in table 14.1.

Surface potential ψ_s	Charge condition
$\psi_\mathrm{s} > 0$	accumulation of electrons
$\psi_\mathrm{s} = 0$	flat-band condition
$\phi_\mathrm{B} < \psi_\mathrm{s} < 0$	depletion
$2\phi_\mathrm{B} \lesssim \psi_\mathrm{s} < \phi_\mathrm{B}$	weak inversion
$\psi_\mathrm{s} \lesssim 2\phi_\mathrm{B}$	strong inversion

Table 14.1: Charge conditions at the silicon surface as function of the surface potential ψ_s for a n-doped MOS capacitance [193].

The semiconductor capacitance, C_D, can then be written in the closed form approx-

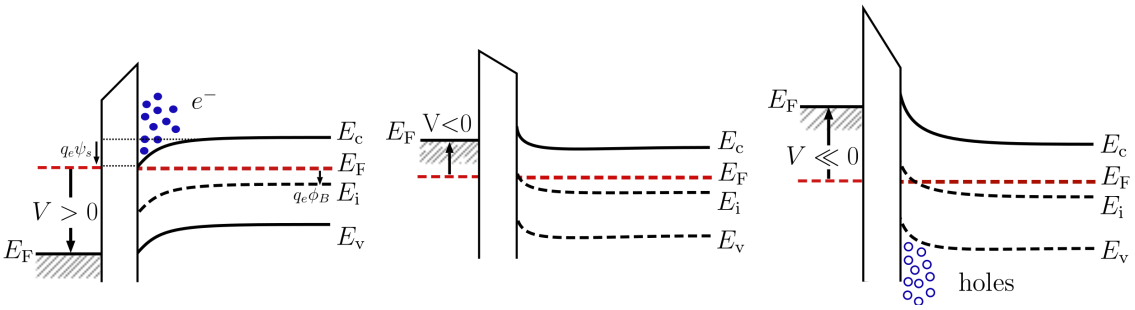

(a) Accumulation (b) Depletion (c) Inversion

Figure 14.7: Band diagrams for a MOS device under (a) accumulation, (b) depletion, and (c) inversion conditions.

imation after Lindner [193, 201] as function of the dimensionless surface potential, v_s,

$$C_D(v_s) \approx C_L(v_s) = \frac{1}{\sqrt{2}} \operatorname{sign}(v_s) C_{fb} \frac{\exp(v_s) - 1}{\sqrt{-(v_s + 1) + \exp v_s}} , \tag{14.3}$$

where A_{ox} denotes the oxide area and C_{fb} the flat-band capacitance given by

$$C_{fb} = \frac{\epsilon_0 \epsilon_{Si}}{\lambda_n} A_{ox} . \tag{14.4}$$

Here, ϵ_0 and ϵ_{Si} are the dielectric permittivities of the vacuum and of silicon, respectively, and λ_i and λ_n denote the intrinsic and extrinsic Debye length, respectively:

$$\lambda_i = \sqrt{\frac{\epsilon_{Si} \epsilon_0 k_B T}{2 q_e^2 n_i}} \quad \text{and} \quad \lambda_n = \sqrt{\frac{k_B T \epsilon_0 \epsilon_{Si}}{q_e^2 N_D}} , \tag{14.5}$$

with the intrinsic charge carrier density taken as $n_i = 1. \cdot 10^{10}\,\text{cm}^{-3}$ [193] and the doping concentration typically being of the order of $N_D = 5 \cdot 10^{12}\,\text{cm}^{-3}$ for the investigated structures.

If v_s is smaller than the so-called *match point potential*, v_m, then C_L should assume the (constant) value of $C_L(v_m)$ to describe the inversion condition, with

$$v_m = (-2.10 \cdot u_B + 2.08) - 0.75 , \tag{14.6}$$

where u_B denotes the dimensionless potential over the bulk $u_B = \frac{q_e \phi_B}{k_B T} = \ln(N_D / n_i)$.

The gate voltage can be expressed as function of the surface potential

$$V^s_{gate}(v_s) = -Q_s(v_s) \frac{A_{ox}}{C_{ox}} + \frac{k_B T}{q_e} v_s , \tag{14.7}$$

where Q_s denotes the surface charge density for a given potential v_s,

$$Q_s(v_s) = \frac{\epsilon_{Si}\epsilon_0}{\lambda_i} \cdot \frac{k_B T}{q_e} \operatorname{sign}(-v_s) \cdot \sqrt{\frac{N_D}{n_i}} \cdot \sqrt{(-v_s - 1) + \exp(v_s) + \frac{n_i^2}{N_D^2} \exp(-v_s)} \; . \tag{14.8}$$

So far, contributions from the interface capacitance C_{it} and resistor R_{it} have been neglected. For the calculation of the total capacitance, only the real part of C_{it} is needed:

$$\mathfrak{Re}\,(C_{it}) = A_{ox} \frac{q_e^2}{k_B T} \int_{-1.12\,\text{eV}}^{0\,\text{eV}} \frac{D_{it}(E_t) f_t^0 (1 - f_t^0)}{1 + \omega^2 \tau^2} \, dE_t \; . \tag{14.9}$$

The function f_t^0 denotes the steady-state interface state occupancy as given by

$$f_t^0(E_t, \psi_s, \eta, T) = \frac{1}{1 + \exp\left((E_t - \psi_s - \eta)\frac{q_e}{k_B T}\right)} \; , \tag{14.10}$$

and the interface state lifetime, τ, can be calculated using

$$\tau = \frac{f_t^0}{\sigma v_{th} n_s} \; , \tag{14.11}$$

where the capture cross section is taken as $\sigma = 2.5 \cdot 10^{-16}\,\text{cm}^2$ [179]. The thermal velocity, $v_{th} = \sqrt{\frac{3 \cdot k_B T}{m_n}}$, can be calculated assuming an effective electron mass of $m_n = 0.327 m_0$ with $m_0 = 9.1 \cdot 10^{-31}\,\text{kg}$ [193]. Finally, the concentration of charge carriers at the surface is given by

$$n_s = N_D \exp(\psi_s \cdot \frac{q_e}{k_B T}) \; . \tag{14.12}$$

and the bulk potential with respect to E_C is given by

$$\eta = \frac{k_B T}{q_e} \ln(\frac{N_D}{N_c}) \; , \text{where } N_c = 2 \cdot \left(\frac{2\pi m_n k_B T}{h^2}\right)^{\frac{3}{2}} \; , \tag{14.13}$$

denotes the density of states in the conduction band.

The total capacitance can then be calculated under the assumption of the equivalent parallel circuit shown in figure 14.3 by first calculating the capacitance for the parallel circuit of C_{it} and C_L in series with C_{ox}

$$C_{\text{ox, L, it}} = \frac{C_{ox} C_L + C_{ox} \mathfrak{Re}(C_{it})}{C_L + C_{ox} + \mathfrak{Re}(C_{it})} \; , \tag{14.14}$$

and then adding the bulk resistor R_{bulk} to the total capacitance

$$C_p^{\text{model}} = \frac{C_{\text{ox, L, it}}}{1 + \omega^2 R_{bulk}^2 C_{\text{ox, L, it}}^2} \; . \tag{14.15}$$

The gate voltage needs to be adjusted for the additional charges stored at the interface,

$$V_{\text{gate}}(\psi_s) = V^s_{\text{gate}}(\psi_s) - \frac{1}{C_{\text{ox}}}\left(Q^A_{\text{it}}(\psi_s) + Q^D_{\text{it}}(\psi_s) + Q_{\text{ox}}\right) \;, \tag{14.16}$$

where the oxide charge density Q_{ox} is determined by the measurement and the interface charge densities $Q^{A,D}_{\text{it}}$ are given by

$$Q^A_{\text{it}}(\psi_s) = -q_e A_{\text{ox}} \int_{E_c}^{E_v} D_{\text{it}}(E_t) \cdot f^0_t(E_t, \psi_s)\, \mathrm{d}E_t \;, \tag{14.17}$$

in case of interface states that act as acceptors, and

$$Q^D_{\text{it}}(\psi_s) = q_e A_{\text{ox}} \int_{E_c}^{E_v} D_{\text{it}}(E_t) \cdot \left(1 - f^0_t(E_t, \psi_s)\right) \mathrm{d}E_t \;, \tag{14.18}$$

for donor-like interface states.

Results

Examples for C/V curves derived with this model are shown in figure 14.8a for frequencies of 3 and 30 kHz. The calculations were performed assuming a homogeneous distribution of donor interface states with an average value of $D_{\text{it}} = 4.2 \cdot 10^{10}\,\text{eV}^{-1}\text{cm}^{-2}$ and an oxide charge density of $Q_{\text{ox}} = 1.692 \cdot 10^{-10}\,\text{C}$. Values determined experimentally were the temperature $T = 294\,\text{K}$, the doping concentration $N_{\text{D}} = 5 \cdot 10^{12}\,\text{cm}^{-3}$, and the oxide capacitance $C_{\text{ox}} = 34.8\,\text{pF}$. Other parameters were used as described in the text above, specifically $\sigma = 2.5 \cdot 10^{-16}\,\text{cm}^2$, $v_{\text{th}} = 2.0 \cdot 10^7\,\text{cm/s}$, and $n_{\text{i}} = 1 \cdot 10^{10}\,\text{cm}^{-3}$.

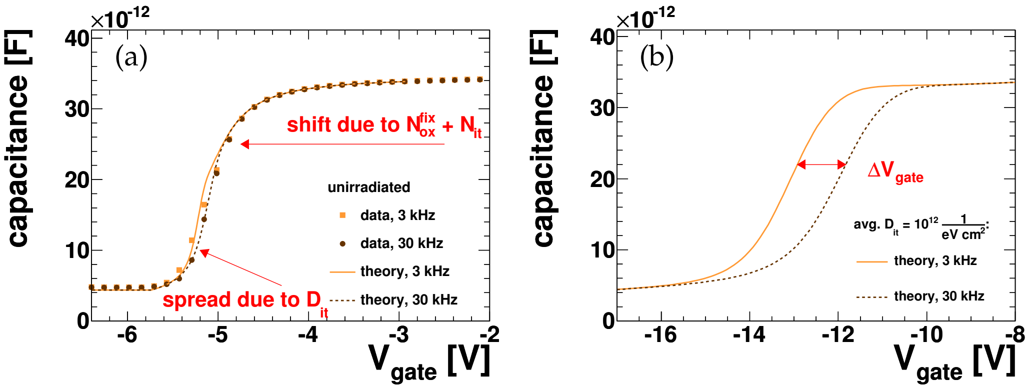

Figure 14.8: *Left*: Comparison of the measured capacitance of an unirradiated gate-controlled diode with the model prediction based on an average value of $D_{\text{it}} = 4.2 \cdot 10^{10}\,\text{eV}^{-1}\text{cm}^{-2}$ at different frequencies; *Right*: model predictions based on an increased average value of $D_{\text{it}} = 1 \cdot 10^{12}\,\text{eV}^{-1}\text{cm}^{-2}$. See text for details.

With these parameters, the model can give a qualitative description of the data measured on an unirradiated gate-controlled diode. Especially the shape, i.e. slope of the C/V curve and the spread between curves of different frequencies are quite well reproduced, even with the simplified assumption of a uniform distribution of interface states. This frequency dependence of the C/V measurement is directly related to the interface state density, as demonstrated by equation 14.9, while the total shift in gate voltage is a result of the total number of charges at the interface, i.e. N_{it} and N_{ox}, a result of equation 14.16.

Figure 14.8b shows model calculations at two different frequencies using the same parameters as above, except for the average value of D_{it} which was set to $1 \cdot 10^{12}\,\mathrm{eV}^{-1}\mathrm{cm}^{-2}$ i.e. increased by almost two orders of magnitude. This modification causes the curves to be shifted by $\sim 7\,\mathrm{V}$ toward higher gate voltages. Also, the curves exhibit both a decreased slope in depletion, and a shift of $\sim 1\,\mathrm{V}$ between the two curves at different frequencies as indicated in the figure.

By calculating the value of the shift between two fixed frequencies for various values of D_{it} for uniform donor-like interface state distributions, the C/V measurements can be directly related to a D_{it} value, similarly as the I/V measurements using equations 14.1 and 14.2. Figure 14.9 shows the resulting average D_{it} in logarithmic scale as function of the gate voltage difference between the 10 and 100 kHz C/V curves determined at a fixed capacitance of 22 pF. The calculated points were fitted with a linear function resulting in

$$D_{\mathrm{it}}^{\mathrm{calc}}(\Delta V_{100\,\mathrm{kHz}}^{10\,\mathrm{kHz}}) = \left(9.5 \cdot 10^{11}\,\mathrm{eV}^{-1}\mathrm{cm}^{-2}\mathrm{V}^{-1} \times \Delta V_{100\,\mathrm{kHz}}^{10\,\mathrm{kHz}}\right) - 5.5 \cdot 10^{9}\,\mathrm{eV}^{-1}\mathrm{cm}^{-2} \ . \tag{14.19}$$

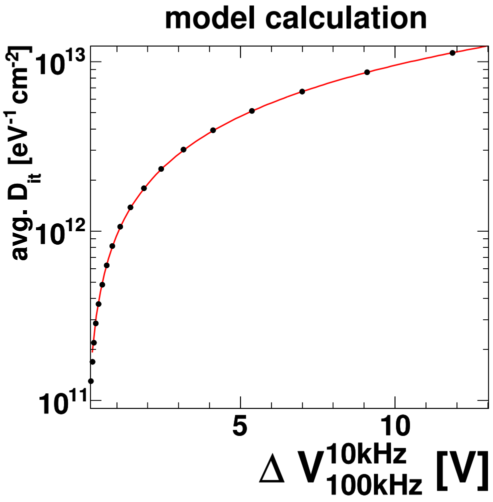

Figure 14.9: The calculated average D_{it} in logarithmic scale as function of the gate voltage difference between the 10 and 100 kHz C/V curves determined at a fixed capacitance of 22 pF. See text for details.

15. Results

A total of 18 gate-controlled diodes have been irradiated in various steps to doses of 1 kGy – 1 GGy. Immediately[1] after each irradiation step C/V, I/V, and later also TDRC measurements were performed.

In this chapter, the dose dependence of both the measured data and of the extracted interface parameters is studied. The chapter concludes with a brief overview of a study aiming at a determination of the individual charge densities of the different traps at or near the interface and in the oxide.

15.1. Results from I/V Measurements

Figure 15.1a shows I/V measurements of the same gate-controlled diode for different irradiation doses. While the curve for the unirradiated sample is barely visible, the current is increased considerably after irradiation. In fact, the surface generation current, I_{surf}, as determined from the curves, increased by two orders of magnitude after irradiation to 2 kGy and increases further for higher doses.

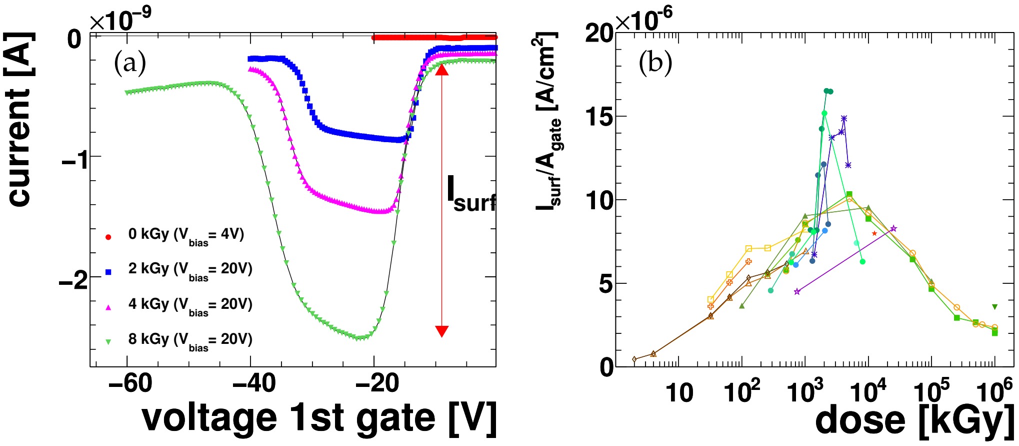

Figure 15.1: *Left:* I/V measurements for three different irradiation steps of the same sample. The curve for the unirradiated diode is included for comparison. The arrow indicates the change in measured current due to the surface current I_{surf}. *Right:* The surface current normalized to area versus dose. Shown are results for all 18 gate-controlled diodes.

---

[1] All measurements on irradiated structures have been performed within 4 h of the irradiation unless stated otherwise.

In figure 15.1b the surface current normalized to gate area, $I_{\mathrm{surf}}/A_{\mathrm{gate}}$, is shown versus the dose for all 18 diodes and all irradiation steps. The plot shows that $I_{\mathrm{surf}}/A_{\mathrm{gate}}$ reaches a maximum of $\approx 15\,\mu\mathrm{A\,cm^{-2}}$ at approximately 3 MGy and then drops by almost a factor 5 when increasing the dose to 1 GGy. This behavior is independent of the dose rate during irradiation as the curve is reproduced by samples irradiated at less than 10% of the maximum dose rate. Monitoring of the temperature during irradiation indicates that temperature induced annealing is most likely not the cause of this effect.

As figure 15.1a illustrates, the determination of the value of I_{surf} relies on the recognition of the characteristic shape of the I/V curve. However, in the dose region of the peak ($\sim 2-6$ MGy), the I/V measurements were sometimes found to be distorted and less well-defined [202], resulting in larger systematic uncertainties on the values of I_{surf}.

Consequently, the interpretation of the absolute values in the peak region has to be treated with care. This will be discussed again in section 15.3.

15.2. Results from C/V Measurements

Figure 15.2a shows the capacitance versus the gate voltage for an unirradiated sample and six subsequent irradiation steps measured at a frequency of $f_{\mathrm{AC}} = 10\,\mathrm{kHz}$ with a small-signal amplitude of $V_{\mathrm{AC}} = 0.5\,\mathrm{V}$. The C/V curves exhibit both a change in slope and a shift in gate voltage depending on the irradiation dose. For doses below 5 MGy the curves are shifted toward more negative gate voltages with higher doses. For doses higher than 10 MGy the shift decreases with increasing dose.

As function of the dose, this shift[2] in gate voltage shows a similar behavior as the $I_{\mathrm{surf}}/A_{\mathrm{gate}}$ curve: Figure 15.2 shows the flat-band voltage V_{fb} at which the C/V curves reach the calculated flat-band capacitance[3] as function of the irradiation dose. The curve reaches a broad maximum at approximately 5 MGy and is independent of the dose rate at which the irradiation was performed. The difference from the peak value 5 MGy → 1 GGy is almost a factor 2. Compared to the $I_{\mathrm{surf}}/A_{\mathrm{gate}}$ curve, the drop is not as pronounced.

This difference in drop-off from the peak value between V_{fb} and I_{surf} can be interpreted in terms of the number of fixed-oxide charges, N_{ox}, and the number of interface states, N_{it}. While the surface current depends only on the number of interface states, the value of the flat-band voltage is affected by all charges present at the surface, as demonstrated in the previous chapter by equations 14.1 and 14.16, respectively.

The C/V measurements are also directly sensitive to the presence of interface states through the frequency dependence of the measured capacitance, as discussed in chapter 14.3. Figure 15.3a shows an example of this dependence for a sample irradiated to a dose of 0.7 MGy. Presented are C/V curves measured at four frequencies in the range of $3-30\,\mathrm{kHz}$. The curves exhibit the same shape, but are spread out in gate voltage, with the curves measured at higher frequency being shifted to lower values of

---

[2] The shift can be parametrized e.g. by the gate voltage at which a specific capacitance is measured or by the value of the flat-band voltage.

[3] The value of the flat-band capacitance is different for each sample, with $\bar{C}_{\mathrm{fb}} \approx 8.5\,\mathrm{pF}$.

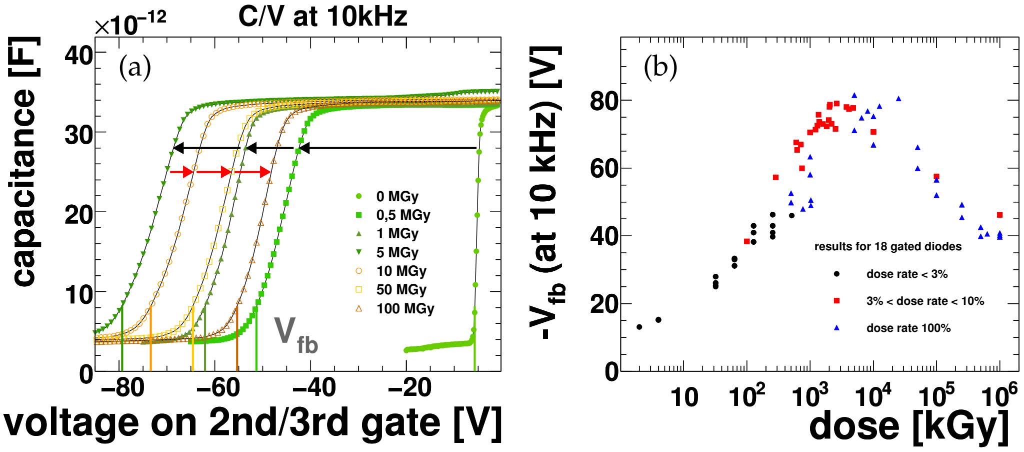

Figure 15.2: *Left:* The capacitance versus the gate voltage measured at $f_{AC} = 10\,\mathrm{kHz}$ with $V_{AC} = 0.5\,\mathrm{V}$ for an unirradiated sample and six subsequent irradiation steps. The arrows highlight the shift of the curves and the vertical lines indicate the voltage V_{fb} at which the flat-band capacitance C_{fb} is measured. *Right:* The voltage V_{fb} from C/V measurements at $f_{AC} = 10\,\mathrm{kHz}$ for all 18 gate-controlled diodes. The irradiation was performed at different dose rates as indicated by marker shape and color ($100\% \mathrel{\hat{=}} 150\,\mathrm{kGy/s}$).

V_{gate}. This is the result of interface states being unable to follow the voltage variation V_{AC} at increasing f_{AC}, thus no longer contributing to the measured capacitance.

This frequency dependence can be parametrized by ΔV_{gate}, the difference of gate voltages at which a specific capacitance is reached between two different frequencies, as illustrated by the arrow in figure 15.3a for 3 and 30 kHz. The resulting distribution of ΔV_{gate} as function of dose, determined at 22 pF between the 10 and 100 kHz curves, is presented in figure 15.3b for all 18 gate-controlled diodes.

The distribution exhibits a broad peak around a dose value of $\sim 2\,\mathrm{MGy}$ and drops off toward higher doses. The ratio between the peak value and the value at 1 GGy is ≈ 3, and therefore more pronounced than in the V_{fb} curve.

However, the samples irradiated in the last irradiation campaign feature smaller peak values of ΔV_{gate} compared to the other gate-controlled diodes, as highlighted in figure 15.3b. This behavior could be caused by the changeover to the scanning irradiation technique, but more likely is the result of modifications to the C/V measurement procedure: in the last batch of gate-controlled diodes, the C/V measurements were performed at three additional frequencies, to allow more detailed studies of the frequency dependence, and at lower alternating voltage V_{AC}, to ensure the requirement of $V_{AC} \ll V_{gate}$ for the small-signal range at all gate voltages.

While the number of frequencies measured mainly affects the total measurement time[4], the V_{AC} parameter is more crucial to the C/V measurement: if, on the one hand,

---

[4] As will be discussed in section 15.4, the duration of the applied bias at each measurement point might in fact influence the resulting capacitance if border traps are present.

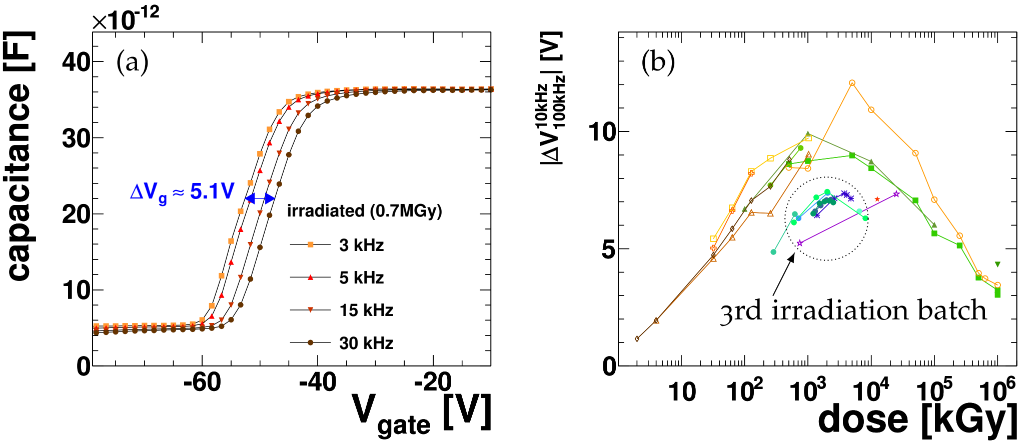

Figure 15.3: *Left*: C/V measurements for an irradiated sample of 0.7 MGy at different frequencies. The arrows indicate the frequency-dependent shift in gate voltage, ΔV_{gate}. *Right*: ΔV_{gate}, determined at the point where the C/V curves measured at 10 and 100 kHz reach the capacitance $C_p = 22\,\text{pF}$, as function of dose. Highlighted is the group of gate-controlled diodes irradiated in the last irradiation campaign. See the text for details.

the amplitude is chosen too large, harmonics of the signal frequency can give rise to spurious capacitance values, while on the other hand lower values of the small-signal amplitude reduce the sensitivity of the bridge [193].

It is therefore possible, that the observed differences in the peak value of ΔV_{gate} result from non-ideal measurement parameters.

The slope of the C/V curves is the final characteristic of the C/V measurements investigated. The C/V slope was parametrized as the (linear) change in capacitance with gate voltage between the points where the measured capacitance dropped by 15% and by 66% of the total drop from accumulation to inversion, i.e.

$$C_1 = C_{\text{ox}} - 15\% \cdot (C_{\text{ox}} - C_{\text{inv}}) \quad \text{and} \quad C_2 = C_{\text{ox}} - 66\% \cdot (C_{\text{ox}} - C_{\text{inv}}) \tag{15.1}$$

where C_{ox} and C_{inv} denote the capacitance in accumulation and in inversion, respectively.

Figure 15.4 illustrates the definition of the C/V slope and presents the results as determined from C/V measurements at a frequency of 100 kHz as function of the dose. The slope of the C/V curves drops significantly with increased irradiation, until it reaches a plateau of ≈ 1 pF/V at a dose of ∼ 300 kGy. Starting from ∼ 10 MGy, the C/V slope increases again toward higher doses. The ratio between the peak value and the value at a dose of 1 GGy is approximately a factor 2. The values of the C/V slope are very close together for samples of similar doses.

As seen in the previous chapter 14.3, the slope of the C/V curves is sensitive to the number of interface states. It is, however, also very sensitive to the actual density distribution of the interface states. This will again be discussed in section 15.5.

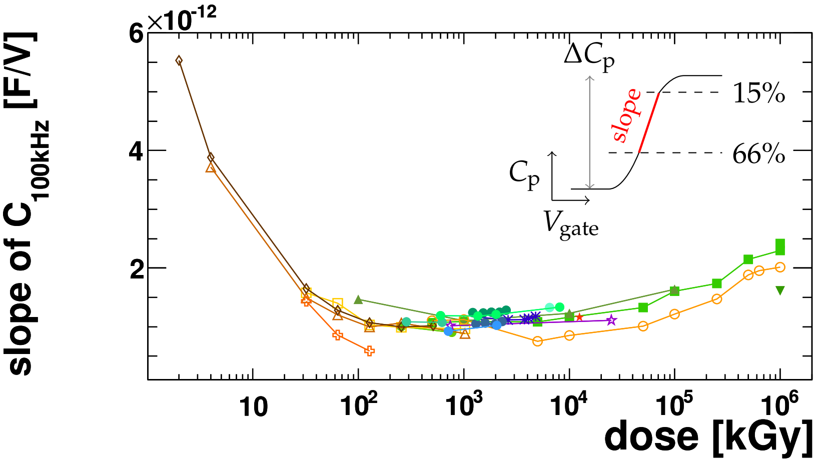

Figure 15.4: The slope of the C/V curves, as defined in the illustration in the top right, at $f_{AC} = 100\,\text{kHz}$ as function of dose. See the text for details.

15.3. Extraction of the Interface State Density

Based on the equations 14.1 and 14.19 of the previous chapter and the assumption of a uniform distribution of interface states, the measured surface current, I_{surf}, and the frequency-dependent gate voltage shift, ΔV_{gate}, shown in figures 15.1b and 15.3, respectively, can be used to determine the interface state density.[5]

The resulting distributions of average D_{it} as function of dose extracted from the I/V and C/V measurements are presented in figure 15.5. The curves exhibit the familiar shape with the peak at a dose of $\approx 2\,\text{MGy}$.

Overall, the D_{it} values determined from both measurement techniques are compatible in magnitude over the studied dose range, with the exception of the peak region. Here, the values from the I/V measurements are larger by approximately a factor of 3, while they otherwise tend to be no more than 25% above the values from the C/V measurements.

The reason for these large discrepancy seen in the peak region is likely found in the systematic effects of the measurements discussed in the previous sections. However, the other parameters entering the calculations such as the capture cross-section, σ, and the thermal velocity, v_{th}, or the intrinsic charge carrier density, n_i, also have a large effect on the extracted D_{it} values. Using other values for these parameters, e.g. found in [191, 203], can yield significantly different results, especially in the case of D_{it} derived from I_{surf}.

The results presented in figure 15.5 can therefore only serve as a guidance point for the actual interface state density.

In principle, the thus derived D_{it} values could be used to extract the number of fixed

---

[5] Additionally, the temperature ($T = 294\,\text{K}$) and the doping concentration ($N_D = 5 \cdot 10^{12}\,\text{cm}^{-3}$) need to be experimentally determined. Other parameters were used as described in the text of chapter 14.3, specifically $\sigma = 2.5 \cdot 10^{-16}\,\text{cm}^2$ [179], $v_{th} = 2.0 \cdot 10^7\,\text{cm/s}$ [193], and $n_i = 1 \cdot 10^{10}\,\text{cm}^{-3}$ [193].

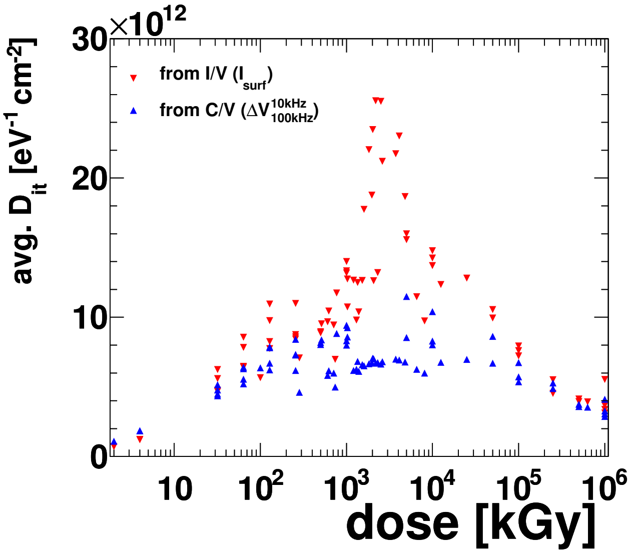

Figure 15.5: Values of *average* D_{it} determined from I/V measurements using I_{surf} (down-pointing triangles) and from C/V measurements using ΔV_g between C/V curves measured at 10 kHz and at 100 kHz (up-pointing triangles).

oxide charges, e.g. by predicting a shift of the flat-band voltage due to the interface charges and subtracting this from the measured values presented in figure 15.2b.

However, this introduces additional assumptions on the electric nature of the interface states, i.e. whether they are donors or acceptors, and hardly gives reliable results with the "naive" model of D_{it} used in the calculations.

Section 15.5 therefore presents a more elaborate study based on the D_{it} spectra determined in TDRC measurements. The study aims at a separation of traps present at the interface, including border traps which will be discussed in the following section.

15.4. Border Traps and Reproducibility of Measurements

The C/V measurements of irradiated samples featured strong "hysteresis" effects as shown in the left plot of figure 15.6: there is a significant shift between the "up" and "down" curves[6]. The shape of the C/V curve however is not affected. The voltage shift of the "up" curve depends on the history and storage condition of the diode. The voltage shift of the "down" curve depends on the maximum value of V_{gate} to which the MOS capacitor was biased and the time it remained at this voltage. This can be interpreted as evidence for the presence of near-interfacial oxide traps that can communicate with the Si, i.e. border traps.

These border traps build up during biasing and can exchange charge with the underlying Si on times scales from less than 1 μs to many years [198]. They can

---

[6] "Up" corresponds to the measurement when V_{gate} is ramped from zero to negative values; the "up" curve is always below the "down" curve.

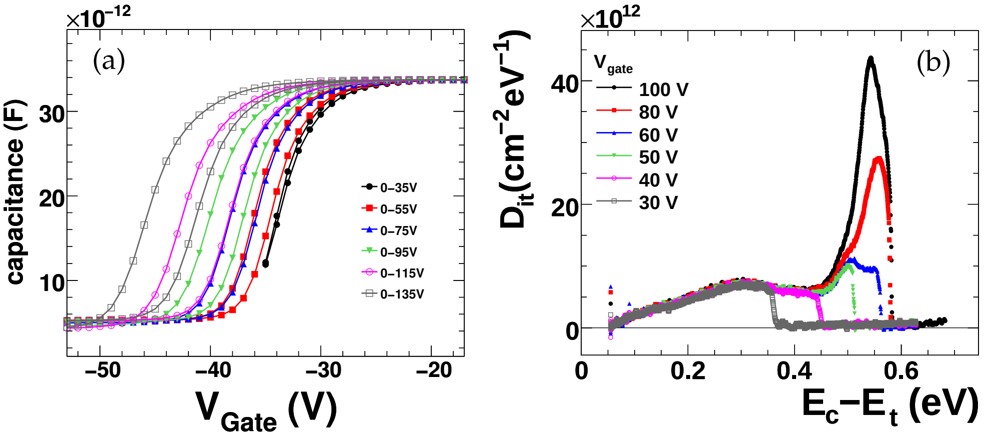

Figure 15.6: *Left:* C/V of a 1 MGy sample. The gate voltage is varied from 0 V to $V_{\mathrm{gate}}^{\mathrm{max}}$ and back to 0 V for increasing maximum gate voltages $V_{\mathrm{gate}}^{\mathrm{max}}$. *Right:* D_{it} versus position in band gap as function of the energy distance from the conduction band. Measured on a 5 MGy sample after annealing for 60 min at 80° C with different values for V_{gate}.

therefore not always be clearly distinguished from interface traps based on their electrical response alone. Border traps are also believed to be the main cause of $1/f$ noise in MOS devices [204, 205]. Furthermore, they effectively prevent reproducible measurements of C/V curves. Only the very first "up" curve measured can be assumed not to be distorted by mobile oxide charges.

All results presented in the previous section 15.2 were produced based on measurements starting in accumulation and using only the first[7] "up" curve of each C/V measurement. They should therefore be unaffected by border traps with response times much greater than the small-signal frequency f_{AC} or by border traps sufficiently deep in the oxide to be only charged when biasing far in inversion.

The TDRC measurements are similarly affected, as shown in figure 15.6b, where at higher gate voltages a significant increase of D_{it} is observed at $E_c - E_t \approx 0.55\,\mathrm{eV}$.

The following section presents a study, which aims at a separation of the different types of charges present at the Si-SiO$_2$ surface.

15.5. Separation of Extracted Trap Densities

To further investigate the radiation induced reduction in $I_{\mathrm{surf}}/A_{\mathrm{gate}}$, the shift of the C/V curves, and D_{it} additional measurements were performed on the 9 gate-controlled diodes of the last irradiation campaign [202]. The study[8], which aims at determining the interface charge trap density D_{it}, the fixed oxide charge density N_{ox}, and the border

---

[7] The frequency is continuously switching between the different values while the gate voltage is ramped up, therefore allowing to measure the curves at all frequencies "simultaneously".

[8] This study was performed together with T. Theedt and S. Veljovic.

trap charge density N_{border}, proceeds in the following steps:

1. bring the sample into a well-defined state by annealing it for 60 minutes at 80° C,
2. obtain D_{it} as function of $E_c - E_t$ from the TDRC spectrum,
3. compare the calculated shape and frequency dependence of the C/V curve from model calculations, based on the extracted D_{it}, with the measurements; from N_{it}, the integral over D_{it}, the voltage shift ΔV_{it} due to the interface traps is calculated,
4. subtract from the voltage shift of the first "up" C/V curve the voltage shift ΔV_{it} to obtain the fixed oxide charge density N_{ox},
5. obtain the border trap charge density N_{border} from the difference of the voltage shift "down" minus first "up" C/V curve.

It should be noted that in particular the values obtained for N_{border} depend on the maximum value of V_{gate} and on the time the MOS capacitance was biased at this value. The chosen measurement parameters have therefore been kept constant, with $V_{\text{gate}}^{\text{max}} = -100\,\text{V}$, in order to obtain comparable results.

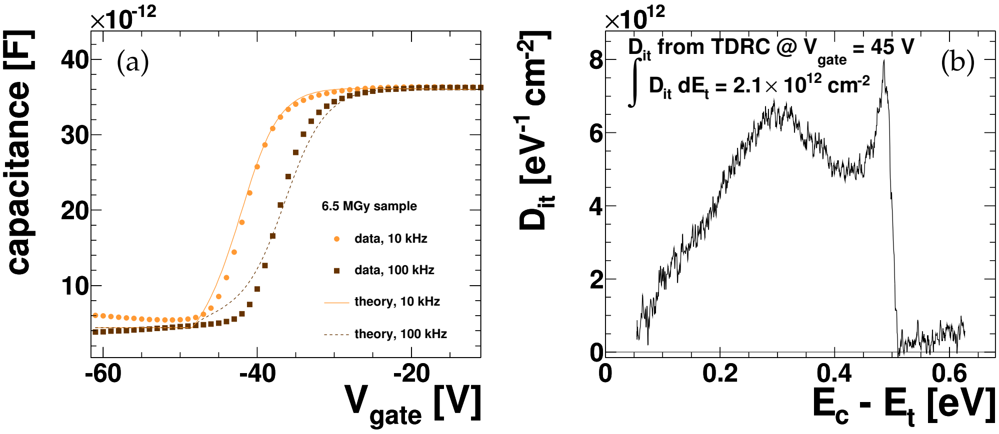

Figure 15.7: C/V measurements of an irradiated sample at different frequencies compared to model calculations (*left*). The calculations are based on a D_{it} spectrum measured from the same sample (*right*) and the assumptions of acceptor-like interface states and $N_{\text{ox}} = 2.9 \cdot 10^{12}\,\text{cm}^{-2}$. The sample was irradiated to 6.5 MGy and annealed at 80° C for 60 min before the measurements.

Figure 15.7 shows the comparison between the measured "up" C/V curves of a 6.5 MGy sample and the model prediction[9] on the left hand side, and the D_{it} spectrum from TDRC measurements of the same sample on the right.

Using the extracted D_{it} spectrum, the model can give a qualitative description of the measured C/V curves. The calculations were performed assuming the interface

---

[9] Using parameters as introduced in the previous chapter 14.3, specifically $\sigma = 2.5 \cdot 10^{-16}\,\text{cm}^2$ [179], $v_{\text{th}} = 2.0 \cdot 10^7\,\text{cm/s}$ [193], and $n_{\text{i}} = 1 \cdot 10^{10}\,\text{cm}^{-3}$ [193].

states to behave only acceptor-like, and a number of fixed oxide charges of $N_{\text{ox}}^{\text{A}} = 2.9 \cdot 10^{12}\,\text{cm}^{-2}$ to match the gate voltages observed in the measurement. By alternatively assuming a purely donor-like nature of the interface states, the possible range for the number of fixed oxide charges can be determined.

Figure 15.8 presents, as function of dose, the results for the thus derived range of N_{ox}, for N_{it} obtained from the TDRC measurement, and for N_{border} determined from the relative shift of the "down" C/V curves.

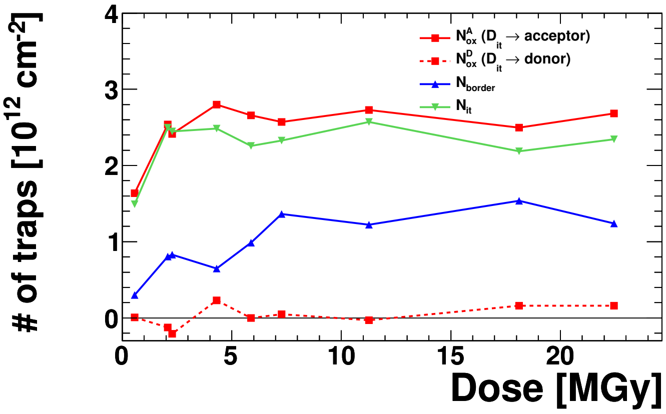

Figure 15.8: As function of dose: the number of interface states, N_{it}, number of border traps, N_{border}, and the number of fixed oxide charges, N_{ox}, assuming either purely donor-like or acceptor-like interface states.

The curves exhibit a rapid increase at doses below $\sim 6\,\text{MGy}$ after which they become flat with only smaller variations. The number of border traps shows the largest increase of almost a factor of 10 over the investigated dose range. It is therefore of similar magnitude as the number of interface states, which is typically larger by a factor of ~ 2. Compared to the average values of D_{it} determined in section 15.3, the values of N_{it} are compatible, albeit smaller[10].

The possible range for the number of fixed oxide charges covers values larger than N_{it} down to negative values (indicating a negative charge contribution). Most likely, the interface states are composed of both donors and acceptors, with a majority of donor-states[11], resulting in N_{ox} being of similar magnitude as N_{it}, for an irradiated sample, but with $N_{\text{it}} > N_{\text{ox}}$.

It must be noted, however, that the extracted values are associated with significant uncertainties. As shown in figure 15.6b, approximately half of the band gap is accessible by the TDRC measurement, but only at high gate-voltages. Such high voltages, on the other hand, introduce border traps into the alleged D_{it} spectrum. The number of interface states and consequently the number of fixed oxide charges would therefore be either overestimated or underestimated, depending on the choice of gate-voltage at

---

[10] The respective $N_{\text{it}}^{\text{homog.}}$ for a homogeneous D_{it} distribution depends on the limits of the integration; as indicated by figure 15.7b, $0 \rightarrow 0.5\,\text{eV}$ seems reasonable.

[11] See [193], section 7.3.6(c).

which the TDRC measurements are performed.

Furthermore, the model calculations depend on parameters, that are not known a priori for the specific samples investigated, but directly impact the presented results.

This analysis can therefore be regarded as first step toward an extraction and separation of the individual interface properties that determine the electrical behavior of irradiated gate-controlled diodes. A more sophisticated study currently in progress is introduced in the outlook at the end of the next chapter.

16. Summary

For the study of radiation damage of silicon sensors by 12 keV X-rays for doses up to 1 GGy an irradiation facility has been set up at HASYLAB at DESY.

Measurements performed on gate-controlled diodes immediately after X-ray irradiation show a strong increase of the surface current, of the flat-band voltage, and of the frequency dependence of the C/V curves, as well as a significant change in the slope of the C/V curves. These quantities reach maxima at a dose of 1 – 5 MGy and decrease for higher doses in the measured dose range up to 1 GGy.

From measurements of samples irradiated at different dose rates and through temperature monitoring, it can be concluded that the decrease at high doses is most likely not caused by temperature-induced effects during irradiation.

Using model calculations for the C/V curves and assuming a homogeneous distribution of interface states, the average D_{it} can be independently extracted from I/V and C/V measurements. The resulting values are typically of the order of 10^{12} – $10^{13}\,\mathrm{eV}^{-1}\mathrm{cm}^{-2}$ for both measurement techniques and show the previously observed strong increase and subsequent drop-off at higher doses.

However, due to the "naivety" of the assumption of a uniform D_{it} and additional parameters not known a priori, the result is associated with considerable uncertainties.

Additionally to the large number of interface states, evidence was found for the presence of border traps in both C/V and TDRC measurements of irradiated samples. These near-interfacial oxide traps pose a complication for the reproducibility of the measurements, as their electrical behavior strongly depends on the previous biasing conditions of the sample.

The different types of traps present at the Si-$\mathrm{SiO_2}$ surface were shown to exhibit some distinct electrical characteristics as observed in I/V, C/V, and TDRC measurements of the gate-controlled diodes. The individual number of traps and their density distributions therefore constitute important parameters for simulations of the sensor performance, and need to be known for accurate predictions of the sensor response as function of the irradiation dose.

A further study was presented, that quantified for irradiated samples in the dose range of 0.25 – 25 MGy the number of interface traps, N_{it}, of fixed oxide charges, N_{ox}, and of border traps[1], N_{border}. The measurements were performed after after an annealing of the samples for 60 min at 80° C. From C/V and TDRC measurements together with model calculations based on this data, N_{it} and N_{border} as well as limits for N_{ox} were determined as function of dose.

The curves exhibit a rapid increase at doses below ~ 6 MGy after which they remain almost flat. For all trap types, the number of traps for higher doses is of the order of $10^{12}\,\mathrm{cm}^{-2}$. The precise value for the number of oxide charges depends on assumptions

---

[1] Since the effect of border traps on the measurement depends on the biasing conditions, the measurement parameters were kept constant, with a maximum gate voltage of -100 V.

whether the interface states act donor- or acceptor-like, which leads to a wide range of possible values for N_{ox}. However, for most configurations, where the interface states are acting as a mixture of donors and acceptors, N_{it} constitutes the dominant trap type.

The fact that after annealing, the number of interface states appears to saturate with dose is in striking contrast to the previous observations directly after irradiation. This points to a unstable type of defect at the interface being responsible for the observed decrease of the surface current, the flat-band voltage, and the frequency dependence of the C/V measurements at higher doses. Such defects could be generated through the initial irradiation, and would become electrically inactive through exposure to increased temperatures or further irradiation.

The results are generally compatible with the presence of such a kind of defect, and the saturation of oxide trapped charges and the remaining interface states due to other defect types.

However, to verify this possibility, additional studies are required, exploiting the full sensitivity of both C/V and TDRC measurements to traps present at the Si-SiO_2 surface. In order to deliver a reliable and quantitative extraction of the relevant parameters, improvements to the model and experimental determination of the parameters entering the calculations might be necessary.

Outlook

Improving upon the results presented in this thesis, a study is currently in progress, that aims at a clear separation of the different charges present at the surface and at identifying individual traps contributing to D_{it} as well as their properties as function of dose [206].

The parameters extracted in these studies are to be implemented into a TCAD [207] simulation with the goal of reproducing the measurements and of later using them for the design of radiation hard sensors for the AGIPD project [208].

Appendix

A. Purities, Efficiencies, and Acceptance Corrections

This chapter shows purities, efficiencies, and acceptance correction factors for cross-sections not previously shown in chapter 8.2.

Inclusive Jets

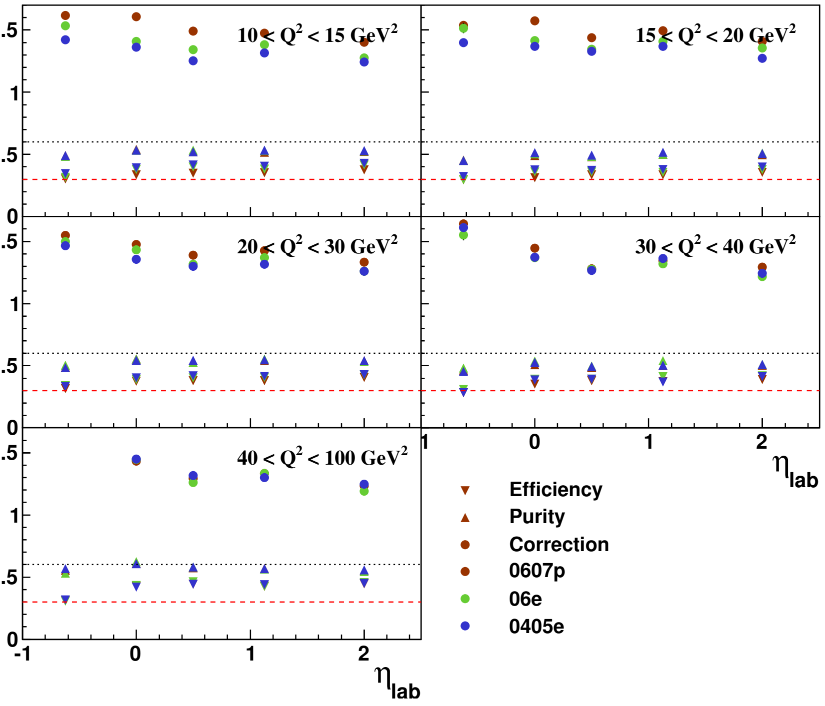

Figure A.1: Purities (up-pointing triangles), efficiencies (down-pointing triangles), and acceptance correction factors (circles) as function of η_{lab} in regions of Q^2 for inclusive jet production. The different data taking periods are shown with different colors.

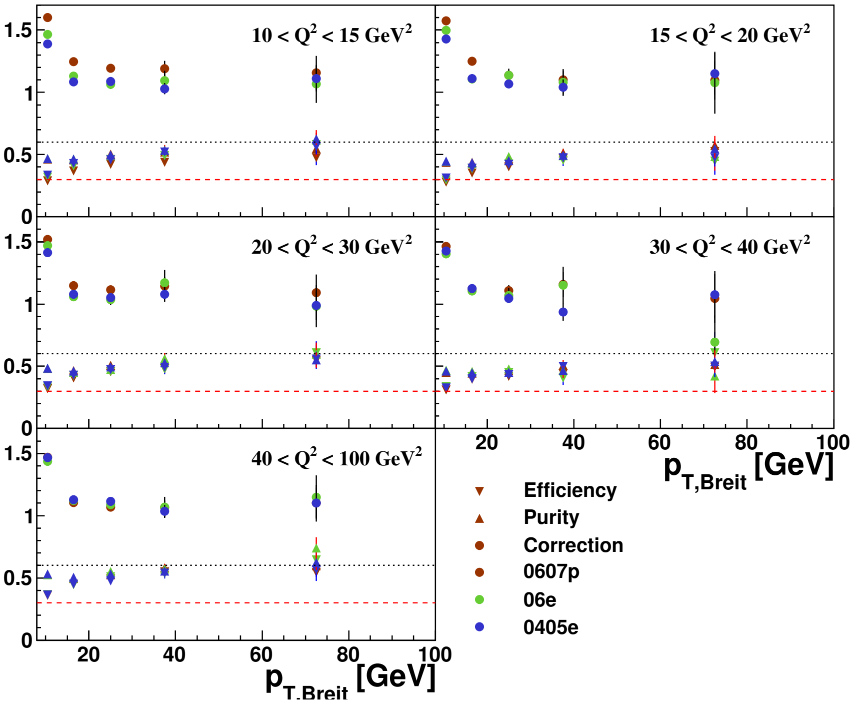

Figure A.2: Purities, efficiencies, and acceptances as function of $p_{T,\mathrm{B}}$ for inclusive jet production in regions of Q^2. For details, see caption to figure A.1.

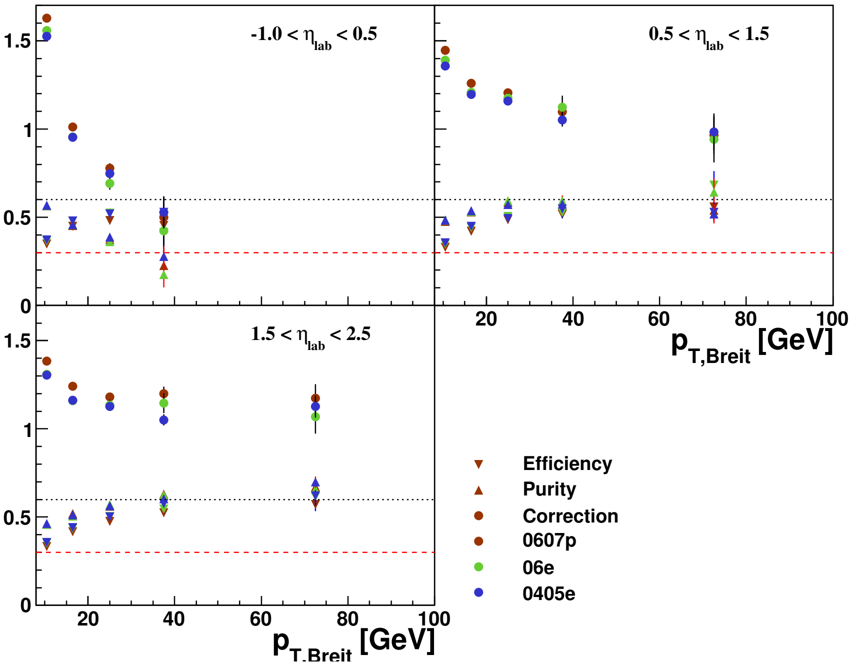

Figure A.3: Purities, efficiencies, and acceptances as function of $p_{T,\mathrm{B}}$ in regions of η_{lab} for inclusive jet production. For details, see caption to figure A.1.

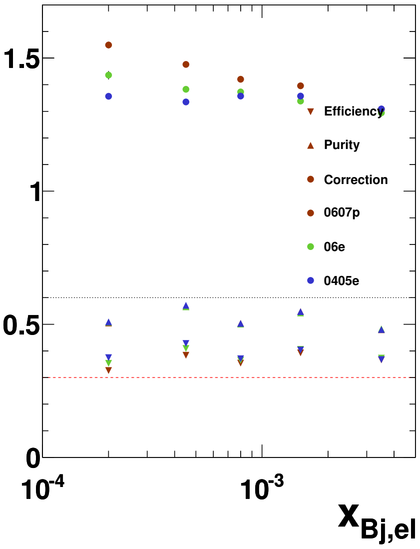

Figure A.4: Purities, efficiencies, and acceptances as function of x_{Bj} for inclusive jet production. For details, see caption to figure A.1.

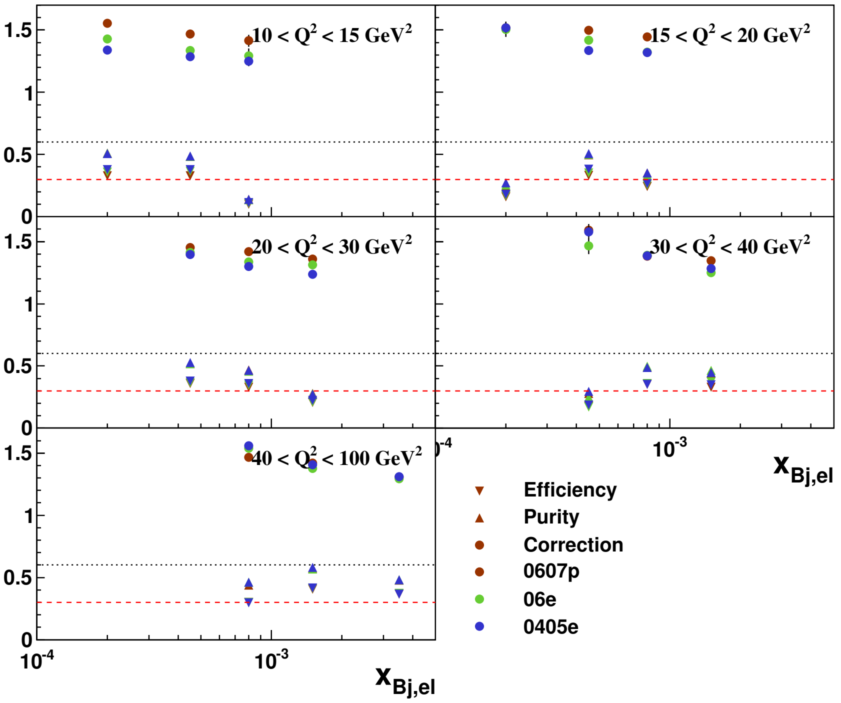

Figure A.5: Purities, efficiencies, and acceptances as function of x_{Bj} for inclusive jet production in regions of Q^2. For details, see caption to figure A.1.

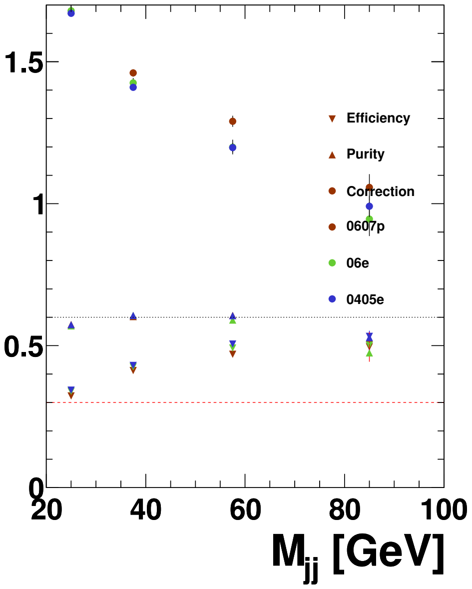

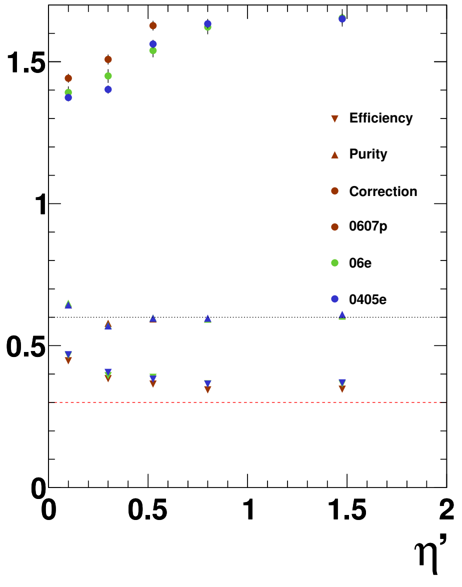

Figure A.6: Purities, efficiencies, and acceptances as function of M_{jj} (left) and η' (right) for the inclusive dijet production. For details, see caption to figure A.1.

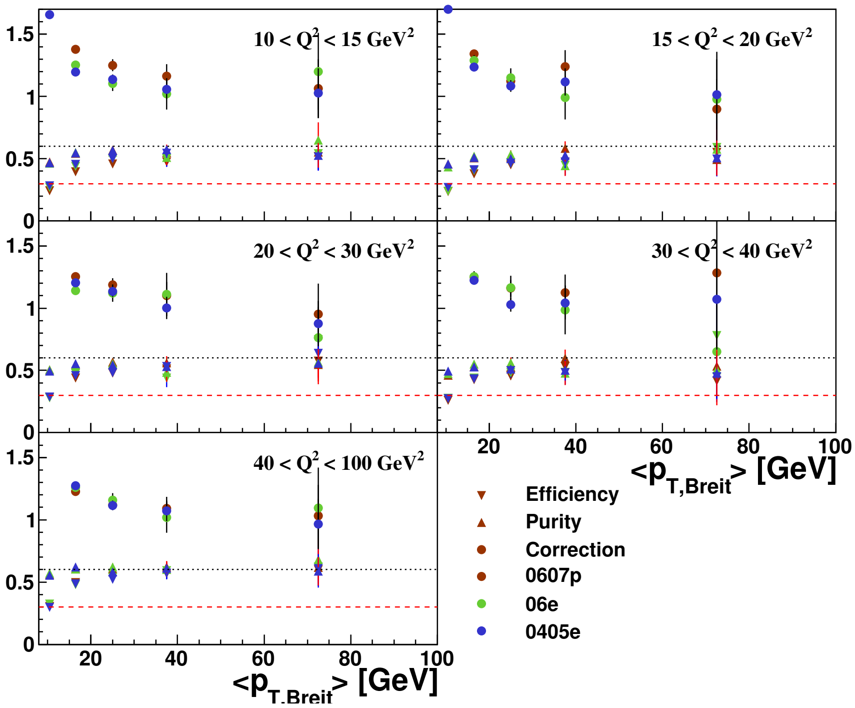

Figure A.7: Purities, efficiencies, and acceptances as function of $\langle p_{T,B} \rangle$ in regions of Q^2 for the inclusive dijet production. For details, see caption to figure A.1.

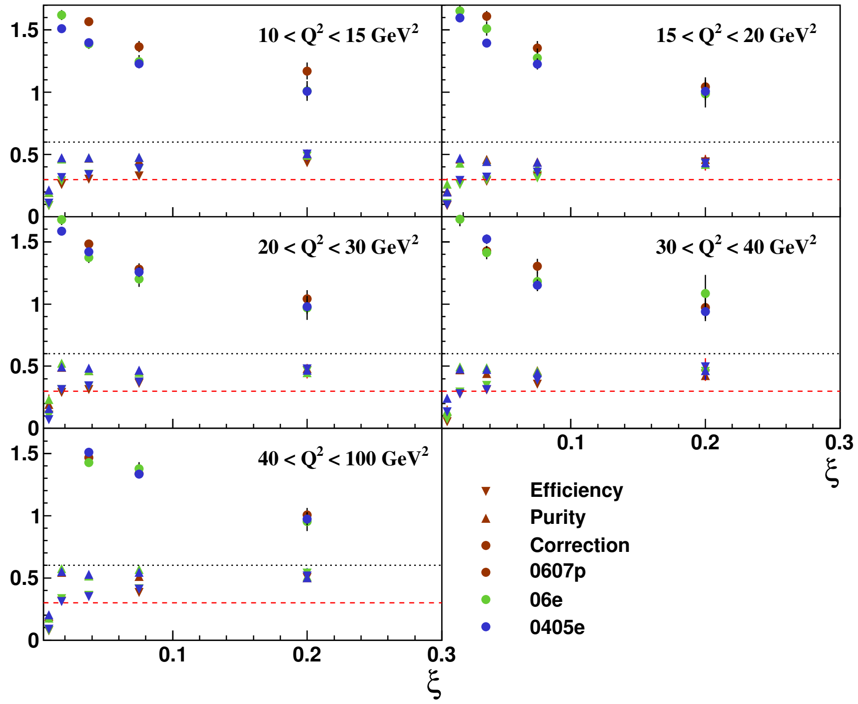

Figure A.8: Purities, efficiencies, and acceptances as function of ξ in regions of Q^2 for the inclusive dijet production. For details, see caption to figure A.1.

Trijet Cross-Sections

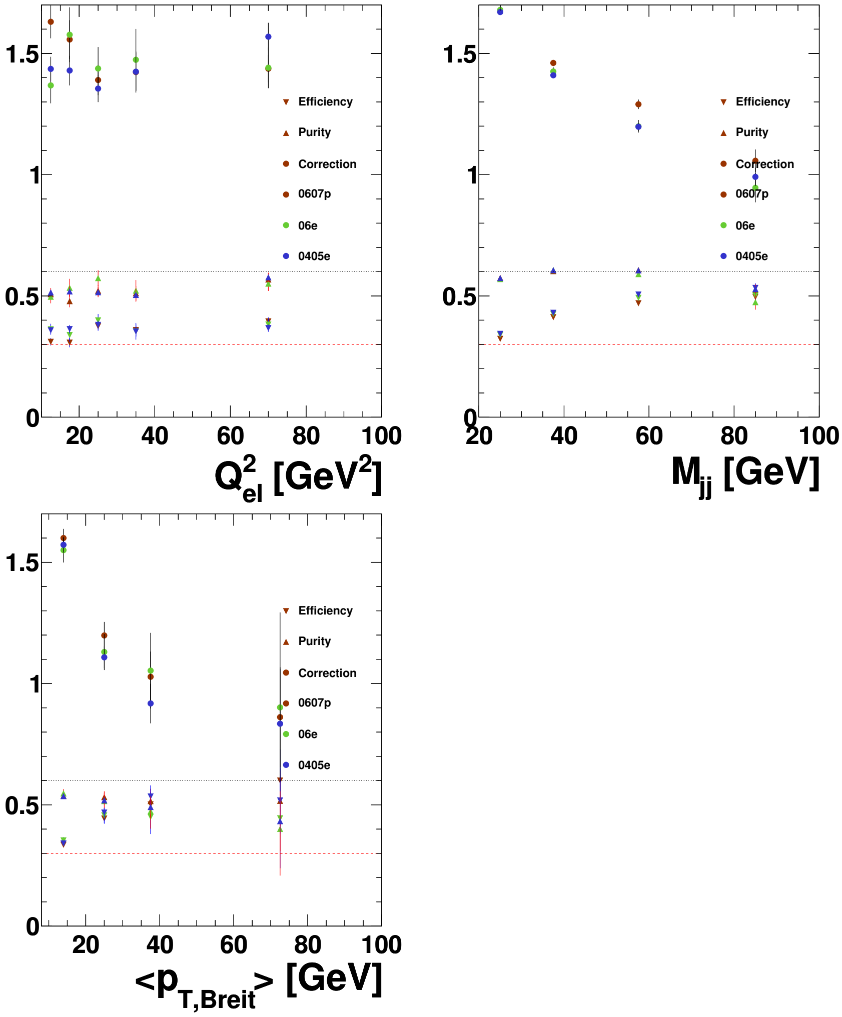

Figure A.9: Purities, efficiencies, and acceptances as function of Q^2 (top left), M_{jj} (top right), and $\langle p_{T,B} \rangle$ (bottom) for the inclusive trijet production. For details, see caption to figure A.1.

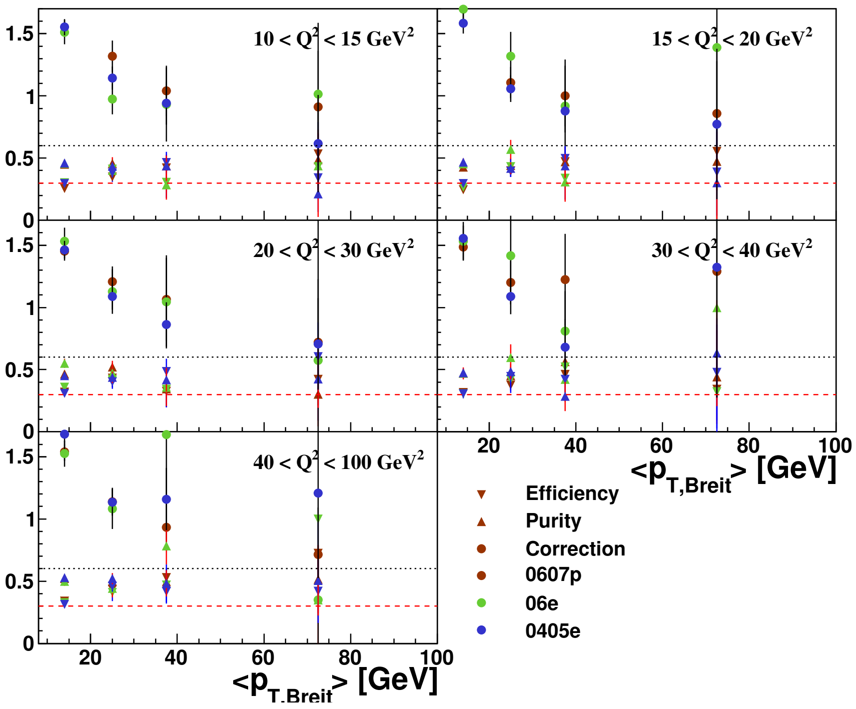

Figure A.10: Purities, efficiencies, and acceptances as function of $\langle p_{T,B} \rangle$ in regions of Q^2 for the inclusive trijet production. For details, see caption to figure A.1.

B. Cross-Section Tables

The following tables give the numerical values for cross-sections presented in the previous chapter 10, together with statistical, uncorrelated systematic, and jet-energy scale uncertainties. The multiplicative factors applied to the data to correct for QED effects and to the NLO calculations to correct for hadronization are listed as well for each bin.

Inclusive Jet Cross-Sections

Q^2 bin [GeV^2]	$d\sigma/dQ^2$ [pb/GeV^2]	δ_{stat} [±%]	δ_{MC} [±%]	δ_{syst} [%]	δ_{ES} [%]	C^{QED}	C^{hadr}
10...15	67.01	0.37	0.30	$^{+2.43}_{-2.37}$	$^{+8.50}_{-7.46}$	0.97	0.86
15...20	43.37	0.46	0.38	$^{+2.56}_{-2.58}$	$^{+9.05}_{-7.82}$	0.97	0.87
20...30	27.78	0.40	0.33	$^{+2.90}_{-2.41}$	$^{+8.89}_{-7.81}$	0.97	0.88
30...40	17.45	0.50	0.42	$^{+2.81}_{-2.98}$	$^{+9.11}_{-7.67}$	0.96	0.90
40...100	7.21	0.32	0.25	$^{+2.77}_{-4.04}$	$^{+8.73}_{-7.59}$	0.95	0.93

Table B.1: Binning, measured values, and uncertainties for the differential cross-section $d\sigma/dQ^2$ for inclusive jet production. The statistical, the uncorrelated systematic (δ_{syst}) and the jet-energy scale uncertainties (δ_{ES}) are stated separately. The statistical uncertainty is shown for data, δ_{stat}, and acceptance correction, δ_{MC}, separately. The last two columns show multiplicative factors applied to the data to correct for higher order QED effects and the running of α_{em} (C^{QED}) and to the NLO calculations to correct for hadronization (C^{hadr}).

η_{lab} bin	$\mathrm{d}\sigma/\,\mathrm{d}\eta_{\mathrm{lab}}$ [pb]	δ_{stat} [±%]	δ_{MC} [±%]	δ_{syst} [%]	δ_{ES} [%]	C^{QED}	C^{hadr}
−1…−0.25	268.17	0.51	0.41	$^{+2.51}_{-2.46}$	$^{+13.86}_{-11.48}$	0.97	0.78
−0.25…0.25	560.61	0.41	0.32	$^{+1.78}_{-2.11}$	$^{+9.80}_{-8.34}$	0.96	0.88
0.25…0.75	621.28	0.37	0.30	$^{+3.22}_{-3.29}$	$^{+8.23}_{-7.15}$	0.96	0.92
0.75…1.5	462.02	0.36	0.28	$^{+3.99}_{-3.91}$	$^{+7.32}_{-6.48}$	0.96	0.93
1.5…2.5	295.70	0.38	0.31	$^{+3.38}_{-3.95}$	$^{+7.30}_{-6.42}$	0.97	0.91

Table B.2: Binning, measured values, and uncertainties for the differential cross-section $\mathrm{d}\sigma/\,\mathrm{d}\eta_{\mathrm{lab}}$ for inclusive jet production. For details see caption to table B.1

η_{lab} bin	$\mathrm{d}^2\sigma/\,\mathrm{d}\eta_{\mathrm{lab}}\,\mathrm{d}Q^2$ [pb/GeV^2]	δ_{stat} [±%]	δ_{MC} [±%]	δ_{syst} [%]	δ_{ES} [%]	C^{QED}	C^{hadr}
$10 < Q^2 < 15\,\mathrm{GeV}^2$							
−1…−0.25	12.15	1.05	0.91	$^{+1.93}_{-2.06}$	$^{+14.16}_{-11.54}$	0.97	0.73
−0.25…0.25	25.35	0.86	0.74	$^{+1.61}_{-1.49}$	$^{+9.86}_{-8.25}$	0.96	0.85
0.25…0.75	27.87	0.80	0.69	$^{+2.87}_{-2.88}$	$^{+8.09}_{-7.20}$	0.96	0.89
0.75…1.5	21.78	0.75	0.62	$^{+3.92}_{-3.19}$	$^{+6.77}_{-6.33}$	0.98	0.89
1.5…2.5	14.96	0.76	0.63	$^{+2.72}_{-3.49}$	$^{+6.99}_{-6.10}$	0.97	0.89
$15 < Q^2 < 20\,\mathrm{GeV}^2$							
−1…−0.25	7.89	1.28	1.12	$^{+2.71}_{-1.95}$	$^{+14.56}_{-11.84}$	0.98	0.75
−0.25…0.25	16.85	1.06	0.92	$^{+2.26}_{-1.86}$	$^{+10.29}_{-8.26}$	0.96	0.86
0.25…0.75	18.42	0.99	0.88	$^{+2.62}_{-2.70}$	$^{+8.68}_{-7.29}$	0.97	0.90
0.75…1.5	13.97	0.94	0.80	$^{+2.81}_{-3.56}$	$^{+7.20}_{-6.71}$	0.96	0.91
1.5…2.5	9.33	0.97	0.83	$^{+3.92}_{-3.92}$	$^{+7.39}_{-6.62}$	0.97	0.90
$20 < Q^2 < 30\,\mathrm{GeV}^2$							
−1…−0.25	4.95	1.15	0.95	$^{+2.80}_{-2.04}$	$^{+14.06}_{-11.44}$	0.97	0.78
−0.25…0.25	10.80	0.92	0.76	$^{+2.14}_{-2.16}$	$^{+10.36}_{-8.57}$	0.96	0.88
0.25…0.75	12.23	0.85	0.74	$^{+3.41}_{-2.67}$	$^{+8.02}_{-7.33}$	0.97	0.91
0.75…1.5	8.85	0.82	0.68	$^{+4.38}_{-3.35}$	$^{+7.36}_{-6.67}$	0.97	0.92
1.5…2.5	5.85	0.85	0.73	$^{+3.44}_{-3.34}$	$^{+7.10}_{-6.46}$	0.97	0.90
$30 < Q^2 < 40\,\mathrm{GeV}^2$							
−1…−0.25	3.45	1.42	1.23	$^{+3.30}_{-3.06}$	$^{+13.35}_{-11.64}$	0.97	0.80

Table B.3 – continued from previous page

η_{lab} bin	$\mathrm{d}^2\sigma/\,\mathrm{d}\eta_{\text{lab}}\,\mathrm{d}Q^2$ [pb/GeV^2]	δ_{stat} [±%]	δ_{MC} [±%]	δ_{syst} [%]	δ_{ES} [%]	C^{QED}	C^{hadr}
$-0.25\ldots0.25$	7.01	1.15	0.95	$^{+1.83}_{-2.53}$	$^{+10.34}_{-8.48}$	0.98	0.89
$0.25\ldots0.75$	7.44	1.05	0.93	$^{+3.71}_{-3.55}$	$^{+8.59}_{-7.11}$	0.96	0.93
$0.75\ldots1.5$	5.64	1.01	0.88	$^{+4.09}_{-3.97}$	$^{+7.85}_{-6.42}$	0.95	0.94
$1.5\ldots2.5$	3.37	1.10	0.97	$^{+3.81}_{-4.28}$	$^{+7.33}_{-6.19}$	0.96	0.92
$40 < Q^2 < 100\,\text{GeV}^2$							
$-1\ldots-0.25$	1.39	0.96	0.76	$^{+2.52}_{-4.04}$	$^{+13.40}_{-11.20}$	0.95	0.84
$-0.25\ldots0.25$	2.86	0.73	0.57	$^{+1.60}_{-3.27}$	$^{+8.97}_{-8.22}$	0.95	0.92
$0.25\ldots0.75$	3.22	0.66	0.54	$^{+3.54}_{-4.50}$	$^{+8.13}_{-6.97}$	0.94	0.95
$0.75\ldots1.5$	2.29	0.64	0.53	$^{+4.55}_{-5.29}$	$^{+7.62}_{-6.40}$	0.95	0.98
$1.5\ldots2.5$	1.36	0.70	0.62	$^{+3.86}_{-4.99}$	$^{+7.72}_{-6.72}$	0.95	0.95

Table B.3: Binning, measured values, and uncertainties for the double-differential cross-section $\mathrm{d}^2\sigma/\,\mathrm{d}Q^2\,\mathrm{d}\eta_{\text{lab}}$ for inclusive jet production. For details see caption to table B.1

$p_{T,\text{B}}$ bin [GeV]	$\mathrm{d}\sigma/\,\mathrm{d}p_{T,\text{B}}$ [pb/GeV]	δ_{stat} [±%]	δ_{MC} [±%]	δ_{syst} [%]	δ_{ES} [%]	C^{QED}	C^{hadr}
$8\ldots13$	231.32	0.20	0.17	$^{+3.12}_{-3.28}$	$^{+10.23}_{-8.48}$	0.96	0.88
$13\ldots20$	33.02	0.40	0.34	$^{+2.89}_{-3.12}$	$^{+4.89}_{-5.36}$	0.96	0.91
$20\ldots30$	4.39	0.90	0.72	$^{+3.55}_{-3.91}$	$^{+3.75}_{-3.67}$	0.97	0.93
$30\ldots45$	$4.76\cdot10^{-1}$	2.24	1.54	$^{+5.18}_{-5.74}$	$^{+4.35}_{-3.74}$	0.98	0.95
$45\ldots100$	$1.39\cdot10^{-2}$	6.82	3.37	$^{+8.81}_{-10.48}$	$^{+4.76}_{-5.23}$	0.97	0.93

Table B.4: Binning, measured values, and uncertainties for the differential cross-section $\mathrm{d}\sigma/\,\mathrm{d}p_T$ for inclusive jet production. For details see caption to table B.1

$p_{T,\text{B}}$ bin [GeV]	$\mathrm{d}^2\sigma/\,\mathrm{d}p_{T,\text{B}}\,\mathrm{d}Q^2$ [pb/GeV^3]	δ_{stat} [±%]	δ_{MC} [±%]	δ_{syst} [%]	δ_{ES} [%]	C^{QED}	C^{hadr}
$10 < Q^2 < 15\,\text{GeV}^2$							
$8\ldots13$	11.09	0.42	0.38	$^{+2.83}_{-2.75}$	$^{+10.30}_{-8.56}$	0.97	0.84
$13\ldots20$	1.46	0.86	0.72	$^{+2.75}_{-2.59}$	$^{+4.05}_{-4.58}$	0.96	0.89
$20\ldots30$	$1.81\cdot10^{-1}$	2.02	1.46	$^{+3.19}_{-4.15}$	$^{+3.01}_{-3.37}$	0.98	0.92

Table B.5 – continued from previous page

$p_{T,\mathrm{B}}$ bin [GeV]	$\mathrm{d}^2\sigma/\,\mathrm{d}p_{T,\mathrm{B}}\,\mathrm{d}Q^2$ [pb/GeV^3]	δ_{stat} [$\pm$%]	δ_{MC} [$\pm$%]	δ_{syst} [%]	δ_{ES} [%]	C^{QED}	C^{hadr}
30...45	$1.90\cdot10^{-2}$	5.06	3.08	$^{+5.23}_{-4.78}$	$^{+4.53}_{-4.20}$	0.98	0.95
45...100	$5.59\cdot10^{-4}$	15.08	6.64	$^{+9.85}_{-9.46}$	$^{+4.67}_{-4.18}$	0.93	0.93
$15 < Q^2 < 20\,\mathrm{GeV}^2$							
8...13	7.05	0.53	0.48	$^{+2.90}_{-3.20}$	$^{+10.82}_{-8.91}$	0.96	0.86
13...20	$9.83\cdot10^{-1}$	1.05	0.93	$^{+3.05}_{-2.63}$	$^{+4.36}_{-4.88}$	0.97	0.90
20...30	$1.26\cdot10^{-1}$	2.40	1.94	$^{+4.10}_{-3.11}$	$^{+3.85}_{-3.25}$	0.97	0.92
30...45	$1.36\cdot10^{-2}$	5.91	4.05	$^{+4.98}_{-5.42}$	$^{+4.57}_{-2.46}$	0.99	0.94
45...100	$3.91\cdot10^{-4}$	17.97	9.65	$^{+8.53}_{-8.73}$	$^{+3.82}_{-8.04}$	0.93	0.94
$20 < Q^2 < 30\,\mathrm{GeV}^2$							
8...13	4.50	0.46	0.41	$^{+3.33}_{-2.95}$	$^{+10.35}_{-8.70}$	0.96	0.87
13...20	$6.25\cdot10^{-1}$	0.91	0.81	$^{+3.28}_{-2.82}$	$^{+4.95}_{-5.35}$	0.97	0.90
20...30	$7.85\cdot10^{-2}$	2.12	1.72	$^{+3.86}_{-3.12}$	$^{+3.96}_{-3.83}$	0.97	0.91
30...45	$9.43\cdot10^{-3}$	5.25	3.77	$^{+5.23}_{-4.66}$	$^{+3.13}_{-4.39}$	1.03	0.97
45...100	$2.65\cdot10^{-4}$	15.64	8.34	$^{+11.47}_{-8.45}$	$^{+5.98}_{-4.00}$	1.02	0.90
$30 < Q^2 < 40\,\mathrm{GeV}^2$							
8...13	2.79	0.58	0.51	$^{+3.34}_{-3.18}$	$^{+10.54}_{-8.31}$	0.96	0.89
13...20	$4.07\cdot10^{-1}$	1.14	1.05	$^{+2.84}_{-3.45}$	$^{+4.77}_{-5.90}$	0.97	0.92
20...30	$5.34\cdot10^{-2}$	2.54	2.35	$^{+3.79}_{-5.32}$	$^{+4.38}_{-3.85}$	0.95	0.93
30...45	$5.80\cdot10^{-3}$	6.42	5.50	$^{+5.50}_{-6.82}$	$^{+3.53}_{-3.53}$	0.98	0.91
45...100	$1.44\cdot10^{-4}$	22.43	12.58	$^{+9.76}_{-11.17}$	$^{+6.37}_{-3.42}$	1.13	0.99
$40 < Q^2 < 100\,\mathrm{GeV}^2$							
8...13	1.13	0.37	0.31	$^{+3.33}_{-4.29}$	$^{+9.70}_{-8.15}$	0.95	0.93
13...20	$1.74\cdot10^{-1}$	0.70	0.64	$^{+2.87}_{-4.55}$	$^{+5.92}_{-6.04}$	0.95	0.94
20...30	$2.53\cdot10^{-2}$	1.54	1.46	$^{+3.86}_{-4.86}$	$^{+4.04}_{-4.06}$	0.97	0.95
30...45	$2.59\cdot10^{-3}$	3.74	3.28	$^{+5.97}_{-9.33}$	$^{+5.30}_{-3.62}$	0.92	0.94
45...100	$8.85\cdot10^{-5}$	11.25	7.46	$^{+8.35}_{-20.97}$	$^{+4.34}_{-5.77}$	0.99	0.93

Table B.5: Binning, measured values, and uncertainties for the double-differential cross-section $\mathrm{d}^2\sigma/\,\mathrm{d}Q^2\,\mathrm{d}p_T$ for inclusive jet production. For details see caption to table B.1

$p_{T,\mathrm{B}}$ bin [GeV]	$\mathrm{d}^2\sigma/\,\mathrm{d}p_{T,\mathrm{B}}\,\mathrm{d}\eta$ [pb/GeV]	δ_{stat} [±%]	δ_{MC} [±%]	δ_{syst} [%]	δ_{ES} [%]	C^{QED}	C^{hadr}
$-1.00 < \eta_{\mathrm{lab}} < 0.50$							
8…13	74.65	0.30	0.25	$^{+2.08}_{-2.28}$	$^{+11.18}_{-9.23}$	0.96	0.86
13…20	6.91	0.66	0.61	$^{+3.88}_{-3.84}$	$^{+8.25}_{-8.36}$	0.97	0.84
20…30	$4.15 \cdot 10^{-1}$	1.96	2.15	$^{+7.38}_{-6.70}$	$^{+6.47}_{-6.20}$	0.94	0.80
30…45	*omitted*						
45…100	*omitted*						
$0.50 < \eta_{\mathrm{lab}} < 1.50$							
8…13	74.50	0.35	0.31	$^{+4.59}_{-4.47}$	$^{+9.13}_{-7.55}$	0.96	0.92
13…20	14.14	0.63	0.53	$^{+3.28}_{-3.45}$	$^{+3.67}_{-4.42}$	0.96	0.94
20…30	2.25	1.31	1.05	$^{+3.07}_{-4.02}$	$^{+3.67}_{-3.35}$	0.97	0.93
30…45	$2.43 \cdot 10^{-1}$	3.13	2.45	$^{+5.47}_{-5.55}$	$^{+4.95}_{-4.39}$	0.98	0.92
45…100	$5.75 \cdot 10^{-3}$	9.95	7.03	$^{+11.50}_{-11.95}$	$^{+3.81}_{-6.28}$	0.95	0.85
$1.50 < \eta_{\mathrm{lab}} < 2.50$							
8…13	44.09	0.44	0.42	$^{+3.83}_{-4.34}$	$^{+9.84}_{-8.23}$	0.96	0.88
13…20	8.43	0.81	0.67	$^{+3.01}_{-3.58}$	$^{+2.44}_{-2.51}$	0.97	0.96
20…30	1.44	1.62	1.15	$^{+3.51}_{-3.50}$	$^{+2.71}_{-2.90}$	0.98	0.97
30…45	$2.03 \cdot 10^{-1}$	3.50	2.05	$^{+4.70}_{-6.20}$	$^{+3.58}_{-2.88}$	0.98	0.98
45…100	$7.52 \cdot 10^{-3}$	9.54	3.97	$^{+7.38}_{-10.58}$	$^{+5.02}_{-4.83}$	0.98	0.97

Table B.6: Binning, measured values, and uncertainties for the double-differential cross-section $\mathrm{d}^2\sigma/\,\mathrm{d}\eta_{\mathrm{lab}}\,\mathrm{d}p_T$ for inclusive jet production. For details see caption to table B.1

x_{Bj} bin	$\mathrm{d}\sigma/\,\mathrm{d}x_{\mathrm{Bj}}$ [pb]	δ_{stat} [±%]	δ_{MC} [±%]	δ_{syst} [%]	δ_{ES} [%]	C^{QED}	C^{hadr}
$1.0 \cdot 10^{-4} \ldots 3.0 \cdot 10^{-4}$	$7.89 \cdot 10^{5}$	0.55	0.47	$^{+3.04}_{-2.96}$	$^{+7.75}_{-6.87}$	0.97	0.88
$3.0 \cdot 10^{-4} \ldots 6.0 \cdot 10^{-4}$	$1.51 \cdot 10^{6}$	0.32	0.26	$^{+2.48}_{-2.29}$	$^{+8.67}_{-7.48}$	0.97	0.87
$6.0 \cdot 10^{-4} \ldots 1.0 \cdot 10^{-3}$	$8.26 \cdot 10^{5}$	0.37	0.32	$^{+2.55}_{-2.84}$	$^{+9.08}_{-8.02}$	0.96	0.89
$1.0 \cdot 10^{-3} \ldots 2.0 \cdot 10^{-3}$	$3.47 \cdot 10^{5}$	0.36	0.30	$^{+3.03}_{-3.51}$	$^{+9.04}_{-7.78}$	0.95	0.91
$2.0 \cdot 10^{-3} \ldots 5.0 \cdot 10^{-3}$	$4.94 \cdot 10^{4}$	0.53	0.47	$^{+2.96}_{-4.55}$	$^{+9.06}_{-7.79}$	0.95	0.93

Table B.7: Binning, measured values, and uncertainties for the differential cross-section $\mathrm{d}\sigma/\,\mathrm{d}x_{\mathrm{Bj}}$ for inclusive jet production. For details see caption to table B.1

x_{Bj} bin	$\mathrm{d}^2\sigma/\,\mathrm{d}x_{\mathrm{Bj}}\,\mathrm{d}Q^2$ [pb/GeV^2]	δ_{stat} [±%]	δ_{MC} [±%]	δ_{syst} [%]	δ_{ES} [%]	C^{QED}	C^{hadr}
$10 < Q^2 < 15\,\mathrm{GeV}^2$							
$1.0 \cdot 10^{-4} \ldots 3.0 \cdot 10^{-4}$	$1.42 \cdot 10^5$	0.58	0.49	$^{+2.84}_{-2.89}$	$^{+7.67}_{-6.80}$	0.97	0.87
$3.0 \cdot 10^{-4} \ldots 6.0 \cdot 10^{-4}$	$1.21 \cdot 10^5$	0.50	0.43	$^{+2.40}_{-2.45}$	$^{+9.01}_{-7.85}$	0.97	0.85
$6.0 \cdot 10^{-4} \ldots 1.0 \cdot 10^{-3}$	*omitted*						
$1.0 \cdot 10^{-3} \ldots 2.0 \cdot 10^{-3}$	*omitted*						
$2.0 \cdot 10^{-3} \ldots 5.0 \cdot 10^{-3}$	*omitted*						
$15 < Q^2 < 20\,\mathrm{GeV}^2$							
$1.0 \cdot 10^{-4} \ldots 3.0 \cdot 10^{-4}$	*omitted*						
$3.0 \cdot 10^{-4} \ldots 6.0 \cdot 10^{-4}$	$9.62 \cdot 10^4$	0.57	0.49	$^{+2.61}_{-2.47}$	$^{+8.74}_{-7.50}$	0.97	0.87
$6.0 \cdot 10^{-4} \ldots 1.0 \cdot 10^{-3}$	$2.82 \cdot 10^4$	0.88	0.84	$^{+2.15}_{-2.71}$	$^{+9.95}_{-8.63}$	0.96	0.86
$1.0 \cdot 10^{-3} \ldots 2.0 \cdot 10^{-3}$	*omitted*						
$2.0 \cdot 10^{-3} \ldots 5.0 \cdot 10^{-3}$	*omitted*						
$20 < Q^2 < 30\,\mathrm{GeV}^2$							
$1.0 \cdot 10^{-4} \ldots 3.0 \cdot 10^{-4}$	*omitted*						
$3.0 \cdot 10^{-4} \ldots 6.0 \cdot 10^{-4}$	$3.82 \cdot 10^4$	0.64	0.54	$^{+2.78}_{-2.36}$	$^{+8.17}_{-6.93}$	0.97	0.89
$6.0 \cdot 10^{-4} \ldots 1.0 \cdot 10^{-3}$	$3.14 \cdot 10^4$	0.59	0.53	$^{+2.91}_{-2.59}$	$^{+9.23}_{-8.38}$	0.96	0.88
$1.0 \cdot 10^{-3} \ldots 2.0 \cdot 10^{-3}$	*omitted*						
$2.0 \cdot 10^{-3} \ldots 5.0 \cdot 10^{-3}$	*omitted*						
$30 < Q^2 < 40\,\mathrm{GeV}^2$							
$1.0 \cdot 10^{-4} \ldots 3.0 \cdot 10^{-4}$	*omitted*						
$3.0 \cdot 10^{-4} \ldots 6.0 \cdot 10^{-4}$	*omitted*						
$6.0 \cdot 10^{-4} \ldots 1.0 \cdot 10^{-3}$	$2.18 \cdot 10^4$	0.72	0.63	$^{+2.77}_{-3.43}$	$^{+8.59}_{-7.32}$	0.97	0.90
$1.0 \cdot 10^{-3} \ldots 2.0 \cdot 10^{-3}$	7435.53	0.75	0.67	$^{+3.21}_{-3.13}$	$^{+9.95}_{-8.17}$	0.95	0.89
$2.0 \cdot 10^{-3} \ldots 5.0 \cdot 10^{-3}$	*omitted*						
$40 < Q^2 < 100\,\mathrm{GeV}^2$							
$1.0 \cdot 10^{-4} \ldots 3.0 \cdot 10^{-4}$	*omitted*						
$3.0 \cdot 10^{-4} \ldots 6.0 \cdot 10^{-4}$	*omitted*						
$6.0 \cdot 10^{-4} \ldots 1.0 \cdot 10^{-3}$	2039.04	1.00	0.90	$^{+2.90}_{-3.96}$	$^{+8.20}_{-7.26}$	0.95	0.93
$1.0 \cdot 10^{-3} \ldots 2.0 \cdot 10^{-3}$	3924.37	0.44	0.36	$^{+2.78}_{-3.85}$	$^{+8.60}_{-7.52}$	0.95	0.93
$2.0 \cdot 10^{-3} \ldots 5.0 \cdot 10^{-3}$	823.96	0.53	0.47	$^{+2.96}_{-4.55}$	$^{+9.06}_{-7.79}$	0.95	0.93

Table B.8: Binning, measured values, and uncertainties for the double-differential cross-section $\mathrm{d}^2\sigma/\,\mathrm{d}Q^2\,\mathrm{d}x_{\mathrm{Bj}}$ for inclusive jet production. For details see caption to table B.1

Dijet Cross-Sections

Q^2 bin [GeV^2]	$\mathrm{d}\sigma/\,\mathrm{d}Q^2$ [pb/GeV^2]	δ_{stat} [±%]	δ_{MC} [±%]	δ_{syst} [%]	δ_{ES} [%]	C^{QED}	C^{hadr}
10...15	14.45	0.83	0.62	$^{+2.23}_{-1.65}$	$^{+9.09}_{-7.89}$	0.97	0.87
15...20	9.75	1.02	0.80	$^{+2.31}_{-1.59}$	$^{+9.16}_{-8.49}$	0.97	0.89
20...30	6.35	0.88	0.67	$^{+2.35}_{-1.66}$	$^{+9.60}_{-8.14}$	0.97	0.90
30...40	4.20	1.10	0.87	$^{+2.17}_{-2.23}$	$^{+9.80}_{-7.93}$	0.97	0.91
40...100	1.81	0.69	0.51	$^{+1.61}_{-3.79}$	$^{+9.43}_{-8.09}$	0.94	0.94

Table B.9: Binning, measured values, and uncertainties for the differential cross-section $\mathrm{d}\sigma/\,\mathrm{d}Q^2$ for inclusive dijet production. For details see caption to table B.1

M_{jj} bin [GeV]	$\mathrm{d}\sigma/\,\mathrm{d}M_{jj}$ [pb/GeV]	δ_{stat} [±%]	δ_{MC} [±%]	δ_{syst} [%]	δ_{ES} [%]	C^{QED}	C^{hadr}
20...30	18.96	0.54	0.43	$^{+2.44}_{-2.21}$	$^{+10.78}_{-8.97}$	0.96	0.89
30...45	7.38	0.65	0.52	$^{+1.69}_{-2.18}$	$^{+8.38}_{-7.50}$	0.97	0.93
45...70	1.22	1.15	0.91	$^{+2.43}_{-2.59}$	$^{+6.43}_{-5.90}$	0.97	0.91
70...100	$9.62 \cdot 10^{-2}$	3.41	2.62	$^{+8.13}_{-8.29}$	$^{+6.36}_{-6.03}$	0.99	0.90

Table B.10: Binning, measured values, and uncertainties for the differential cross-section $\mathrm{d}\sigma/\,\mathrm{d}M_{jj}$ for inclusive dijet production. For details see caption to table B.1

η' bin	$\mathrm{d}\sigma/\,\mathrm{d}\eta'$ [pb]	δ_{stat} [±%]	δ_{MC} [±%]	δ_{syst} [%]	δ_{ES} [%]	C^{QED}	C^{hadr}
$0.0 \ldots 2.0 \cdot 10^{-1}$	285.49	0.89	0.65	$^{+1.96}_{-2.03}$	$^{+8.31}_{-7.41}$	0.96	0.89
0.2...0.4	301.01	0.88	0.70	$^{+2.10}_{-1.98}$	$^{+8.57}_{-7.79}$	0.96	0.91
0.4...0.65	318.97	0.80	0.64	$^{+2.41}_{-2.16}$	$^{+9.13}_{-7.79}$	0.96	0.90
0.65...0.95	268.83	0.82	0.68	$^{+2.16}_{-2.94}$	$^{+9.47}_{-8.14}$	0.96	0.93
0.95...2	56.19	0.97	0.79	$^{+1.86}_{-1.85}$	$^{+12.31}_{-9.77}$	0.97	0.88

Table B.11: Binning, measured values, and uncertainties for the differential cross-section $\mathrm{d}\sigma/\,\mathrm{d}\eta'$ for inclusive dijet production. For details see caption to table B.1

$\langle p_{T,\mathrm{B}}\rangle$ bin [GeV]	$\mathrm{d}\sigma/\,\mathrm{d}\langle p_{T,\mathrm{B}}\rangle$ [pb/GeV]	δ_{stat} [±%]	δ_{MC} [±%]	δ_{syst} [%]	δ_{ES} [%]	C^{QED}	C^{hadr}
8…13	43.86	0.52	0.42	$^{+2.29}_{-2.09}$	$^{+12.07}_{-9.68}$	0.96	0.89
13…20	13.57	0.65	0.50	$^{+2.40}_{-2.66}$	$^{+6.49}_{-6.44}$	0.96	0.92
20…30	1.73	1.47	1.07	$^{+3.45}_{-3.85}$	$^{+4.27}_{-3.84}$	0.97	0.93
30…45	$1.92\cdot 10^{-1}$	3.55	2.46	$^{+6.57}_{-7.20}$	$^{+4.88}_{-3.99}$	0.99	0.95
45…100	$5.24\cdot 10^{-3}$	10.66	6.55	$^{+11.49}_{-11.77}$	$^{+5.83}_{-4.41}$	0.97	0.94

Table B.12: Binning, measured values, and uncertainties for the differential cross-section $\mathrm{d}\sigma/\,\mathrm{d}\langle p_{T,\mathrm{B}}\rangle$ for inclusive dijet production. For details see caption to table B.1

$\langle p_{T,\mathrm{B}}\rangle$ bin [GeV]	$\mathrm{d}^2\sigma/\,\mathrm{d}\langle p_{T,\mathrm{B}}\rangle\,\mathrm{d}Q^2$ [pb/GeV^3]	δ_{stat} [±%]	δ_{MC} [±%]	δ_{syst} [%]	δ_{ES} [%]	C^{QED}	C^{hadr}
$10 < Q^2 < 15\,\mathrm{GeV}^2$							
8…13	1.95	1.09	0.95	$^{+2.59}_{-1.53}$	$^{+12.18}_{-9.88}$	0.97	0.84
13…20	$5.88\cdot 10^{-1}$	1.42	1.10	$^{+2.46}_{-2.14}$	$^{+6.45}_{-5.87}$	0.96	0.90
20…30	$6.98\cdot 10^{-2}$	3.32	2.24	$^{+3.25}_{-4.13}$	$^{+2.66}_{-3.90}$	0.97	0.93
30…45	$7.59\cdot 10^{-3}$	7.99	4.98	$^{+7.03}_{-6.28}$	$^{+6.12}_{-4.06}$	0.99	0.94
45…100	$2.09\cdot 10^{-4}$	24.31	13.50	$^{+12.22}_{-10.27}$	$^{+6.67}_{-4.53}$	0.93	0.94
$15 < Q^2 < 20\,\mathrm{GeV}^2$							
8…13	1.28	1.36	1.18	$^{+2.61}_{-1.84}$	$^{+12.34}_{-10.64}$	0.96	0.87
13…20	$4.02\cdot 10^{-1}$	1.74	1.43	$^{+2.39}_{-1.96}$	$^{+5.67}_{-6.39}$	0.98	0.90
20…30	$5.09\cdot 10^{-2}$	3.81	2.96	$^{+4.15}_{-3.20}$	$^{+5.13}_{-3.12}$	0.98	0.91
30…45	$4.94\cdot 10^{-3}$	10.07	6.82	$^{+6.31}_{-6.87}$	$^{+3.88}_{-4.63}$	0.97	0.95
45…100	$1.53\cdot 10^{-4}$	26.76	18.26	$^{+11.66}_{-9.87}$	$^{+10.84}_{-5.03}$	0.95	1.04
$20 < Q^2 < 30\,\mathrm{GeV}^2$							
8…13	$8.52\cdot 10^{-1}$	1.16	1.00	$^{+2.67}_{-2.03}$	$^{+12.35}_{-9.67}$	0.96	0.88
13…20	$2.47\cdot 10^{-1}$	1.52	1.23	$^{+2.73}_{-2.14}$	$^{+6.83}_{-6.67}$	0.97	0.91
20…30	$3.23\cdot 10^{-2}$	3.46	2.65	$^{+5.11}_{-3.33}$	$^{+4.06}_{-3.68}$	0.99	0.93
30…45	$3.64\cdot 10^{-3}$	8.20	6.24	$^{+7.86}_{-7.63}$	$^{+3.30}_{-3.50}$	1.02	0.94
45…100	$1.09\cdot 10^{-4}$	22.98	15.65	$^{+14.87}_{-10.42}$	$^{+3.24}_{-3.10}$	1.03	0.86
$30 < Q^2 < 40\,\mathrm{GeV}^2$							
8…13	$5.54\cdot 10^{-1}$	1.46	1.25	$^{+2.27}_{-1.91}$	$^{+12.19}_{-9.19}$	0.98	0.90

Table B.13 – continued from previous page

$\langle p_{T,\mathrm{B}}\rangle$ bin [GeV]	$\mathrm{d}^2\sigma/\,\mathrm{d}\langle p_{T,\mathrm{B}}\rangle\,\mathrm{d}Q^2$ [pb/GeV^3]	δ_{stat} [±%]	δ_{MC} [±%]	δ_{syst} [%]	δ_{ES} [%]	C^{QED}	C^{hadr}
13...20	$1.65\cdot 10^{-1}$	1.86	1.59	$^{+2.95}_{-2.97}$	$^{+6.79}_{-6.66}$	0.95	0.93
20...30	$2.17\cdot 10^{-2}$	4.05	3.55	$^{+3.37}_{-5.24}$	$^{+6.04}_{-3.97}$	0.95	0.92
30...45	$2.15\cdot 10^{-3}$	10.92	8.36	$^{+5.41}_{-8.52}$	$^{+5.85}_{-2.99}$	1.06	0.95
45...100	$7.62\cdot 10^{-5}$	32.05	25.49	$^{+11.21}_{-13.19}$	$^{+4.81}_{-4.31}$	1.11	0.97
$40 < Q^2 < 100\,\mathrm{GeV}^2$							
8...13	$2.27\cdot 10^{-1}$	0.93	0.75	$^{+1.93}_{-3.63}$	$^{+11.66}_{-9.28}$	0.94	0.94
13...20	$7.46\cdot 10^{-2}$	1.13	0.94	$^{+2.16}_{-4.18}$	$^{+6.66}_{-6.71}$	0.94	0.95
20...30	$9.62\cdot 10^{-3}$	2.50	2.20	$^{+3.53}_{-5.18}$	$^{+4.85}_{-4.33}$	0.95	0.94
30...45	$1.16\cdot 10^{-3}$	5.73	5.16	$^{+7.29}_{-9.50}$	$^{+4.80}_{-4.35}$	0.95	0.96
45...100	$2.72\cdot 10^{-5}$	18.92	14.16	$^{+11.98}_{-22.01}$	$^{+4.23}_{-4.09}$	0.94	0.93

Table B.13: Binning, measured values, and uncertainties for the double-differential cross-section $\mathrm{d}^2\sigma/\,\mathrm{d}Q^2\,\mathrm{d}\langle p_{T,\mathrm{B}}\rangle$ for inclusive dijet production. For details see caption to table B.1

ξ bin	$\mathrm{d}\sigma/\,\mathrm{d}\xi$ [pb]	δ_{stat} [±%]	δ_{MC} [±%]	δ_{syst} [%]	δ_{ES} [%]	C^{QED}	C^{hadr}
$1.0\cdot 10^{-3}\ldots 2.5\cdot 10^{-2}$	7453.13	0.56	0.45	$^{+2.35}_{-2.37}$	$^{+10.26}_{-8.46}$	0.96	0.89
$2.5\cdot 10^{-2}\ldots 4.5\cdot 10^{-2}$	4919.39	0.70	0.60	$^{+2.36}_{-1.92}$	$^{+9.41}_{-8.25}$	0.96	0.93
$4.5\cdot 10^{-2}\ldots 8.0\cdot 10^{-2}$	1254.21	1.00	0.87	$^{+1.42}_{-2.99}$	$^{+7.57}_{-7.48}$	0.97	0.90
$8.0\cdot 10^{-2}\ldots 1.6\cdot 10^{-1}$	145.47	1.77	1.45	$^{+4.75}_{-4.92}$	$^{+6.56}_{-5.69}$	0.97	0.89
0.16...0.5	4.58	4.48	3.37	$^{+12.67}_{-12.36}$	$^{+7.19}_{-5.61}$	0.99	0.88

Table B.14: Binning, measured values, and uncertainties for the differential cross-section $\mathrm{d}\sigma/\,\mathrm{d}\xi$ for inclusive dijet production. For details see caption to table B.1

ξ bin	$\mathrm{d}^2\sigma/\,\mathrm{d}\xi\,\mathrm{d}Q^2$ [pb/GeV^2]	δ_{stat} [±%]	δ_{MC} [±%]	δ_{syst} [%]	δ_{ES} [%]	C^{QED}	C^{hadr}
$10 < Q^2 < 15\,\mathrm{GeV}^2$							
$1.0\cdot 10^{-3}\ldots 2.5\cdot 10^{-2}$	341.00	1.16	0.98	$^{+2.73}_{-1.91}$	$^{+10.01}_{-8.25}$	0.96	0.85
$2.5\cdot 10^{-2}\ldots 4.5\cdot 10^{-2}$	202.53	1.54	1.33	$^{+2.91}_{-2.04}$	$^{+8.75}_{-7.92}$	0.97	0.90
$4.5\cdot 10^{-2}\ldots 8.0\cdot 10^{-2}$	51.42	2.20	1.90	$^{+1.60}_{-3.64}$	$^{+7.84}_{-7.56}$	0.97	0.88

Table B.15 – continued from previous page

ξ bin	$\mathrm{d}^2\sigma/\,\mathrm{d}\xi\,\mathrm{d}Q^2$ [pb/GeV^2]	δ_{stat} [±%]	δ_{MC} [±%]	δ_{syst} [%]	δ_{ES} [%]	C^{QED}	C^{hadr}
$8.0\cdot10^{-2}\ldots1.6\cdot10^{-1}$	5.72	4.06	2.95	$^{+3.63}_{-3.84}$	$^{+6.90}_{-5.57}$	0.98	0.88
$0.16\ldots0.5$	$1.91\cdot10^{-1}$	9.96	6.59	$^{+11.34}_{-12.84}$	$^{+5.71}_{-6.54}$	0.96	0.88
$15 < Q^2 < 20\,\mathrm{GeV}^2$							
$1.0\cdot10^{-3}\ldots2.5\cdot10^{-2}$	223.58	1.45	1.22	$^{+2.77}_{-2.06}$	$^{+10.20}_{-8.96}$	0.97	0.87
$2.5\cdot10^{-2}\ldots4.5\cdot10^{-2}$	141.71	1.86	1.67	$^{+2.55}_{-1.33}$	$^{+9.21}_{-8.51}$	0.97	0.92
$4.5\cdot10^{-2}\ldots8.0\cdot10^{-2}$	34.00	2.71	2.41	$^{+2.79}_{-1.34}$	$^{+6.69}_{-8.25}$	0.96	0.89
$8.0\cdot10^{-2}\ldots1.6\cdot10^{-1}$	4.23	4.83	3.82	$^{+4.83}_{-4.13}$	$^{+6.61}_{-4.98}$	1.03	0.87
$0.16\ldots0.5$	$1.24\cdot10^{-1}$	11.87	9.50	$^{+13.61}_{-11.84}$	$^{+9.03}_{-6.48}$	0.92	0.87
$20 < Q^2 < 30\,\mathrm{GeV}^2$							
$1.0\cdot10^{-3}\ldots2.5\cdot10^{-2}$	145.20	1.25	1.05	$^{+2.36}_{-2.09}$	$^{+10.63}_{-8.34}$	0.97	0.89
$2.5\cdot10^{-2}\ldots4.5\cdot10^{-2}$	93.00	1.59	1.45	$^{+3.50}_{-2.27}$	$^{+9.49}_{-8.62}$	0.96	0.92
$4.5\cdot10^{-2}\ldots8.0\cdot10^{-2}$	22.12	2.35	2.08	$^{+1.72}_{-1.53}$	$^{+7.75}_{-7.28}$	0.98	0.90
$8.0\cdot10^{-2}\ldots1.6\cdot10^{-1}$	2.53	4.22	3.51	$^{+6.41}_{-5.14}$	$^{+5.76}_{-6.57}$	0.98	0.87
$0.16\ldots0.5$	$8.22\cdot10^{-2}$	10.61	8.37	$^{+12.57}_{-10.92}$	$^{+7.54}_{-4.92}$	1.04	0.91
$30 < Q^2 < 40\,\mathrm{GeV}^2$							
$1.0\cdot10^{-3}\ldots2.5\cdot10^{-2}$	94.05	1.59	1.34	$^{+2.56}_{-2.17}$	$^{+10.66}_{-8.29}$	0.98	0.90
$2.5\cdot10^{-2}\ldots4.5\cdot10^{-2}$	61.30	1.96	1.80	$^{+2.59}_{-1.91}$	$^{+9.99}_{-7.46}$	0.96	0.94
$4.5\cdot10^{-2}\ldots8.0\cdot10^{-2}$	15.35	2.79	2.64	$^{+1.80}_{-4.05}$	$^{+7.87}_{-8.75}$	0.95	0.91
$8.0\cdot10^{-2}\ldots1.6\cdot10^{-1}$	1.78	4.93	4.74	$^{+5.08}_{-5.64}$	$^{+6.19}_{-4.92}$	0.97	0.92
$0.16\ldots0.5$	$5.22\cdot10^{-2}$	13.78	11.09	$^{+13.17}_{-16.48}$	$^{+6.34}_{-4.93}$	1.11	0.85
$40 < Q^2 < 100\,\mathrm{GeV}^2$							
$1.0\cdot10^{-3}\ldots2.5\cdot10^{-2}$	37.27	1.03	0.83	$^{+1.83}_{-3.78}$	$^{+10.09}_{-8.50}$	0.94	0.94
$2.5\cdot10^{-2}\ldots4.5\cdot10^{-2}$	27.49	1.20	1.06	$^{+2.05}_{-3.65}$	$^{+9.70}_{-8.45}$	0.94	0.96
$4.5\cdot10^{-2}\ldots8.0\cdot10^{-2}$	7.58	1.69	1.57	$^{+1.02}_{-4.61}$	$^{+7.54}_{-6.70}$	0.97	0.92
$8.0\cdot10^{-2}\ldots1.6\cdot10^{-1}$	$8.45\cdot10^{-1}$	2.89	2.85	$^{+5.46}_{-6.64}$	$^{+6.93}_{-5.95}$	0.93	0.91
$0.16\ldots0.5$	$2.81\cdot10^{-2}$	7.36	6.91	$^{+14.37}_{-12.83}$	$^{+7.76}_{-4.99}$	1.01	0.91

Table B.15: Binning, measured values, and uncertainties for the double-differential cross-section $\mathrm{d}^2\sigma/\,\mathrm{d}Q^2\,\mathrm{d}\xi$ for inclusive dijet production. For details see caption to table B.1

Trijet Cross-Sections

Q^2 bin [GeV^2]	$\mathrm{d}\sigma/\,\mathrm{d}Q^2$ [pb/GeV^2]	δ_{stat} [±%]	δ_{MC} [±%]	δ_{syst} [%]	δ_{ES} [%]	C^{QED}	C^{hadr}
10…15	$8.21 \cdot 10^{-1}$	3.42	2.40	$^{+2.42}_{-2.51}$	$^{+12.67}_{-10.26}$	0.95	0.79
15…20	$5.30 \cdot 10^{-1}$	4.36	3.01	$^{+3.47}_{-2.46}$	$^{+12.76}_{-10.95}$	0.99	0.80
20…30	$3.53 \cdot 10^{-1}$	3.59	2.72	$^{+3.72}_{-1.94}$	$^{+11.52}_{-10.67}$	0.97	0.78
30…40	$2.40 \cdot 10^{-1}$	4.37	3.68	$^{+3.40}_{-2.14}$	$^{+12.69}_{-10.38}$	0.95	0.75
40…100	$1.11 \cdot 10^{-1}$	2.71	2.44	$^{+2.43}_{-2.17}$	$^{+11.80}_{-10.90}$	0.96	0.79

Table B.16: Binning, measured values, and uncertainties for the differential cross-section $\mathrm{d}\sigma/\,\mathrm{d}Q^2$ for inclusive trijet production. For details see caption to table B.1

$\langle p_{T,\mathrm{B}}\rangle$ bin [GeV]	$\mathrm{d}\sigma/\,\mathrm{d}\langle p_{T,\mathrm{B}}\rangle$ [pb/GeV]	δ_{stat} [±%]	δ_{MC} [±%]	δ_{syst} [%]	δ_{ES} [%]	C^{QED}	C^{hadr}
8…20	1.36	1.77	1.40	$^{+1.88}_{-0.67}$	$^{+13.94}_{-11.58}$	0.96	0.76
20…30	$2.67 \cdot 10^{-1}$	3.77	2.77	$^{+3.09}_{-4.32}$	$^{+7.23}_{-7.73}$	0.98	0.83
30…45	$2.92 \cdot 10^{-2}$	8.44	6.13	$^{+4.50}_{-6.37}$	$^{+7.79}_{-6.48}$	0.94	0.89
45…100	$5.13 \cdot 10^{-4}$	31.64	18.56	$^{+10.99}_{-8.95}$	$^{+15.75}_{-7.88}$	0.97	0.88

Table B.17: Binning, measured values, and uncertainties for the differential cross-section $\mathrm{d}\sigma/\,\mathrm{d}\langle p_{T,\mathrm{B}}\rangle$ for inclusive trijet production. For details see caption to table B.1

$\langle p_{T,\mathrm{B}}\rangle$ bin [GeV]	$\mathrm{d}^2\sigma/\,\mathrm{d}\langle p_{T,\mathrm{B}}\rangle\,\mathrm{d}Q^2$ [pb/GeV^3]	δ_{stat} [±%]	δ_{MC} [±%]	δ_{syst} [%]	δ_{ES} [%]	C^{QED}	C^{hadr}
$10 < Q^2 < 15\,\mathrm{GeV}^2$							
8…20	$6.00 \cdot 10^{-2}$	3.81	2.88	$^{+1.95}_{-1.60}$	$^{+14.45}_{-11.04}$	0.95	0.77
20…30	$1.03 \cdot 10^{-2}$	8.68	5.60	$^{+2.81}_{-4.88}$	$^{+7.01}_{-7.58}$	0.97	0.84
30…45	$1.26 \cdot 10^{-3}$	17.69	12.99	$^{+5.58}_{-11.51}$	$^{+10.51}_{-8.64}$	0.91	0.84
45…100	$1.09 \cdot 10^{-5}$	70.71	63.31	$^{+15.44}_{-7.86}$	$^{+22.05}_{-4.05}$	0.72	0.87
$15 < Q^2 < 20\,\mathrm{GeV}^2$							
8…20	$3.84 \cdot 10^{-2}$	4.95	3.66	$^{+4.29}_{-1.03}$	$^{+14.45}_{-12.41}$	1.00	0.77
20…30	$7.37 \cdot 10^{-3}$	9.99	6.76	$^{+5.00}_{-7.19}$	$^{+8.62}_{-6.91}$	0.96	0.84

Table B.18 – continued from previous page

$\langle p_{T,\mathrm{B}}\rangle$ bin [GeV]	$\mathrm{d}^2\sigma/\,\mathrm{d}\langle p_{T,\mathrm{B}}\rangle\,\mathrm{d}Q^2$ [pb/GeV^3]	δ_{stat} [±%]	δ_{MC} [±%]	δ_{syst} [%]	δ_{ES} [%]	C^{QED}	C^{hadr}
30…45	$5.81\cdot10^{-4}$	26.78	15.87	$^{+4.92}_{-9.19}$	$^{+5.24}_{-6.09}$	0.98	0.91
45…100	$4.73\cdot10^{-5}$	58.95	133.88	$^{+8.31}_{-18.98}$	$^{+58.65}_{-24.95}$	1.06	1.55
$20 < Q^2 < 30\,\mathrm{GeV}^2$							
8…20	$2.40\cdot10^{-2}$	4.02	3.25	$^{+2.94}_{-1.44}$	$^{+13.11}_{-11.50}$	0.94	0.77
20…30	$5.32\cdot10^{-3}$	8.85	6.46	$^{+7.56}_{-3.08}$	$^{+6.97}_{-8.41}$	1.08	0.79
30…45	$5.62\cdot10^{-4}$	19.35	17.20	$^{+8.91}_{-5.48}$	$^{+4.75}_{-7.20}$	0.96	0.99
45…100	$1.23\cdot10^{-5}$	71.15	124.35	$^{+45.26}_{-2.79}$	$^{+48.34}_{-24.98}$	1.54	0.76
$30 < Q^2 < 40\,\mathrm{GeV}^2$							
8…20	$1.63\cdot10^{-2}$	4.99	4.29	$^{+3.56}_{-1.22}$	$^{+14.52}_{-11.67}$	0.95	0.71
20…30	$4.07\cdot10^{-3}$	9.95	9.09	$^{+4.99}_{-5.98}$	$^{+6.73}_{-5.42}$	0.98	0.87
30…45	$3.87\cdot10^{-4}$	23.22	22.04	$^{+4.31}_{-5.92}$	$^{+9.10}_{-6.12}$	0.90	0.88
45…100	$5.40\cdot10^{-6}$	100.00	79.12	$^{+29.63}_{-3.37}$	$^{+0.00}_{-0.00}$	0.66	0.96
$40 < Q^2 < 100\,\mathrm{GeV}^2$							
8…20	$7.83\cdot10^{-3}$	3.05	2.86	$^{+1.95}_{-1.08}$	$^{+13.41}_{-11.65}$	0.96	0.78
20…30	$1.42\cdot10^{-3}$	6.48	6.11	$^{+3.10}_{-5.64}$	$^{+6.61}_{-8.66}$	0.94	0.81
30…45	$1.97\cdot10^{-4}$	14.73	13.56	$^{+7.73}_{-8.78}$	$^{+4.63}_{-4.59}$	0.96	0.90
45…100	$2.45\cdot10^{-6}$	73.01	40.66	$^{+15.44}_{-22.94}$	$^{+2.35}_{-8.29}$	1.25	0.82

Table B.18: Binning, measured values, and uncertainties for the double-differential cross-section $\mathrm{d}^2\sigma/\,\mathrm{d}Q^2\,\mathrm{d}\langle p_{T,\mathrm{B}}\rangle$ for inclusive trijet production. For details see caption to table B.1

Bibliography

[1] E. Rutherford, The scattering of α and β particles by matter and the structure of the atom, Phil.Mag. 21 (1911) 669–688.
`doi:10.1080/14786440508637080`.

[2] G. H., M. E., On a diffuse reflection of the α-particles, Proceedings of the Royal Society A 82 (1909) 495–500.

[3] B. Bistrovic, et al., Understanding hadron structure from lattice QCD in the SciDAC era, J. Phys. Conf. Ser. 16 (2005) 150–159.

[4] C. Adloff, et al., Measurement and QCD analysis of jet cross-sections in deep inelastic positron - proton collisions at $\sqrt{s}$ of 300 GeV, Eur.Phys.J. C19 (2001) 289–311.
`arXiv:hep-ex/0010054`, `doi:10.1007/s100520100621`.

[5] S. Chekanov, et al., Inclusive jet cross-sections in the breit frame in neutral current deep inelastic scattering at HERA and determination of α_s, Phys.Lett. B547 (2002) 164–180.
`arXiv:hep-ex/0208037`, `doi:10.1016/S0370-2693(02)02763-6`.

[6] C. Adloff, et al., Measurement of inclusive jet cross-sections in deep inelastic ep scattering at HERA, Phys.Lett. B542 (2002) 193–206.
`arXiv:hep-ex/0206029`, `doi:10.1016/S0370-2693(02)02375-4`.

[7] F. D. Aaron, et al., Jet production in ep collisions at low Q^2 and determination of α_s, Eur. Phys. J. C67 (2010) 1–24.
`arXiv:0911.5678`, `doi:10.1140/epjc/s10052-010-1282-x`.

[8] J. Breitweg, et al., Measurement of dijet production in neutral current deep inelastic scattering at high Q^2 and determination of α_s, Phys.Lett. B507 (2001) 70–88.
`arXiv:hep-ex/0102042`, `doi:10.1016/S0370-2693(01)00421-X`.

[9] S. Chekanov, et al., Multijet production in neutral current deep inelastic scattering at HERA and determination of α_s, Eur.Phys.J. C44 (2005) 183–193.
`arXiv:hep-ex/0502007`, `doi:10.1140/epjc/s2005-02347-1`.

[10] S. Chekanov, et al., An NLO QCD analysis of inclusive cross-section and jet-production data from the ZEUS experiment, Eur. Phys. J. C42 (2005) 1–16.
`arXiv:hep-ph/0503274`.

[11] S. Chekanov, et al., Inclusive-jet and dijet cross-sections in deep inelastic scattering at HERA, Nucl.Phys. B765 (2007) 1–30.
`arXiv:hep-ex/0608048`, `doi:10.1016/j.nuclphysb.2006.09.018`.

[12] S. Chekanov, et al., Multijet production at low x_{Bj} in deep inelastic scattering at HERA, Nucl. Phys. B786 (2007) 152–180.

arXiv:0705.1931, doi:10.1016/j.nuclphysb.2007.05.027.

[13] H. Perrey, Dijets in photoproduction at Hera, Diploma thesis, University of Hamburg (2007).

[14] R. Hofstadter, Electron scattering and nuclear structure, Rev.Mod.Phys. 28 (1956) 214–254.
doi:10.1103/RevModPhys.28.214.

[15] R. E. Taylor, Deep inelastic scattering: The early years, Rev.Mod.Phys. 63 (1991) 573–595.
doi:10.1103/RevModPhys.63.573.

[16] E. D. Bloom, D. Coward, H. DeStaebler, J. Drees, G. Miller, et al., High-energy inelastic *ep* scattering at 6-degrees and 10-degrees, Phys.Rev.Lett. 23 (1969) 930–934.
doi:10.1103/PhysRevLett.23.930.

[17] M. Breidenbach, J. I. Friedman, H. W. Kendall, E. D. Bloom, D. Coward, et al., Observed behavior of highly inelastic electron-proton scattering, Phys.Rev.Lett. 23 (1969) 935–939.
doi:10.1103/PhysRevLett.23.935.

[18] J. I. Friedman, H. W. Kendall, Deep inelastic electron scattering, Ann.Rev.Nucl.Part.Sci. 22 (1972) 203–254.
doi:10.1146/annurev.ns.22.120172.001223.

[19] J. Bjorken, Asymptotic sum rules at infinite momentum, Phys.Rev. 179 (1969) 1547–1553.
doi:10.1103/PhysRev.179.1547.

[20] J. I. Friedman, Deep inelastic scattering: Comparisons with the quark model, Rev.Mod.Phys. 63 (1991) 615–629, reprint.
doi:10.1103/RevModPhys.63.615.

[21] R. P. Feynman, Very high-energy collisions of hadrons, Phys.Rev.Lett. 23 (1969) 1415–1417.
doi:10.1103/PhysRevLett.23.1415.

[22] R. Feynman, Photon-hadron interactions, Reading, 1973.

[23] M. Gell-Mann, A schematic model of baryons and mesons, Phys.Lett. 8 (1964) 214–215.
doi:10.1016/S0031-9163(64)92001-3.

[24] G. Zweig, An SU(3) model for strong interaction symmetry and its breaking, in: D. Lichtenberg, S. Rosen (Eds.), Developments in the Quark Theory of Hadrons, Vol. 1, Nonantum, Mass., Hadronic Press, printed 1980, 1964, pp. 22–101, CERN Geneva - TH-401 and TH-412.

[25] F. Halzen, A. D. Martin, Quarks And Leptons: An Introductory Course In Modern Particle Physics, Wiley, New York, USA, 1984.

[26] H. Fritzsch, M. Gell-Mann, H. Leutwyler, Advantages of the color octet gluon picture, Phys. Lett. B47 (1973) 365–368.

[27] K. Koller, T. Walsh, Three gluon jets as a test of QCD, Phys.Lett. B72 (1977) 227. `doi:10.1016/0370-2693(77)90708-0`.

[28] W. Bartel, et al., Observation of planar three jet events in e^+e^- annihilation and evidence for gluon bremsstrahlung, Phys.Lett. B91 (1980) 142. `doi:10.1016/0370-2693(80)90680-2`.

[29] D. Barber, U. Becker, H. Benda, A. Boehm, J. Branson, et al., Discovery of Three Jet Events and a Test of Quantum Chromodynamics at PETRA Energies, Phys.Rev.Lett. 43 (1979) 830. `doi:10.1103/PhysRevLett.43.830`.

[30] C. Berger, et al., Evidence for Gluon Bremsstrahlung in e^+e^- Annihilations at High-Energies, Phys.Lett. B86 (1979) 418. `doi:10.1016/0370-2693(79)90869-4`.

[31] R. Brandelik, et al., Evidence for planar events in e^+e^- annihilation at high-energies, Phys.Lett. B86 (1979) 243. `doi:10.1016/0370-2693(79)90830-X`.

[32] R. Brandelik, et al., Evidence for a Spin One Gluon in Three Jet Events, Phys.Lett. B97 (1980) 453. `doi:10.1016/0370-2693(80)90639-5`.

[33] G. 't Hooft, M. Veltman, Regularization and renormalization of gauge fields, Nucl.Phys. B44 (1972) 189–213. `doi:10.1016/0550-3213(72)90279-9`.

[34] J. C. Collins, Choosing the renormalization / factorization scale, J.Phys.G G17 (1991) 1547–1549. `doi:10.1088/0954-3899/17/10/009`.

[35] J. Blumlein, $\Lambda_{\rm QCD}$ and $\alpha_s(M_Z^2)$ from DIS Structure Functions, in: G. Grindhammer, K. Sachs (Eds.), Proceedings to the 15th International Workshop on Deep-Inelastic Scattering and Related Subjects (DIS 2007), April 16-20, 2007 Munich, Germany, Vol. 1 of Progress in High Energy Physics, SciWiPub, 2007, pp. 1099–1101. `arXiv:0706.2430`, `doi:10.3360/dis.2007.212`.

[36] C. Glasman, Precision measurements of α_s at HERA, AIP Conf. Proc. 792 (2005) 689–692. `arXiv:hep-ex/0506035`.

[37] D. Gross, F. Wilczek, Ultraviolet behavior of nonabelian gauge theories, Phys.Rev.Lett. 30 (1973) 1343–1346. `doi:10.1103/PhysRevLett.30.1343`.

[38] H. Politzer, Reliable perturbative results for strong interactions?, Phys.Rev.Lett. 30 (1973) 1346–1349. `doi:10.1103/PhysRevLett.30.1346`.

[39] H. Plothow-Besch, PDFLIB: A library of all available parton density functions of the nucleon, the pion and the photon and the corresponding α_s calculations, Comput.Phys.Commun. 75 (1993) 396–416.

`doi:10.1016/0010-4655(93)90051-D`.

[40] M. Whalley, D. Bourilkov, R. Group, The Les Houches accord PDFs (LhaPDF) and Lhaglue, in: A. De Roeck, H. Jung (Eds.), Proceedings to Hera And The Lhc: A Workshop On The Implications Of Hera And Lhc Physics, 21 – 24 March, 2005, Hamburg, Germany, 2005.
`arXiv:hep-ph/0508110`.
URL `http://projects.hepforge.org/lhapdf/`

[41] F. D. Aaron, et al., Combined measurement and QCD analysis of the inclusive *ep* scattering cross sections at Hera, JHEP 01 (2010) 109.
`arXiv:0911.0884`, `doi:10.1007/JHEP01(2010)109`.

[42] V. Gribov, L. Lipatov, e^+e^- pair annihilation and deep inelastic *ep* scattering in perturbation theory, Sov.J.Nucl.Phys. 15 (1972) 675–684.

[43] V. Gribov, L. Lipatov, Deep inelastic *ep* scattering in perturbation theory, Sov.J.Nucl.Phys. 15 (1972) 438–450.

[44] G. Altarelli, G. Parisi, Asymptotic freedom in parton language, Nucl.Phys. B126 (1977) 298.
`doi:10.1016/0550-3213(77)90384-4`.

[45] Y. L. Dokshitzer, Calculation of the structure functions for deep inelastic scattering and e^+e^- annihilation by perturbation theory in quantum chromodynamics, Sov.Phys.JETP 46 (1977) 641–653.

[46] E. Kuraev, L. Lipatov, V. S. Fadin, The pomeranchuk singularity in nonabelian gauge theories, Sov.Phys.JETP 45 (1977) 199–204.

[47] I. Balitsky, L. Lipatov, The pomeranchuk singularity in quantum chromodynamics, Sov.J.Nucl.Phys. 28 (1978) 822–829.

[48] M. Ciafaloni, Coherence Effects in Initial Jets at Small q**2 / s, Nucl.Phys. B296 (1988) 49.
`doi:10.1016/0550-3213(88)90380-X`.

[49] S. Catani, F. Fiorani, G. Marchesini, QCD Coherence in Initial State Radiation, Phys.Lett. B234 (1990) 339.
`doi:10.1016/0370-2693(90)91938-8`.

[50] S. Catani, F. Fiorani, G. Marchesini, Small x Behavior of Initial State Radiation in Perturbative QCD, Nucl.Phys. B336 (1990) 18.
`doi:10.1016/0550-3213(90)90342-B`.

[51] R. Devenish, A. Cooper-Sarkar, Deep inelastic scattering, Oxford University Press, 2004.

[52] M. D. Corcoran, et al., Evidence that high p_T jet pairs give direct information on parton parton scattering, Phys. Rev. Lett. 44 (1980) 514.

[53] G. P. Salam, Towards Jetography, Eur.Phys.J. C67 (2010) 637–686.
`arXiv:0906.1833`, `doi:10.1140/epjc/s10052-010-1314-6`.

[54] J. E. Huth, et al., Toward a standardization of jet definitions., in: E. L. Berger (Ed.), Research directions for the decade. Proceedings, 1990 Summer Study

on High-Energy Physics, Snowmass, USA, June 25 - July 13, 1990, World Scientific, 1992, p. 134, FERMILAB-CONF-90-249-E.

[55] G. Sterman, S. Weinberg, Jets from quantum chromodynamics, Phys. Rev. Lett. 39 (1977) 1436.

[56] S. Catani, Y. L. Dokshitzer, M. H. Seymour, B. R. Webber, Longitudinally invariant k_T-clustering algorithms for hadron hadron collisions., Nucl. Phys. B406 (1993) 187–224.
`doi:10.1016/0550-3213(93)90166-M`.

[57] S. D. Ellis, D. E. Soper, Successive combination jet algorithm for hadron collisions, Phys.Rev. D48 (1993) 3160–3166.
`arXiv:hep-ph/9305266`, `doi:10.1103/PhysRevD.48.3160`.

[58] H. Abramowicz, et al., Inclusive-jet cross sections in NC DIS at HERA and a comparison of the k_T, anti-k_T and SIScone jet algorithms, Phys.Lett. B691 (2010) 127–137.
`arXiv:1003.2923`, `doi:10.1016/j.physletb.2010.06.015`.

[59] M. Cacciari, G. P. Salam, G. Soyez, The anti-k_T jet clustering algorithm, JHEP 0804 (2008) 063.
`arXiv:0802.1189`, `doi:10.1088/1126-6708/2008/04/063`.

[60] G. P. Salam, G. Soyez, A practical seedless infrared-safe cone jet algorithm, JHEP 0705 (2007) 086.
`arXiv:0704.0292`, `doi:10.1088/1126-6708/2007/05/086`.

[61] O. Gónzalez, J. Terrón, Analyses in the Breit frame and the related problems, ZEUS note 02-006 (2002).

[62] B. Webber, Factorization and jet clustering algorithms for deep inelastic scattering, J.Phys.G G19 (1993) 1567–1575.
`doi:10.1088/0954-3899/19/10/012`.

[63] ZEUS Collaboration, The ZEUS detector: Status report 1993, Tech. rep., ZEUS, unpublished (1993).
URL `http://www-zeus.desy.de/bluebook/bluebook.html`

[64] N. Harnew, et al., Vertex triggering using time difference measurements in the ZEUS central tracking detector, Nucl. Instrum. Meth. A279 (1989) 290–296.

[65] B. Foster, et al., The design and construction of the ZEUS central tracking detector, Nucl. Instrum. Meth. A338 (1994) 254–283.

[66] R. Hall-Wilton, N. McCubbin, P. Nylander, M. Sutton, M. Wing, The CTD tracking resolution, ZEUS-99-024 (1999).

[67] M. Derrick, D. Gacek, N. Hill, B. Musgrave, R. Noland, et al., Design and construction of the ZEUS barrel calorimeter, Nucl.Instrum.Meth. A309 (1991) 77–100.
`doi:10.1016/0168-9002(91)90094-7`.

[68] A. Andresen, et al., Construction and beam test of the ZEUS forward and rear calorimeter, Nucl.Instrum.Meth. A309 (1991) 101–142.
`doi:10.1016/0168-9002(91)90095-8`.

[69] A. Bernstein, et al., Beam tests of the Zeus barrel calorimeter, Nucl. Instrum. Meth. A336 (1993) 23–52.

[70] P. Saull, An overview of the Zeus CAL system, lecture given at Desy (2001).

[71] D. Kisielewska, et al., Fast luminosity monitoring at Hera, Hera report 85-25 (1985).

[72] L. Suszycki, Luminosity monitoring, photon tagging and QED tests, in: R. Peccei (Ed.), Proc. of the Hera workshop, Oct. 1987, Vol. 2, Hamburg, Germany, 1988, p. 505ff.

[73] J. Andruszków, et al., First measurement of Hera luminosity by Zeus lumi monitor, Zeus note 92-024 (1992).

[74] L. Adamczyk, et al., Luminosity measurement in the Zeus experiment, Zeus note 01-004 (2001).

[75] M. Helbich, Y. Ning, S. Paganis, Z. Ren, W. Schmidke, et al., The spectrometer system for measuring Zeus luminosity at Hera, Nucl.Instrum.Meth. A565 (2006) 572–588.
`arXiv:physics/0512153`, `doi:10.1016/j.nima.2006.06.049`.

[76] J. Chwastowski, J. Figiel, A. Kotarba, K. Olkiewicz, L. Suszycki, Aerogel cherenkov detectors for the luminosity measurement at Hera, Nucl.Instrum.Meth. A504 (2003) 222–227.
`doi:10.1016/S0168-9002(03)00794-0`.

[77] U. Klein, Zeus luminosity webpage, last visited 16.04.2011.
URL `http://www-zeus.desy.de/physics/lumi/lumi.html`

[78] M. Seidel, The upgraded interaction regions of Hera, DESY (2000).

[79] U. Schneekloth (ed.), The Hera luminosity upgrade, DESY (1998).

[80] S. Frixione, B. R. Webber, Matching NLO QCD computations and parton shower simulations, JHEP 0206 (2002) 029.
`arXiv:hep-ph/0204244`.

[81] P. Nason, A new method for combining NLO QCD with shower Monte Carlo algorithms, JHEP 0411 (2004) 040.
`arXiv:hep-ph/0409146`, `doi:10.1088/1126-6708/2004/11/040`.

[82] S. Alioli, P. Nason, C. Oleari, E. Re, A general framework for implementing NLO calculations in shower Monte Carlo programs: the Powheg Box, JHEP 1006 (2010) 043.
`arXiv:1002.2581`, `doi:10.1007/JHEP06(2010)043`.

[83] S. Alioli, P. Nason, C. Oleari, E. Re, Vector boson plus one jet production in Powheg, JHEP 1101 (2011) 095.
`arXiv:1009.5594`, `doi:10.1007/JHEP01(2011)095`.

[84] G. Aad, et al., Expected performance of the Atlas experiment - detector, trigger and physics (2009).
`arXiv:0901.0512`.

[85] A. Kwiatkowski, H. Spiesberger, H. Mohring, HERACLES: An event generator for *ep* interactions at HERA energies including radiative processes: Version 1.0, Comput.Phys.Commun. 69 (1992) 155–172.
`doi:10.1016/0010-4655(92)90136-M`.

[86] K. Charchula, G. Schuler, H. Spiesberger, Combined QED and QCD radiative effects in deep inelastic lepton - proton scattering: The Monte Carlo generator DJANGO6, Comput.Phys.Commun. 81 (1994) 381–402.
`doi:10.1016/0010-4655(94)90086-8`.

[87] G. Ingelman, A. Edin, J. Rathsman, LEPTO 6.5: A Monte Carlo generator for deep inelastic lepton - nucleon scattering, Comput.Phys.Commun. 101 (1997) 108–134.
`arXiv:hep-ph/9605286`, `doi:10.1016/S0010-4655(96)00157-9`.

[88] L. Lönnblad, ARIADNE version 4: A program for simulation of QCD cascades implementing the color dipole model, Comput.Phys.Commun. 71 (1992) 15–31.
`doi:10.1016/0010-4655(92)90068-A`.

[89] L. Lönnblad, Rapidity gaps and other final state properties in the color dipole model for deep inelastic scattering, Z.Phys. C65 (1995) 285–292.
`doi:10.1007/BF01571885`.

[90] H. Lai, et al., Global QCD analysis of parton structure of the nucleon: CTEQ5 parton distributions, Eur.Phys.J. C12 (2000) 375–392.
`arXiv:hep-ph/9903282`, `doi:10.1007/s100529900196`.

[91] G. Gustafson, Dual description of a confined color field, Phys.Lett. B175 (1986) 453.
`doi:10.1016/0370-2693(86)90622-2`.

[92] G. Gustafson, U. Pettersson, Dipole Formulation of QCD Cascades, Nucl.Phys. B306 (1988) 746.
`doi:10.1016/0550-3213(88)90441-5`.

[93] B. Andersson, G. Gustafson, L. Lonnblad, U. Pettersson, Coherence effects in deep inelastic scattering, Z.Phys. C43 (1989) 625.
`doi:10.1007/BF01550942`.

[94] T. Sjöstrand, High-energy physics event generation with PYTHIA 5.7 and JETSET 7.4, Comp. Phys. Comm. 82 (1994) 74–90.
`doi:10.1016/0010-4655(94)90132-5`.

[95] T. Sjöstrand, PYTHIA 5.7 and JETSET 7.4: Physics and manual, long version of [94] (1995).
`arXiv:hep-ph/9508391`.

[96] B. Andersson, G. Gustafson, G. Ingelman, T. Sjostrand, Parton fragmentation and string dynamics, Phys. Rept. 97 (1983) 31.

[97] B. Andersson, The Lund model, Camb.Monogr.Part.Phys.Nucl.Phys.Cosmol. 7 (1997) 1–471.

[98] B. Webber, A QCD model for jet fragmentation including soft gluon interference, Nucl. Phys. B 238 (1984) 492.

[99] G. Marchesini, B. Webber, G. Abbiendi, I. Knowles, M. Seymour, et al., HERWIG: A Monte Carlo event generator for simulating hadron emission reactions with interfering gluons. version 5.1 - april 1991, Comput.Phys.Commun. 67 (1992) 465–508.
`doi:10.1016/0010-4655(92)90055-4`.

[100] G. Corcella, I. Knowles, G. Marchesini, S. Moretti, K. Odagiri, et al., HERWIG 6: An event generator for hadron emission reactions with interfering gluons (including supersymmetric processes), JHEP 0101 (2001) 010.
`arXiv:hep-ph/0011363`.

[101] R. Brun, F. Bruyant, M. Maire, A. McPherson, P. Zanarini, GEANT3, CERN-DD-EE-84-1 (1987).

[102] T. Sjöstrand, S. Mrenna, P. Z. Skands, PYTHIA 6.4 physics and manual, JHEP 0605 (2006) 026.
`arXiv:hep-ph/0603175`, `doi:10.1088/1126-6708/2006/05/026`.

[103] G. P. Salam, Perturbative QCD for the LHC, PoS ICHEP2010 (2010) 556.
`arXiv:1103.1318`.

[104] Z. Nagy, Z. Trocsanyi, Multijet cross-sections in deep inelastic scattering at next-to-leading order, Phys.Rev.Lett. 87 (2001) 082001.
`arXiv:hep-ph/0104315`, `doi:10.1103/PhysRevLett.87.082001`.

[105] R. K. Ellis, D. A. Ross, A. E. Terrano, The perturbative calculation of jet structure in e^+e^- annihilation, Nucl. Phys. B178 (1981) 421.

[106] W. A. Bardeen, A. Buras, D. Duke, T. Muta, Deep inelastic scattering beyond the leading order in asymptotically free gauge theories, Phys.Rev. D18 (1978) 3998.
`doi:10.1103/PhysRevD.18.3998`.

[107] P. M. Nadolsky, H.-L. Lai, Q.-H. Cao, J. Huston, J. Pumplin, et al., Implications of CTEQ global analysis for collider observables, Phys.Rev. D78 (2008) 013004.
`arXiv:0802.0007`, `doi:10.1103/PhysRevD.78.013004`.

[108] S. Frixione, G. Ridolfi, Jet photoproduction at HERA, Nucl.Phys. B507 (1997) 315–333.
`arXiv:hep-ph/9707345`, `doi:10.1016/S0550-3213(97)00575-0`.

[109] A. Banfi, M. Dasgupta, Dijet rates with symmetric E_T cuts, JHEP 0401 (2004) 027.
`arXiv:hep-ph/0312108`, `doi:10.1088/1126-6708/2004/01/027`.

[110] J. Behr, Jets at high Q^2 at HERA and test beam measurements with the EUDET pixel telescope, Ph.D. thesis, University of Hamburg (2010).

[111] G. M. Briskin, Diffractive dissociation in ep deep inelastic scattering., Ph.D. thesis, U. Tel Aviv (1998).

[112] T. Theedt, Measurement of dijet cross sections in deep inelastic ep scattering at HERA, Ph.D. thesis, University of Hamburg, DESY-THESIS-2009-046 (2009).

[113] J. Grosse-Knetter, Corrections for the hadronic final state, ZEUS note 98-031 (1998).

[114] H. Abramowicz, A. Caldwell, R. Sinkus, Neural network based electron identification in the ZEUS calorimeter, Nucl. Instrum. Meth. A365 (1995) 508–517. `arXiv:hep-ex/9505004`.

[115] B. Straub, The `em` electron finder, ZEUS internal webpage, last visited 25.02.2011 (1998).
URL `http://www-zeus.desy.de/~straub/ZEUS_ONLY/doc/em.ps`

[116] A. Kappes, Measurement of neutral current deep inelastic scattering cross sections using the ZEUS detector at HERA, Ph.D. thesis, Physikalisches Institut der Universität Bonn, BONN-IR-2001-16 (2001).

[117] S. Bentvelsen, J. Engelen, P. Kooijman, Reconstruction of (x, Q^2) and extraction of structure functions in neutral current scattering at HERA, in: W. Buchmüller, G. Ingelman (Eds.), Proc. of the workshop Physics at HERA, Vol. 1, 1991, p. 23ff, NIKHEF-H-92-02.

[118] U. Bassler, G. Bernardi, Structure function measurements and kinematic reconstruction at HERA, Nucl. Instrum. Meth. A426 (1999) 583–598. `arXiv:hep-ex/9801017`, `doi:10.1016/S0168-9002(99)00044-3`.

[119] G. Bernardi, W. Hildesheim, A detailed simulation of F_2 measurability at HERA, in: W. Buchmüller, G. Ingelman (Eds.), Proc. of the workshop Physics at HERA, Vol. 1, 1991, p. 79ff.

[120] F. Jacquet, A. Blondel, in: U. Amaldi (Ed.), Proceedings of the study of an *ep* facility for Europe, Vol. 79/48, 1979, pp. 391 – 394.

[121] K. C. Hoeger, Measurement of x, y, Q^2 in neutral current events, in: W. Buchmüller, G. Ingelman (Eds.), Proc. of the workshop Physics at HERA, Vol. 1, 1991, p. 43ff.

[122] H. Abramowicz, et al., Inclusive dijet cross sections in neutral current deep inelastic scattering at HERA, Eur.Phys.J. C70 (2010) 965–982. `arXiv:1010.6167`, `doi:10.1140/epjc/s10052-010-1504-2`.

[123] U. Bassler, G. Bernardi, On the kinematic reconstruction of deep inelastic scattering at HERA: The Sigma method, Nucl. Instrum. Meth. A361 (1995) 197–208. `arXiv:hep-ex/9412004`, `doi:10.1016/0168-9002(95)00173-5`.

[124] C. Adloff, et al., Measurement and QCD analysis of neutral and charged current cross sections at HERA, Eur. Phys. J. C30 (2003) 1–32. `arXiv:hep-ex/0304003`, `doi:10.1140/epjc/s2003-01257-6`.

[125] A. Aktas, et al., Measurement of inclusive jet production in deep-inelastic scattering at high Q^2 and determination of the strong coupling, Phys. Lett. B653 (2007) 134–144. `arXiv:0706.3722`, `doi:10.1016/j.physletb.2007.07.050`.

[126] U. Stösslein, EVTAKE for post-upgrade data, ZEUS internal webpage, last visited 28.01.2011.
URL `http://www-zeus.desy.de/~ifhuta/ZEUS_ONLY/evtake/`

[127] Y. Yamazaki, GFLT status report: mis-configuration for the risoe 2ir slots and impact on the mid-Q^2 NC analysis, talk presented at ZEUS collaboration meeting (10 2006).
URL https://www-zeus.desy.de/zems/ZEUS_ONLY/display.php?p_active=7837

[128] W. H. Smith, et al., ZEUS calorimeter first level trigger (version 1.0), ZEUS note 89-085 (1989).

[129] Y. Yamazaki, CTD FLT classes and track veto, ZEUS internal webpage, last visited 01.02.2011 (2003).
URL http://www-zeus.desy.de/components/gflt/yycontents/trkv.html

[130] D. Bailey, B. Foster, G. Heath, C. Morgado, N. Harnew, et al., The design and performance of the ZEUS central tracking detector z-by-timing system, Nucl. Instrum. Meth. A396 (1997) 320–349.
arXiv:hep-ex/9707032, doi:10.1016/S0168-9002(97)00790-0.

[131] S. Chekanov, et al., Measurement of the Longitudinal Proton Structure Function at HERA, Phys.Lett. B682 (2009) 8–22.
arXiv:0904.1092, doi:10.1016/j.physletb.2009.10.050.

[132] A. Geiser, Trigger and rate studies, talk presented at ZEUS NC e^+p task force meeting (9 2009).

[133] M. Derrick, et al., Observation of events with a large rapidity gap in deep inelastic scattering at HERA, Phys.Lett. B315 (1993) 481–493.
doi:10.1016/0370-2693(93)91645-4.

[134] F. Goebel, Measurement of the diffractive contribution to the DIS cross section using the ZEUS forward plug calorimeter, Ph.D. thesis, University of Hamburg, DESY-THESIS-2001-049 (2001).

[135] M. Derrick, et al., Inclusive jet differential cross-sections in photoproduction at HERA, Phys. Lett. B342 (1995) 417–432.
doi:10.1016/0370-2693(94)01510-J.

[136] S. Chekanov, et al., Dijet photoproduction at HERA and the structure of the photon, Eur. Phys. J. C23 (2002) 615–631.
arXiv:hep-ex/0112029, doi:10.1007/s100520200936.

[137] A. H. Ochs, Dijet photoproduction at high transverse energies with the ZEUS detector at HERA, Ph.D. thesis, McGill University, Montreal, DESY-THESIS-2003-005 (2003).

[138] J. Breitweg, et al., Measurement of Dijet photoproduction at high transverse energies at HERA, Eur. Phys. J. C11 (1999) 35–50.
arXiv:hep-ex/9905046, doi:10.1007/s100520050612.

[139] M. Wing, Setting the jet energy scale for the ZEUS calorimeter, in: R.-Y. Zhu (Ed.), Proceedings to the 10th International Conference On Calorimetry In High Energy Physics (CALOR 2002), River Edge, N.J., World Scientific, 2002, pp. 767–772.
arXiv:hep-ex/0206036.

[140] F. Pelucchi, S. Schlenstedt, J. Vossebeld, Study of the calorimeter energy scale in the ZEUS Monte Carlo, ZEUS note 96-104 (1996).

[141] C. Glasman, Jet production at HERA with the ZEUS detector: Resolved and direct processes in photoproduction and the gluon content of the proton and the photon, Ph.D. thesis, Weizmann Institute of Science, Rehovot, Israel (1995).

[142] J. Butterworth, E. Heaphy, M. Sutton, How to determine correction factors, ZEUS note 98-032 (1998).

[143] T. Sjöstrand, S. Mrenna, P. Z. Skands, A brief introduction to PYTHIA 8.1, Comput.Phys.Commun. 178 (2008) 852–867.
`arXiv:0710.3820`, `doi:10.1016/j.cpc.2008.01.036`.

[144] ZEUS Monte Carlo production facility: Available FUNNEL versions, ZEUS internal webpage, last visited 24.01.2011 (2010).
URL `http://www-zeus.desy.de/components/funnel/MONTE_CARLO/Funnel_versions.html`

[145] K. Oliver, J. Ferrando, R. Devenish, A minimum bias z vertex distribution for 2005–2007 ep interactions at ZEUS, ZEUS note 07-008 (2007).

[146] ZEUS Collaboration, Measurement of high Q^2 neutral current deep inelastic e^+p scattering cross sections with longitudinally polarised electrons with ZEUS at HERA, publication exp. 2011.

[147] T. Stewart, NC DIS in 06/07 e^+p data, talk presented at ZEUS collaboration meeting (10 2010).

[148] F. Januschek, Measurement of high Q^2 neutral current deep inelastic e^+p scattering cross sections with longitudinally polarised electrons with ZEUS at HERA, Ph.D. thesis, University of Hamburg, in preparation (exp. 2011).

[149] V. Blobel, Unfolding methods in high-energy physics experiments, in: CERN School Of Computing: proceedings, European Organization for Nuclear Research, Geneva, Switzerland, 1984.

[150] G. Cowan, A survey of unfolding methods for particle physics, in: M. Whalley, L. Lyons (Eds.), Proceedings: Advanced Statistical Techniques In Particle Physics, Inst. For Particle Physics Phenomenology, Durham, UK, 2002, pp. 248–257.

[151] V. Blobel, An unfolding method for high-energy physics experiments, in: M. Whalley, L. Lyons (Eds.), Proceedings: Advanced Statistical Techniques In Particle Physics, Inst. For Particle Physics Phenomenology, Durham, UK, 2002, pp. 258–267.
`arXiv:hep-ex/0208022`.

[152] G. D'Agostini, A Multidimensional unfolding method based on Bayes' theorem, Nucl. Instrum. Meth. A362 (1995) 487–498.
`doi:10.1016/0168-9002(95)00274-X`.

[153] V. Anikeev, A. Spiridonov, V. Zhigunov, Correcting factors method as an unfolding technique, Nucl. Instrum. Meth. A322 (1992) 280–285.
`doi:10.1016/0168-9002(92)90041-2`.

[154] A. Abulencia, et al., Measurement of the inclusive jet cross section using the k_T algorithm in p anti-p collisions at $\sqrt{s} = 1.96$ TeV, Phys.Rev.Lett. 96 (2006) 122001.
`arXiv:hep-ex/0512062`, `doi:10.1103/PhysRevLett.96.122001`.

[155] G. Aad, et al., Measurement of inclusive jet and dijet cross sections in proton-proton collisions at 7 TeV centre-of-mass energy with the ATLAS detector, Eur.Phys.J. C71 (2011) 1512.
`arXiv:1009.5908`, `doi:10.1140/epjc/s10052-010-1512-2`.

[156] M. Wobisch, T. Wengler, Hadronization corrections to jet cross-sections in deep inelastic scattering, in: A. T. Doyle, G. Grindhammer, G. Ingelman, H. Jung (Eds.), Monte Carlo generators for HERA physics. Proceedings, Workshop, Hamburg, Germany, 1998.
`arXiv:hep-ph/9907280`.

[157] N. Brook, T. Carli, E. Rodrigues, M. Sutton, N. Tobien, et al., A comparison of deep inelastic scattering Monte Carlo event generators to HERA data, in: A. T. Doyle, G. Grindhammer, G. Ingelman, H. Jung (Eds.), Monte Carlo generators for HERA physics. Proceedings, Workshop, Hamburg, Germany, 1998.
`arXiv:hep-ex/9912053`.

[158] S. Chekanov, et al., Measurement of the neutral current cross-section and F_2 structure function for deep inelastic e^+p scattering at HERA, Eur. Phys. J. C21 (2001) 443–471.
`arXiv:hep-ex/0105090`, `doi:10.1007/s100520100749`.

[159] D. Vladimir, Luminosity measurement, talk presented at ZEUS Analysis Forum meeting (5 2010).

[160] S. Bethke, Experimental tests of asymptotic freedom, Prog.Part.Nucl.Phys. 58 (2007) 351–386.
`arXiv:hep-ex/0606035`, `doi:10.1016/j.ppnp.2006.06.001`.

[161] K. Nakamura, et al., Review of particle physics, J.Phys.G G37 (2010) 075021.
`doi:10.1088/0954-3899/37/7A/075021`.

[162] T. Schörner-Sadenius, Messung inklusiver Jet-Wirkungsquerschnitte in tiefunelastischer ep-Streuung mit dem H1-Detektor bei HERA, Ph.D. thesis, University of Munich (2001).

[163] C. Adloff, et al., Forward jet and particle production at HERA, Nucl.Phys. B538 (1999) 3–22.
`arXiv:hep-ex/9809028`, `doi:10.1016/S0550-3213(98)00745-7`.

[164] J. Breitweg, et al., Measurement of the $E^2_{T,\text{jet}}/Q^2$ dependence of forward jet production at HERA, Phys.Lett. B474 (2000) 223–233.
`arXiv:hep-ex/9910043`, `doi:10.1016/S0370-2693(99)01478-1`.

[165] H. Jung, L. Jonsson, H. Kuster, The Role of resolved virtual photons in the production of forward jets at HERA, Eur.Phys.J. C9 (1999) 383–388.
`arXiv:hep-ph/9903306`, `doi:10.1007/s100529900080`.

[166] J. M. Campbell, J. Huston, W. Stirling, Hard interactions of quarks and gluons: A primer for LHC physics, Rept.Prog.Phys. 70 (2007) 89.
`arXiv:hep-ph/0611148`, `doi:10.1088/0034-4885/70/1/R02`.

[167] J. Huston, LO, NLO, LO* and jet algorithms, PoS RADCOR2009 (2010) 079.
`arXiv:1001.2581`.

[168] A. Aktas, et al., Forward jet production in deep inelastic scattering at HERA, Eur.Phys.J. C46 (2006) 27–42.
`arXiv:hep-ex/0508055`, `doi:10.1140/epjc/s2005-02471-x`.

[169] S. Chekanov, et al., Forward-jet production in deep inelastic *ep* scattering at HERA, Eur.Phys.J. C52 (2007) 515–530.
`arXiv:0707.3093`, `doi:10.1140/epjc/s10052-007-0418-0`.

[170] J. R. Andersen, et al., Small *x* phenomenology: Summary and status, Eur.Phys.J. C35 (2004) 67–98.
`arXiv:hep-ph/0312333`, `doi:10.1140/epjc/s2004-01780-x`.

[171] F. D. Aaron, et al., Multi-leptons with high transverse momentum at HERA, JHEP 10 (2009) 13.
`arXiv:0907.3627`, `doi:10.1088/1126-6708/2009/10/013`.

[172] F. D. Aaron, et al., Events with an isolated lepton and missing transverse momentum and measurement of *W* production at HERA, JHEP 03 (2010) 35.
`arXiv:0911.0858`, `doi:10.1007/JHEP03(2010)035`.

[173] A. Glazov, Averaging of DIS cross section data, in: W. Smith, S. Dasu (Eds.), Proceedings of the 13th International Workshop On Deep Inelastic Scattering (DIS 05), Vol. 792 of AIP conference proceedings, AIP, Madison, Wisconsin, USA, 2005, pp. 237–240.
`doi:10.1063/1.2122026`.

[174] F. D. Aaron, et al., Measurement of the inclusive *ep* scattering cross section at low Q^2 and x at HERA, Eur.Phys.J. C63 (2009) 625–678.
`arXiv:0904.0929`, `doi:10.1140/epjc/s10052-009-1128-6`.

[175] A. Aktas, et al., Inclusive dijet production at low Bjorken-x in deep inelastic scattering, Eur.Phys.J. C33 (2004) 477–493.
`arXiv:hep-ex/0310019`, `doi:10.1140/epjc/s2004-01644-5`.

[176] M. Mikailov, Y. Litvinov, Y. Matveenko, S. Mazurenko, V. Stratonov, Synchrotron radiation spectral distribution and dose influence on the surface states at the Si-SiO_2 interface, Nucl.Instrum.Meth. A308 (1-2) (1991) 301 – 304.
`doi:DOI:10.1016/0168-9002(91)90653-8`.

[177] G. Kulipanov, Y. Litvinov, S. Mazurenko, M. Mikhailov, V. Panchenko, Generation of surface states on the Si-SiO_2 interface under the influence of synchrotron radiation, Nucl.Instrum.Meth. A282 (2-3) (1989) 590 – 591.
`doi:DOI:10.1016/0168-9002(89)90053-3`.

[178] R. Wunstorf, H. Feick, E. Fretwurst, G. Lindström, G. Lutz, C. Osius, R. Richter, T. Rohe, A. Rolf, P. Schlichthärle, Damage-induced surface effects in silicon detectors, Nucl.Instrum.Meth. A377 (2-3) (1996) 290 – 297.

doi:DOI:10.1016/0168-9002(96)00218-5.

[179] C. Becker, C. Gossling, C. Lichau, T. Wubben, J. Wüstenfeld, et al., Gate-controlled diodes for characterization of the Si-SiO_2 interface with respect to surface effects of silicon detectors, Nucl.Instrum.Meth. A444 (2000) 605–613. doi:10.1016/S0168-9002(99)01177-8.

[180] D.-S. Lee, C.-Y. Chan, Oxide charge accumulation in metal oxide semiconductor devices during irradiation, Journal of Applied Physics 69 (10) (1991) 7134–7141. doi:10.1063/1.347603.

[181] H. Perrey, Radiation damage studies for silicon sensors for the XFEL, in: A. Zichichi (Ed.), The Most Unexpected At LHC And The Status Of High Energy Frontier, Proceedings of the International School of Subnuclear Physics (ISSP), Erice, Italy, 29 August - 7 September, 2009, Vol. 47 of The Subnuclear Series, World Scientific, exp. 2011.

[182] E. Fretwurst, F. Januschek, R. Klanner, H. Perrey, I. Pintilie, F. Renn, Study of the radiation hardness of silicon sensors for the XFEL, in: Nuclear Science Symposium Conference Record, IEEE, 2008, pp. 2535 – 2538.

[183] T. Tanaka, H. Kitamura, SPECTRA: a synchrotron radiation calculation code, Journal of Synchrotron Radiation 8 (6) (2001) 1221–1228. doi:10.1107/S090904950101425X.

[184] T. Tanaka, H. Kitamura, Recent progress of the synchrotron radiation calculation code SPECTRA, AIP Conference Proceedings 879 (1) (2007) 355–358. doi:10.1063/1.2436073.

[185] J. H. Hubbell, S. M. Seltzer, Tables of X-ray mass attenuation coefficients and mass energy-absorption coefficients from 1 keV to 20 MeV for elements $Z = 1$ to 92 and 48 additional substances of dosimetric interest, National Institute of Standards and Technology, NISTIR 5632 (1996). URL http://www.nist.gov/pml/data/xraycoef/index.cfm

[186] F. Renn, A practical guide for measuring and radiating diodes intended for research on intense x-ray radiation tolerant silicon detectors, DESY summer student report (2007). URL http://www.desy.de/f/students/2007/reports/renn.pdf

[187] A. S. Grove, D. J. Fitzgerald, Surface effects on p-n junctions: Characteristics of surface space-charge regions under non-equilibrium conditions, Solid-State Electronics 9 (8) (1966) 783 – 806. doi:DOI:10.1016/0038-1101(66)90118-3.

[188] ROSE Collaboration, Proposal for further work on radiation hardening on silicon detectors, CERN/LHCC 96-23, P62/LHC R&D (April 1996).

[189] ATLAS Collaboration, ATLAS pixel detector technical design report, CERN/LHCC 98-13 Vol. 1 (May 1998).

[190] H. Feick, Radiation tolerance of silicon particle detectors for high-energy physics

experiments, Ph.D. thesis, Hamburg University, Hamburg (1997).
URL `http://cdsweb.cern.ch/record/335685`

[191] S. M. Sze, Physics of Semiconductor Devices, Wiley, New York, 1969.

[192] A. S. Grove, Physics and Technology of Semiconductor Devices, Wiley, John & Sons, 1967.

[193] E. H. Nicollian, J. R. Brews, MOS (Metal Oxide Semiconductor) Physics and Technology, Wiley, New York, 1982.

[194] D. J. Fitzgerald, A. S. Grove, Surface recombination in semiconductors, Surface Science 9 (2) (1968) 347 – 369.
`doi:DOI:10.1016/0039-6028(68)90182-9.`

[195] J. S. Uranwala, J. G. Simmons, H. A. Mar, Nonsteady-state techniques for determining the energy distribution of interface traps in MNOS (memory) devices, Appl. Phys. Lett. 26 (1975) 697.
`doi:10.1063/1.88040.`

[196] D. Fleetwood, Fast and slow border traps in mos devices, IEEE Trans. Nucl. Sci. 43 (3) (1996) 779 –786.
`doi:10.1109/23.510713.`

[197] D. Fleetwood, 'border traps' in mos devices, IEEE Trans. Nucl. Sci. 39 (2) (1992) 269 –271.
`doi:10.1109/23.277495.`

[198] D. M. Fleetwood, P. S. Winokur, J. R. A. Reber, T. L. Meisenheimer, J. R. Schwank, M. R. Shaneyfelt, L. C. Riewe, Effects of oxide traps, interface traps, and "border traps" on metal-oxide-semiconductor devices, J. Appl. Phys. 73 (10) (1993) 5058–5074.
`doi:10.1063/1.353777.`

[199] D. M. Fleetwood, M. R. Shaneyfelt, W. L. Warren, J. R. Schwank, T. L. Meisenheimer, P. S. Winokur, Border traps: Issues for mos radiation response and long-term reliability, Microelectronics and Reliability 35 (3) (1995) 403 – 428.
`doi:DOI:10.1016/0026-2714(95)93068-L.`

[200] I. Pintilie, C. M. Teodorescu, F. Moscatelli, R. Nipoti, A. Poggi, S. Solmi, L. S. Løvlie, B. G. Svensson, Analysis of electron traps at the 4H-SiC/SiO_2 interface; influence by nitrogen implantation prior to wet oxidation, Journal of Applied Physics 108 (2) (2010) 024503.
`doi:10.1063/1.3457906.`

[201] R. Lindner, Semiconductor surface varactor, Bell System Technical Journal 41 (1962) 803–831.
URL `http://www.alcatel-lucent.com/bstj/vol41-1962/articles/bstj41-3-803.pdf`

[202] S. Veljovic, X-ray radiation damage studies for silicon surfaces, Studienarbeit am Institut für Experimentalphysik, Universität Hamburg, (unpublished) (June 2009).

[203] F. J. Morin, J. P. Maita, Electrical properties of silicon containing arsenic and boron, Phys. Rev. 96 (1) (1954) 28–35.
`doi:10.1103/PhysRev.96.28`.

[204] T. Meisenheimer, D. Fleetwood, Effect of radiation-induced charge on $1/f$ noise in MOS devices, Nuclear Science, IEEE Transactions on 37 (6) (1990) 1696 –1702.
`doi:10.1109/23.101179`.

[205] D. M. Fleetwood, W. L. Warren, M. R. Shaneyfelt, R. A. B. Devine, J. H. Scofield, Enhanced MOS $1/f$ noise due to near-interfacial oxygen deficiency, Journal of Non-Crystalline Solids 187 (1995) 199 – 205, amorphous Insulating Thin Films II.
`doi:10.1016/0022-3093(95)00138-7`.

[206] J. Zhang, I. Pintilie, E. Fretwurst, R. Klanner, Study of radiation damage induced by 12 keV X-rays in MOS structures built on high resistivity n-type silicon, to be submitted to APL.

[207] Synopsys, Inc., TCAD software.
URL `http://www.synopsys.com/products/tcad/tcad.html`

[208] Adaptive gain integrating pixel detector, web page (2009).
URL `http://hasylab.desy.de/science/developments/detectors/agipd`

The Final Page…

… of this thesis is dedicated to all the people who made the previous ones and the results presented therein possible.

First of all, I would like to thank Prof. Robert Klanner and Prof. Peter Schleper for allowing me to be a part of their outstanding working group, for their strong support, and for the opportunity to study on exciting research topics of current physics.

Many thanks also to Andreas Meyer for preparing the second "Gutachten" for this thesis.

Special thanks go to Thomas Schörner-Sadenius and Claudia Glasman for their constant help, their encouragement, and their insights into difficult technical and physics issues that they always found the time to share. And I would also like to thank Thomas specifically for the the detailed annotations to all the rough early drafts of this thesis, and for his enthusiasm for particle physics that he conveys to his students as well. Thank you both!

For the proofreading of this thesis, a multitude of lines of code, and many discussions not limited to physics I am much obliged to Jörg Behr. Thank you, Jörg!

Furthermore, I would like to thank all members of our group for the friendly, helpful, and relaxed working climate. Especially, Jula Dräger, Friederike Januschek, Alexandra Junkes, Torben Schum, and Thorben Theedt for the manifold discussions and controversies regarding physics and topics far beyond.

Whenever unexpected problems or difficulties of any kind arose, someone was there to assist and help out. For this I would like to extend my gratitude especially to Peter Buhmann, Doris Eckstein, Eckhart Fretwurst, Michael Matysek, Uwe Pein, Ioana Pintilie, André Rothkirch, and Monica Turcato.

Of course, the interest and support by the ZEUS and AGIPD collaborations are also very much appreciated and helped considerably to bring this work to fruition.

I would like to thank my parents, Gudrun and Hans-Jürgen Perrey, my sister Katharina, and my brother Heiner for their on-going support and their sincere interest in the subject matter of my career choice, despite particle physics not being all that easily accessible, particularly when explained by me.

In the same way, I would like to extend my gratitude to Vera Möller, to whom I am also deeply obliged for her constant encouragement, strong support, and patient understanding, in particular in the more stressful times during my time as PhD student.

Thank you all!